The Influence of 3D Interfaces on Mechanical Behavior of Nanolaminated Bimetallic Composites

A DISSERTATION SUBMITTED TO THE FACULTY OF THE

UNIVERSTIY OF MINNESOTA BY

Justin Yutong Cheng

IN PARTIAL FULFILLMENT OF THE REQUIREMENTS FOR

THE DEGREE OF DOCTOR OF PHILOSOPHY

Advisor: Nathan A. Mara

January 2024

“God made the bulk; the surface was invented by the devil”

-Wolfgang Pauli

“Nathan Mara invented 3D interfaces.”

-Justin Y. Cheng

“Also, what happens in New Mexico stays in New Mexico”

-J.Y.C.

Acknowledgements

My thanks goes out to everyone I've met who made life worth living. I couldn't have weathered the storm of the Ph.D. process without the company of friends who made it seem to go by much faster. Thanks to Kevin, Eeshani, Supriya, Nolan, and Hannah, a group of truly intelligent and kind friends with whom I shared the dubious pleasures of not only graduate school, but the Covid-19 pandemic. Barry and Sierra receive my eternal gratitude for keeping New Jersey feeling like my second home even after I left to the wintry tundra of the Land of 10,000 Lakes. Thanks to Frederico, Cutler, and friends who shared my passion for Filipino martial arts and taught me more than I wanted to know about stick fighting. To everyone concerned at our stick bruises, just know that it's our way of sharing affection. I can't thank Annie, Kenny, Ez, Tom, Jessye, and friends enough for keeping the RUFMA family alive and continuing our shenanigans during my visits home. To Ophelia, Nate, Alejandro, Chris, Kim, Matias, and other friends I met during my otherwise disastrous time at Sandia, I am truly blessed to have been adopted by you as an honorary postdoc. I hope I can cook more pizza for you in the future. 媽媽 and 爸爸, thanks for finally moving away from Jacksonville, Florida so that I can now look forward to visiting you. 哥哥, thanks so much helping me bake cookies for my defense.

I would not be where I am as a scientist without mentoring and help from my colleagues. Extra thanks go to John Carpenter, who acted as my surrogate advisor during my visits to Los Alamos and without whom I couldn't have finished my work on ARB Cu/Nb. Youxing, your guidance as a researcher in the trenches was invaluable during your too-short time at UMN. Shuozhi and Irene, thanks so much for being an absolute pleasure to work with and fostering my interest in understanding the simulations you worked on. Nico, thanks for taking so much interest in my work on nanolaminates and I hope you go far with your work in MD and PFDD. To (the

other) Kevin, Khanh, Cody, Ryan, and Sven, thank you for being crucial and willing collaborators who got things done where I couldn't at LANL. Thank you Nick, Jason, Michael, and Javier for sharing tips as seasoned veterans at Charfac and keeping the banter flowing when my results weren't. Last but not least, thank you Nate for your relentless (and sometimes thankless) input on my experiments and manuscripts. My work wouldn't be anywhere near as good as it is without it.

Acknowledgement of funding

This work was supported in part by the Department of Energy National Nuclear Security Administration Stewardship Science Graduate Fellowship program, which is provided under grant number DENA003960.

Abstract

Cu/Nb nanolaminates containing 3D interfaces (3D Cu/Nb) are used in this study to demonstrate the effects of controlled interface structure on mechanical behavior and unit deformation activity in nanostructured alloys. 3D interfaces are internal boundaries that exist on length scales relevant to unit deformation mechanisms and contain nanoscale chemical and crystallographic heterogeneities in all spatial dimensions. 3D interfaces are a new method to manipulate alloy microstructure whose effects on plastic deformation have not been previously explored in depth. Elucidation of the link between 3D interface structure and mechanical behavior will provide key insights into nanoscale metallic deformation allowing for materials that exhibit near-theoretical strengths while also being highly deformable. The exploration of these themes requires understanding of a wide range of topics in physical metallurgy, which is reflected in the structure of this thesis. Chapter 1 begins with a high-level overview of the motivation and methodology of this work. Chapters 2 introduces fundamental concepts of metallic deformation at the macroscale and the atomic scale. Chapter 3 explores the participation and influence of interfaces in atomic scale deformation and ties the nanoscale to the mesoscale by discussing previous findings about atomically sharp 2D interfaces on nanocrystalline alloy mechanical behavior. Chapter 4 introduces the experimental methods required to characterize 3D interfaces structurally and mechanically. Chapter 5 presents structural characterization results, while Chapter 6 presents mechanical characterization results. Chapter 6 contains findings from mechanical testing, while also providing discussion connecting 3D interface structure detailed in Chapter 5 to observed 3D Cu/Nb mechanical behavior. The information from these techniques are crucial to forming structure-behavior relationships detailing the effect of 3D interfaces on unit deformation, but they cannot probe the atomic scale alone, so synthesis of computational results with

experimental results is also discussed in Chapter 6. Chapter 7 concludes with a summary of key findings of this and proposes future work addressing new scientific issues raised by this work.

Table of Contents

Table of Figures

1. Introduction

1.1. Background

Nanocrystalline alloys are of great interest to the scientific community due to their outstanding mechanical properties. One commonality between most nanocrystalline metals is their high strength compared to coarser grained counterparts. Nanocrystalline strength often approaches the theoretical limit as estimated by $\mu/30$ for a defect free material, where μ is the shear modulus of the material[1]. This high strength often comes at the expense of limited ductility, leading to the "strength-ductility" tradeoff. One way to combat this tradeoff is control of grain boundary and heterophase interface structure, which is possible due to the high interface-to-volume ratio of nanocrystalline materials. Another strategy involves gradient heterostructuring, where grain size gradients combine the benefits of highly deformable large grains and strong nanocrystalline grains. Incorporating multiple phases in a composite offers another opportunity to combine high strength and deformability, which takes the forms of precipitate strengthening or synthesizing alloys incorporating multiple bulk phases. Lastly, manipulation of deformation mechanism energetics such as encouragement of deformation twinning or stress-induced phase transformation can improve strength and ductility simultaneously. This list of strategies to enhance mechanical performance without the strength-ductility tradeoff are a few examples out of many possibilities, and often breakthrough strength and ductility arises from multiple contributions in a given material. This work focuses on studying the manipulation of interface content and structure by introducing so-called "3D interfaces" into bimetallic nanolamellar composites. 3D interfaces have a significant footprint in all three spatial dimensions and contain chemical, crystallographic, and morphological heterogeneities in those dimensions. 3D interfaces are synthesized in a controlled fashion using physical vapor deposition (PVD), in which parameters such as deposition rate, substrate

temperature, and substrate bias produce desired layer thickness and interface structure. While the approach of introducing thick, graded interfaces to produce desired material properties has been studied before in contexts such as thermal barrier coatings on turbine blades, previous studies focused on interfaces that are a few microns to millimeters thick[2]. The current work is unique in that it elucidates the influence of atomic-level interface structure on unit deformation mechanisms.

1.2. Motivation

This thesis comprises an investigation of the relationship between controlled heterophase interface structure and unit deformation activity in a model nanostructured composite system. The motivation for this work arises from the following scientific issues:

1. 3D interfacial structure has not been quantified for materials with controlled microstructure. When synthesized via PVD by grading target powers in between deposition of pure layers, the first approximation of 3D interface structure would comprise a smooth chemical gradient in the deposition direction according to deposition power profile. However, this prediction is unrealistic owing to the significant contribution of surface diffusion to the final microstructure of PVD-synthesized materials. There is a competition between interface structure thermodynamics and kinetics of surface diffusion that makes the final interface structure ambiguous.
2. It is not known how unit deformation processes such as dislocation slip are affected by 3D interfaces. The interaction between dislocations and more conventional “2D interfaces” that are atomically sharp is better explored. For example, molecular dynamics and experimental work reveals the effect of 2D interfaces on dislocation transmission and nucleation for selected interface

structure, material systems, and loading conditions[3–9]. Other phenomena such as dislocation storage at interfaces are less understood. The interplay between plasticity-carrying defects and 3D interfaces must be established to understand how they can be used to manipulate mechanical properties.

These scientific issues must be studied in a model material system made by a suitable synthesis protocol using appropriate structural and mechanical characterization procedures. The results of characterization are combined with theory and simulations to draw conclusions about the effect of 3D interfaces on unit deformation activity at the nanoscale.

1.3. Methodology

1.3.1. Choice of model material system

Cu/Nb nanolaminates, or simply Cu/Nb, with controlled interfaces are used as a model system to study the influence of interface structure on mechanical behavior and unit deformation mechanisms. There are numerous characteristics that make Cu/Nb amenable to addressing the scientific issues posed above. First, when using bottom-up synthesis methods like PVD, layer thickness is monodisperse within a very narrow distribution. Second, nanolaminate composites tend to contain a limited distribution of interface types due to the energetics of interface structure at phase boundaries. For example, FCC/FCC composites like Cu-Ni often contain predominantly {100} or {111} cube-on-cube interfaces due to epitaxy during synthesis and the similarity between Cu and Ni FCC lattices[10]. Cu/Nb is a FCC/BCC system which highly prefers Nishiyama-Wasserman (NW) and Kurdjumov-Sachs (KS) (111) Cu||(110) Nb type interfaces when made using PVD[11]. The NW and KS orientation relationships are predominant in ubiquitous ferritic martensitic steels[12], making fundamental research conducted in Cu/Nb applicable to industrial alloys. Third, Cu and Nb are immiscible with a large, positive heat of mixing[13]. This provides a

driving force for phase separation during PVD synthesis of 3D interfaces, which is likely to yield heterogeneities on the length scale of a few nanometers when depositing few to tens of nanometers-thick interfaces. Additionally, the immiscibility of Cu and Nb tend to provide significant metastability of Cu/Nb interfaces[14]. This contrasts with miscible systems like Cu/Ni in which there is a strong force for mutual interdiffusion which would make preservation of as-sputtered interface structure more difficult. Lastly, Cu/Nb with 2D interfaces (2D Cu/Nb) has been very well characterized in the literature to produce a good understanding of 2D interface structure and its effect on mechanical behavior[4,15–21]. Thus, 2D Cu/Nb acts as a well-characterized experimental control for comparison of Cu/Nb with 3D interfaces (3D Cu/Nb).

1.3.2. Introduction to synthesis of 3D Cu/Nb

The specific PVD method chosen for this work is direct current (DC) magnetron sputtering. In this method, an argon plasma is struck near the surface of a permanent magnet-backed target with an applied DC bias such that argon ions are accelerated into the target by the magnetic field[22]. The argon ions then knock off, or sputter, target ions and atoms towards a substrate on which samples are grown. This synthesis method has many adjustable parameters such as target power, Ar working pressure, substrate bias, and substrate temperature that control sample microstructure[23–25]. These parameters precisely control deposition rate, allowing for fabrication of 3D interfaces and for precise and repeatable deposition of layer and interface thicknesses. An added benefit is strong epitaxy between Cu and Nb, giving a desirable limited distribution of NW and KS interface types. This method allows for the deposition of 2-10 micron thick 3D Cu/Nb films for microstructural and mechanical characterization.

1.3.3. Structural characterization of 3D Cu/Nb

1.3.3.1. FIB/SEM

Microstructural characterization of nanoscale features such as those found in 3D Cu/Nb requires electron-transparent lamellae and needle-like specimens. Lamellae thickness and needle diameters need to be less than 100 nm, requiring the use of a focused ion beam (FIB) to machine specimens. A FIB consists of a high-voltage gallium ion source and an electromagnetic focusing column to accelerate and focus an ion beam with few-nanometer spot size towards a sample to be machined[26]. The ion beam can be rastered to sputter away material in desired patterns to fabricate lamellae and needles. Most FIB work is done in dual-beam focused ion beam/scanning electron microscope (FIB/SEM) systems to allow for imaging of specimens being prepared without modifying their geometry. FIB/SEM work was also done to create micropillars for mechanical characterization.

1.3.3.2. Transmission electron microscopy

Transmission electron microscopy (TEM) is a characterization method used to resolve microstructural features in samples with sub-nanometer resolution[27]. In TEM, an electron beam accelerated to a few hundred keV is passed through an electron transparent specimen and information from the resultant scattered beam is collected. Many beam-matter interactions can occur, which arise from elastic scattering and inelastic scattering. Elastic scattering can give rise to forward scattering, low-angle coherent scattering, or high-angle incoherent scattering, all of which can be recorded to give rise to images in different modalities. Low-angle coherent scattering can also be used to produce electron diffraction patterns, allowing for local characterization of specimen crystallography. Inelastic scattering removes some kinetic energy from the incoming electron beam to generate Auger and secondary electrons, X-rays, phonons, and in some materials,

electron-hole pairs. Inelastically scattered electrons can give rise to electron-energy loss spectra, providing information about the electronic structure of the specimen. Auger electrons are not typically used in TEM, while secondary electrons are sometimes used to form images. X-rays are separated into two categories, Bremsstrahlung and characteristic. Bremsstrahlung X-rays have a broad distribution of energies that do not provide useful information, while characteristic X-rays are peaked at specific energies representing electron transitions between orbitals in specimen atoms. Characteristic X-rays are used to conduct energy dispersive X-ray spectroscopy (EDS), which allows for semi-quantitative chemical quantification in specimens. Phonons produce specimen heating, which usually is not a concern due to the low scattering cross section of most atoms under an incident few hundred keV electron beam. Electron-hole pairs are only generated in semiconductor samples and so are not relevant to metallic nanostructures. It is also important to note the two most-used imaging modalities in TEM, which are parallel-beam, or conventional TEM (CTEM) and scanning TEM (STEM). In CTEM, a parallel beam is used to image specimens in bright field, dark field, and record diffraction patterns with and without selected area apertures. TEMs with sufficiently coherent sources can perform high-resolution TEM (HRTEM), where lattice fringes can be captured in images at high magnification. In STEM, the electron beam is converged to a small probe and rastered across the specimen to capture bright field (BF), low-angle annular dark field (LAADF), and high-angle annular dark field (HAADF) images. These imaging modalities capture the beam scattered from the specimen at different angles, each of which are dominated by different contrast mechanisms. Thus, BF, LAADF, and HAADF images are used to capture different microstructural details from a given specimen. STEM is especially useful for capturing location-specific information, which is leveraged in STEM-based energy dispersive X-ray spectroscopy (STEM-EDS) to produce elemental maps. In this work, bright field CTEM and

HRTEM images, electron diffraction patterns, and STEM-EDS are used to measure microstructural metrics and evaluate crystallographic orientation in 3D Cu/Nb specimens. In particular, STEM-EDS is used to investigate chemical distribution in 3D interfaces.

1.3.3.3. Atom probe tomography

Atom probe tomography, or APT, is a technique that produces three-dimensional, nanometer resolution chemical maps of needle-shaped specimens[28]. In APT, a needle-shaped specimen is vaporized layer by layer to produce ions for characterization. These ions are funneled into a time-of-flight mass spectrometer (TOF-MS) to measure their mass-to-charge ratios. Combining prior knowledge of the sample with complex reconstruction algorithms, a three-dimensional chemical map of the needle specimen is produced in hemispherical layers. APT is used in this work to supplement STEM-EDS maps and address the limitations of TEM-based techniques. Since TEM is based on transmission of an electron beam through a specimen of finite thickness, it projects volumetric information onto a two dimensional image. For most samples, this is not an issue, but since this work aims to resolve three-dimensional chemical heterogeneities on the length scale of a few nanometers in 3D interfaces, TEM-based characterization is not sufficient to achieve the goals of this project. In other words, TEM-based characterization is limited in that it averages out nanometer-scale three-dimensional chemical heterogeneities through the thickness of 3D Cu/Nb specimens. APT is invaluable in overcoming this difficulty, but it does not come without its own shortcomings. Unfortunately, the maps that APT produce are ambiguous due to several artifacts inherent to the technique. The most prominent artifacts in multiphase samples occur from from evaporation field mismatches, trajectory aberration, and reconstruction errors. These effects will be discussed in further detail in Chapter 4. APT is used in 3D Cu/Nb to prove

the existence of chemical heterogeneities in 3D interfaces and identify the length scale associated with them.

1.3.4. Mechanical Characterization

1.3.4.1. Micropillar compression

Pillar compression is a powerful tool to study the mechanical behavior of many plastically deforming materials. It is complimentary to the "gold standard" of tensile testing. This is because it imposes a simple uniaxial stress state on a material and can extract its complete stress-strain curve. This provides many mechanical properties such as Young's modulus, yield stress, ultimate compressive stress, and work hardening rate from samples. To perform this test on thin film 3D Cu/Nb samples made by PVD, micropillar compression is employed. Put simply, a micropillar compression test is a compression test conducted on a pillar that is below 50 microns in diameter[29]. These tests are useful for sampling mechanical behavior in small volumes of material, which is well suited to testing of coatings, welds, composites, and thin films. To conduct micropillar compression, specimens of appropriate geometry must be prepared. While this can be done using various methods such as lithographic patterning with electrodeposition[30,31] and additive manufacturing[32], by far the most popular method for fabricating micropillars is through FIB/SEM[33,34]. Although use of a FIB may introduce artifacts arising from ion bombardment damage and non-ideal geometry, it remains an invaluable tool for investigating mechanics at the nanoscale. Once suitable pillars are made on a sample, compression may be carried out using nanoindentation equipment *ex situ* in ambient conditions or *in situ* inside an SEM or a TEM. *In situ* testing allows for direct observation of a compression test and recording footage of deforming specimens. Here *in situ* SEM micropillar compression is employed to study the mechanics of 3D Cu/Nb under a simple uniaxial stress state. The main advantage of using an *in situ* technique is

that strain localization can be monitored during compression tests. Testing may be aborted before catastrophic instability occurs, facilitating further post-mortem TEM characterization. Characterization of such specimens is crucial, as once strain localization begins, the stress state inside the micropillar starts to deviate from the assumed uniaxial stress state. The other advantage of directly imaging deformation is that strain localization can be observed from start to finish, whereas an *ex situ* test can only provide information about specimen morphology and microstructure at the end of the test. Micropillar compression is used in conjunction with other test methods to provide a holistic picture of mechanical behavior in 3D Cu/Nb.

1.3.4.2. Nanoindentation

Indentation techniques have been used for decades as high-throughput non-destructive mechanical test methods requiring relatively little sample preparation[35]. In this method, a hard indenter is pressed into a sample of interest, leaving a residual imprint of the indenter. The ratio of the load applied to the area of the residual indent is then computed as the "indentation hardness" of the sample. Regardless, indentation is a useful method for probing mechanical behavior in a statistically significant, location and depth-specific fashion for samples off-limits to other test techniques, such as thin films. Instrumented nanoindentation, or simply nanoindentation, has been investigated heavily as a way to extract mechanical properties from samples at the nanoscale[36]. Technically, nanoindentation is distinguished from other classes of indentation by penetration depths below a few hundred nanometers and applied loads below a few tens of millinewtons. However, colloquial usage of the term "nanoindentation" usually implies instrumented indentation, or continuous measurement of load and displacement during a test, and use of the Oliver-Pharr method to infer residual indent area from unloading stiffness during the test. Given knowledge of Hertzian contact mechanics and assumption of an incompressible sample material with a flat,

quasi-infinite geometry, nanoindentation hardness and reduced modulus can be extracted from load-displacement curves obtained from nanoindentation.

1.3.4.3. Comparison of micropillar and nanoindentation testing

Micropillar compression and nanoindentation have distinct characteristics that allow them to synergize well in mechanical characterization. Most nanoindentation platforms also support automation of arrays of indentations and data analysis, making nanoindentation a high-throughput method of obtaining flow stress estimates across tens or hundreds of indents with only a few hours of operator time. The only specimen requirement for nanoindentation is that in most cases specimens must have level, smooth surfaces and must be mounted securely to the indenter stage, meaning that in most cases less sample preparation time is required in comparison to micropillar compression. The high-throughput nature of nanoindentation is offset by difficulty of data interpretation and analysis, as well as sensitivity to calibration errors and phenomena such as indentation size effect and indentation pileup[37]. In short, nanoindentation is simple in concept, but complex to execute consistently across different specimens, instruments, and operators. Another aspect of nanoindentation worth mentioning is that it imposes a triaxial stress state, which may complicate extraction of flow stress for comparison to results from other mechanical test methods, theory, or simulations. Common practice in nanoindentation often correlates hardness measured with a pyramidal Berkovich or Vickers tip to the uniaxial tensile strength by dividing by a constant factor of 2.7-3 independent of material properties. This factor is called the Tabor factor or constraint factor. Tabor factor is in fact a function of many other variables, such as sample Young's modulus, and work hardening behavior[38,39], and work is ongoing to understand the assumptions needed to use the Tabor factor accurately.

Micropillar compression comes with its own benefits and drawbacks. Sample preparation can be time-consuming when done using FIB, which can make data collection from statistically representative populations costly in money and/or effort. However, data analysis is more straightforward than nanoindentation provided that commonly held assumptions for uniaxial testing apply. Chief among these is the presumption of right cylindrical gage section geometry through the entirety of the test. Realities such as pillar taper from FIB preparation and presence of plastic instability during the test complicate proper accounting of gage length and cross-section. In addition, micropillar compression can be susceptible to phenomena such as specimen size effects[40]. Regardless, if the stress-strain curve extracted from micropillar compression accurately accounts for changes in gage geometry, yield and flow stresses can be extracted that are unequivocally comparable to other test methodologies and theoretical and computational predictions. It should be noted that both nanoindentation and micropillar compression are highly sensitive to specimen-specific characteristics such as surface oxides and subsurface damage left over from insufficient mechanical polishing.

1.3.4.4. Synergy of micropillar and nanoindentation testing

Because of the differing and sometimes opposing characteristics between nanoindentation and micropillar compression, they can be combined to produce synergy in mechanical characterization. Here, the differing stress states produced by each technique produces different trends in mechanical properties with respect to interface structure. This provides information about the stress-state dependence of 3D interface-affected mechanical behavior. Incidentally, nanoindentation provided quick, time-efficient mechanical characterization in deposited films to verify that deposited 3D Cu/Nb samples were not overly porous and possessed layer and interface thicknesses close to desired values.

1.4. Hypotheses

The experimental methods described above were used to test the following hypotheses to address the scientific issues presented in Section 1.2.

1. 3D interfaces contain chemical and structural heterogeneities a few nm wide in all spatial dimensions
2. 3D interfaces increase resistance to interfacial slip transmission and shearing when compared to 2D interfaces
3. 3D interfaces can modify dislocation activity to enhance deformability and strength simultaneously
4. 3D interface contribution to mechanical characterization is dependent on the relative length scale between interface structural features and strength-limiting unit deformation active in abutting phases.

Hypothesis 1 will be addressed using TEM and APT results, and Hypotheses 2-4 will mainly be addressed with micropillar compression, nanoindentation, and post-mortem TEM of deformed microstructures.

1.5. Overview of dissertation

This work is split up into Chapters that expand upon the concepts described in the Introduction in greater detail. Chapters comprise the top levels of headings in this document (1. corresponds to Chapter 1, 2. corresponds to Chapter 2, and so on). Chapter 2 features a general background of plasticity in metals and the role of defect-interface interactions in determining mechanical behavior. Chapter 3 expands upon the concepts in Chapter 2 in the context of metallic nanolaminates and 3D Cu/Nb. Chapter 4 describes the experimental techniques covered in Sections 1.3.3-1.3.4 in greater detail. Chapter 5 describes results obtained from structural

characterization of 3D Cu/Nb via TEM and APT. Chapter 6 details mechanical testing results from micropillar compression and nanoindentation on 3D Cu/Nb. These results are compared with past 2D Cu/Nb work to draw conclusions about the role of interface structure on mechanical behavior in nanostructured composites. These conclusions are combined with observations from Chapter 5 and additional simulations and theory to provide insights into the effect of 3D interface structure on dislocation activity. Chapter 7 will summarize the results and findings from Chapter 5 and 6 and use them to motivate future work.

2. Fundamentals of metallic deformation

The basics of metallic deformation can be found in Dieter[41] and will be recounted here. Metals are a class of materials generally known for substantial ductility and versatility in structural applications. Uniaxial deformation is the simplest form of understanding mechanical behavior, where load is applied to a cylindrical specimen only along its long axis[41]. When a tensile or compressive load is applied the ends of the specimen will undergo displacement due to the deformation across the entire specimen. Load and displacement are often normalized by the sample's cross-sectional area and gage length, respectively, to compute stress and strain. The advantage of stress and strain is that they are intensive quantities, meaning that they are comparable among many different sizes and shapes of specimens made of the same material. When considering deformation, there are two types: elastic and plastic. Elastic deformation is characterized by a linear stress-strain relationship and reversibility. Reversibility entails that a sample undergoing only elastic deformation will return to its initial geometry after unloading. Plastic deformation is often characterized by a non-linear stress-strain relationship and is irreversible, meaning that a sample will not return to its original shape after unloading. The geometry of elastic and plastic deformation is depicted in Figure 2-1.

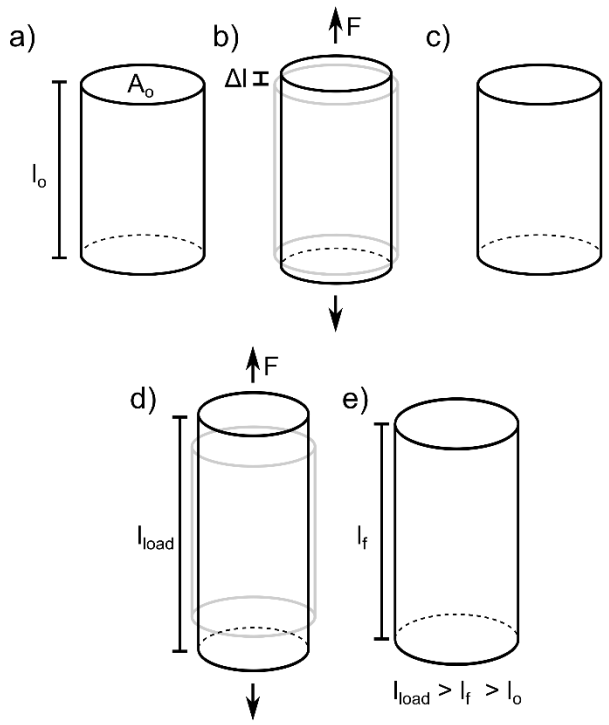

Figure 2-1 – An illustration of the differences between elastic and plastic deformation. a) Computation of stress and strain requires a specimen of known geometry for which cross-sectional area A and gage length l are well-defined. b) A small amount of tensile force F can deform the specimen in a), giving rise to an increase in gage length ∆l. c) Small enough forces produce only elastic deformation. d) Here, a larger force F is applied to the specimen, taking the gage length to l_{load}, the length under loading. e) After removal of the load some elastic recovery occurs and residual deformation remains, constituting plastic deformation.

To quantify deformation and mechanical properties, stress-strain curves are obtained using uniaxial tensile or compressive tests. A generalized tensile engineering stress-strain curve representative of a material that undergoes both elastic and plastic deformation is presented in Figure 2-2. Engineering stress (σ_e) and strain (ε_e) are calculated using the equations below:

$$\sigma_e = \frac{F}{A_o}$$

$$\varepsilon_e = \frac{\Delta l}{l_o} = \frac{l_i - l_o}{l_o} \tag{2-1}$$

Here, F is the instantaneous applied load, A_o is the initial cross-sectional area of the specimen gage, and l_i and l_o are the instantaneous and initial gage lengths, respectively. The initial linear portion of the curve represents elastic deformation and is followed by the non-linear portion of the curve representing plastic deformation. The slope of the elastic portion of this curve gives the Young's modulus of the material. The two regimes are delineated by the yield point, which is characterized by a yield stress and strain past which the material deforms irreversibly. While the yield point is often thought of as a sharp delineation between elastic and plastic deformation, in practice many materials undergo an elastic-to-plastic transition over finite stress and strain. This is due to heterogeneities in material microstructure and properties in the specimen and is pertinent to polycrystalline metals and alloys containing precipitates or multiple phases. Thus, a few different mathematical criteria are often used to define yield point. The one used in this work is deviation from linearity, where a straight line is fit to the linear portion of the stress-strain curve and the yield point is defined by where the curve deviates from the straight line by 5%. This criterion is more easily used for stress-strain curves produced from mechanical tests with non-ideal contact conditions such as those found in micropillar compression testing.

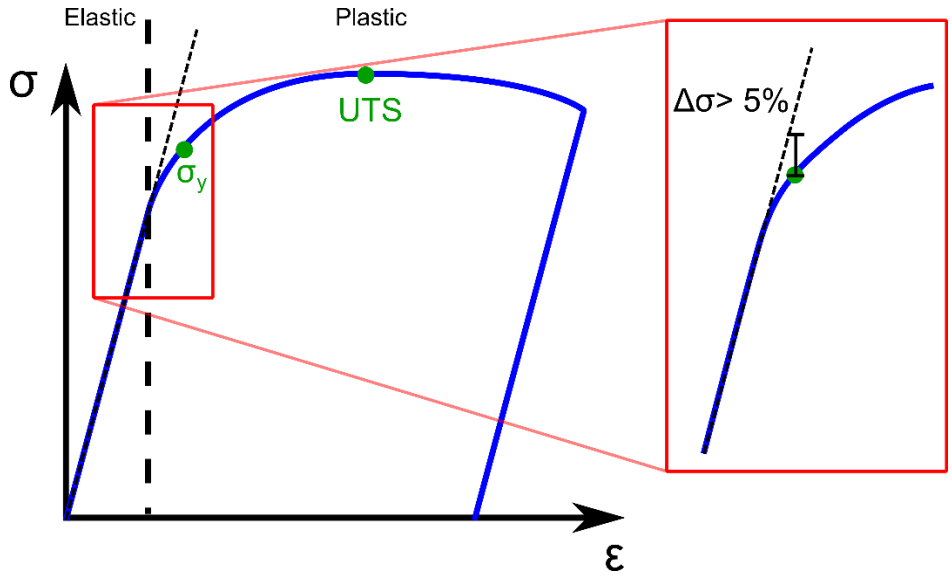

Figure 2-2 – An engineering stress-strain curve typical of many metals. The curve can be split into two portions, the linear elastic portion to the left of the dotted line, and the nonlinear plastic portion to the right. Typically useful quantities are depicted by σ_y and UTS, standing for yield stress and ultimate tensile stress. The inset demonstrates one method of finding the deviation from linearity that is used to define σ_y.

The plastic portion of the curve also has a few important features. First, it is important to note that the strength of the material increases as plastic strain accumulates. This phenomenon is called strain hardening or work hardening and is characteristic of most plastically deforming metals. This is caused by the accumulation and interaction of many (up to 10^{14}-10^{16} dislocations intersecting 1 m^2 of material), the mechanism of which will be discussed in Section 2.2. Second, a maximum in engineering stress occurs at extended plastic strain. This point is referred to as the ultimate tensile strength, or the UTS. For compression tests, the analogous quantity is the ultimate compressive strength. For most metals, there is little to no asymmetry between tension and compression, leading to similar stress-strain curves between tension and compression up to and near yield. The last important feature is the point at which the curve ends. This point is associated with the fracture or rupture strain, at which the specimen breaks into two or more pieces. While the engineering stress-strain curve is instrumental in characterizing many structural materials,

often it is important to account for changing specimen cross-sectional area and gage length to produce a true stress-strain curve. The equations used for the true stress σ_t and strain ε_t are found below:

$$\sigma_t = \frac{F}{A_i} = \frac{F}{A_o} \cdot \frac{A_o}{A_i} = \sigma_e \cdot \frac{l_i}{l_o} = \sigma_e \left(\frac{l_o + l_i - l_o}{l_o} \right) = \sigma_e (1 + \varepsilon_e)$$

$$\varepsilon_t = \int_{l_o}^{l_i} d\varepsilon_t = \int_{l_o}^{l_i} \frac{dl_i'}{l_i'} = \ln\left(\frac{l_i}{l_o}\right) = \ln\left(\frac{l_o + l_i - l_o}{l_o}\right) = \ln(1 + \varepsilon_e)$$

(2-2)

The only new quantity introduced here over Equation (2-1) is A_i, the instantaneous cross-sectional area of the specimen gage. Note that volume conservation is used to re-express the ratio (A_o/A_i) in terms of gage length for the σ_t equation. Also, ε_t accounts for continuously changing gage length so it must be expressed differentially, giving rise to an integral in its calculation. Lastly, it is important to note that Equations (2-2) are only valid while the sample deforms uniformly, a point that will be discussed below.

True stress and strain allow for a more accurate quantification of properties past plastic instability. At the UTS, a localized portion of the specimen's gage length narrows faster than the rest of the gage length. This phenomenon is called necking and represents the point at which the material cannot work harden fast enough to overcome the increasing stress on the material. Past this point, most of the plastic strain accumulates inside the neck and the specimen eventually ruptures at the neck. The true plastic strain between yield and necking is defined as ductility in a tensile test, or equivalently uniform deformability. While it may appear on the engineering stress-strain curve that the material softens past the UTS, this is not the case. If a true-stress strain curve

is constructed by direct measurement of sample area in the neck after the onset of necking, then the material continues work hardening after necking. This can be seen in Figure 2-3.

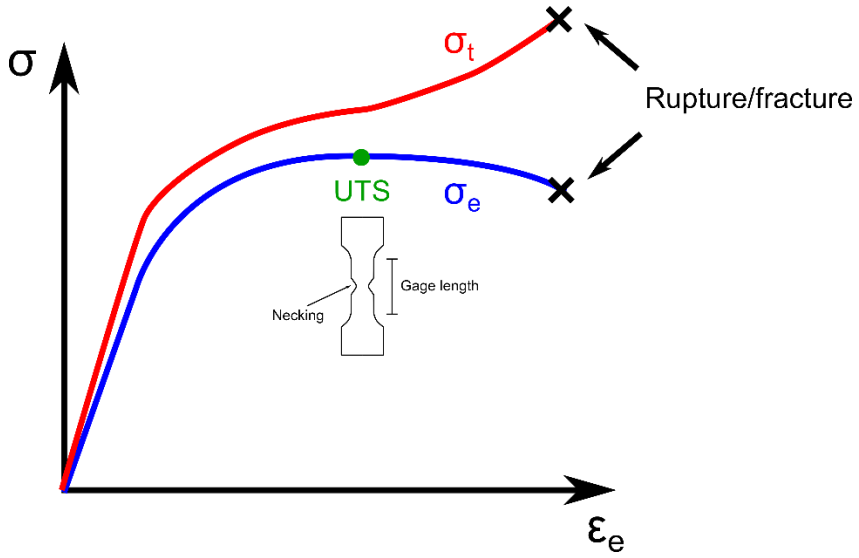

Figure 2-3 – A depiction of the differences between true and engineering stress. Note that strain is engineering between the two curves so that they are comparable. Past UTS, necking occurs in the specimen and produces non-uniform deformation. Past necking, true stress rises while engineering stress decreases. Here, true stress accounts for changes in specimen geometry, while engineering stress does not.

Note that the only material that continues work hardening past necking is found mostly in the neck. Since plastic strain localizes to the neck, surrounding material that does not plastically deform stops work hardening. The true-stress strain curve is useful in that it accurately depicts stress and strain at large plastic deformation and work hardening rate after necking. Because of the latter characteristic, work hardening rate can be quantified according to a variety of models. Many metals obey the Holloman work hardening law, which is:

$$\sigma_t - \sigma_{y,t} = K\left(\epsilon_t - \epsilon_{y,t}\right)^n \tag{2-3}$$

Here, σ_t and $\sigma_{y,t}$ are true stress and true yield stress, K is a constant, ε_t and $\varepsilon_{y,t}$ are true strain and true yield strain, and n is the Holloman work hardening parameter. The work hardening parameter is often used to compare plastic behavior among different metals and alloys. Other work hardening models have been developed, but they will not be discussed here.

2.1. Plastic deformation in single crystal metals

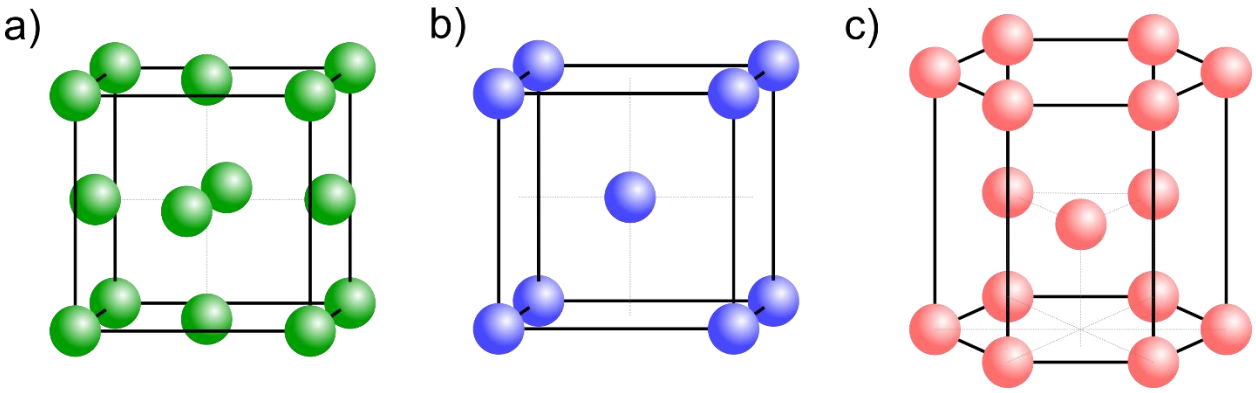

Figure 2-4 – Illustrations of the unit cells of a) FCC, b) BCC, and c) HCP crystal structures. These are the most commonly found in elemental metals.

Here, pure crystal mechanical behavior is discussed to underscore the plastic anisotropy that arises from atomic structure and is important for understanding deformation in polycrystal metals studied in this work and commonly used in engineering. The fundamental nature of metallic deformation was historically studied in simple, model systems. These systems comprised single crystals of pure metals such as iron, aluminum, or zinc[42,43]. Many metal single crystals display appreciable work hardening and significant ductility. However, this is a function of the crystal structure of the metal, the most common of which are depicted in Figure 2-4. In their pure form, FCC and BCC metals tend to be more ductile and work hardenable, while HCP metals tend to be brittle or not as work hardenable[44]. During plastic deformation metal single crystals deform by forming slip steps, which form on the specimen surface due to shearing exclusively on one or a few sets of parallel planes. While one might assume that these planes correspond to specific

crystallographic planes, this is only true in certain cases for FCC and HCP crystals[45,46]. While slip steps also form in BCC metals, they can form along arbitrary planes depending on loading orientation[42]. The relationship between slip and crystallography will be covered in detail for FCC and BCC metals in Section 2.3. Another key observation from single crystals is that mechanical behavior can be very anisotropic, both in terms of work hardening behavior and strength. For example, while work hardening occurs in all single crystal orientations for FCC crystals, in some orientations work hardening can be split up into three distinct stages, while for other orientations no such distinction can be made[47]. This loading anisotropy is depicted in Figure 2-5.

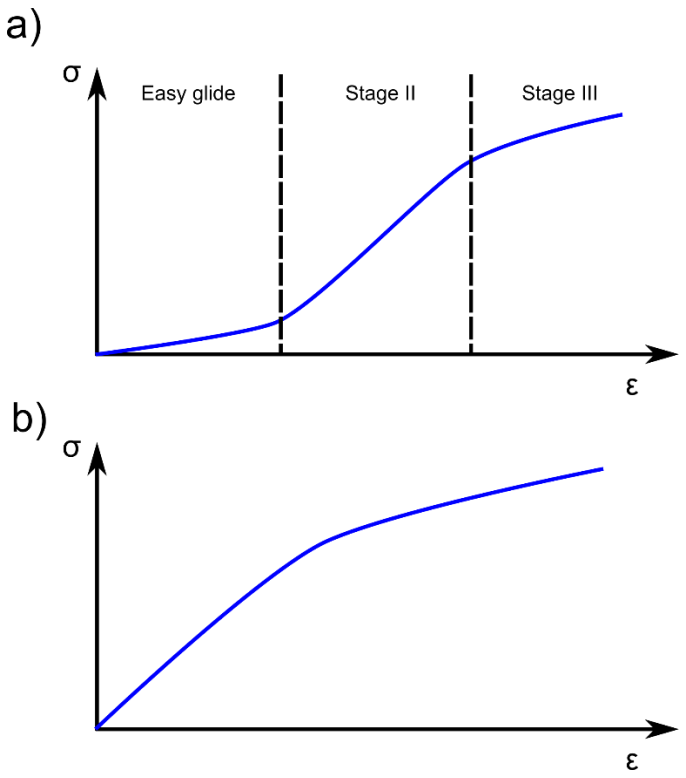

Figure 2-5 – Metallic single crystals can behave drastically differently under different loading conditions. a) Three-stage hardening characteristic of FCC single crystals oriented for primary slip followed by secondary slip. b) The same FCC crystal loaded in another orientation may show no such behavior due to multiple slip. Note that elastic deformation is not included in these stress-strain curves here since yield stress and strain are negligible for most single crystals.

The yield stress of single crystals are extremely low compared to theoretical strength as estimated by the stress required to shear a perfect lattice by sliding two perfect, adjacent atomic planes[1]. The elastic distortion required for this deformation requires a stress on the order of $\mu/30$, where μ is the shear modulus of the material. In practice, the yield strength of well-annealed single crystal metals is usually three or four orders of magnitude lower than the theoretical strength. The significant work hardenability and ductility of metal single crystals, as well as their anisotropy in work hardening behavior and observed strength can be explained by examination of atomic scale microstructure in metals.

2.2. Microscopic description of plasticity

2.2.1. Dislocations and dislocation strain fields

Generally, the theoretical strength is usually only achievable in perfect, defect-free crystals. In practice, a wide variety of point, line, and planar defects are often found in even well-annealed single crystals[48]. Other defects such as stacking fault tetrahedra and voids can be conceptualized as volumetric defects. Point defects are thermodynamically stable and must be found in any metal that is in thermodynamic equilibrium[49]. The most pertinent defect to plastic deformation in metals is the dislocation. A dislocation is a line defect defined relative to a perfect crystal lattice. To make this comparison, a loop of fixed length called a Burgers circuit (Figure 2-6) is drawn on a perfect lattice as a reference, and then again around the dislocation line. The loop drawn on the perfect lattice will be closed, while the loop drawn around the dislocation line will be open. The distance required to close the loop around the dislocation line is called the Burgers vector. There are two commonly discussed types of dislocations, edge and screw. Edge dislocations have Burgers vectors perpendicular to the dislocation line, while screw dislocations have Burgers vectors parallel to the dislocation line. Any dislocation with a Burgers vector that is angled between 0 and

90 degrees with respect to the dislocation line is called a mixed dislocation. An edge dislocation can be created by inserting an extra half plane of atoms into a perfect lattice, while a screw dislocation is created by shearing half of a perfect lattice by one Burgers vector along the dislocation line.

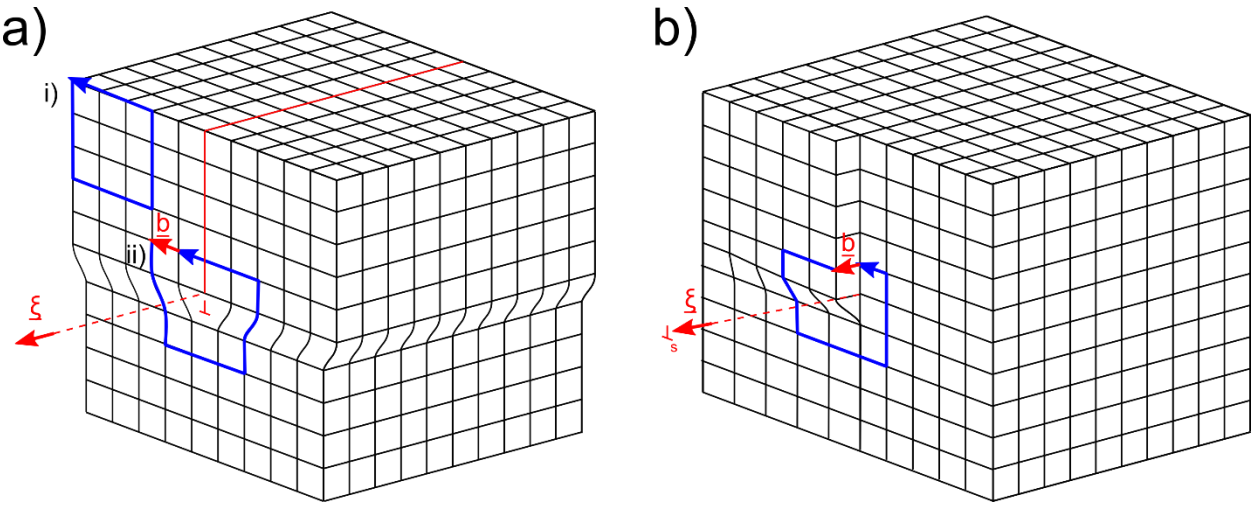

Figure 2-6 – Illustrations of the a) edge and b) screw dislocation. In a), the Burgers vector is perpendicular to the dislocation line sense vector ξ and in b) it is parallel.

Dislocations enable large plastic strains and act as the predominant "carriers" of plastic deformation in most metals. The way that dislocations enable large plastic strain is that they act as stress concentrators that allow metal lattices to locally shear at much lower applied stresses than predicted for a perfect lattice. As a metal plastically deforms on a macroscopic level, dislocations move across the material at the atomic scale to accommodate the plastic strain. This process is called dislocation slip, or glide. Each dislocation that moves contributes one Burgers vector's worth of displacement to the overall plastic strain. Without dislocations, any attempt to plastically deform metals would likely require so much strain energy that the material would fracture before plastically deforming.

Dislocations introduce displacements in perfect crystal lattices, generating elastic stress and strain fields that have a profound influence on plastic deformation. For simplicity, only screw dislocation stress and strain fields are discussed as they have a simpler functional form than edge dislocations. A suitable expression for the displacement around a screw dislocation is as follows:

$$u = 0\,, v = 0, w = \frac{b}{2\pi}\tan^{-1}\frac{y}{x} \tag{2-4}$$

where u, v, and w stand for x, y, and z displacements, b is the Burgers vector length, and r is the distance away from the dislocation line. Computation of strain fields are simpler in Cartesian coordinates, but are expressed more easily in polar coordinates, so both will be used. The strain field associated with a screw dislocation is:

$$\epsilon_{xz} = \frac{\partial u}{\partial z} + \frac{\partial w}{\partial x} = \frac{b}{2\pi}\frac{y}{x^2 + y^2}$$

$$\epsilon_{yz} = \frac{\partial v}{\partial z} + \frac{\partial w}{\partial y} = \frac{b}{2\pi}\frac{x}{x^2 + y^2}$$

$$\epsilon_{xx} = \epsilon_{yy} = \epsilon_{zz} = \epsilon_{xy} = 0 \tag{2-5}$$

The only symbol introduced over Equation (2-5) is θ, which is the polar angle measured using the dislocation line as the origin. From these equations, only shear strains acting in the z direction are nonzero. The stresses associated with these strains are:

$$\sigma_{xz} = \frac{b\mu}{2\pi}\frac{y}{x^2 + y^2}$$

$$\sigma_{yz} = \frac{b\mu}{2\pi}\frac{x}{x^2 + y^2}$$

$$\sigma_{xx} = \sigma_{yy} = \sigma_{zz} = \sigma_{xy} = 0$$

(2-6)

Likewise, only stresses acting along the z direction are nonzero. Expressed in polar coordinates, the nonzero terms of stress and strain are:

$$\epsilon_{\theta z} = \frac{b}{2\pi r}$$

$$\sigma_{\theta z} = \frac{b\mu}{2\pi r}$$

(2-7)

From these equations, stresses rise asymptotically to infinity as the dislocation line is approached. However, this does not mean that the strain energy of a dislocation is infinite. The energy of a dislocation can be split up into two contributions: one from elastic strain energy far from the dislocation line and another from elastic strain energy close to the dislocation line. The elastic strain energy contributed by the dislocation can be obtained by integrating elastic strain energy density from a finite distance from the dislocation line, usually taken to be 5b, to infinity. This energy is expressed as:

$$\xi = \frac{\mu b^2}{4\pi} \ln \frac{R}{5b}$$

(2-8)

Here, ξ is the elastic dislocation-self energy per unit length and R is the size of the crystal in consideration. Far from the dislocation line, continuum solid mechanics is valid and so the

dislocation self-energy from that portion of material can be calculated from Equations (2-8). This is not the case for the dislocation self-energy close to the dislocation line. Continuum mechanics assumes that solids are homogeneous and that volume elements can be infinitesimally small. As r approaches 0, energetics are determined at atomic scale and the finite size of atoms and their deviation from continuum behavior must be considered. One such deviation is that atoms close to the dislocation line rearrange to minimize their energy according to their quantum mechanically determined bonding, which is not captured in purely continuum mechanical approaches. This rearranged structure is called the dislocation core[50]. The dislocation core can occupy anywhere from a few atomic layers surrounding the dislocation line to many nanometers across, usually ~5-10b. Well-studied dislocation core structures include extended dislocations in FCC crystals[51] and relaxed [111]-type screw dislocation cores in BCC crystals[52]. The dislocation core structure possesses a finite energy that must be taken into account not only in experiments[53], but also theoretical predictions[54] and simulations[55]. While not directly within the scope of the current work, experimental findings presented here may have implications for validating and guiding such dislocation-based deformation models.

2.2.2. Dislocation-dislocation interactions

The more important consequence from Equations (2-7) is that each dislocation possesses an elastic strain field that interacts with other strain fields in the material. These strain fields may result from far-field deformation, or defects such as vacancies, dislocations, or grain boundaries. Here, one of the most important interactions will be discussed: dislocation-dislocation interactions. To do so requires consideration of forces on a dislocation that resulting from an external strain fields.

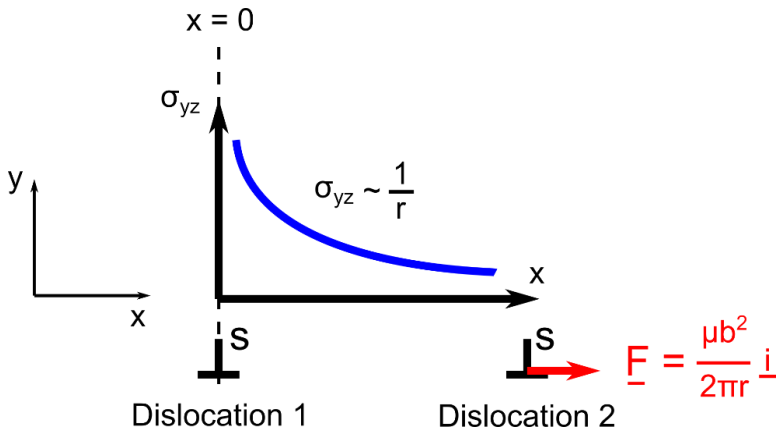

Figure 2-7 – An illustration of the interaction of two screw dislocation of the same sign. Dislocation 1 possesses a stress field that decays with 1/r. Dislocation 2 then experiences a repulsive force in accordance with the Peach Koehler equation. This force also decays with 1/r and is only a function of the shear stress component σ_{yz} of Dislocation 1's stress field.

This force is called the Peach Koehler force, and is calculated using the geometry of the dislocation. If $\underline{b}$ represents the Burgers vector, $\underline{t}$ represents the dislocation line sense vector, and $\underline{\underline{\sigma}}$ represents the stress tensor corresponding to an applied strain, then the force $\underline{F}$ experience by a dislocation is expressed as:

$$\underline{F} = (\underline{\underline{\sigma}} \cdot \underline{b}) \times \underline{t} \tag{2-9}$$

From this equation, it is possible to predict what the interaction between two dislocations is. For example, if two screw dislocations of parallel line sense and Burgers vector are placed next to each other on the x-axis at a distance r (as in Figure 2-7), then the force that the left dislocation exerts on the right dislocation can be expressed as:

$$\underline{F} = \frac{\mu b^2}{2\pi r}\,\underline{i}$$

(2-10)

Since this force acts to push the right dislocation away from the left dislocation, this is a repulsive force. If one of the dislocations' Burgers vector is flipped, then the sign of the force exerted by the right dislocation on the left dislocation is also flipped – the force becomes attractive.

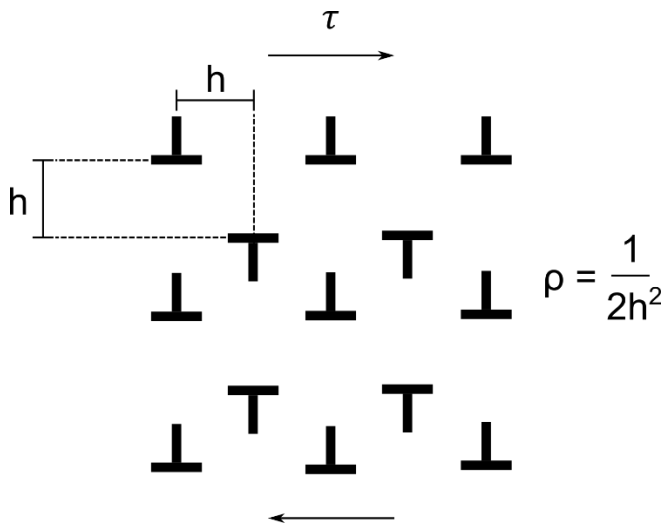

Figure 2-8 – A common way to model a dislocation forest in a cold-worked metal. This forest extends infinitely in all directions and the shear stress required to move the dislocations past each other control the strength. This shear stress is controlled by the dislocation density ρ.

This simple illustration demonstrates that dislocations have profound influences on each other and thus drive one of the characteristic properties of metals – they enable significant amounts of work hardening. One common model proposed to explain work hardening involves a "dislocation forest" depicted in Figure 2-8. As discussed before, plastic strain in metals involves the movement of dislocations. Each dislocation contributes one Burgers vector of worth of displacement, so as plastic strain increases, dislocations must be generated to produce the macroscopic strain observed in the material. Dislocation content, or dislocation density, is measured in length of dislocation lines per unit volume, but it may be idealized as a regular array of dislocations normal to some reference plane. In this simple model, it may be useful to think of

dislocation content in terms of the number of dislocations intersecting a unit area. One way to compute the strength of a metal in this model is to compute the shear stress required for a dislocation to move through this dislocation forest. In the well-known Taylor strengthening model, shear stress is expressed as a function of dislocation density[48]:

$$\tau_c = \alpha \mu b \sqrt{\rho} \tag{2-11}$$

Here, τ_c is the critical shear stress required to move the cutting dislocation across the dislocation forest, α is equal to about 0.1, and ρ is the dislocation density. It is important to note that in most cases, and indeed in engineering alloys with complex microstructures, dislocation microstructure is much more complex than presented in the Taylor hardening model. However, it is generally true that if a metallic sample can store significant dislocation content, then as cold work increases, dislocation content increases and the metal work hardens.

2.3. Relationship between dislocations and crystallography

2.3.1. General considerations of dislocation geometry

A dislocation's propagation geometry is inextricably tied to the crystal structure housing it, meaning that dislocation Burgers vectors and line sense vectors do not take on arbitrary values. The slip plane and direction constrain these vectors according to crystal structure. The slip plane is a plane that a dislocation is restricted to as it slips, while the slip direction describes the motion of atoms as the dislocation moves (this is defined by the Burgers vector). Edge dislocations are confined to a single slip plane, while screw dislocations can undergo cross-slip to change slip planes. In general, dislocations favor the closest packed crystal planes for slip planes and the

closest packed interplanar direction for slip directions. Together, a combination of slip plane and slip direction is called a slip system. Different crystal structures have different favored slip systems. Here, FCC and BCC slip systems will be discussed because they underpin deformation of Cu and Nb, respectively, in the nanolaminates studied for this work.

2.3.2. Dislocations in FCC metals

The face-centered cubic, or FCC, crystal structure consists of atoms at every corner and face center of a cubic unit cell. This crystal structure is close-packed, meaning that it represents one of the ways to arrange spherical atoms of uniform size such that maximum density is achieved. The close-packed planes in this crystal structure belong to the {111} family, while the close-packed direction in those planes belong to the <110> family. Thus, favored slip systems in FCC are of the {111}<110> type. There are 48 distinct, but symmetrically equivalent variants of {111}<110> slip systems (24 if differently signed slip along a given slip direction is considered equivalent). An illustration of one such slip system is found in Figure 2-10. This is the highest number out of the three predominant elemental metal crystal structures, conferring higher ductility in general to FCC metals as compared to other crystal structures. FCC dislocations do not exclusively have <110> type Burgers vectors – they can also have <112> type Burgers vectors. The <110> type Burgers vector is a type of full, or perfect, dislocation which preserves periodicity of the lattice after slip. In contrast, <112> type dislocations are called partial dislocations, because they disturb lattice periodicity. A single a/2<110> perfect dislocation can dissociate into two a/6<112> dislocations, or Shockley partials, leaving a stacking fault in between the partials. Here, a is the lattice parameter of the FCC material. The splitting of a perfect dislocation into Shockley partials is illustrated in Figure 2-9.

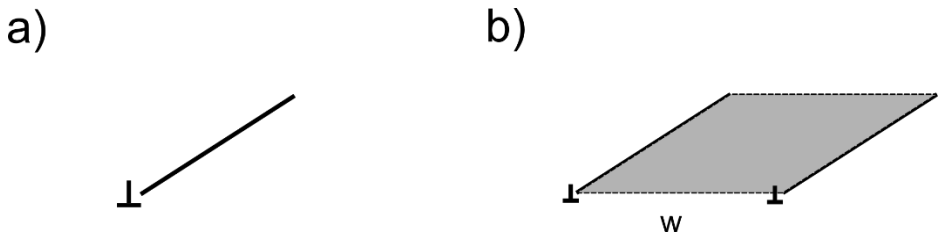

Figure 2-9 – Depiction of a) perfect dislocation and its associated line. The dislocation self-energy of two FCC partial dislocations is lower than a single perfect, so the dislocation dissociates as seen in b). Since partials do not preserve the periodicity of the lattice, the shaded region in b) forms a stacking fault. Faulted material contributes an energetic penalty, so there is an attractive force between the two partials that is balanced out by the mutual repulsion of their strain fields. Each stacking fault has an equilibrium width w that is determined by these energetics.

A dissociated full dislocation can also be described as having an extended core. Although the two Shockley partial dislocations have lower self-energy in total than the initial perfect dislocation, the stacking fault is energetically unfavorable, so the predominant type of dislocation depends on the extra energy contributed per unit area of faulted material, or stacking fault energy. For FCC materials, propagation of a single Shockley partial leaves behind faulted material with a locally minimal energy on the stacking fault energy curve (not covered here) termed the intrinsic stacking fault energy γ_{ISF}. Perfect dislocations are not expected to spontaneously form dissociated partials in materials with high or moderate γ_{ISF}, while they are expected to dissociate in low γ_{ISF} materials. Propagation of a leading and trailing Shockley partial on a slip plane produces the same deformation as a perfect dislocation. Partial dislocations also play important roles in deformation mechanisms such as deformation twinning, but such discussion is outside the scope of this work.

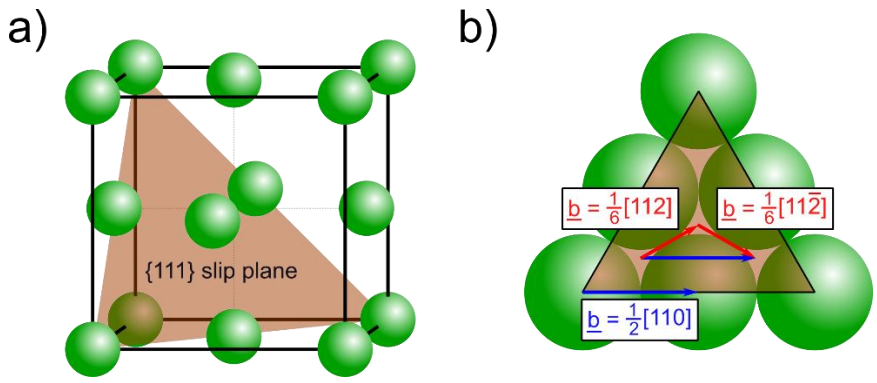

Figure 2-10 – Illustration of a) one {111} slip plane in the FCC unit cell and b) plan-view of space-filling atoms in the slip plane in a). b) demonstrates the slip direction for perfect and partial Burgers vectors to the atomic positions on {111} planes. Combining a slip plane with slip direction defines one slip system.

2.3.3. Dislocations in BCC metals

The body-centered cubic, or BCC, crystal structure consists of atoms occupying the corners and center of a cubic unit cell. The BCC structure is not close-packed but possesses only slightly less density compared to close packing. The closest-packed planes in BCC structures are {110} type planes, while the closest-packed directions are <111> type. This is illustrated in Figure 2-11. While this may suggest that the favored slip system is {110}<111> type, in practice slip in BCC is more complicated. Because screw dislocations with <111> Burgers vectors have relaxed core structures compared to other types of dislocations, they have much lower mobility than other dislocation types[52]. During plastic deformation, dislocation types other than <111> screw dislocations move much more quickly, leaving behind the low-mobility dislocations which dominate deformation behavior[56,57]. Because screw dislocations change slip plane easily in a process called cross-slip, they can glide along any crystal plane containing a <111> direction. In practice, these planes are the {110}, {112}, and {123} planes, which activate in sequence at increasing temperatures or decreasing strain rate since slip in these materials relies heavily on thermal activation[57]. For simplicity, {110}<111> slip systems are assumed for niobium in this

work. There are 36 {110}<111> symmetrically equivalent slip systems, making BCC metals somewhat less ductile than FCC metals. BCC metals also tend to have higher Peierls barriers than FCC metals, further decreasing the ductility of the former. Perfect <111> type dislocations can also dissociate like <110> type dislocations in FCC metals, but the process is much more complicated and less understood. As such, BCC dislocation dissociation will not be discussed.

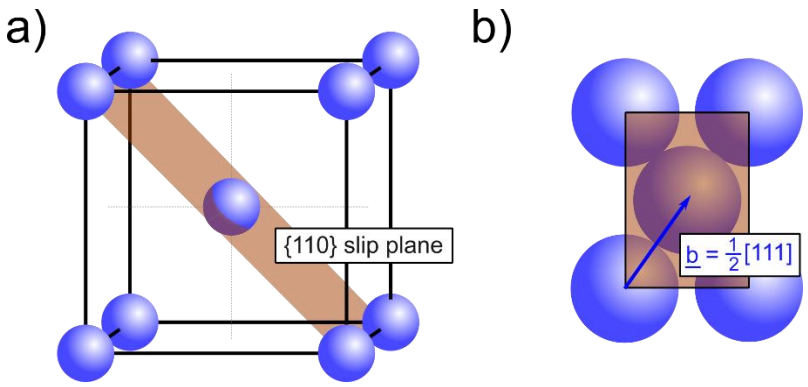

Figure 2-11 – Illustration of a) one {110} slip plane in the BCC unit cell. b) Plan-view of space-filling atoms in the slip plane in a). Partial dislocations are less understood in BCC metals, so only the perfect Burgers vector is shown here.

2.3.4. Geometric factors influencing slip

The orientation dependence of yield stress and work hardening in single crystals arises from the interaction of far-field applied stress and dislocations. The geometry of this interaction in uniaxial tests like micropillar compression requires the resolution of a uniaxial normal stress to a shear stress on a slip plane. The mathematics underlying this calculation is presented here. This is done by rotating the uniaxial reference frame where there is only uniaxial normal stress to a rotated reference frame aligned with the slip plane. This is commonly done using a construction called Mohr's circle, to calculate shear stress on a slip plane as function of the rotation angle from the uniaxial frame of reference[58]. This construction gives rise to the following equations:

$$\sigma'_{xx} = \frac{1}{2}\sigma_{xx}(1 + \cos(2\theta))$$

$$\sigma'_{yy} = \frac{1}{2}\sigma_{xx}(1 - \cos(2\theta))$$

$$\sigma'_{xy} = -\frac{1}{2}\sigma_{xx}\sin 2\theta$$

(2-12)

Where σ_{xx} is the uniaxially normal stress in the initial frame of reference, σ'_{xx}, σ'_{yy}, σ'_{xy} are the resolved stresses in the new frame of reference, and θ is the counter-clockwise (right-handed) rotation between initial and final frames of reference. Note that σ'_{xx} and σ'_{yy} are normal stresses while σ'_{xy} is a shear stress, which is the stress important for slip. The maximum shear stress σ'_{xy} arising from a uniaxially applied σ_{xx} is $\sigma'_{xy} = 0.5\sigma_{xx}$ at $\theta = 45°$, which will be used to analyze micropillar results in Chapter 6.

According to the calculation for Peach-Koehler force in Equation (2-9), only shear stresses produce forces on dislocations with nonzero components in their slip planes. This can be demonstrated by imagining a model case of an FCC edge dislocation with Burgers vector $\underline{b} = \frac{a}{2}[1\ 1\ 0]$, slip plane $(1\ \bar{1}\ 1)$, and line sense $[1\ \bar{1}\ \bar{2}]$. If the x, y, and z axes are rotated to align with these directions, the force produced on this dislocation by an arbitrary applied stress is:

$$\underline{F} = -(\sigma_{xy}b_x + \sigma_{yz}b_z)\underline{i} + (\sigma_{xx}b_x + \sigma_{xz}b_z)\underline{j} = -\sigma_{xy}a\underline{i} + \sigma_{xx}a\underline{j}$$

(2-13)

Here, a is the lattice parameter of the material. Only the x component of this force has a nonzero value when resolved along the slip direction $\underline{b}$, and so only the shear stress σ_{xy} contributes to dislocation slip. For a screw dislocation with the same Burgers vector, σ_{yz} is the only stress

component that produces slip (also a shear stress). This example demonstrates that only shear stresses contribute to dislocation motion in perfect dislocations, barring movement involving diffusion such as climb.

After resolution of stress to shear stress on a slip planes, further resolution of the stress along a slip direction in the slip plane is required to evaluate slip behavior. This is done using Schmid's Law, which is depicted in Figure 2-12 and expressed as follows[59]:

$$\tau_C = \sigma_y \cos\phi \cos\lambda \tag{2-14}$$

Here, τ_c is called the critical resolved shear stress, σ_y is the yield stress, φ is the angle between the loading axis and the slip plane normal, and λ is the angle between the loading axis and the slip direction. The critical resolved shear stress describes the shear stress required to drive dislocation motion on a given slip direction in an orientation specified by φ and λ. If the critical resolved shear stress, crystal structure, and crystal orientation is given, it should be possible to predict yield for any metallic single crystal. However, the entire flow curve is not as simple to predict. Lattice rotation occurs as single crystals are plastically strained due to the constraints imposed on the crystal at its ends[60]. This reorientation may be enough to activate a second or even multiple slip systems as plastic deformation progresses. The activation of additional slip systems influences work hardening rate, as does formation of dislocation substructures[61]. Slip system evolution as a function of strain and lattice rotation can be addressed by computational methods, as done in Chapter 6.

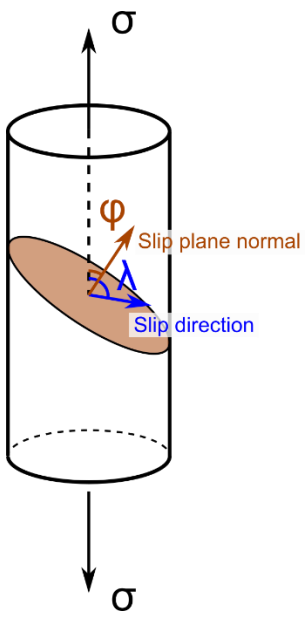

Figure 2-12 – Illustration of Schmid's law. The resolved shear stress on a given slip system is a function of the inclination of the loading axis to both the slip plane normal and slip direction.

2.4. Deformation of polycrystalline metals: Size and internal boundary effects

Although single crystal systems reveal the fundamentals of plastic deformation in metals, they are not representative of most metals used in structural applications. As mentioned before, single crystals possess low strength and pronounced property anisotropy, making them unsuitable for construction of engineering structures such as bridges, car chassis, or aircraft fuselages. One way to tackle this limitation is to use metals that are aggregates of distinctly oriented crystals, or crystallites. Such a metal is referred to as polycrystalline and has macroscopic properties that distinguish it from metallic single crystals. For most metals at room temperature, polycrystalline materials can be orders of magnitude stronger than single crystal samples, depending on grain size. Also, polycrystalline metals tend to work harden more quickly than single crystals. Lastly, polycrystalline metals tend to behave more isotropically in elastic and plastic deformation than single crystals due to the wide distribution of crystal orientations found within them. This last point

is less true for polycrystalline samples with a strong preferred orientation, or texture. Cu/Nb nanolaminates tend to be strongly textured, which influences analysis of its mechanical behavior.

2.4.1. Size effect strengthening

Strengthening in metals tends to hinge on the controlled inclusion of defect content. Strengthening methods like solution hardening constitute inclusion of substitutional or interstitial defects. Others like work hardening comprise tailoring of dislocation density, which involves line defects, through plastic deformation. The focus of this section is the planar defect – namely internal boundaries found in various alloys. The most common internal boundary found in alloys is the grain boundary, which separates two crystals of the same phase but different orientation. Heterophase interfaces the focus of the current work, separate regions of different phase. Many grain boundary concepts can be directly applied to heterophase interfaces, such as grain size effects on strength.

The models underlying grain size effects on strength argue that the more grain boundaries there are in a material, the harder it is to drive a dislocation through it. This is because grain boundaries act as barriers to dislocation motion. Grain boundary content can be related simply to metallic microstructure through the grain size. A metallic grain, or crystallite, is a region in a metal where crystal structure and orientation are uniform. The smaller the grain size, the greater the grain boundary content, normalized to the volume of material under consideration. This relationship is characterized by the well-known Hall-Petch relation[62,63]:

$$\sigma_y = \sigma_o + kd^{-\frac{1}{2}} \tag{2-15}$$

Where σ_y is the yield stress, σ_o and k are fitting parameters, and d is the average grain size of the material under consideration. This relationship is obeyed by most metals when the grain size is above 10 to 100 nm, depending on the metal[64].

2.4.1.1. Dislocation-pileup models of Hall-Petch behavior

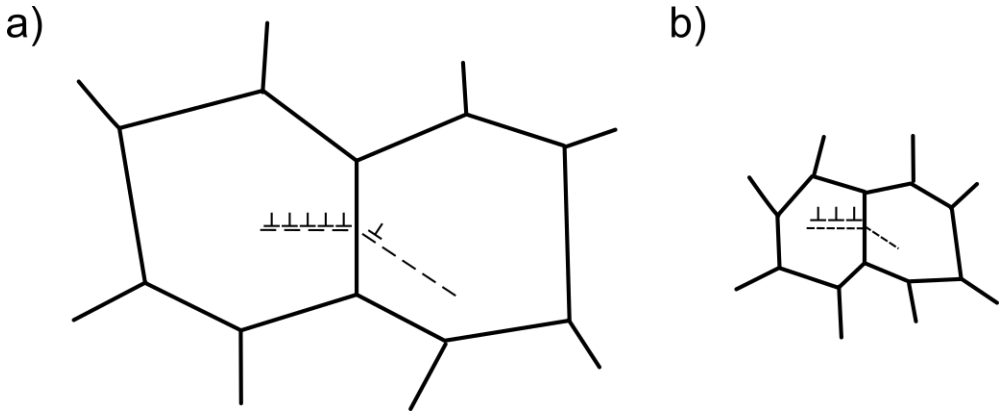

Figure 2-13 – A depiction of one commonly accepted model of grain size effects in metals. In a), grains are coarse and significantly large dislocation pileups can develop. The pileup exerts enough of a mechanical advantage on a misaligned slip system in a neighboring grain to activate it, allowing plastic deformation to continue. In b), the grains are fine compared to a) and it is energetically unfavorable to accommodate large pileups. Thus, the pileup in b) does not have a large enough mechanical advantage to activate slip in a neighboring grain. Thus, plastic deformation is halted and the yield and flow stress is higher in b) as compared to a).

While the Hall-Petch relationship is widely agreed to exist for most metals, the mechanism producing it is not definitively agreed upon. Dislocation pileups are invoked in many mechanisms as shown in Figure 2-13. A dislocation pileup occurs when successive dislocations on the same slip system are blocked by some obstacle in the material, which is a grain boundary in the case of Hall-Petch models. The grain boundary stress barrier for continued slip is opposed by the stress field in front of the dislocation pileup, which scales with the number of dislocations in the pileup. Thus, larger pileups have a larger mechanical advantage for driving continued slip across the grain boundary[41]. The maximum allowable size of a pileup in a given grain is limited by the grain's size, which then gives rise to the Hall-Petch relation. There are several proposed atomic scale

mechanisms of dislocation-grain boundary interactions that produce Hall-Petch grain size effect scaling. Some specify that the lead dislocation is transmitted across the grain boundary, others prescribe that a dislocation source across the grain boundary is activated, and yet others predict that the grain boundary weakens locally, allowing dislocations to transmit across the grain boundary. More detailed discussion is found in Cordero, et al.[65], covering various mechanisms producing Hall-Petch behavior.

It is important to note that all models for explaining the Hall-Petch relationship rely on the assumption that significant dislocation content can be stored in the metal. Also, they treat grain boundaries as uniform boundaries with no atomic structure. However, as grain size decreases, this necessitates more and more overlap of dislocation stress fields, which constitutes an energy penalty. This means that active deformation mechanisms must shift to a regime where dislocations content accumulates slowly or not at all as grain size shrinks to a size scale comparable to that of a few dislocation cores. Also, as grain size shrinks, the effect of atomic scale structure of grain boundaries on dislocation activity must be considered.

2.5. Deformation at the nanoscale

Deformation of nanocrystalline metals, or those that have grain sizes below 100 nm, is different at the macroscopic and microscopic length scales from that of coarser grained metals. On the macroscale, a few hallmarks in mechanical behavior distinguish nanocrystalline metals from coarse-grained metals. The most well-known property of nanocrystalline metals and alloys is that they possess high strengths, often on the order of magnitude of the theoretical strength of the metal[66,67]. This remarkable property does not come without costs, however. High strength in metals is often correlated with low plastic deformability, a phenomenon termed the “strength-ductility” tradeoff[68]. This tradeoff, demonstrated in Figure 2-14, is due to the fundamentals of dislocation-

based plasticity discussed above. As strength approaches theoretical levels in nanocrystalline metals, it becomes more energetically favorable to activate deformation mechanisms other than dislocation nucleation, motion, and storage. Dislocation-based mechanisms produce work hardening and extended ductility, while non-dislocation based mechanisms such as grain boundary sliding often cause failure of the material[69]. This shift in deformation mechanism often manifests at the macroscale as flow instability or fracture. Lastly, nanocrystalline alloys demonstrate Hall-Petch breakdown, where strength-grain size dependency departs from a $d^{-1/2}$ scaling, which is an indicator of a shift away from the dislocation-forest based multiplication and storage mechanisms found in coarser grained materials[65,70]. A large contributor to this phenomenon is the high content of grain boundaries relative to material volume at small grain sizes. High content of interfaces of any type, grain boundaries or heterophase interfaces, significantly alters dislocation activity and mechanical behavior. Thus, deformation at the nanoscale can be described in general through the lens of dislocation-interface interaction, with heterophase interface-specific interactions discussed separately.

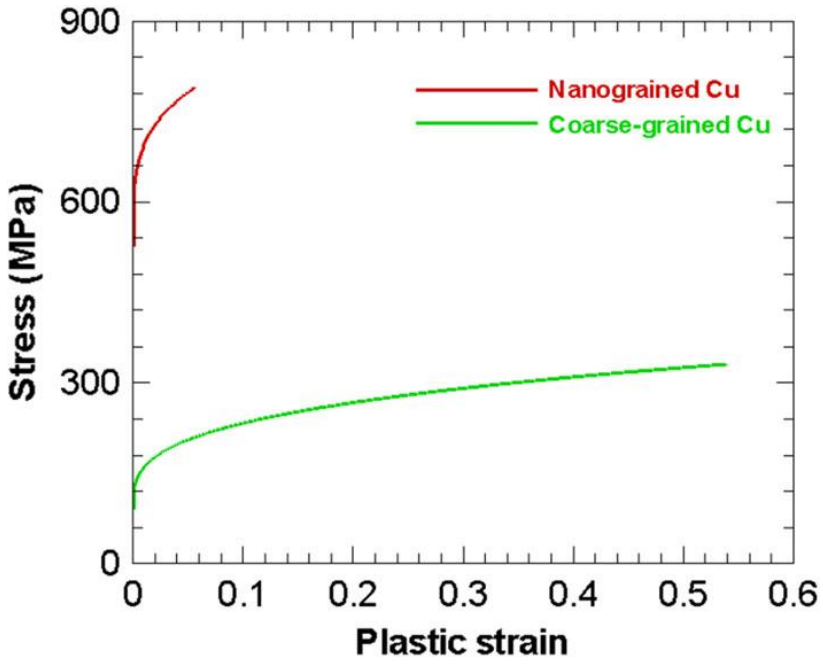

Figure 2-14 – Tensile stress strain curves of a coarse-grained and nanocrystalline sample of pure Cu. While the nanocrystalline sample is much stronger than its coarse-grained counterpart, it has much less ductility due to the energetic unfavorability of storing dislocations in nanoscale grains. Reproduced from Ref. 71.

3. Interface-mediated deformation

3.1. Atomic structure of interfaces

Interface-mediated deformation hinges on far-field stress-induced interface reconfiguration and few- or single dislocation interactions with interfaces[72–74], both of which depend on the atomic structure of interfaces[75,76]. Interface atomic structure is especially relevant to deformation in nanocrystalline alloys. Here, atomistic fidelity is required to understand nanoscale unit deformation processes dominating mechanical behavior[9,67,77]. Interfaces with simply defined atomic structure include coherent interfaces where atomic position mismatch, or misfit, is accommodated by long-range atomic strain fields and semicoherent interfaces that form misfit dislocation arrays (semicoherent interfaces henceforth)[78]. 2D Cu/Nb contains the latter type of interfaces, so semi-coherent interfaces will be the focus of this discussion. One of the simplest illustrative examples of a semicoherent interface structure defined by misfit dislocation arrays is the low angle coherent tilt boundary, which is shown in Figure 3-1(a). Here, although misfit dislocations contribute their line energy to the interface, they relieve the energetic penalty associated with high interfacial misfit[78]. A more complex misfit dislocation structure is found at 2D Cu/Nb interfaces, one model of which can be described by arrays of two different sets of dislocations as shown in Figure 3-1(b). Other atomic scale interface features such as ledges are also found at interfaces, which are important for deformation involving some types of 2D Cu/Nb interfaces[79,80].

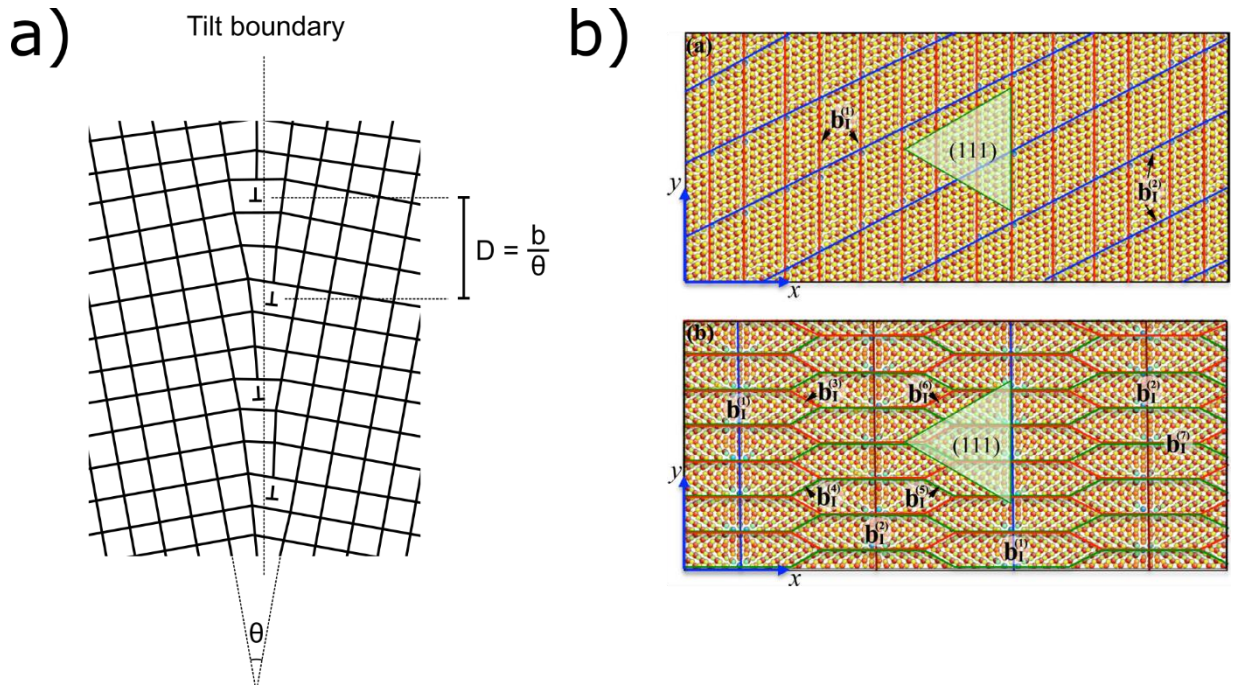

Figure 3-1 – a) Illustration of a low-angle tilt boundary. The distortion that such a boundary introduces to an otherwise perfect crystal can be described by an array of misfit dislocations. b) PVD Cu/Nb 2D interfaces obtained by molecular dynamics simulations. Kurdjumov-Sachs (top) and Nishiyama-Wasserman (bottom) interfaces are shown in plan view. Yellow and red circles are Cu and Nb atoms, while misfit dislocations are represented by blue, red, and green lines. Misfit dislocations can be grouped into sets having the same Burgers vector, all of which occur in regular patterns. The superposition of all misfit dislocation sets forms the regular misfit dislocation array defining the interface atomic structure. Reproduced from Ref. 5.

The atomic structure defining an interface is a function of the orientation relationship between the grains abutting the interface. This relationship determines the amount of atomic-level elastic misfit across the grain boundary. Misfit is defined per interfacial atom by the displacement required to bring an atom on one side of the interface into coincidence with the atom on the other side. There are five geometric parameters defining an interface, three associated with the misorientation of the abutting grains, and two independent normal vector components defining the interface plane joining the two grains[81]. Certain interfaces that meet special geometric conditions result in low misfit across the interface, while others that do not are higher in misfit. Simplified models relating interface geometry and structure predict that boundaries with more misfit possess

more misfit dislocations to accommodate geometric incompatibility between the abutting grains[78]. More refined theories of interface structure exist to account for interfaces features like point defects, repeating atomic motifs, and ledges, some of which are described in further detail in Ref 78.

3.2. Interface-mediated deformation

3.2.1. Deformation and dislocation activity at general interfaces

The atomic structure of interfaces is directly involved in deformation mechanisms such as interface migration[82], interface sliding[83], and grain rotation[84]. These mechanisms can directly contribute to failure of a material if they provide a low energy pathway to rupture or fracture. In terms of dislocation activity, interfaces and their structure have an outsize effect on dislocation motion, nucleation, and annihilation[66,85]. Interface-dislocation interactions are depicted in Figure 3-2. Interfaces can block, nucleate, annihilate, dissociate, or trap incoming glide dislocations. The atomic structure of interfaces determine how dislocations are blocked or nucleated (Figure 3-2(a-b)), mediating dislocation density and distribution among slip systems during deformation[9,86–88]. The structure of interfaces also influences how interfaces accommodate incoming glide dislocations, producing dislocation annihilation[89], transmission with deposition of dislocation debris[90], or dislocation trapping[9,74,86,88,91] (Figure 3-2(c-e)). It should be noted that many aspects of interfacial dislocation transmission can be understood with Lee-Robertson-Birnbaum (LRB)-type criteria quantifying the effect of bicrystal misorientation on dislocation transmission[92–94]. However, these criteria do not explicitly account for interface atomic structure, rearrangement of which is key in understanding dislocation transmission in some cases[95]. Trapping has been found at PVD Cu/Nb interfaces, enabled by local deformation leading to glide dislocation core spreading withing the interface[96]. The misfit dislocation structure presented in Figure 3-1(b) accommodates this interface deformation. Glide dislocation core spreading lowers the self-energy of the

dislocation, which means that extra energy must be supplied to the dislocation for it to escape the interface.

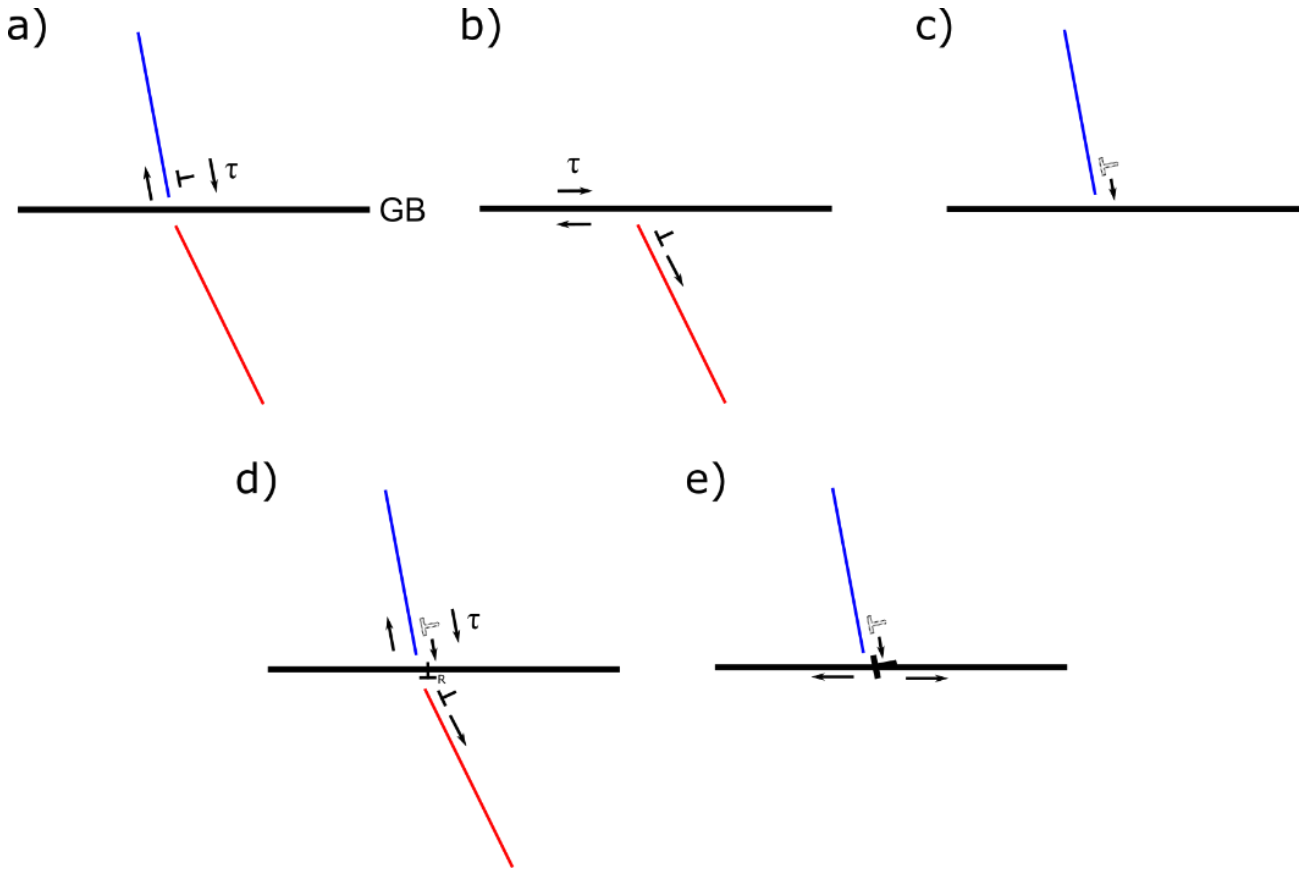

Figure 3-2 – Depiction of dislocation-interface interactions that can happen in metals. The interface here is a grain boundary, denoted by a thick black line. Ingoing slip systems are depicted by blue lines and outgoing slip systems are depicted by red lines. Empty dislocation symbols are used to indicate prior positions of annihilated or trapped dislocations. These interactions are as follows: a) blocking, where the motion of an incoming glide dislocation under a resolved shear stress is arrested by the grain boundary, b) nucleation, where a resolved shear stress acts on the grain boundary to cause emission of a new dislocation, c) annihilation, where an incoming glide dislocation is absorbed by the grain boundary, d) dissociation, where the grain boundary accommodates a portion of the incoming dislocation's Burgers vector (denoted as a residual Burgers vector $\perp_R$) while allowing the remainder to pass into the abutting grain, and e) trapping, where the core structure of an incoming dislocation relaxes into a spread out configuration in the grain boundary.

The relationship between interface structure and mechanical behavior raises the possibility of tailoring deformation metrics by controlling interface structure in nanocrystalline alloys. A

common example in single phase materials comprises controlled introduction of twin boundaries[97–99]. Nanocrystalline copper made with a high content of coherent twin boundaries can be tuned to maximize strength and ductility[97,100,101]. This has been found to be explained partly by the interplay between twin lamella size and effect of interface structure on activity of dislocations on different slip systems[102]. The same concept of interface content control can be applied to heterophase interfaces, which can interact with defects in other ways than for boundaries in single-phase materials.

3.2.2. Heterophase interface-specific effects on deformation

There are a few differences in the ways that that heterophase interfaces influence deformation as compared to grain boundaries. They are illustrated in Figure 3-3 and are described as follows:

1. Image forces: Image forces act on dislocations due to elastic mismatch across interfaces[1]. While they can arise at grain boundaries in single phase materials, they are much weaker since elastic mismatch in single phase materials can only come from elastic anisotropy[86]. In multiphase materials, differences in interatomic forces between different metals can give rise to drastic differences in elastic properties[103–105]. Elastic mismatches give rise to image forces due to compatibility of tractions at interfaces. Figure 3-3(a) shows how image forces on a dislocation can be calculated by introduction of a virtual, "image dislocation" across the heterophase interface that exerts Peach-Koehler forces on the real dislocation[87]. Dislocations tend to be attracted to interfaces across which Young's modulus decreases, while they are repelled by interfaces across which Young's modulus increases[87].

2. Change in crystal geometry: While grain boundaries can influence the motion of dislocations by forcing a change in slip system due to grain misorientation, slip system mismatch may be much more complicated for heterophase interfaces. It is possible that a dislocation must not only change slip system, but also slip system family to cross a heterophase interface. For example, a dislocation moving from an FCC to a BCC crystal must change from a {111}<110>-type slip system to a {110}<111>-type slip system, assuming that only {110} slip planes are active in the BCC crystal. The energetics of this type of slip transfer event are governed in part by LRB criteria accounting for mismatches in lattice parameter, slip system orientation, and Burgers vector[6,94]. However, dislocation trapping occurring at Cu-Nb interfaces may complicate crystal geometry arguments about dislocation transmission[106].
3. Change in chemistry: Chemical mismatches introduce lattice and Peierls barrier mismatches, even at interfaces with no misorientation[107]. For example, a dislocation moving across an interface separating Cu and Ag would need to change Burgers vector and overcome differences in lattice friction when crossing from Cu to Ag. Finally, a change in chemistry across a heterophase interface influences a discontinuity in stacking fault energy curve, which produces interactions between dislocation core structure and interface transmission[108]. In the previous example of a Cu-Ag interface, another change would occur across the interface regarding dislocation behavior. The stacking fault energy, which influences the equilibrium stacking fault width, changes from medium to low moving from Cu to Ag. Thus, a dislocation moving from

Cu to Ag would begin with a near-compact core in Cu and then expand to incorporate an extended stacking fault in Ag. The change in dislocation core structure as it moves from one phase to another introduces a chemical stress on the dislocation associated with the heterophase inferface[109,110]. Stacking fault energy considerations can also influence the interfacial transmission and nucleation of partial dislocations over perfect dislocations[6,111,112]. This in turn determines the favorability of deformation twinning over perfect slip, which while important for some Cu/Nb interfaces[7], will not be addressed in the current work.

4. Interface coherency: Heterophase interfaces have additional degrees of freedom that determine interface coherency as compared to grain boundaries. In grain boundaries, this coherency is mostly determined by interfacial misfit determined by the five geometric degrees of freedom associated with interfaces. In heterophase interfaces, interfacial misfit is also affected by lattice parameter and crystal structure mismatch[113]. Thus, interface coherency and structure are a simultaneous function of crystal structure pairing, interfacial misorientation, and chemistry in multiphase systems[10,21]. Decreasing grain size can also trigger semicoherent-to-coherent transitions in heterophase systems, where pseudomorphic phase transitions or mismatch strains reduce lattice misfit at heterophase interfaces[10,11,114–116]. At limited grain sizes of a few nm and below, it is more energetically favorable to accommodate misfit strain with long-range coherency stress fields rather than misfit dislocation arrays[117]. Semicoherent and coherent interfaces influence dislocation motion differently;

misfit dislocation stress fields act on lattice dislocations via the Peach-Koehler equation presented earlier in the former while misfit stresses dominate dislocation motion in the latter[118,119].

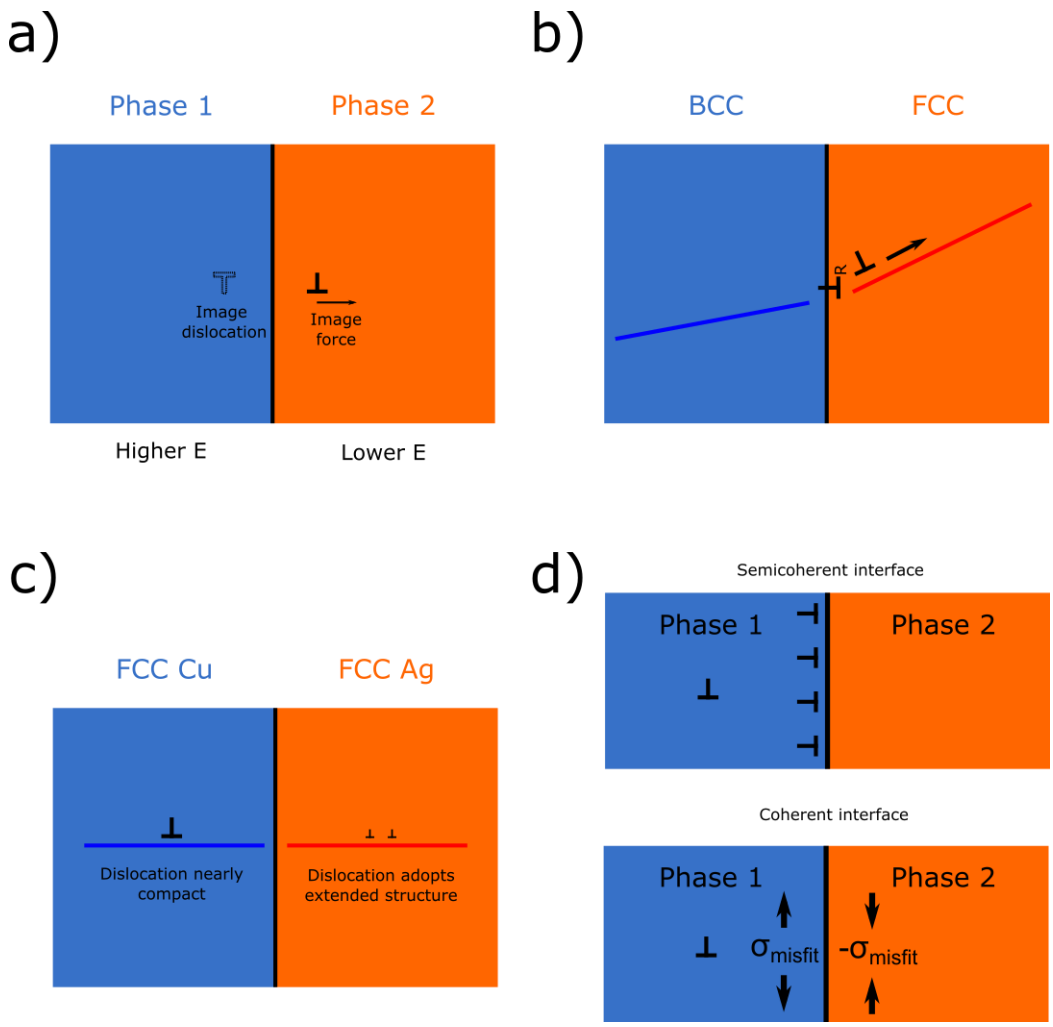

Figure 3-3 – An illustration of the ways that heterophase interfaces contribute to plastic deformation in addition to the defect-interface interactions that occur at grain boundaries. a) Dislocations experience image forces at heterophase interfaces separating regions of different elastic properties. b) Differences in slip system geometry, crystallography, and Burgers vector determine the residual Burgers vector that must be deposited in the interface as a result of slip transfer. This in turn determines the energetic favorability of slip transfer. c) Differences in chemistry can alter dislocation core structure, affecting the energetics of interface slip transfer. Here, the dislocation core expands from a near-compact structure to one incorporating an extended

stacking fault as it moves from Cu to Ag. d) Heterophase interface coherency plays a large role in mechanical behavior, altering dislocation behavior as a function of interface structure.

Heterophase interfaces are found in a variety of engineering alloys such as duplex brasses, ferritic-austenitic stainless steels, ferritic-martensitic steels, and alpha-beta titanium alloys[46]. As useful as these materials are, they tend to have complex microstructures involving deformation textures, anisotropic and heterogeneous grain shapes, and other features such as precipitates or dislocation substructure from cold working. A model system with controlled grain size, morphology, and interphase orientation relationship is needed to study the fundamental deformation physics of heterophase interfaces. Control of these microstructural descriptors allows for independent adjustment of grain size, interface misorientation (quantified by LRB criteria), and interface atomic structure effects on dislocation activity, the last of which is the main motivator for this work.

3.3. Material systems used to study heterophase interfaces

3.3.1. General nanocrystalline systems

General nanocrystalline systems were among the earliest to reveal interface effects on deformation, but they can be difficult to synthesize with strong control over grain size and morphology, as well as interface misorientation and morphology[69]. Examples of general nanocrystalline heterophase systems are Cu-Nb alloys made by high pressure torsion[120] and heavily drawn grain-boundary segregated pearlitic steel wire[121]. While these materials contain high fractions of heterophase interfaces, their mechanical properties are not solely influenced by interface structure. A systematic study of interface-derived mechanical behavior demands a more idealized model material system where microstructural variables can be carefully controlled.

3.3.2. Nanolaminates for studying influence of interface structure on mechanical behavior

Nanolaminates constitute a model nanostructured composite system for studying heterophase interface structure effects on mechanical behavior. The simplest nanolaminates are biphase, consisting of alternating layers of two different phases with nanoscale layer thicknesses. These materials can be made in a bottom-up fashion via physical vapor deposition[122] (PVD) or by top-down methods such as accumulative roll-bonding[123,124] (ARB). These processes are illustrated in Figure 3-4. Figure 3-4(a) depicts DC magnetron sputtering PVD, where Ar ions in a plasma are accelerated towards metal targets to sputter atoms towards a substrate to grow a film. DC magnetron sputtering will be covered in further detail in Chapter 4 due to its relevance to this work. Figure 3-4(b) shows ARB in which stacks of alternating Cu and Nb plates are rolled bonded together to form a multilayered composite. The composite can be cut and stacked to repeat this process until individual layer thickness reaches the nanoscale. Metallic nanolaminates possess many advantageous characteristics that simplify the analysis of interface structure on deformation. Nanolaminates made by PVD or ARB can be synthesized with a narrow distribution of orientation relationships at heterophase interfaces due to the energetic favorability of generating certain interface types during synthesis[19,125]. Heterophase interfaces in nanolaminates are planar, which eliminates boundary curvature as an interface structure variable. Lastly, PVD nanolaminates have layer thicknesses that are controllable to within a few nm, as well as in-layer grain sizes with narrow distributions[15,126,127].

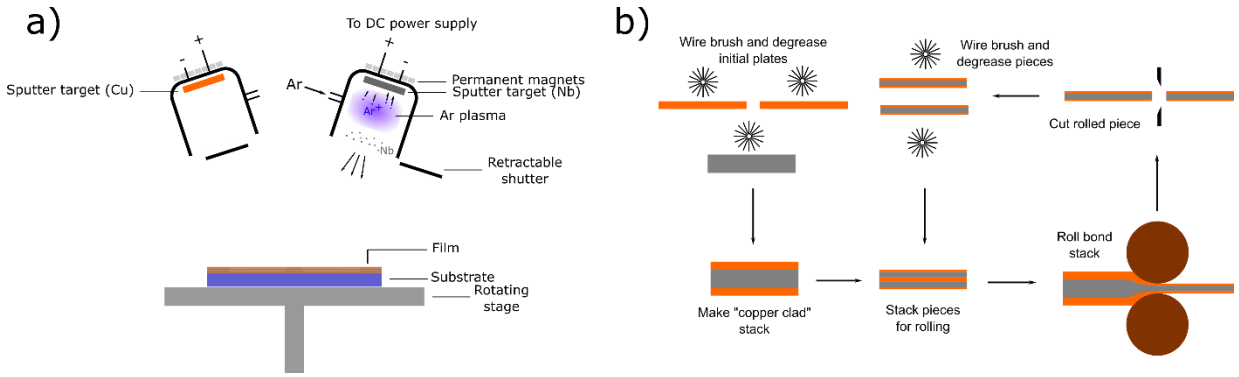

Figure 3-4 – Illustrations of a) physical vapor deposition (PVD) and b) accumulative roll bonding (ARB).

3.4. Mechanical behavior of nanoscale metallic laminates

Some of the earliest work on the mechanical behavior of metallic nanolaminates focused on the interplay between layer thickness and nanohardness or yield strength. Material systems like Al/Cu[128], Ti/Al[129], and Cu/Ni[122] were some of the earliest material systems used to study this topic. Above a layer thickness of a few tens of nm, nanolaminates follow the Hall-Petch relationship if hardness is substituted for yield strength and layer thickness is the effective grain size[126]. While establishing this relationship is important, it does not constitute a fundamental understanding of the relationship between interface structure and mechanical behavior. A study by Misra, et al.[130] started to bridge this gap with a study of layer thickness-hardness relationships in Cu/X multilayers, where X was Nb, Cr, or Ni depending on the material. Here, the effects of heterophase interfacial structure were examined based upon the lattice parameter and elastic modulus mismatch of the constituent phases. Cu-Nb interfaces are semicoherent with low interfacial shear modulus mismatch, Cu-Cr interfaces are semicoherent with high interfacial shear modulus mismatch, and Cu-Ni interfaces are mostly coherent with low interfacial shear modulus mismatch[21]. This work demonstrated that interface coherency and elastic modulus mismatch provide separate

strengthening contributions in nanolaminates, prompting further investigation into how such microstructural features influence dislocation activity. An understanding of this phenomenon was developed at the unit deformation mechanism level in Cu/Ni by Anderson, et al.[118] and Cu/Nb by Misra, et al.[15], which will be covered in the next Section.

3.4.1. Mechanistic understanding of layer size effects on nanolaminate strength

The dependence of nanolaminate mechanical behavior on layer thickness is depicted in Figure 3-5, and can be divided into three different regimes. Above a layer thickness of about 100 nanometers, nanolaminates follow the Hall-Petch relationship. At layer thicknesses ranging from several nm to a few tens of nm, hardness follows a modified scaling law. At this length scale, hardness is proportional to $\frac{\log(h)}{h}$, where h is the layer thickness. Finally, below a length scale of several nm, hardness is a weak function of h. These three regimes of mechanical behavior can be tied to three distinct dominant deformation mechanisms. In the Hall-Petch regime, dislocation pileup size controls strength. In the $\frac{\log(h)}{h}$ regime, strength has been postulated to be dominated by confined layer slip (CLS). CLS describes deformation where a single dislocation is confined to a material layer and is bowed out under applied far-field stress by drag forces at the interfaces bounding the layer[118]. In the few-nm layer thickness regime, single dislocations are no longer confined to single layers and can cut across multiple interfaces[21].

The different size-dependent scaling of strength for the dislocation configurations in the proposed mechanisms described above lead to the development of the different regimes[75]. At coarse h, grain interiors are large enough to store significant pileups. For intermediate h of ~10-100 nm, grain volume becomes limited and only a few dislocations can be stored in pileups and no substantial mechanical advantage can be generated by pileups. Instead, strength is limited by

the propagation of single dislocation loops that adopt hairpin configurations due to confinement by lamellar grains. The Orowan stress required to bow these hairpins is taken to dictate the strength of the material. At h < ~10 nm, the hairpin radius dictated by the layer thickness becomes too small to be energetically favorable, as dislocation line tension increases as a function of local radius of curvature. Additionally, the straight segments of the hairpin approach are confined to be closer to each other with decreasing h, further increasing the dislocation line tension. Instead, dislocations adopt straight configurations and strength is directly dictated by the stress barrier posed by interfaces to slip transmission.

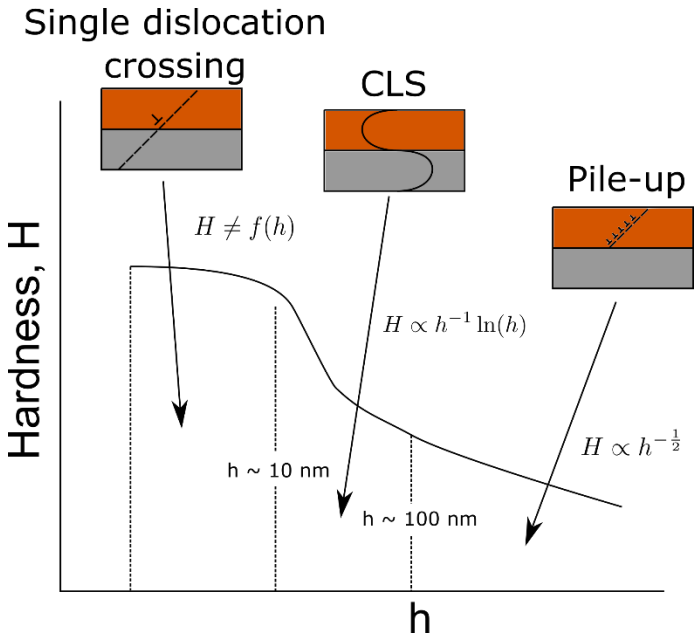

Figure 3-5 – A depiction of the hardness-controlling deformation mechanism for nanolaminates as a function of layer thickness h. Above about h = 100 nm, dislocation pileup size controls hardness. This gives rise to Hall-Petch behavior consistent with metallic deformation at larger length scales than the nanoscale. Between h = 10 and 100 nm, hardness is controlled by confined layer slip and is proportional to h^{-1} *ln(h)*. Below about h = 10 nm, hardness is controlled by single dislocation crossing events and is no longer a strong function of h. Figure adapted from Ref. 15.

3.4.2. Effect of semi-coherent to coherent interface transition at $h < 10$ nm

In the single dislocation crossing regime where layer thickness is low, nanolaminate interface structure tends to transition from misfit dislocation-bearing semi-coherent interfaces to misfit dislocation-free coherent interfaces[131]. This is due to the energetic unfavorability of misfit dislocation strain field overlap at opposing sides of a layer for low h[132]. Instead, long-range misfit stresses produce strain over the interface lateral dimensions to relieve atomic misfit. This change in interface structure likely causes a peak in hardness with respect to layer thickness in Cu/Ni and Cu/Nb at length scales of $h < 10$ nm. For Cu/Ni, the coherency layer thickness is about 2-2.5 nm for both the (100) and (111) growth directions[10,133], which roughly coincides with peak hardness at $h = 5$ nm for the (100) growth direction and $h = 2.5$ nm for the (111) growth direction[10]. For Cu/Nb the coherency layer thickness is 1.2 nm[11] for the (111) growth direction, and peak stress is found at $h = 1.2$-2.5 nm for the same growth direction[15]. Coherency layer thickness correlates well with peak hardness in Cu/Ni and Cu/Nb because of the shift from "opaque" semi-coherent interfaces that block dislocations efficiently to coherent interfaces that are "transparent" and transmit dislocations easily[21]. Additional effects of decreasing h are decreasing coherency stress and image forces on dislocations, weakening the material[10]. These phenomena may shift the h at which peak hardness is found, weakening the correlation to coherency layer thickness. The coherency-peak strength layer thickness correlation demonstrates the strong tie between interface structure and mechanical behavior, which will be discussed in further detail.

3.4.3. Heterophase interface structure and interface-mediated deformation in Cu/Nb

PVD Cu/Nb demonstrates strong epitaxy between Cu and Nb layers, characterized by alignment of {111} Cu and {110} Nb planes normal to the growth direction, and where fcc Cu and bcc Nb share mutual compact planes and directions[134]. Two orientation relationships (OR)

dominate this system, Nishiyama-Wasserman (N-W) and Kurdjumov-Sachs (K-S). In the N-W OR, Cu <110> type directions are parallel to Nb <100> directions[11], while the K-S has Cu <110> aligned with Nb <111> directions[135]. The interface types found in PVD Cu/Nb are fully defined by an orientation relationship and interface plane. Orientation relationship is established by pairs of aligned planes and directions, while interface plane geometry is established by noting that interface planes are parallel to compact {111} Cu and {110} Nb planes normal to the growth direction. Thus, these interface types are notated by specifying pairs of parallel crystal planes and directions. Here, the specified planes are parallel to the interface plane, or normal to the film growth direction. N-W interface types are notated {111}<121>||{110}<111>, while K-S are notated {111}<110>||{110}<111>. The last degrees of freedom associated with PVD Cu/Nb interfaces is associated with the interface planes relative to the Cu and Nb crystal lattices. Thankfully, this relationship is simple; since the favored growth planes in Cu and Nb align along interface planes, the interface plane is given as parallel to Cu {111} and Nb {110}. The last aspect of PVD Cu-Nb interfaces to note is that they are atomically flat[11].

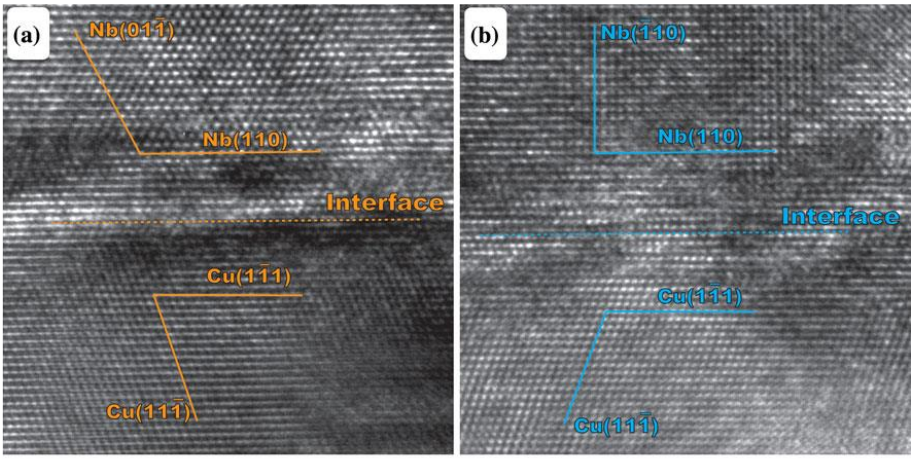

Figure 3-6 – High-resolution transmission electron micrographs (HRTEM) of a) Kurdjumov-Sachs and b) Nishiyama-Wasserman type interface in PVD-grown Cu/Nb. Interfaces are normal to the growth direction and found to be atomically flat and sharp. Reproduced from Ref. 106.

MD work has shown that PVD Cu-Nb interfaces are potent dislocation traps, behavior that arises from the weak shear strength of N-W interfaces in some directions and K-S interfaces in all directions[3]. This behavior is tied to the interface misfit dislocation array structure. As an example, the atomic structure of K-S interfaces contains spatial non-uniformity of shear strength for in-plane sliding, efficiently nucleating in-plane screw dislocation loops that enable sliding at low stresses[4]. This weak shear strength allows the interface to deform locally to accommodate an incoming dislocation core. This local deformation relaxes the impinging dislocation's core structure in the interface plane, lowering its energy. This energy must be supplied to the material on top of other impediments to dislocation transmission across the interface supplied by image forces and misfit dislocation strain fields. This positive energy must also be supplied to compact the dislocation core and enable cross slip on a different slip system across the interface. The weak shear strength of PVD Cu-Nb interfaces influences mechanical behavior in other ways that will be discussed later in this Chapter.

Interfaces in ARB-synthesized Cu/Nb (ARB Cu/Nb) have also been studied using MD. Since ARB is a top-down mechanical forming synthesis technique and PVD is a bottom-up deposition synthesis technique, the interface structures formed by each technique are different. In ARB Cu/Nb systems, crystallographic texture evolves as a function of rolling strain[136], but stabilizes somewhat at nanoscale layer thicknesses. At this length scale, the predominant interface type (depicted in Figure 3-7) is characterized by a K-S OR[137]. However, the interface plane is different than in PVD Cu/Nb. Here, interface planes are parallel to Cu {112} and Nb {112}. Cu {112}|| Nb {112} K-S interfaces are faceted, which affects how they deform and contribute to deformation[80].

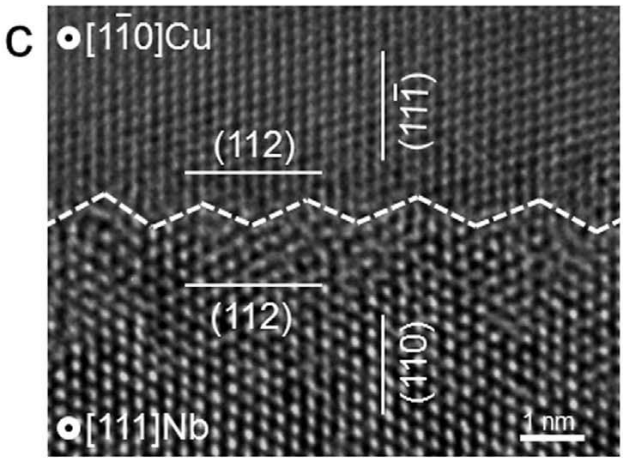

Figure 3-7 – HRTEM of the predominant K-S OR interface type in ARB Cu/Nb. Interface planes and morphology here are different than found in PVD ARB. The interface plane is parallel Cu {112} and Nb{112}, while the morphology is serrated. Reproduced from Ref. 138.

ARB Cu {112}|| Nb {112} K-S interfaces have high interfacial shear strength due to their faceted structure and deform differently depending on applied shear stress[137]. Some shear directions produce sliding in these interfaces, while others cause the interface to emit dislocations into the surrounding lattice. One notable aspect of ARB Cu/Nb interfaces is that in some cases they facilitate nucleation of certain types of dislocations over others. It has been found that Cu twins do not nucleate favorably at Cu {111}|| Nb {110} K-S interfaces, but they do at faceted Cu {112}|| Nb {112} K-S interfaces[7]. This behavior is explained through the mechanism by which twins form in FCC structures by propagation of leading partial <112>-type dislocations on successive {111} planes without propagation of trailing <112> partials. This causes stacking faults on consecutive planes, leading to the formation of a twin. Thus for an interface to facilitate twinning, it must be energetically favorable to nucleate leading partials without nucleating trailing partials that can "heal" stacking faults. It must also be favorable to nucleate partial dislocations over perfect dislocations at these interfaces. The finding that Cu {112}|| Nb {112} K-S interfaces facilitate twinning, while Cu {111}|| Nb {110} K-S interfaces do not shows that the former is more

efficient at nucleating leading partial <112> dislocations without nucleating trailing partials. The reader is encouraged to refer to Ref. 7 for further details about geometric criteria determining favorability of leading partial emission for other interface types found in ARB and PVD Cu.

3.4.4. Shear instability in metallic nanolaminates

While nanolaminates possess high hardness characteristic of most nanocrystalline alloys, their deformability can be limited due to early onset of flow instability[139]. In tension, deformability quantified by ductility is very low for many nanolaminates due to limited work hardenability and synthesis defects[140]. In compression, deformability is quantified by plastic strain to formation of a shear instability, which concentrates strain in a limited portion of the sample gage and causes localized softening which limits uniform deformability[141]. Other tests used to probe plastic behavior of nanolaminates include nanoindentation[15], clamped beam bending[142], and micro-cantilever bending[143], which produce non-uniaxial stress states that can be used to test effect of stress state on mechanical response. However, these other test methods may be more difficult to extract physically meaningful flow stresses from and do not easily allow observation of failure modes such as plastic instability or fracture in the same way that uniaxial tests do. There are many examples of shear banding in nanolaminates, including in micropillar compression of ARB Cu/Nb[141] and eutectic nanolamellar Cu/Ag[141], as well as under Berkovich nanoindentation of PVD Cu/Nb[144]. While these works shed considerable light on the relationship between shear localization and interface-mediated deformation of nanolaminates, the most pertinent literature to this work was conducted on micropillar compression of PVD Cu/Nb. This literature will be discussed below.

Mara, et al. conducted micropillar compression on PVD Cu/Nb with h = 40 nm, using *post mortem* TEM sectioning to demonstrate the role that Cu-Nb heterophase interfaces play in plastic instability[16]. SEM and TEM micrographs of post-deformation PVD Cu/Nb micropillars are found

in Figure 3-8. This work demonstrated that PVD Cu/Nb has a flow stress of 1.75 GPa, which is consistent with nanoindentation testing of the same material[15]. It should be noted that this strength is higher than the rule of mixtures expected for pure nanocrystalline Cu and Nb with comparable grain size[145]. h = 40 nm Cu/Nb begins shear softening at a true plastic strain of about 10%, until it ruptures at 36% true total strain. *Post mortem* TEM of a pillar compressed to 14% true total strain reveals the presence of a shear band in which the local strain is much higher than in the rest of the pillar. The most severe strain in the shear band is associated with an engineering layer-normal strain of 77%. In the deformation model presented, the mechanism of shear band formation is split into two stages. The first stage is characterized by cooperative lattice rotation and interface plane rotation across multiple layers. This rotation must be supplied by the activation of favorable slip systems, and can be induced by moments at micropillar top corners. In the second stage of shear localization, a common easy shear direction is formed across multiple layers and most plastic strain becomes concentrated in the shear band. Interface sliding from increased resolved shear stress on interface planes is proposed to supply the localized deformation found in the shear band. This is corroborated with MD simulations that demonstrate low shear strengths of KS PVD Cu/Nb interfaces[4], as well as micropillar compression on 45° inclined Cu/Nb in which failure is precipitated by interface sliding[20].

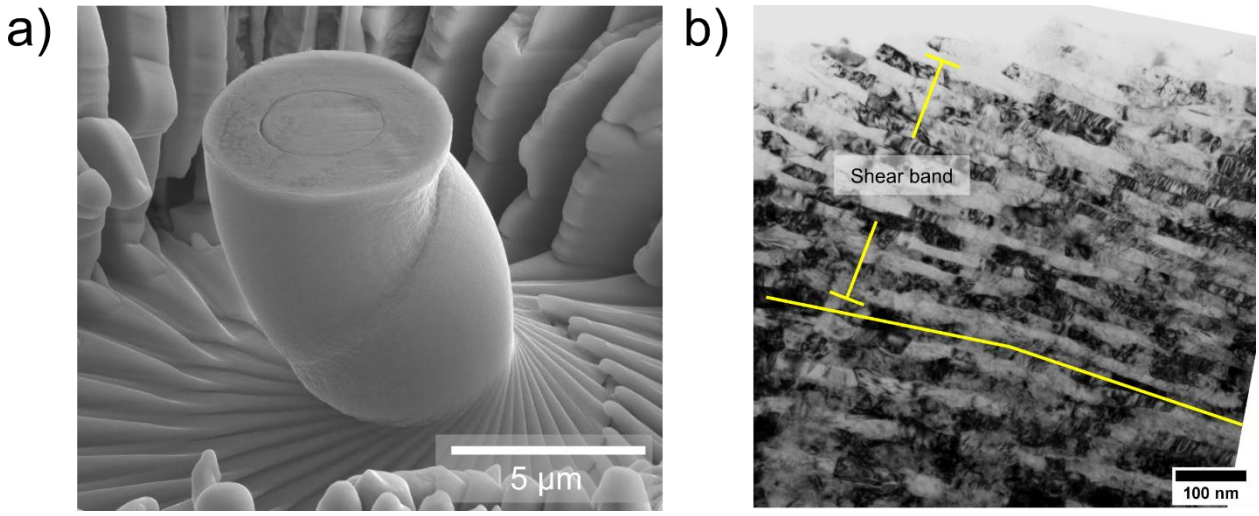

Figure 3-8 – a) SEM micrograph of a PVD Cu/Nb micropillar with *h* = 40 nm compressed to high plastic strain. One large shear band runs through the pillar, indicating plastic instability. b) Transmission electron micrograph (TEM) of a cross-sectioned micropillar of the same material as in a). Layers are thinner inside the shear band, indicating concentration of plastic strain. Reproduced from Ref. 16.

Further work by Mara, et al. also investigated the contribution of Cu-Nb interfaces to shear localization at much smaller length scales[17]. When h drops from 40 to 5 nm, the favored dislocation propagation mechanism switches from CLS to single dislocation across interfaces[15]. The flow stress of h = 5 PVD Cu/Nb is 2.4 GPa, demonstrating strengthening at low layer thickness consistent with Ref. 15. The maximum true stress in this material occurs at 15% true plastic strain, with rupture occurring at 26% true total strain. Post-mortem SEM of the compressed pillar reveals that rupture occurs due to fracture along a sharp plane inclined to the compression axis. No evidence of shear banding is found in the post-mortem SEM. This deformation behavior is distinct to that seen in h = 40 PVD Cu/Nb, and is hypothesized to occur due to the shift from CLS to single dislocation crossing. If this is true, then the strength of the material is controlled by the barrier that Cu-Nb interfaces pose to dislocation transmission, which is calculated to be around 1 GPa resolved shear stress for KS interfaces. This would translate to 2.5 GPa compressive stress given a Schmid

factor of 0.408, which is the maximum Schmid factor out of Cu and Nb in the Cu (111)||Nb (110) out-of-plane texture observed for PVD Cu/Nb[146].

ARB Cu/Nb deforms differently to PVD Cu/Nb consistent with divergent interface structures in Figure 3-6 and Figure 3-7. SEM and TEM micrographs of post-deformed ARB Cu/Nb micropillars can be found in Figure 3-9. The flow stress of ARB Cu/Nb with h = 18 nm is 1.7 GPa, with a true plastic strain to fracture of 10%[19]. Additionally, Figure 3-9 shows that the shear banding behavior of ARB Cu/Nb is completely divergent to that of PVD Cu/Nb. The former forms many small shear bands along the gage length of the pillar, while the latter forms a single large shear band traversing the pillar. The ARB Cu/Nb does not soften before fracture, while PVD Cu/Nb shows noticeable strain softening from the onset of shear localization to pillar rupture[19]. The differences in plastic instability and mechanical behavior between ARB and PVD Cu/Nb has been attributed to the differences in their interface structure; while PVD Cu-Nb interfaces shear easily and precipitate gross shear localization, ARB Cu-Nb interfaces do not slide easily and prevent the formation of a single large shear band[137,147]. This likely explains the difference in strain softening before pillar failure between the two materials. The sliding of weak interfaces in advanced stages of shear banding in PVD Cu/Nb causes plastic deformation without much dislocation storage in the material, causing the material to soften as it shear bands. Strong interfaces in ARB Cu/Nb prevent the propagation of a large shear band, causing dislocation content to build in the material until fracture becomes energetically favorable. This dislocation storage may prevent strain softening in ARB Cu/Nb micropillars.

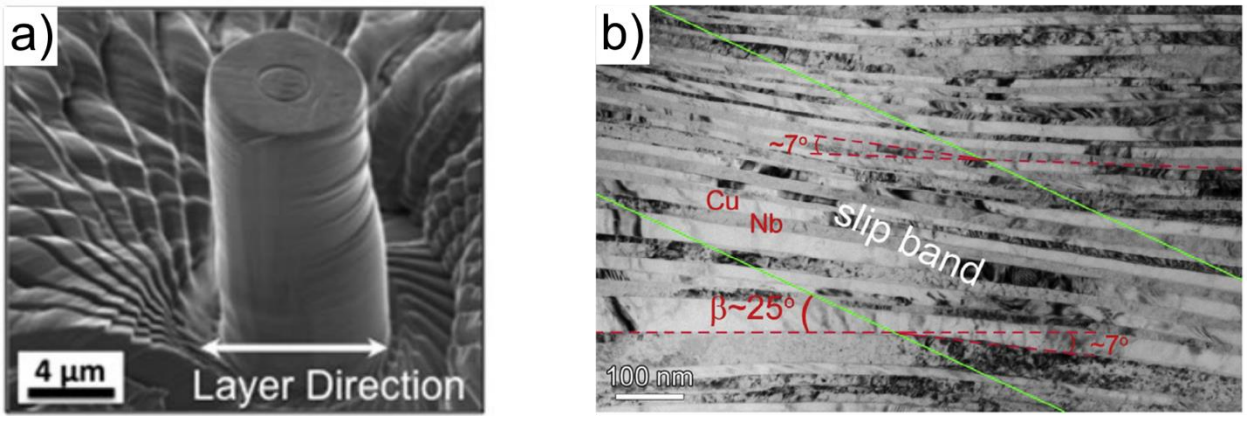

Figure 3-9 – a) An SEM micrograph of a post-deformation ARB Cu/Nb micropillar with h = 18 nm. This material forms many small slip steps instead of one large shear band as seen in PVD Cu/Nb. b) A TEM micrograph of the slip band morphology in ARB Cu/Nb. The slip band angle here is 25° as compared to 35° in PVD Cu/Nb[16]. (a,b) are reproduced from Ref. 19.

These studies on PVD and ARB Cu/Nb using micropillar compression demonstrate the importance of interface structure and properties in plastic instability at the nanoscale. The crucial role of interfaces in plasticity presents an opportunity for tailoring the mechanical behavior of nanocrystalline metals and alloys. If interfaces can be tailored in terms of their ability to transmit, nucleate, and annihilate dislocations, then undesired behavior such as strain softening or early shear localization can be avoided. Following the logic of structure-property relationships that underpin material science, the possibility of repeatably controlling interface structure to influence their interactions with dislocations should be studied. This topic is the foundation of this work, and its fundamental approach will be outlined below.

3.5. Introducing 3D character to interface structure to influence mechanical behavior

This work revolves around three dimensional interfaces (3D interfaces), a particular type of interface whose structure is repeatably controlled to influence the energetic favorability of different unit deformation mechanisms. A 3D interface is defined as a boundary separating two phases that possesses chemical, crystallographic, and topological heterogeneities in all spatial

dimensions. The differences between a 3D interface and previously studied "2D" interfaces is illustrated in Figure 3-10. In order for interfaces to influence unit deformation activity, they must exist on the same length scale as plasticity carriers such as dislocations. In other words, they must contain the aforementioned heterogeneities on the length scale of a few to a few tens of nanometers.

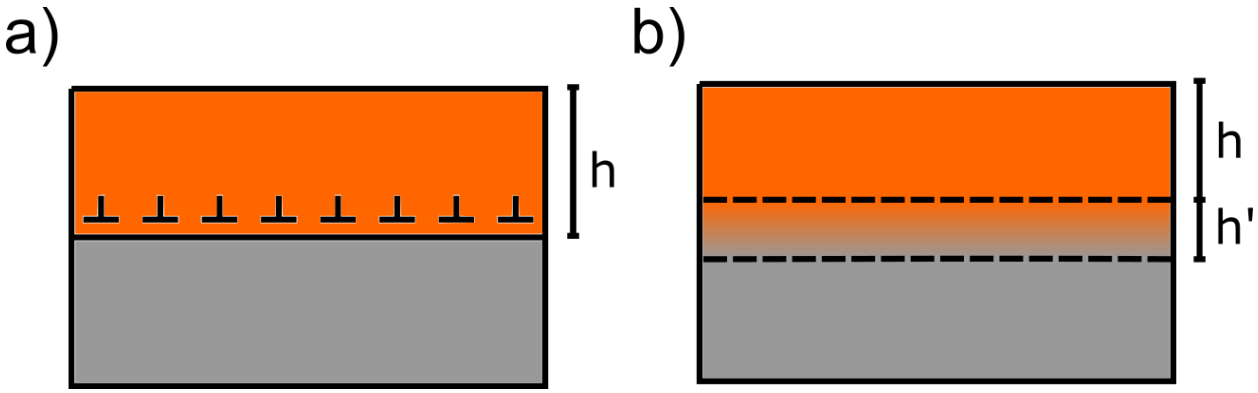

Figure 3-10 – a) A schematic diagram of the atomically sharp interfaces in Cu/Nb made via PVD and ARB that have been previously studied in the literature. This interface is referred to as a "2D interface" because its atomic structure does not occupy the interface normal dimension significantly. b) An illustration of a "3D interface" that is the topic of this thesis. This interface is extended in the interface normal dimension, meaning that a 3D interface-containing nanolaminate can be characterized not only by *h*, but also *h'*, the interface thickness.

Thus, although 3D interfaces may evoke earlier studies on graded interfaces used in applications such as wear coatings and turbine thermal barrier coatings[148,149], the latter exist on the length scale of a few to many microns. Microstructural gradients on the micron scale are too large to study dislocation-interface interactions on the unit scale, so they will not be considered as 3D interfaces. One example of an interface that exists on the nanoscale and has significant dimensionality in the interface normal direction is a complexion. Complexions are thermodynamically stable phases that exist between grains and are single-atom to a few tens of nanometers thick[150]. Another similar concept to 3D interfaces is the inclusion of nanoscale amorphous layers (amorphous interphases) in nanolaminates[151,152]. Both complexions and amorphous interphases can be used to modify mechanical behavior of nanocrystalline alloys, but they do not exhibit any of the heterogeneities

that are present in 3D interfaces. Chapter 4 will contain a description of how 3D interfaces are synthesized, Chapter 5 will describe the microstructure associated with them, and finally Chapter 6 will discuss the tie between 3D interface microstructural parameters and their influence on mechanical behavior.

4. Experimental methods

4.1. DC magnetron sputtering PVD

4.1.1. Working principles

DC magnetron sputtering (DCMS) physical vapor deposition (PVD) methods are crucial to this work, as they offer sub-nm precision control over the microstructure of a thin film along the growth direction, ensuring repeatable control of layer and 3D interface thickness. For a more detailed discussion of direct current magnetron sputtering (DCMS) than is given here, see Ref [22]. DCMS involves sputtering a target to generate a vapor of atoms that is deposited on a substrate to synthesize a thin film. Most deposited films are below a few microns thick owing to the maximum deposition rate achievable and consumption rate for a given target material. The term sputtering describes the process of bombardment of a target material with energetic atomic scale particles, generating gas phase atoms or ions of the target material. The target material does not need to be heated above ambient temperature for this process. In fact, target materials need to be fluid cooled in DCMS, as without cooling the heat generated by sputtering would eventually melt or vaporize the target. Sputtering is achieved in DCMS by using the configuration depicted in Figure 4-1.

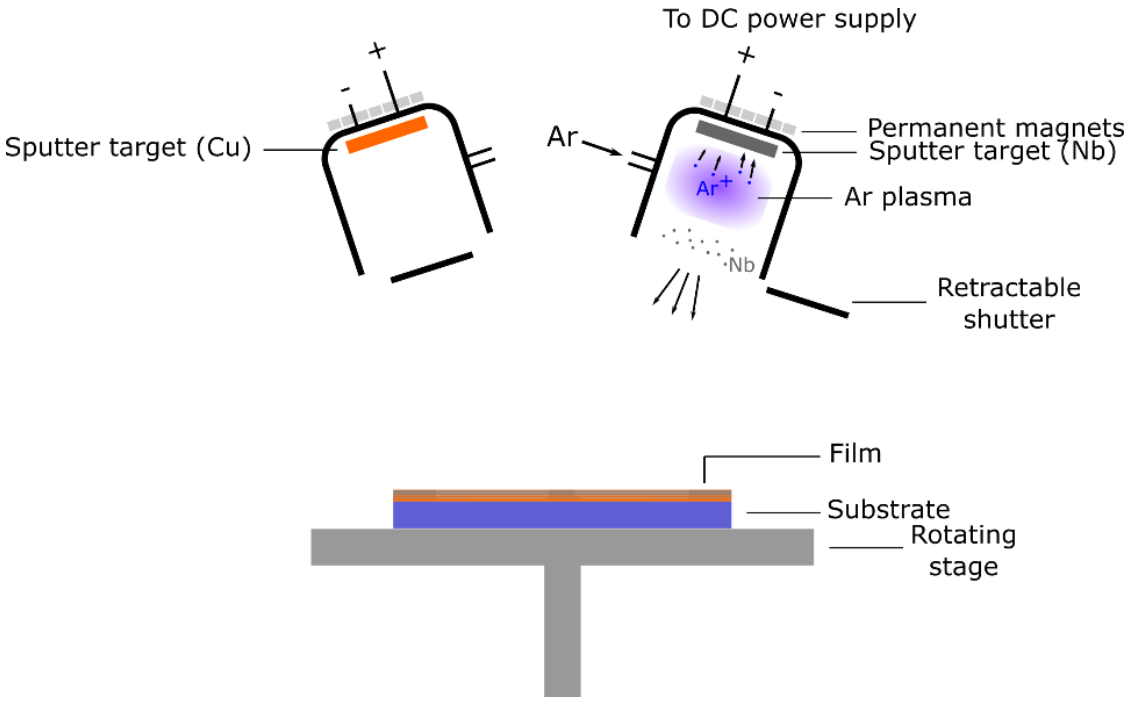

Figure 4-1 – A schematic of a DC magnetron physical vapor deposition chamber. Sputtering is achieved by striking an Ar^+ plasma near metal targets in the sputtering guns at the top of the chamber. Permanent magnets behind the targets provide a magnetic field that accelerates plasma ions towards the targets. The accelerated ions provide enough energy to liberate metal atoms from their lattice, which then fly towards the substrate on which a film is to be grown.

This setup consists of a sputtering "gun", where sputtering of the target occurs, and a stage, where the substrate sits and can be manipulated to influence final thin film microstructure. At a high level, a sputtering gun consists of a target, bias supply, permanent backing magnets, gas supply, and a shutter. Other components are important to gun functioning, but do not contribute to film microstructure and so will not be discussed here. Sputtering is achieved through the following steps:

1. The DCMS chamber is pumped to ultra-high vacuum, about a few 10^{-6} mTorr or below.
2. The gas supply is turned on at a few mTorr to provide bombardment atoms. This pressure is referred to as the working pressure, while the gas used for

sputtering is called the sputter gas. The sputter gas is argon in this work, although other gases such as nitrogen-argon or oxygen-argon can be used to sputter compounds in reactive sputtering.

3. An argon plasma is struck by applying a DC bias of a few hundred volts to the sputter gas.
4. The now-ionized argon is accelerated towards the target by the magnetic field supplied by the backing magnets.
5. Target atoms are sputtered, producing a stream of vaporized target atoms that travel towards and deposit on the substrate.

The most common geometry for DCMS is the planar geometry, where magnets are placed behind a planar surface to provide the magnetic field for sputtering. This configuration was used in this work, where magnets were arranged in a circular pattern behind the target. This configuration produces a circular "racetrack" groove on the target due to nonuniformities in the toroidal magnetic field produced. The depth of this racetrack determines the lifetime of the target; once the groove penetrates the target, it is no longer usable without risking damage to the sputter gun.

4.1.2. Adjustable parameters

Many processing parameters can be adjusted during DCMS to influence thin film microstructure. The most important processing parameters that can be adjusted during DCMS to influence thin film microstructure are sputtering power, working pressure and choice of substrate. The first two parameters are controlled at the gun, while the last is controlled at the chamber stage. Sputtering power is controlled by the bias supply in the sputter gun and is usually maintained using a control loop. In this work, a power control loop was used, but loops can also be set to control

current or voltage. Sputtering power is used mainly to control deposition rate, which is a key processing parameter to control thin film microstructure[153]. Working pressure can also be used to influence thin film microstructure, as it affects film grain size, porosity, morphology, and residual stress[24]. While other gun parameters can be adjusted, they are not relevant to this work.

Stage conditions can be adjusted to control film microstructure as well. Substrate rotation improves film uniformity in terms of thickness and morphology across the substrate, and was used in this work. Substrate heating can be done at moderate homologous temperatures of 0.25-0.5 T_m, where T_m is the melting temperature of the target material, to tailor adsorbed target atom (adatom) surface diffusivity on the substrate. Higher temperatures can trigger significant grain growth in the film[23]. The influences of substrate temperature on film microstructure includes changes in porosity, morphology, grain size, and film stress. Substrate bias is another parameter adjustable in DCMS, and is used to accelerate target atoms towards or away from the substrate. Substrate bias can influence adatom surface diffusivity and influences film microstructure in similar fashion to temperature control, with higher negative bias producing changes similar to higher substrate temperature (assuming positive bias at the target)[154]. Lastly, the substrate itself can be used to influence film growth, as it may contribute to epitaxy during deposition. Films grown on Si with native oxide have no epitaxy with the substrate due to the native oxide's amorphous structure[155]. Strong substrate epitaxy can be achieved with HF-etched Si, demonstrated in in Cu/Fe and Cu/Ni multilayers grown on different Si planes[10,156]. Final film microstructure clearly depends on myriad factors during deposition, which can be summarized in a structure zone diagram found in Figure 4-2.

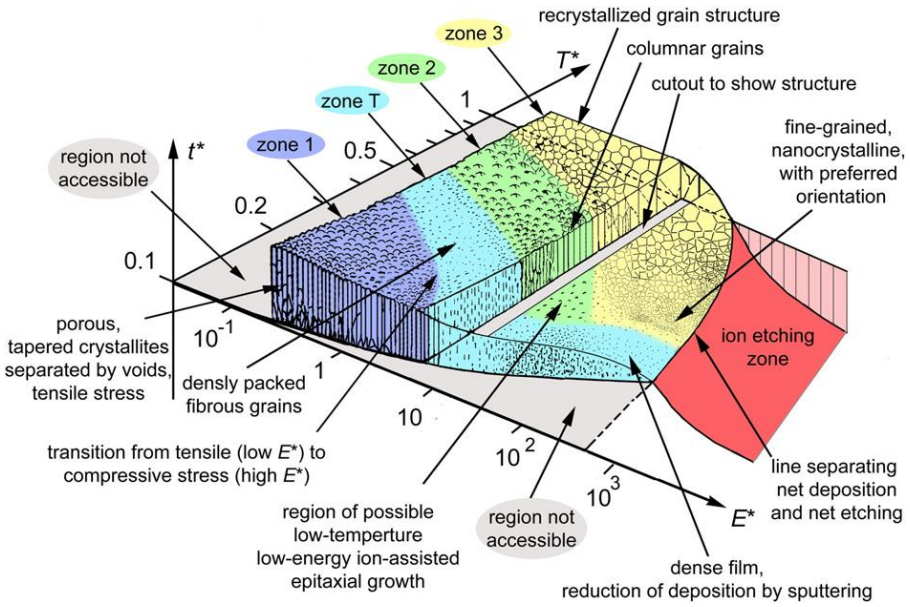

Figure 4-2 – The main parameters influencing metal film morphology are summarized in the zone diagram depicted here (reproduced from Ref. 157). Generalized temperature T* is one major parameter that incorporates the effect of different melting temperatures and lattice energies among different metals. The other parameter is normalized energy flux E* that characterizes the kinetic energy of sputtered atoms. E* is influenced by chamber parameters such as working pressure and substrate bias. T* and E* ultimately determine adatom mobility on the deposited film, which in turn governs the final film microstructure.

4.2. Transmission Electron Microscopy

Transmission electron microscopy (TEM), is an experimental method where electrons are accelerated through an electron-transparent sample to gain information about the structure and chemistry of the sample. This Section will begin with a brief description of TEM working principles, followed by a description of sample preparation, and conclude with a description of imaging modalities and analytical techniques. There are many different signals that can arise from TEM due to the variety of ways that electrons can interact with matter, but the current work focuses on forward scattered electrons and characteristic X-rays. These signals are used for imaging, crystallographic characterization, and chemical characterization. A lens diagram of the TEM used

for most of this work is found in Figure 4-3. Most of the information contained in this section is based upon Williams and Carter's seminal textbook on TEM[27].

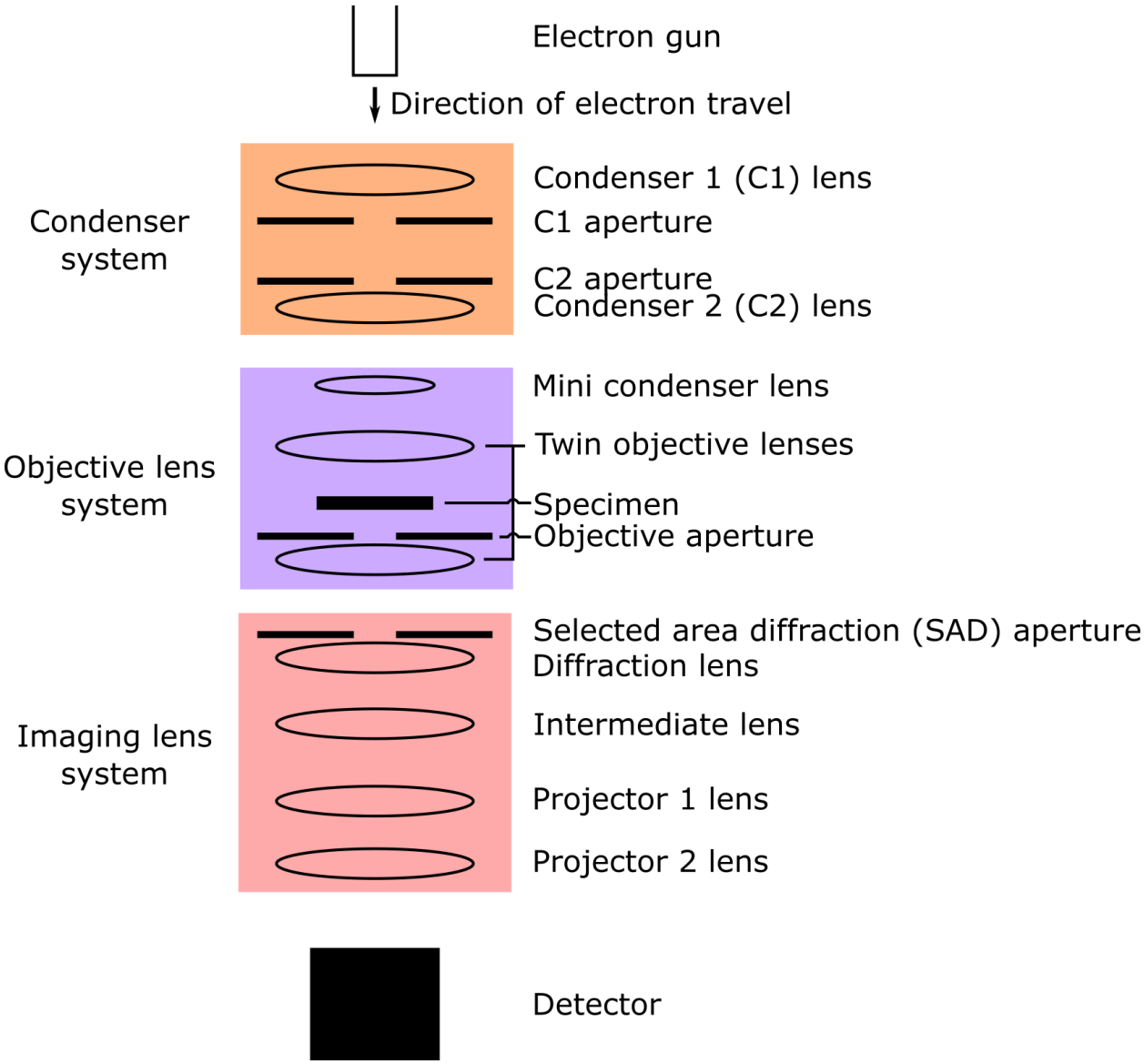

Figure 4-3 – Diagram of a typical field emission gun (FEG) TEM. This diagram is based off the Thermo Fisher Talos F200X, which was used for most of the micrographs in this work. Details can be found in the F200X manual. The TEM can be grouped into three lens systems, the condenser, objective, and imaging lens systems. The condenser lens system controls the intensity and area of illumination on the specimen. The objective lens system determines the focal plane of the image or diffraction information coming from the specimen. Lastly, the imaging lens system controls the magnification of image or diffraction signals heading towards the detector. Elements such as image and beam shift and tilt coils are omitted here.

4.2.1. Working principles of TEM

4.2.1.1. Wave nature of electrons

Imaging with electrons is analogous to imaging with light, which is an intuitive example with which most people are familiar. The light analogue of TEM is the optical microscope, in which photons with wavelengths between 300 and 700 nm are focused on a sample, and the reflected or transmitted light collected to form an image. Optical microscopy is mostly used to study objects that are above a single micron in length scale due to the physical limitations of photons for imaging. The lateral resolution of an optical microscope is given by:

$$\delta = \frac{0.61\lambda}{\mu \sin \beta} \tag{4-1}$$

where δ is the resolution of the microscope, λ is the photon wavelength, μ is the refractive index of the imaging medium (which is air unless performing immersion microscopy), and β is the collection semi-angle of the lens used for microscopy. Usually, μsinβ is approximated as 1. As an example, if green light with a wavelength of 550 nm is used, then the lateral resolution of the microscope is 300 nm. This highlights a limitation of visible light – it cannot probe the structure of materials on the atomic scale. This requires a probing particle with a much smaller wavelength.

Electrons can be used to address the resolution limits of photons. Quantum mechanics establishes that every object in the universe is subject to wave-particle duality. However, the wave nature of objects is only noticeable when the object in question has a very small mass. This is quantified by the de Broglie equation:

$$\lambda = \frac{h}{p} = \frac{h}{mv}\sqrt{1 - \left(\frac{v}{c}\right)^2}$$

(4-2)

where λ is the object wavelength, h is the Planck constant, m is the object mass, v is the object velocity, and c is the speed of light in a vacuum. This version of the equation is relativistic, which is needed to describe the energetics of electrons moving at a significant fraction of c. Equation (4-2) shows why macroscopic objects do not have much wave character – a 150 g baseball traveling at 150 km/h has a wavelength of $1.06 * 10^{-34}$ m. This wavelength is too small to exhibit wave character upon interaction with even the smallest objects in the universe such as fundamental particles. Equation (4-2) can also calculate the imaging resolution of an electron with kinetic energy of 200 keV, which is a commonly used energy for TEM. The relativistic velocity of such an electron is $2.08 * 10^{6}$ m/s, giving a wavelength of 2.51 pm. Thus, according to Equation (4-1), the resolving power of a TEM using 200 keV electrons should be 1.53 pm. In practice, lens imperfections producing aberration limit the resolution of real microscopes. For example, the Thermo Fisher Talos F200X used in this work has a specified lateral resolution of 100 pm.

It is often convenient to refer to electrons in the TEM using their wavenumber and wavevector. The wavenumber k is conveniently specified by $1/\lambda$, while the wavevector is specified by **k**, whose magnitude k and direction specifies the electron's direction of travel.

4.2.1.2. *Electron-matter interactions*

Electron-matter interactions generate different signals providing distinct information about an electron-transparent TEM specimen. These signals can be categorized broadly by whether they arise from scattering events that produce change in kinetic energy of incident electrons or not. Elastic scattering does not change incident electron kinetic energy, while inelastic scattering does. Elastically scattered electrons are most commonly used to generate images in the TEM. They can be scattered into the direct beam, coherently scattered, incoherently scattered, or backscattered.

Coherency is a term describing constructive interference, which will be covered under diffraction in the next subsection. Inelastically scattered electrons can also be collected to generate image signal, but they are mostly used for analytical work such as electron energy loss spectroscopy (EELS, not covered here). Inelastic scattering may also generate secondary particles used for analytical experiments. Among these particles are secondary electrons, Brehmmstralung X-rays, characteristic X-rays, plasmons, phonons, and electron-hole pairs. For this work, characteristic X-rays used for elemental quantification and will be discussed in Section 4.2.4.2.

4.2.1.3. Electron diffraction

Diffraction refers to the coherent scattering of waves off periodic objects such as crystals in TEM specimens. This discussion uses concepts from Chapter 12 of Ref. 27 and *Elements of X-ray Diffraction* by Cullity[158]. Diffraction conditions in crystals are quantified by Bragg's Law. This law, illustrated in Figure 4-4, stipulates the geometric conditions required for constructive interference.

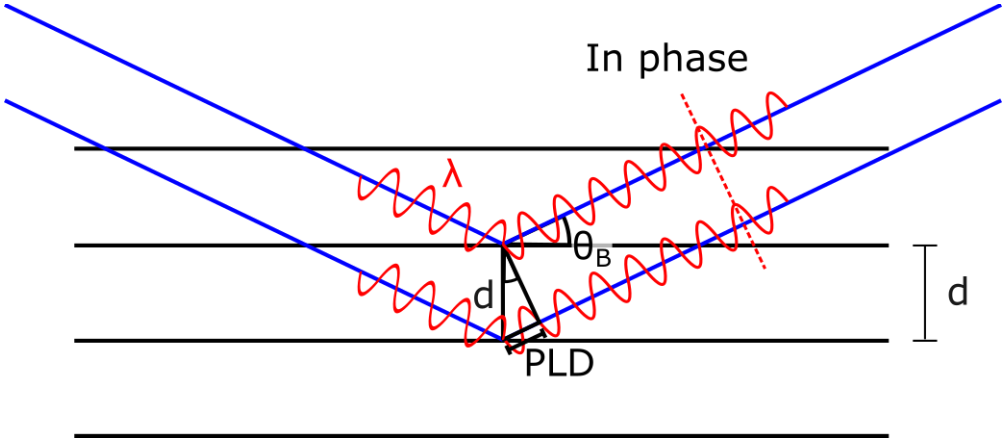

Figure 4-4 – A diagram of Bragg's Law. Incoming waves, such as electron or X-rays for materials characterization, with wavelength λ diffract off crystalline planes with plane spacing d. Diffraction is characterized by constructive interference between waves scattering off different planes of the same family. This requires that the path length difference (PLD) between the two waves is an integer multiple of λ. Diffraction occurs when the scattering angle measured from the crystallographic planes is the Bragg angle θ_B.

For constructive interface, the path length difference between electrons scattering off of adjacent planes must be equal to an integer multiple of λ, nλ. This path length is defined by the incident angle θ of the electron wave and the plane spacing d of the crystal planes. From trigonometry, this length is 2dsinθ. This produces Bragg's Law, $n\lambda = 2d\sin\theta_B$. Diffraction only occurs at specific angles θ_B for a given crystal and set of planes and is called the Bragg angle.

The wave in the TEM is an electron wave, characterized by wavevector $\mathbf{k_o}$. For elastic scattering, this wave scatters off the crystal planes to form the wave $\mathbf{k_f}$, changing only direction. Thus, $|\mathbf{k_o}| = |\mathbf{k_f}| = 1/\lambda$, where λ is the wavelength of the electron. For $\mathbf{k_o}$ to scatter to $\mathbf{k_f}$, it must undergo a momentum change referred to as the scattering vector, or **K**. Consequently, $\mathbf{K = k_f - k_o}$. A diagram of how scattering is treated by wavevectors is found in Figure 4-5.

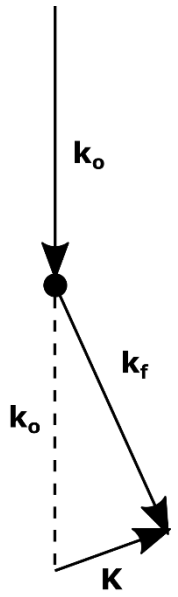

Figure 4-5 – A wavevector scattering diagram describing elastic scattering from the dot-shaped object. An incident wave is described by wavevector $\mathbf{k_o}$, which is scattered to $\mathbf{k_f}$. The scattering vector **K** describes the change in momentum of the scattered wave. Here, $|\mathbf{k_o}| = |\mathbf{k_f}| = 1/\lambda$, meaning that the incident wave does not lose energy after scattering.

When the Bragg condition is satisfied, **K** has a special value $\mathbf{K_B}$, or as used later, **g**. The magnitude of $\mathbf{K_B}$ is given by the spatial frequency of the crystal planes of interest, 1/d. Substituting this into

the Bragg condition, n $\lambda|\mathbf{K_B}|$ = 2dsin θ_B. Nn this treatment, it is assumed that scattering only happens once. This is referred to as kinematical diffraction, and will be assumed in this work. If diffraction is a result of multiple scattering events, it is referred to as dynamical diffraction. Dynamical diffraction will not be discussed in detail in this work. The Bragg condition is the simplest treatment of diffraction and does not account for the three dimensional nature of bulk crystals. Diffraction in three dimensions will be discussed next.

The Laue diffraction equations describe diffraction in three dimensions. Much like the Bragg condition, diffraction requires that electron scattering from adjacent crystallographic planes must be coherent and that such scattering is elastic. The derivation for the Laue equations are found in Ref. 27. They are given as:

$$\boldsymbol{K} \cdot \boldsymbol{a} = h$$

$$\boldsymbol{K} \cdot \boldsymbol{b} = k$$

$$\boldsymbol{K} \cdot \boldsymbol{c} = l \tag{4-3}$$

Where **a**, **b**, and **c** are the unit cell vectors of the diffracting crystal, and h, k, and l are the Miller indices of a diffracting set of planes. Specific values of **K** satisfy diffraction off a specific set of planes (hkl), referred to with $\mathbf{g_{hkl}}$. The Laue condition can be shown to reduce to the Bragg condition (also shown in Figure 4-6):

$$\boldsymbol{K} = \boldsymbol{g_{hkl}} = \boldsymbol{k_f} - \boldsymbol{k_o}$$

$$\boldsymbol{k_o} = \boldsymbol{k_f} - \boldsymbol{g_{hkl}}$$

$$|\boldsymbol{k_o}| = |\boldsymbol{k_f} - \boldsymbol{g_{hkl}}|$$

$$|\boldsymbol{k_o}|^2 = |\boldsymbol{k_f} - \boldsymbol{g_{hkl}}|^2 = (\boldsymbol{k_f} - \boldsymbol{g_{hkl}}) \cdot (\boldsymbol{k_f} - \boldsymbol{g_{hkl}}) = |\boldsymbol{k_f}|^2 - 2\boldsymbol{g_{hkl}} \cdot \boldsymbol{k_f} + |\boldsymbol{g_{hkl}}|^2$$

(4-4)

Since diffraction involves elastic scattering, $|\mathbf{k_o}| = |\mathbf{k_f}|$:

$$|\boldsymbol{k_o}|^2 = |\boldsymbol{k_o}|^2 - 2\boldsymbol{g_{hkl}} \cdot \boldsymbol{k_f} + |\boldsymbol{g_{hkl}}|^2$$

$$|\boldsymbol{g_{hkl}}|^2 - 2\boldsymbol{g_{hkl}} \cdot \boldsymbol{k_f} = \boldsymbol{0}$$

$$|\boldsymbol{g_{hkl}}|^2 = 2|\boldsymbol{g_{hkl}}||\boldsymbol{k_f}| \cos\theta$$

(4-5)

Here, θ is the angle between $\mathbf{g_{hkl}}$ and $\mathbf{k_f}$. Referring to the Bragg condition, the angle $\theta = \frac{\pi}{2} - \theta_B$. Also, $|\mathbf{g_{hkl}}|$ is the spatial frequency of (hkl) planes, more commonly expressed using the plane spacing as $1/d_{hkl}$:

$$|\boldsymbol{g_{hkl}}| = 2|\boldsymbol{k_f}| \cos(\frac{\pi}{2} - \theta_B)$$

$$|\boldsymbol{g_{hkl}}| = 2|\boldsymbol{k_f}| \sin\theta_B$$

$$\frac{1}{d_{hkl}} = \frac{2\sin\theta_B}{\lambda}$$

$$\lambda = 2\, d_{hkl} \sin\theta_B$$

(4-6)

Here, n is 1, indicating that this equation is valid for first order diffraction of (hkl). The lattice parameter a can be used to calculate d_{hkl} for cubic crystal structures,:

$$\frac{1}{a^2} = \frac{h^2 + k^2 + l^2}{d_{hkl}^2}$$

(4-8)

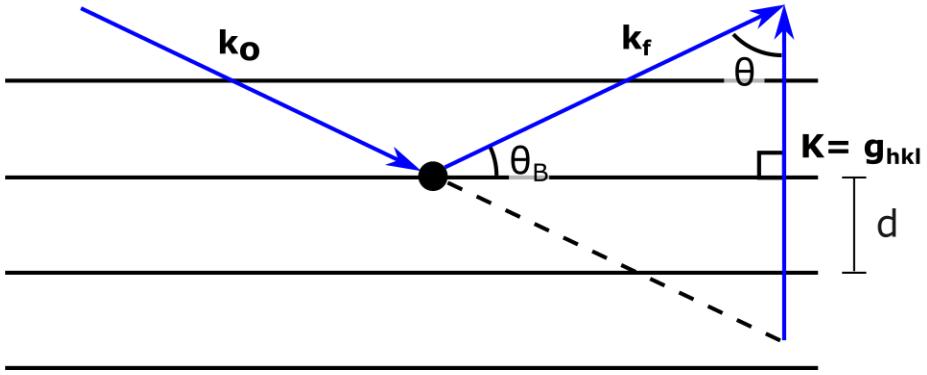

Figure 4-6 – An illustration depicting the relationship between Bragg's Law and the Laue diffraction equations.

The Laue conditions, can be used to construct a locus of all points that satisfy coherent scattering. This is done with $\mathbf{k_f}$, $\mathbf{k_f}$, $\mathbf{g_{hkl}}$, and the reciprocal lattice of the diffracting crystal in Figure 4-7. Since diffraction entails elastic scattering, the scattered beam $\mathbf{k_f}$ must have the same length as $\mathbf{k_o}$. If the tails of $\mathbf{k_f}$ and $\mathbf{k_o}$ are coincident, then acceptable values of $\mathbf{k_f}$ trace out a sphere of radius $|\mathbf{k_o}|$ around the origin. This sphere is called the Ewald sphere with center C. The origin O of the reciprocal lattice is placed at the head of $\mathbf{k_o}$ to determine which reciprocal lattice points produce nonzero scattering intensity. Strong coherent scattering occurs for $\mathbf{K}$ with values $\mathbf{g_{hkl}}$. In theory, if the Ewald sphere is infinitesimally thin (representing no chromatic aberration) and the reciprocal lattice points are infinitesimally small (representing infinite crystalline lattice), then no diffraction occurs except the single reciprocal point where the incident beam scatters. However, in practice any real electron source has finite chromatic aberration and real TEM specimens have finite size. For example, a modestly thinned Cu TEM specimen of 100 nm thickness would contain only a few hundred planes of atoms in the lamella-normal direction. The finite size of TEM samples, which can take the shape of not only lamellae but also nanoparticles and nanowires, ensures that diffraction conditions do not need to be stringently met to produce strong scattering intensity. For

TEM lamellae, reciprocal lattice points are elongated along the thin dimension of the lamellae. These points form elongated rods in reciprocal space known as relrods, short for reciprocal lattice rods. Since the Ewald sphere is large in comparison to the reciprocal lattice and the reciprocal lattice is composed of relrods, many reciprocal lattice points meet the crystal's diffraction conditions.

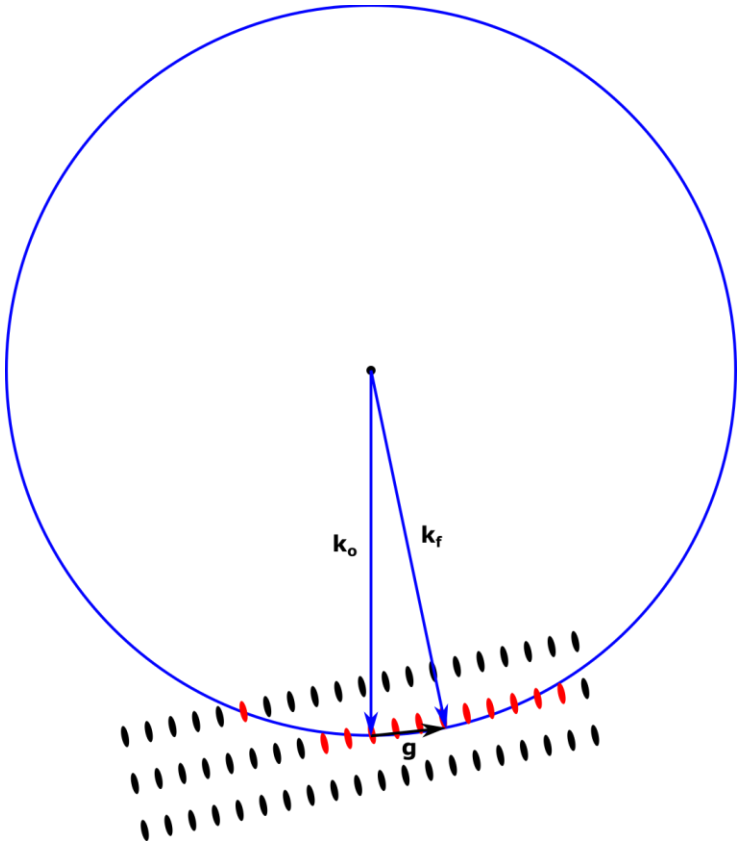

Figure 4-7 – The Ewald sphere construction used to determine which reciprocal lattice sites meet the Laue diffraction condition. The locus of allowable outbound wavevectors $\mathbf{k_f}$ is defined by a sphere with radius $|\mathbf{k_o}|$. The sphere is depicted in blue. For a crystal in an arbitrary orientation, diffraction occurs for crystal planes whose relrods intersect the Ewald sphere.

Strong coherent scattering is produced where the Ewald sphere intersects, or excites, relrods. This geometric constraint is equivalent to requiring elastic scattering of the incident beam and constructive interference between beams scattered from different planes in the same family. The

Ewald sphere construction is used for understanding the origin of zone axis diffraction patterns collected in this work.

4.2.2. TEM sample preparation

TEM requires the preparation of electron-transparent samples whose thickness can be tailored for the desired experiment. High-resolution imaging and certain spectroscopic measurements demand thinner samples, while tasks such as weak beam imaging or energy dispersive spectroscopy may benefit from thicker samples. An appropriate sample preparation technique must be used to prepare an electron transparent sample. Bulk samples are conducive to techniques such as wedge polishing or jet polishing (conductive samples only). Nanoparticle suspensions are easily prepared by deposition of the suspension on a holey carbon grid on which nanoparticles are caught and can be imaged.

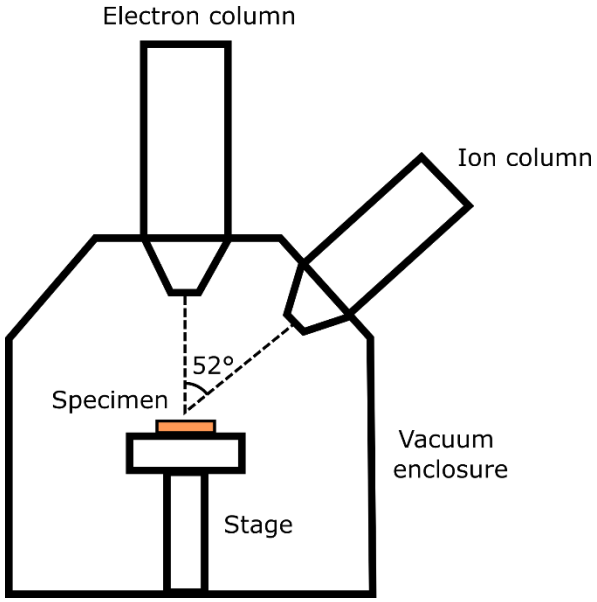

Figure 4-8 – A simplified schematic of a FIB/SEM. The electron and ion column converge at a point called the eucentric height. This is determined by the angle between the columns, which is 52° for FEI instruments.

Since this work relies on thin film samples on substrates, it relies on dual-beam focused ion beam/scanning electron microscope (FIB/SEM) preparation of TEM lamellae. A schematic of a FIB/SEM is found in Figure 4-8. Although bulk sample preparation can be done for thin films, the cross-sectional geometry that is required for this work is more challenging through bulk methods. Thus, FIB/SEM, which can lift out and thin a cross-sectional lamella from a desired location on a sample, is suited for this work. Further discussion of FIB/SEM draws from the seminal textbook edited by Giannuzzi and Stevie, which is an excellent source for the reader interested in the intricacies of the physics and applications of FIB[26]. A FIB/SEM consists of a scanning electron column, which generates a rastered image from secondary or backscattered electrons, an ion column, which accelerates Ga ions towards a sample to mill it to a desired geometry, and other components necessary for functioning such as a moving stage, gas injection sources (GIS), and a micromanipulator needle. Some components such as the GIS or micromanipulator are optional on some FIB/SEM models. The process used is illustrated in Figure 4-9 and is as follows:

1. A protective layer of Pt is deposited using a gas injection source (GIS) and the ion beam on the location of the lift-out. An optional amorphous carbon layer can be deposited first to assist with objective stigmation (CTEM) and condenser stigmation (STEM) correction in the TEM.
2. A rough trench is cut around the protective layer of Pt, leaving a ~1 μm thick lamella which will be later thinned to electron transparency.
3. The thick lamella is attached to a micromanipulator needle by welding it to the needle with a small amount of Pt.
4. The lamella is cut free from the sample and lifted out by the micromanipulator needle.

5. The SEM stage is moved so that a half-moon FIB grid is positioned under the electron and ion beams.
6. The lamella is attached to the FIB grid and cut free from the micromanipulator needle
7. The rough lamella is thinned to electron transparency and given a final ion polish to remove radiation-damaged layers induced by trenching and thinning.

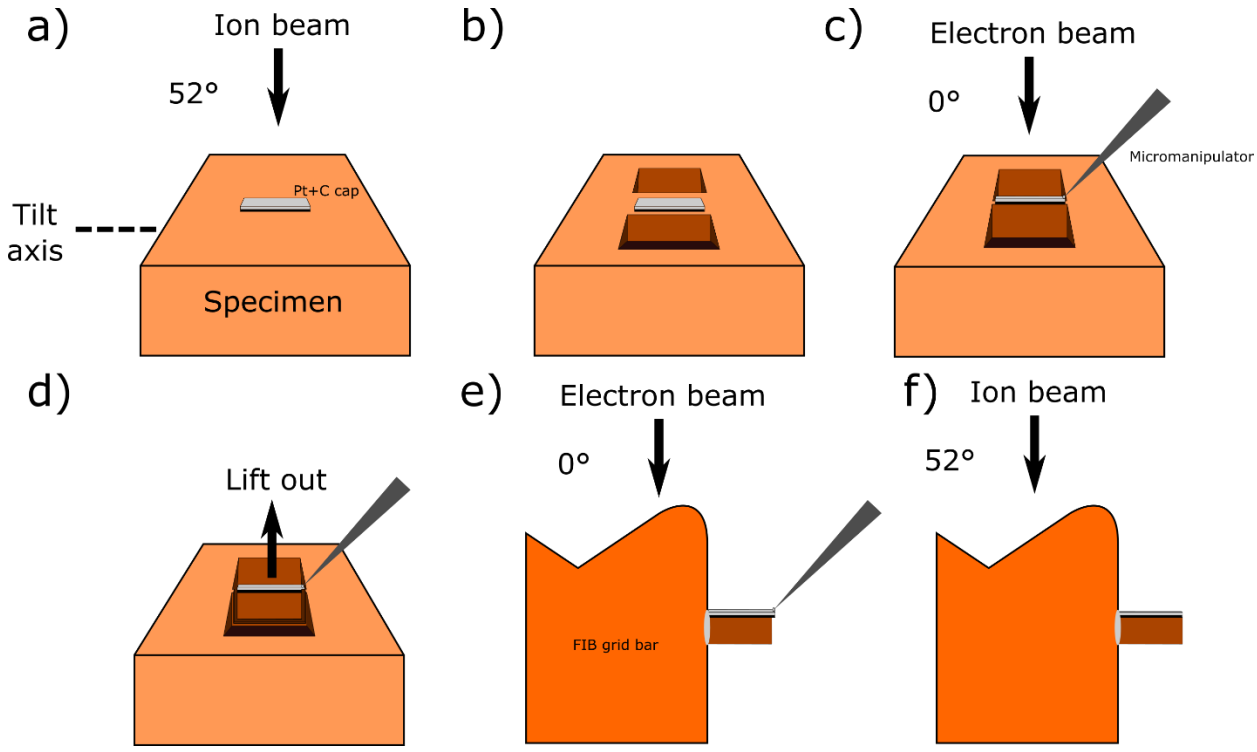

Figure 4-9 – An illustration of the cross-sectional FIB liftout procedure. a) The specimen is tilted to 52°, along the indicated axis normal to the electron beam. A protective Pt cap is deposited, with an optional C layer underneath. b) Rough trenches are milled on either side of the protective cap in a) to make a rough lamella. The lamella can be thinned in place if desired. c) The specimen is tilted to 0°, normal to the electron beam. The lamella is welded to a micromanipulator needle. d) The lamella is cut free from the specimen and lifted out. e) The lamella is Pt welded to a FIB grid bar and then cut free of the needle. f) The FIB grid is tilted to 52° so that the lamella can be thinned to electron transparency.

As alluded to Step 7, care must be taken not to introduce FIB-induced artifacts to the lamella so that the ensuing TEM experiment proceeds smoothly. Rough trenching is carried out at

a FIB accelerating voltage of 30kV, which imparts enough energy to Ga^+ ions to not only sputter sample atoms, but also induce sample amorphization, Ga implantation, and formation of defects such as voids, interstitials, vacancy clusters, and dislocation loops. The beginning stages of thinning are done at 30kV, but as thinning progresses the accelerating voltage is decreased to 5kV to reduce the thickness of the FIB damage layer. Final ion polishing is conducted at 2kV or 1kV to minimize the effects of ion damage. Although this last step still imparts a damage layer to the sample, it is often on the order of a few nm, which should leave about 50-100 nm of undamaged material in a lamella. These sample conditions are sufficient in most cases to produce low-background, high signal images and spectra in the TEM.

It should be noted at this point that while most hard materials can be prepared by FIB/SEM, some materials should be avoided. Most notably is aluminum, which undergoes liquid metal embrittlement as Ga segregates to the Al grain boundaries. Unless precautions such as cryogenic FIBbing are used, many Al TEM specimens will exhibit severe Ga-induced artifacts when prepared in a Ga source FIB. Chemistry-specific problems can also be avoided by using a plasma FIB which uses noble gas ions like Ar^+ or Xe^+ to mill samples. Other samples such as biological or polymeric samples are extremely sensitive to radiation damage and will respond poorly to FIB unless low beam energies, currents, and cryogenic temperatures are used. Lastly, since charged particles are used in FIB, non-conductive samples may pose a challenge in FIB/SEM preparation of lamellae. Coating of the sample in conductive material may circumvent sample charging-induced issues during lamellae preparation in the FIB/SEM. It should be noted that Cu/Nb happens to be conductive, non-reactive with Ga, and not very sensitive to radiation damage[159]. The FIB/SEM used for most of this work is the FEI Helios G4 Nanolab, equipped with C/Pt GIS, an EasyLift micromanipulator needle, and a Ga ion source.

4.2.3. Conventional TEM

Operation of the TEM can often be separated by imaging mode. The two commonly used TEM modalities are conventional TEM (CTEM) and scanning TEM (STEM). CTEM is used to produce diffraction patterns, conduct routine imaging, and conduct atomic resolution characterization of Cu/Nb. STEM is used to access specific diffraction conditions and extract local atomic and chemical information for Cu/Nb. This discussion requires a basic understanding of optical ray diagrams, which can be found in Chapter 6 of Williams and Carter[27] or Chapter 2 of Fultz and Howe[160]. Ray diagrams used in this chapter are made by the dissertation author and adapted from Ref. 27.

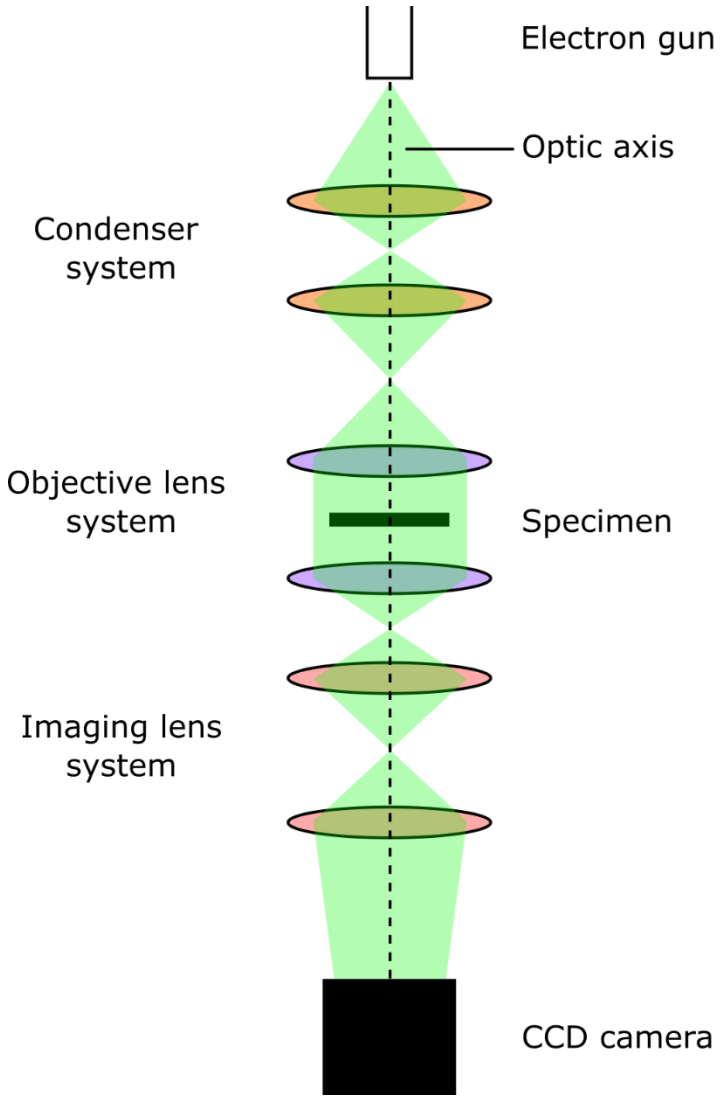

Figure 4-10 – A simplified diagram of the TEM in parallel beam mode. The electron beam is depicted by green shading. The objective lens is excited so that the illumination on the specimen is parallel and covers a wide area.

Conventional, or parallel beam, TEM is one of the two major operation modes used in the TEM. A simplified diagram of a TEM is used to depict CTEM in Figure 4-10. This diagram will be based off FEI/Thermo Fisher instruments, since they were used for this work. In parallel beam TEM, the electron source is magnified by the first condenser, or C1, lens. Then, the C2 lens is used to control sample illumination. In FEI/Thermo Fisher instruments, a mini-condenser lens is included after the C2 lens to make CTEM and STEM operation possible in the same instrument.

The parallel beam then passes through the objective lens and specimen. The beam, now scattered from the specimen, passes through the intermediate and projection lenses. The intermediate lens can be excited differently to achieve imaging or diffraction pattern collection, while the projection lens can be used to change image or diffraction pattern magnification. For diffraction patterns, it is more convenient to quantify magnification by imagining a virtual camera and determining what distance this camera needs to be from the specimen to achieve a given magnification; this distance is called the camera length.

4.2.3.1. CTEM imaging

CTEM is useful for collecting diffraction information from large areas of the specimen and can be used to form images or diffraction patterns. In "imaging mode", diffracted beams from the sample are deflected so that the image plane of the objective lens is the object plane for the intermediate lens. A diagram of this mode is found in Figure 4-11. Diffracted beams from the sample are converged into an image approximately the size of the detector chip in the camera used for data acquisition. At low to moderate magifications (<~100 kx), this image can contain information about the crystallography of the sample if the imaging conditions are set up carefully and the image is carefully analyzed. At high magnifcations (>~100 kx), "high resolution" TEM (HRTEM) may be performed to analyze atomic-scale crystallography provided that instrumental aberrations are sufficiently corrected for. Because many diffracted beams can contribute to the image in CTEM imaging, it sometimes is useful to use an objective aperture to exclude all but a single or few diffracted beam to form an image. When only the direct beam is selected for imaging, a bright field image is formed. When a diffracted beam is selected for imaging, then a dark field image is formed. Dark field images are useful when some feature in the image is tied to changes

in orientation for a specific crystallographic plane. Most CTEM images in this work are bright field images.

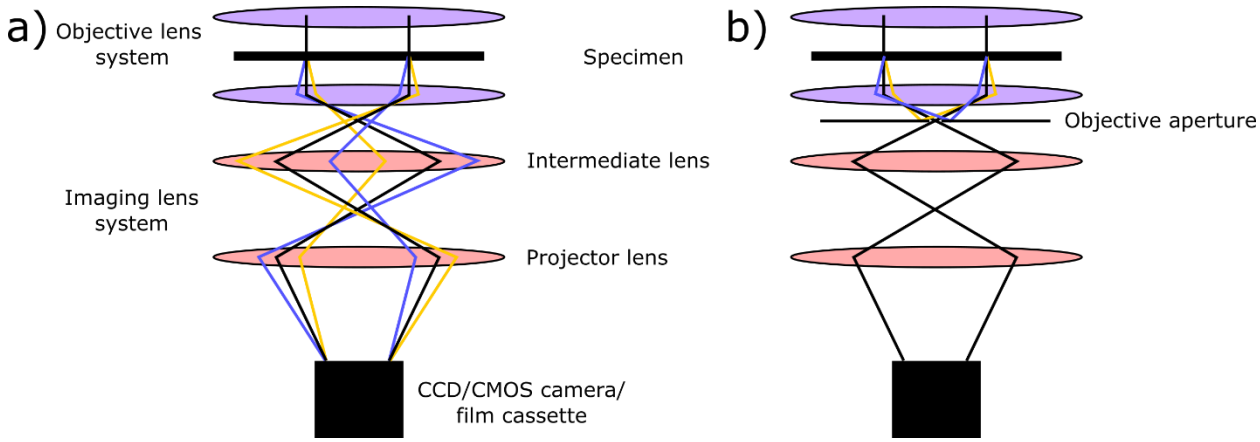

Figure 4-11 – a) A ray diagram of CTEM imaging. Black lines represent electrons traveling in the direction of the incident beam (forward scattered electrons), while blue and yellow lines represent diffracted electrons. Blue lines have the same scattering vector **g**, while yellow lines would have scattering vector **-g**. The resultant image is made up of information from forward scattered electrons, as well as diffracted electrons. b) An objective aperture inserted at the back focal plane of the objective lens selects only forward scattered electrons, forming a bright field CTEM image.

4.2.3.2. Diffraction patterns

Diffraction patterns can also be collected in CTEM using "diffraction mode". Here, diffracted beams from the sample are passed through the intermediate lens so that its object plane is the back focal plane of the objective lens. The diffracted beams pass through to the camera such that beams scattered from different families of crystallographic planes appear as distinct points in a diffraction pattern. A schematic of diffraction mode CTEM is presented in Figure 4-12.

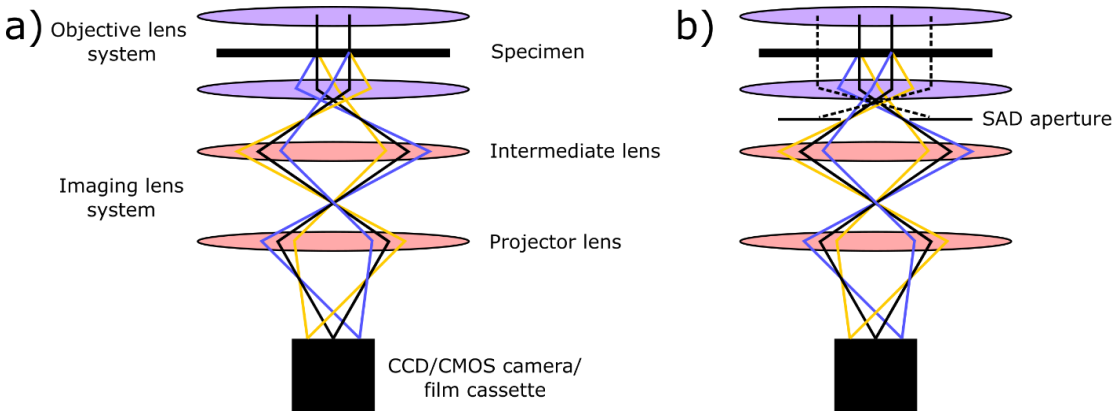

Figure 4-12 – a) A schematic of diffraction mode in CTEM. Color coding for forward scattered and diffracted beams is the same as in Figure 4-11. These beams are converged into spots on the detector to form a diffraction pattern. b) A selected area diffraction (SAD) aperture is inserted into the image plane of the objective lens to only select diffraction information from a portion of the illuminated area on the specimen. Electrons arriving from outside the selected area are blocked by the SAD aperture, as denoted by dotted black lines.

An alternate way to think of diffraction mode CTEM is that it is used to image the reciprocal lattice of the specimen. As discussed before, the visibility of certain spots is described by the intersection of the Ewald sphere with relrods. Specific diffraction conditions are accessed in Cu/Nb where a crystallographic plane in a grain of interest is tangent to the Ewald sphere. The normal direction of the plane under consideration is referred to as the zone axis. The optical axis is then aligned with the zone axis and the grain of interest is said to be “on zone”. The diffraction pattern from an on-zone crystal is referred to as a zone axis pattern, whose formation is illustrated in Figure 4-13.

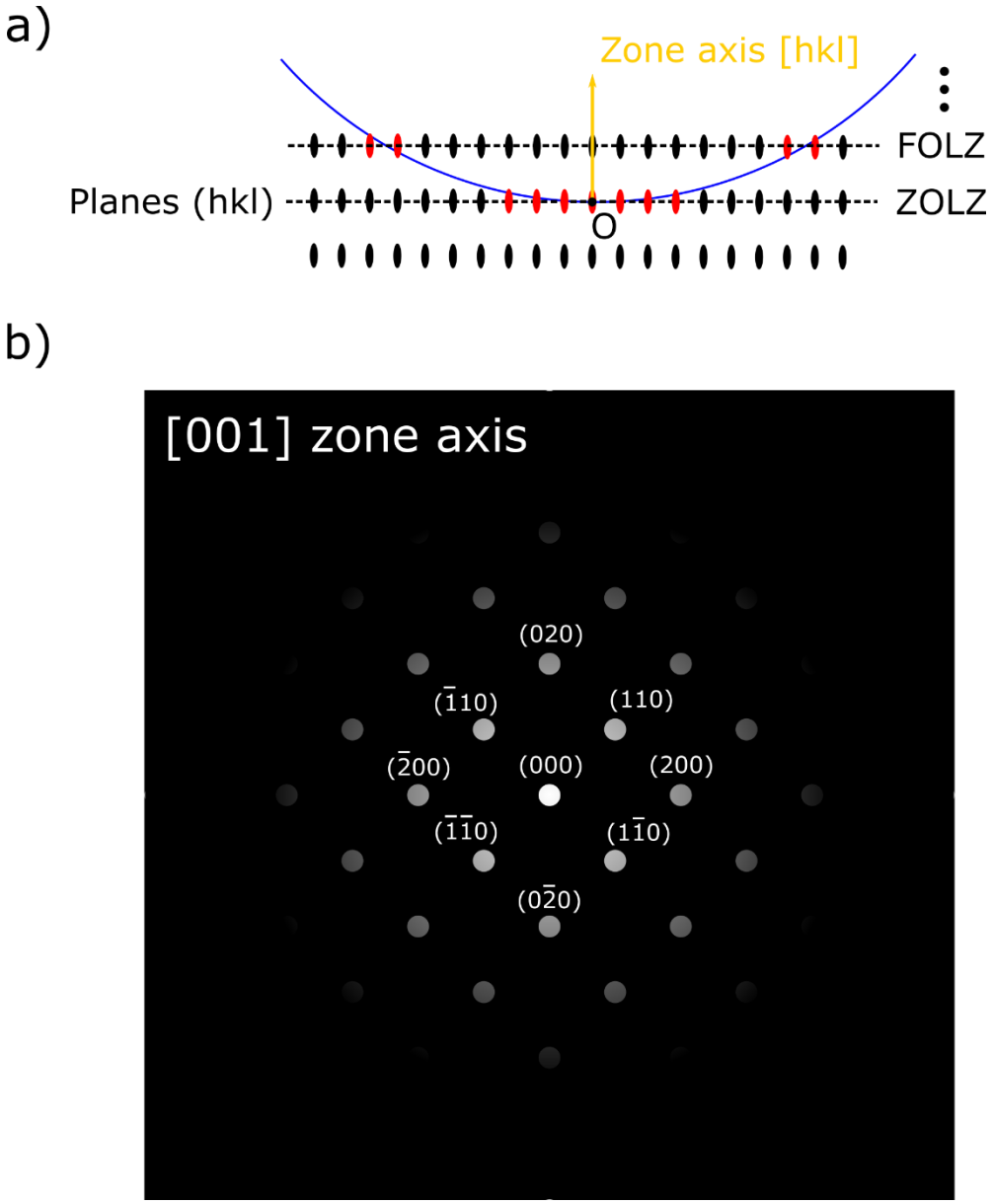

Figure 4-13 – a) Ewald sphere construction for diffraction in the TEM along a zone axis, indicated in yellow. The zone axis [hkl] in reciprocal space is perpendicular to the planes (hkl) in real space. Since the Ewald sphere is relatively flat (not drawn to scale here) due to the high incident electron energy, many relrods are excited. Excited relrods can be grouped according to planes that they belong to along the incident beam direction. Those belonging to the same plane as the forward scattered beam (denoted by the relrod at letter O) are in the zeroth-order Laue zone (ZOLZ), while those in the plane above are in the first-order Laue zone (FOLZ). This continues in subsequent planes, giving rise to second, third, etc.-order Laue zones. b) A zone axis pattern along [001] in a BCC crystal structure (adapted from Ref. 161). Each excited relrod becomes a spot on the detector. The intensity of spots becomes dimmer the farther they are from the direct spot (000) due to the Ewald sphere intersecting those relrods farther from their centers.

Although on-zone diffraction patterns are most desirable when characterizing specimens, it is only practical in specimens whose grain size is above a few microns. Since the specimens studied in this work are nanocrystalline, the diffraction pattern can only be used to characterize the orientation of multiple grains. Although it is possible to select diffraction information from localized regions in an image using selected area diffraction (SAD) apertures, the lowest achievable SAD aperture size is ~10 microns in practice. This corresponds to a selected area a few hundred nanometers across, which is not sufficient to select single crystallites in Cu/Nb nanolaminates. Nonetheless, diffraction patterns and SAD diffraction patterns are highly useful in this work, as they provide some knowledge about local crystallographic alignment. The usage of a SAD aperture is illustrated in Figure 4-12(b).

4.2.3.3. HRTEM

The last major tool used in CTEM in this work is HRTEM. The term "high resolution" refers to images in which individual lattice fringes resulting from diffraction in a sample are visible. In fact, lattice fringe imaging would be a more accurate term for HRTEM; while lattice fringes appear evocative of atoms in a TEM image, it cannot be emphasized enough that HRTEM rarely provides images of atomic positions. Lattice fringes are merely manifestations of crystal geometry in a given region in a sample, which is useful when determining crystal structure and orientation, but not in locating individual atoms or atomic columns. HRTEM has a long list of conditions required for imaging at such fine scales: a well-aligned TEM, high enough accelerating voltage and small enough electron source to ensure a spatially confined point spread function, low chromatic aberration from the electron source, low spherical aberration in the condenser and objective lens, low thermal drift of the specimen, high mechanical stability of the instrument, and a sufficiently high resolution camera or fine enough grain imaging film. It is also important to note

that the terms “high” and “low” are relative: for example, 80 kV is considered a low accelerating voltage to use in TEM, but is sufficient to achieve lattice resolution with enough aberration correction[162]. Likewise, the Thermo Fisher Talos 200FX microscope used in a significant portion of this work has a CTEM spherical aberration of 1.3 mm. While this value is low enough to achieve HRTEM, when compared to optical lenses it is akin to “[looking through] the bottom of a well-known soft drink bottle”[27]. The high accelerating voltage of 200kV and small source size of the field emission gun (FEG) in this instrument is enough to compensate for the significant spherical aberration in the lenses when achieving atomic resolution. In other words, although electromagnetic lenses are very imperfect, the theoretical resolution of electron imaging is so far below typical crystalline interplanar spacings that HRTEM is still achievable on many TEM instruments.

HRTEM is used in lieu of diffraction patterns in this work to characterize local crystallography. Given the high number of grains present in a TEM lamellae for Cu/Nb nanolaminates, it is often a more productive strategy to search for grains that are on zone rather than to tilt a desired grain to on zone conditions. When using HRTEM to image a specimen on a zone axis, it is possible to perform a Fast Fourier Transform (FFT) on the image to obtain a “zone axis pattern”. This term is simply used to refer to a diffraction pattern where the optic axis is coincident with a zone axis. While HRTEM FFTs do not provide the same information as diffraction patterns, they are sufficient to characterize local crystallography and orientation.

4.2.4. Scanning TEM

Scanning TEM is completed with completely different lens conditions than CTEM, with each imaging mode providing complimentary information to each other. Whereas the beam is spread to illuminate a large area simultaneously in CTEM, the beam is converged to a small region

confined to few- or sub-nanometer dimensions in the lateral direction in STEM. STEM imaging is depicted in Figure 4-14. Imaging is achieved in STEM by rastering the beam across the sample while scattering intensities at different angles are captured for each pixel in the raster grid.

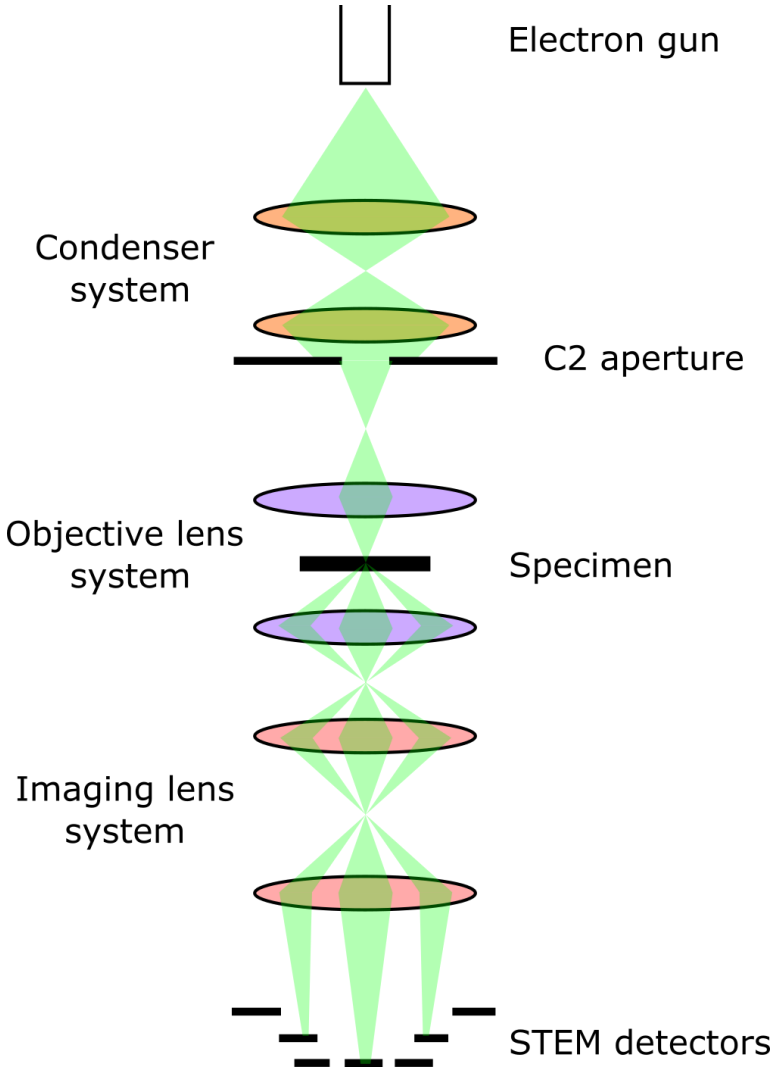

Figure 4-14 – A simplified TEM lens diagram of STEM imaging. The beam is converged on the specimen to obtain highly localized information. Diffracted beams then pass on to the STEM detectors, which record beam intensity for different scattering angles. When the beam is rastered and the intensities stored for many pixels, an image is formed.

The electron beam first passes through the C1 lens, which demagnifies the source and controls the intensity of illumination further down the beam. In practice the C1 lens, along with

the C1 apertures, plays a crucial role in controlling probe current and probe size to a lesser extent. Then, the beam passes through the C2 lens. The C2 lens can be used to coarsely adjust the focus of the probe. At the C2, the C2 apertures can be inserted to control the electron probe's convergence angle, size, and current. Smaller C2 apertures are used to minimize convergence angle, probe size, and probe current. After the C2 apertures sit a set of beam shift, or scan coils that deflect the beam laterally. Their operation is depicted in Figure 4-15. The scan coils are used to raster the beam across a specimen in STEM. After the beam passes through the scan coils, it encounters the mini condenser lens. For FEI/Thermo Fisher microscopes, the mini condenser lens is turned off for nanoprobe mode, which is used for typical STEM imaging. Below the scan coils lie the objective lens and the specimen. The objective lens is used to finely adjust the focal plane of the beam that scatters from the specimen. Just like in CTEM, the beam is diffracted from the specimen depending on the crystallography present in the specimen. However, the scattering from the specimen is highly localized due to the converged beam's small lateral size. Thus, STEM is often more suited to collection of localized crystallographic information CTEM. After the beam passes through the specimen, it passes through the intermediate and projection lenses. The intermediate lens can be used to operate in imaging or diffraction mode, just like in CTEM. However, the function of these modes is different in STEM. Imaging mode is used to examine the probe, which is useful for correction of coarse aberrations. Diffraction mode operates similarly in STEM as it does in CTEM, projecting a diffraction pattern obtained from the specimen onto the STEM detectors. The projection lens functions somewhat similarly in STEM as it does in CTEM. In imaging mode, the projection lens can be used to magnify the electron probe, while in diffraction mode it is used to adjust camera length. Note that image magnification is not handled by the condenser, objective, intermediate, or projection lenses in STEM. The beam shift coils control

magnification, where the beam is rastered over a smaller area with finer raster pixel size using the scan coils to increase magnification in STEM. Lastly, the electron beam passes through the STEM detectors. Image formation using each detector will be briefly discussed.

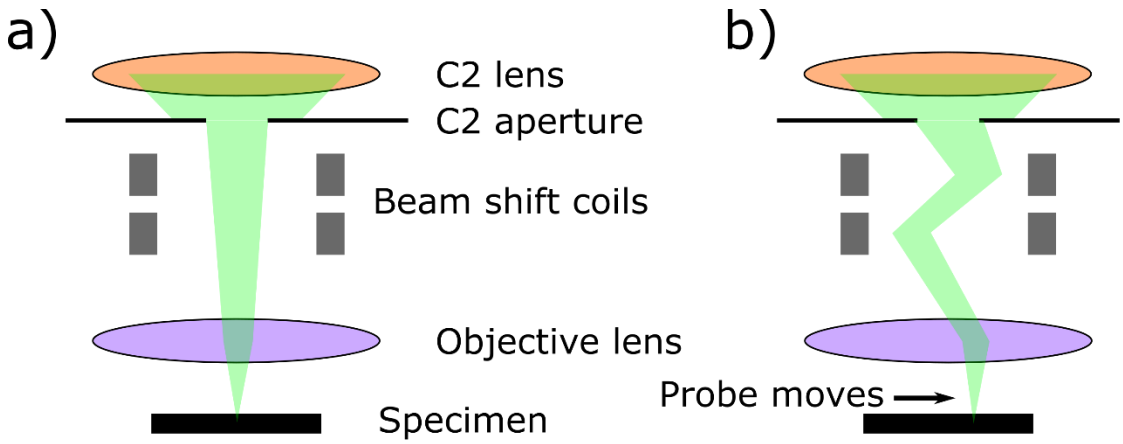

Figure 4-15 – An illustration of beam rastering. a) When the beam shift coils are not excited, the beam travels down the optic axis of the TEM. b) The beam shift coils can move the STEM probe laterally by introducing two tilts.

4.2.4.1. BF, LAADF, and HAADF images

The most common set of detectors used in STEM are the bright field (BF), low angle annular dark field (LAADF), and high angle annular dark field (HAADF) detectors. Use of different detectors allows for collection of elastically scattered electrons at different angles from the sample. This work mostly uses the HAADF detector, as it provides a mix of diffraction and mass-thickness contrast at various imaging conditions. The BF detector is circular and sits on the optical axis, capturing electrons that have little to no scattering angle relative to the optic axis. The LAADF and HAADF detectors are annular, with the HAADF detector having larger inner and outer radius and being positioned much higher in the TEM column than the LAADF. The reason for this geometry is that electrons scattered at low angle will be captured by the LAADF, while electrons scattered at high angle are captured by the HAADF. The specific scattering angles captured by each detector are determined by the camera length, which can be changed to optimize

image formation from different scattering mechanisms. The flexibility to adjust imaging conditions to select for different scattering mechanisms is the main motivation for using different detectors in STEM. Generally speaking, BF images are more dominated by local crystallography, as they contain information from the direct beam and low-order diffraction. Likewise, HAADF images are more dominated by mass-thickness contrast (also known as Z contrast) since the efficiency of high-angle incoherent scattering is proportional to scattering cross section and Z-number. The magnification of the diffraction pattern projected on the STEM detectors is controlled by the strength of the projector lenses, which then determine camera length as they do in CTEM. The higher the camera length is, the more the diffraction pattern is magnified. The camera length must be adjusted correctly to ensure that the desired dominant contrast mechanisms are present in images from each detector. Z-contrast imaging is best done with the HAADF with camera length adjusted so that most of the incident signal is incoherent scattering, which is dominant at high scattering angles. Diffraction contrast imaging can be done with any detector, provided that diffraction spots found at lower scattering angle are incident on the detector. The relationship between signal type and camera length is depicted in Figure 4-16.

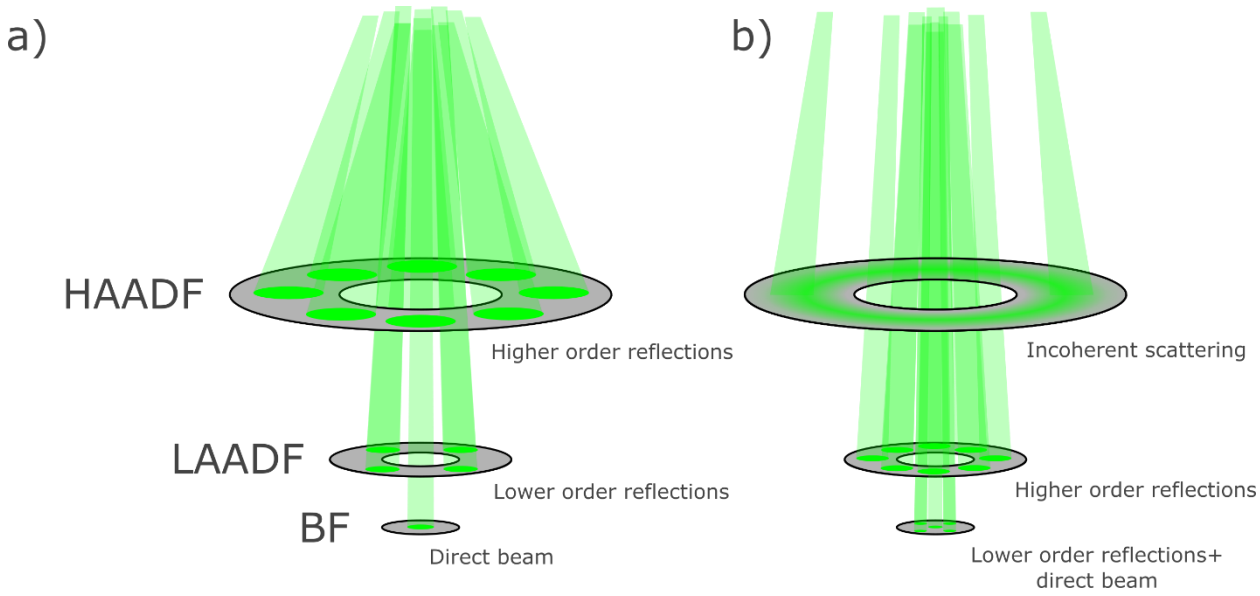

Figure 4-16 – An illustration of signal types incident on the STEM detectors. a) High camera lengths magnify the diffraction pattern coming from the specimen, meaning that low scattering angle signal hits all three detectors. Images are dominated by diffraction contrast on the HAADF, LAADF, and BF detectors. b) Low camera lengths demagnify the diffraction pattern, meaning that the HAADF image is dominated by Z contrast, while the other detectors are dominated by diffraction contrast.

4.2.4.2. STEM-EDS

STEM-energy dispersive spectroscopy (STEM-EDS) harnesses the localized probe used in STEM to extract local chemical information. This is used extensively in this work to generate semi-quantitative chemical quantification of 3D Cu/Nb layers and interfaces. EDS by itself harnesses X-ray generation that occurs during electron-matter interactions as discussed in Section 4.2.1.2. Electron interaction-generated X-rays can be separated into two categories: Brehmsstrahlung and characteristic. Brehmsstrahlung X-rays arise from electrons that are decelerated by the electric field of atomic nuclei (illustrated in Figure 4-17).

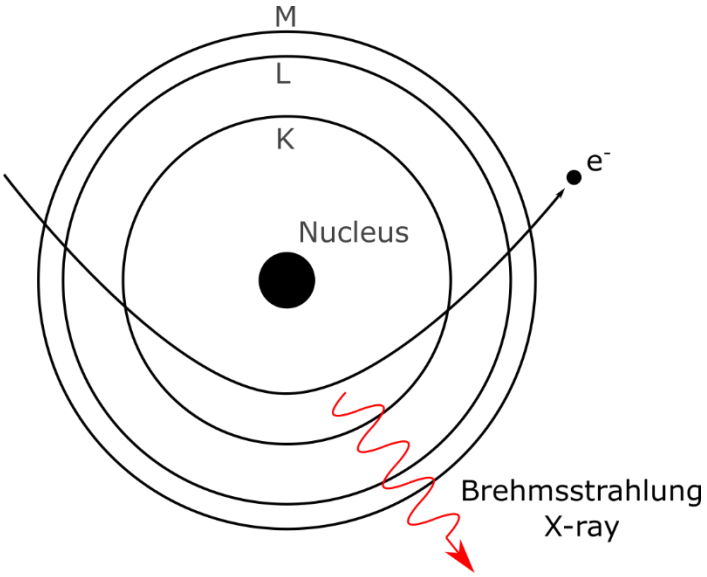

Figure 4-17 – Brehmsstrahlung X-ray generation occurs when an incident electron is decelerated by the electric field of the nucleus. This process produces X-rays with a continuum of energy, which is not useful for elemental identification.

When electrons are decelerated, they emit X-rays to obey conservation of energy. These X-rays have a broad distribution of energies and cannot be used to identify the Z-number of the nucleus that generated them. Characteristic X-rays on the other hand, arise from interaction between electrons generated by the TEM electron source and the electron clouds of atoms in the specimen. The generation of a characteristic X-ray (illustrated in Figure 4-18) proceeds as follows:

1. The incident electron scatters off of a core-level electron in a specimen atom, ejecting it from the electron cloud.
2. An electron from a higher energy level in the electron cloud relaxes to the vacant state left by the ejected core-level electron.
3. During the relaxation process, an X-ray with energy equal to the difference between the electron's initial and final energies is ejected.

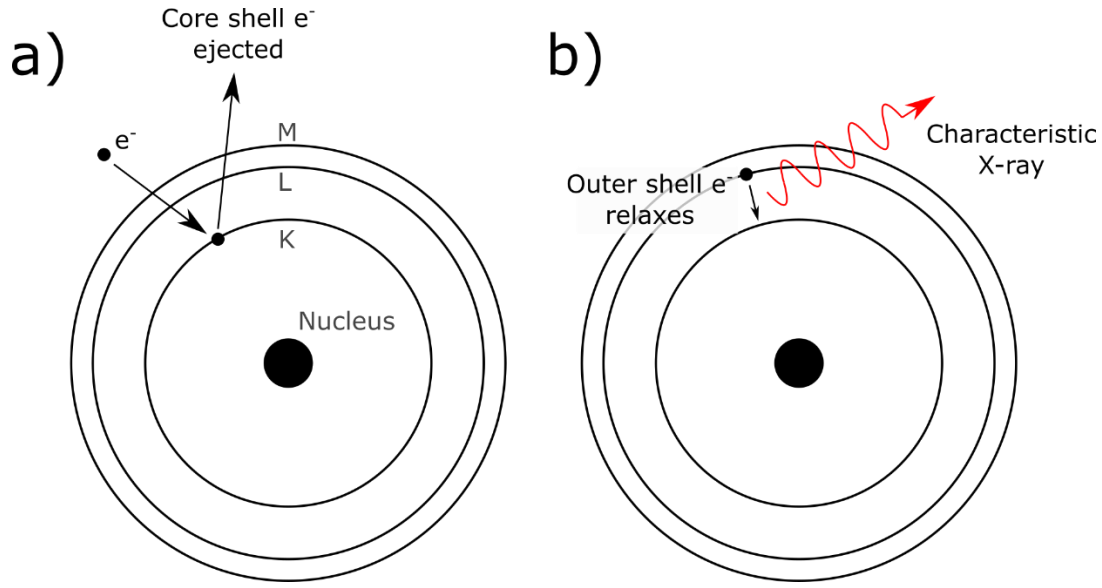

Figure 4-18 – Characteristic X-ray generation. a) An incident electron excites a core shell electron so that it is ejected from its shell (K in this case). This leaves a vacancy in the shell so that b) an outer shell electron in the L shell relaxes to the core shell. An X-ray with energy determined by the difference in binding energies between K and L shells is produced. These X-rays are very tightly distributed in energy, providing a "fingerprint" useful for elemental identification. The X-ray generated here is a K_α X-ray.

Characteristic X-rays are very tightly distributed in energy, meaning that they can readily be used to identify the elemental identity of atoms in a TEM specimen. In STEM-EDS, a map of characteristic X-ray spectra is generated. These spectra are histograms of X-ray energies generated by electron-specimen interactions. For each pixel in the map, elements in each can be identified and quantified in terms of abundance by integration of characteristic X-ray peaks. Then, semi-quantitative composition maps can be generated from this information. STEM-EDS is used in this work for quantification of undeformed and deformed 3D Cu/Nb microstructures.

4.3. Atom Probe Tomography

While TEM characterization is a powerful tool for examining the microstructure of nanostructured materials, observations are confined to the lateral dimensions of the electron-transparent specimen. Signals from heterogeneities in the through-thickness direction of a TEM

lamella are convolved when the electron beam scatters through them and is projected on a two-dimensional plane in CTEM or STEM. Thus, TEM alone cannot provide complete information about the microstructure in 3D interfaces. Atom probe tomography (APT) is a method that provides three dimensional microstructural information about a specimen is required to resolve heterogeneities in all spatial dimensions.

4.3.1. Working principles

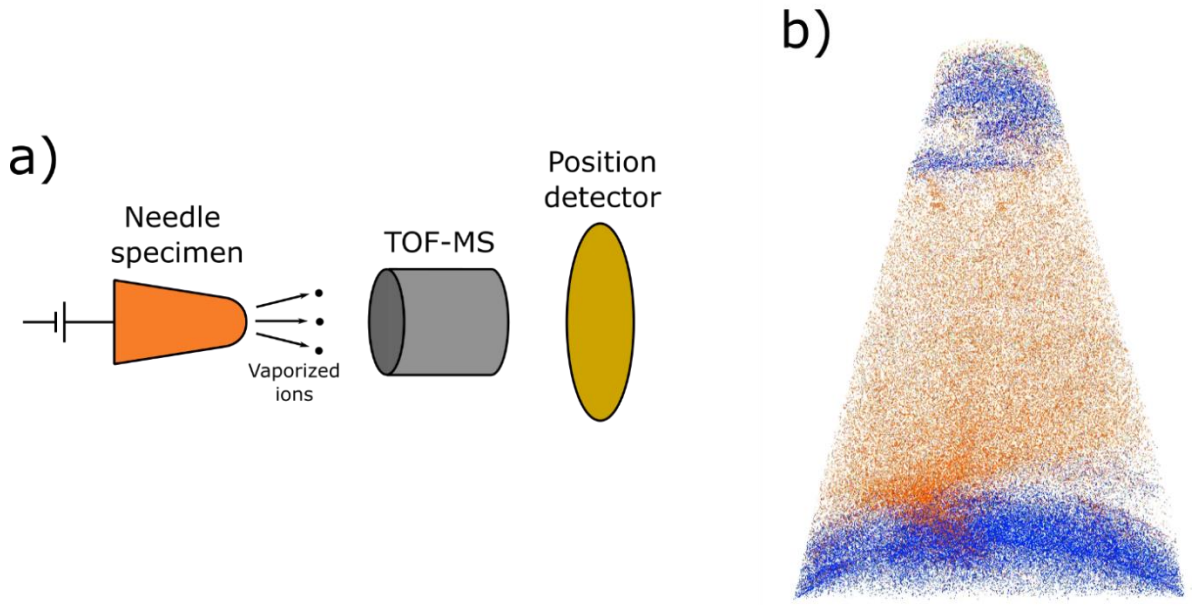

Figure 4-19 – a) A simplified schematic of the atom probe tomography (APT) process. This arrangement is called the local electron atom probe (LEAP). A voltage is applied to a needle shaped specimen, which is then vaporized either by pulsing the voltage or using a pulsed laser. Vaporized ions are produced, which fly towards a time of flight mass spectrometer (TOF-MS), which is used to identify the atomic species of the ions. The ions continue to a position detector, which can determine the position on the needle that the ions came from. The specimen is vaporized layer-by-layer, producing a stack of x-y ion maps, which are reconstructed into a 3D chemical data set like shown in b). In b, orange dots represent Cu atoms, while blue dots represent Nb atoms.

APT destructively vaporizes a needle-shaped specimen using an electric field and captures the vaporized ions on an ion detector as depicted in Figure 4-19. Time-of-flight mass spectroscopy (TOF-MS) determines the origin and mass-to-charge ratio of detected ions to create a 2D map of

ionized species. The specimen is vaporized layer by layer and a map is generated for each layer. The 2D maps are then reconstructed into a 3D chemical map with few-nm resolution. The experimental and instrumental setup of APT is discussed first, followed by a discussion of limitations and application to this work. Information in this section is taken from the APT textbook by Larson, et al.[28].

4.3.1.1. APT needle specimen vaporization

Vaporization in APT is accomplished by applying several kV of potential in vacuum to a cryogenically-cooled 100 nm thick needle-shaped specimen. The geometry of the needle concentrates electric field lines, providing electric fields in excess of 10^{10} V/m at the tip. This liberates electrons from surface atoms on the specimen, ionizing them. The surface ions are then pulled by the electric field towards an electrode that collects them for detection. Vaporization is conducted in a controlled fashion by pulsing either applied voltage or temperature depending on the specimen composition. Pulsing applied voltage is more suitable for conductive specimens, while pulsing temperature is useful for non-conductive specimens and some conductive specimens. Voltage or temperature pulses need to be very fast in order to assist with TOF-MS, so voltage pulses are supplied by solid-state pulse generators, while temperature pulses are delivered using a pulse-picked laser. Vaporization pulses are controlled such that they have a low probability (around 1 in 100) of ionizing surface atoms on the specimen. This way, only one ion hits the ion detector at once. This is crucial, as current systems such as the LEAP 3000X Si use single-particle detectors which do not tolerate multiple particle impacts well. The ion detection process is explored next.

4.3.1.2. Ion detection and TOF-MS

Ions vaporized from an APT needle are channeled towards a detector which can determine the ion origins very precisely. This precision comes in large part from the projection of the vaporized atoms onto the detector. If a specimen has a radius of 100 nm and the detector is 100 mm across, then a difference of 0.2 nm on the specimen tip is projected to a difference of 0.2 mm onto the detector. This represents a magnification factor of around 1,000,00x. To conduct TOF-MS on vaporized ions, time between vaporization and detection needs to be known for a given ion. This time is dependent on the distance between the specimen and detector, as well as the force exerted on the vaporized ion. The detector distance is fixed, and the ion velocity is determined by computing the kinetic energy that the ion should have after crossing an applied potential V. The velocity v of the ion is given by the distance traveled by the ion L divided by the time t it takes for it to reach the detector:

$$v = \frac{L}{t} \tag{4-7}$$

For an ion with mass *m* and charge state *n*, the velocity of the ion at the detector is calculated by assuming that the electric potential energy that the ion has at the specimen is converted into kinetic energy:

$$\frac{1}{2}mv^2 = neV$$

$$v = \left(\frac{n}{m} \cdot 2eV\right)^{\frac{1}{2}} \tag{4-8}$$

Substituting this into Equation (4-7):

$$v = \frac{L}{t} = \left(\frac{n}{m} \cdot 2eV\right)^{\frac{1}{2}}$$

$$\frac{m}{n} = \frac{2eVt^2}{L^2}$$

(4-9)

This results in an expression for the mass-to-charge ratio m/n of a vaporized ion as a function of all known quantities. It should be noted that this is a first order approximation and must be corrected for the fact that the ion takes time to accelerate and that the flight distance from the specimen to the detector is a function of lateral position on the needle. Using appropriate correction factors, the ionic species that hit the detector is identified using Equation (4-9). Each atomic species produces mostly ions with m/n = Z, where Z is the atomic number of the species. These ions are singly charged (n=1) and can be used to identify the elements present in the specimen. Each element also produces lesser amounts of ions where n > 1, representing multiply charged ions. Other species such as dimers and trimers must also be accounted for, but complementary bulk elemental analysis can aid elemental identification. After 2D chemical maps are constructed for all layers of atoms vaporized from the specimen, they must be reconstructed into a 3D chemical map.

4.3.1.3. 3D reconstruction

3D reconstruction describes the process of taking set of 2D chemical maps containing atomic positions in *x* and *y* coordinates and assigning each point a *z* coordinate. Given a hemispherical APT needle tip and a flat ion detector, detector x-y coordinates must be converted to real-space x-y coordinates. This is because the ions are emitted from a hemisphere and then projected onto a plane – this introduces some distortion to the real-space x-y coordinate of the ion. To obtain the z coordinate of an ion, the magnification of the specimen and identity of every

detected ionic species (given by TOF-MS) must be known. Every ionic species is assigned an ionic volume, and for each ion that is detected, the needle is assumed to shorten uniformly over its tip by the ionic volume divided by the surface area of the tip. As the reconstruction proceeds, the geometry of the needle is updated to reflect the subtraction of mass from the needle from vaporization. Other geometric factors like initial tip radius and shank angle of the APT needle can be measured or assumed to apply geometric corrections during reconstruction. Once reconstruction is complete, a 3D chemical map of the specimen is obtained.

4.3.2. Aberrations encountered in APT

Although it is a notable achievement to obtain an APT reconstruction amid difficulties such as needle fracture during vaporization, it must be stated that the obtained dataset must be taken with some caveats. This is due to aberrations that may occur during needle vaporization and data analysis. A few that are pertinent to Cu/Nb nanolaminates are presented below.

4.3.2.1. Trajectory aberration

Most APT analysis protocols assume a hemispherical APT needle tip. If actual tip geometry does not match the geometric model being used for reconstruction, then features in the 3D reconstruction can be distorted. Different needle geometries are presented in Figure 4-20. Some analyses assume that the edges of the needle tip are tangent with the sides of the needle. However, it has been shown that it is possible for the needle tip to have a discontinuous slope with respect to the needle sides. Care must be taken to examine the needle before vaporization to use the correct geometric model for vaporization. Another source of aberration comes from the assumption of a hemispherical needle tip. Consider vaporization of an APT needle containing only one grain. The assumption made during vaporization of a needle with a hemispherical tip is that ion vaporization probability is uniform for all x-y points on the hemisphere. However, after a few vaporization

events, anisotropy in plane surface energy drives crystal faceting. If faceting is severe during vaporization, then the reconstruction obtained from the experiment may be severely distorted.

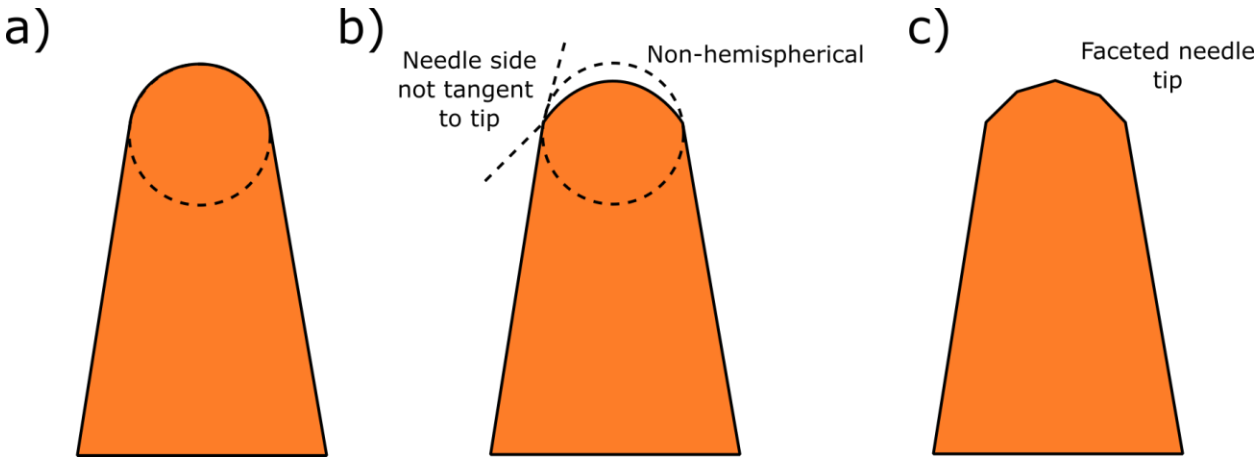

Figure 4-20 – a) An APT needle with a hemispherical tip, whose sides are tangent with the tip. This is a commonly assumed geometry for APT needles. b) Often, needles do not have the ideal geometry assumed in a). The tip can deviate from a hemispherical geometry, and the needle sides can be non-tangent to the tip. c) Severe geometric deviation can happen during needle vaporization if facets develop on the needle tip.

4.3.2.2. Local magnification

The propensity for hemispherical needle vaporization is also a function of vaporization fields of phases found in the specimen. If the specimen is composed of two phases with significantly different vaporization fields, then vaporization will occur nonuniformly over a phase boundary. Phases with lower vaporization fields will vaporize faster than those with higher vaporization fields[163]. This may introduce morphological perturbations on the needle tip that affect the magnification in a localized portion of the tip. Concavities will concentrate vaporized ions on the ion detector, locally demagnifying the atomic positions obtained. Convex regions on the needle tip will spread vaporized ions on the detector, causing local magnification. Effects of material heterogeneity on vaporization geometry are hard to predict, causing inaccuracies in reconstructions

of heterogeneous materials that are difficult to correct. Specimen inhomogeneity effects are illustrated in Figure 4-21.

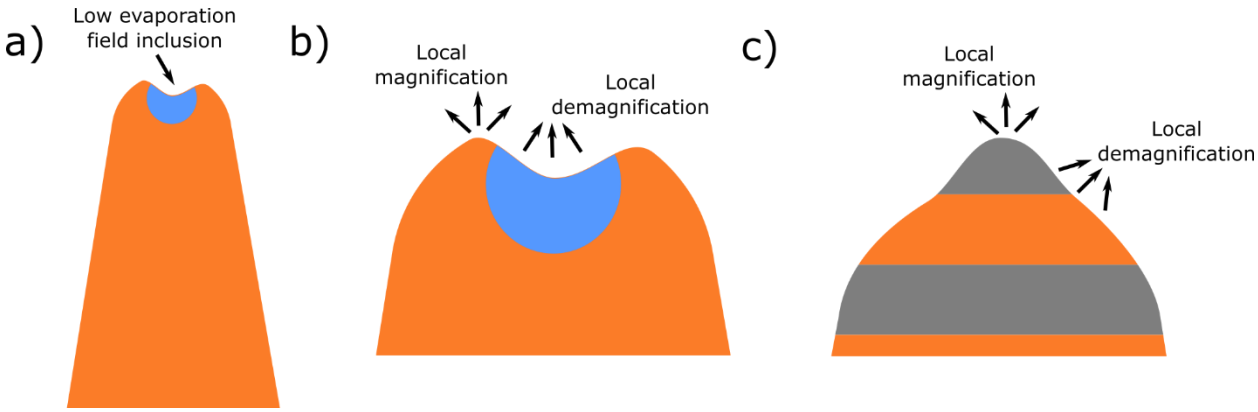

Figure 4-21 – Local magnification effects that can arise from specimen heterogeneity. a) An inclusion that has a lower evaporation field than surrounding material will vaporize faster, leaving a divot in the needle. b) The divot can produce local magnification or demagnification depending on the local sample curvature. c) Multilayer specimens like those in this work undergo similar effects as in (a-b).

4.3.3. Utility of APT for characterization of Cu/Nb

Reconstruction errors based on incorrect geometric assumptions apply mostly uniform distortions to 3D chemical maps[164]. Thus, features may have incorrect aspect ratio or curvature, but their presence and length scale can still be established in spite of aberrations. Local magnification effects from heterogeneous vaporization may introduce local distortions that stretch or compress features by 2-5 times[165]. Given these difficulties and a best-case sub-nm resolution of APT[166], a resolution of a few nm for is estimated for a heterogeneous material like Cu/Nb. This resolution is sufficient for quantifying chemical heterogeneities in all three dimensions in 3D interfaces, given an interface thickness of 10 nm. As such, correlative TEM/APT effectively complement one another. Future work would benefit from such an approach to study 3D interfaces.

4.4. Micropillar compression

As was mentioned in Chapter 2, uniaxial tests are extremely useful for quantifying elastic and plastic deformation in metals and other materials. When applying this technique to small volumes of material, micropillar compression or micro tensile testing must be used. Typically, compression tests are used for characterization of uniaxial stress-strain behavior of nanolaminates due to their suitability to microscale specimens. They are more useful for thin film specimens where deposition defects such as porosity and difficulty of sample preparation and testing limit the utility of tensile tests[167–169]. Additionally, in materials like metals where significant compression-tension anisotropy is not expected, micropillar tests are often comparable to tensile tests near yield and possibly up to the onset of plastic instability.

Micropillar compression refers to the uniaxial compression of a pillar-shaped sample whose dimensions are on the length scale of a few to several tens of microns. The ability for micropillar compression to sample mechanical behavior that is localized to a few microns of volume makes it suited for testing of thin films, few- or single-grain deformation, deformation at welds and interfaces, and surface deformation behavior. For this work, since all samples are synthesized as thin films, micropillar compression provides a suitable method for testing mechanical behavior. There are exist multiple methods for preparing micropillars, such as combined electron lithography and electrodeposition[30,31] or additive manufacturing[30,31,170]. This work uses FIB/SEM, which is discussed below.

4.4.1. Micropillar fabrication

FIB/SEM has been used to fabricate micropillars for uniaxial compression tests for almost two decades at the time of writing[33,34]. There are two commonly used approaches for FIB preparation of micropillars: annular and lathe milling[171]. These methods are illustrated in Figure

4-22. Annular milling is the more commonly used method[172], where milling is conducted normal to the specimen surface. Smaller and smaller annulus patterns are used to mill out a pillar of decreasing dimension until the desired geometry is achieved. Lathe milling is the less-commonly used method where the ion beam is tilted with respect to the pillar's compression axis, and the stage is rotated during milling to cut away an annular trench around a pillar[173]. This method requires scripting of the FIB/SEM instrument and so requires more up-front effort to write a script if a script is not available.

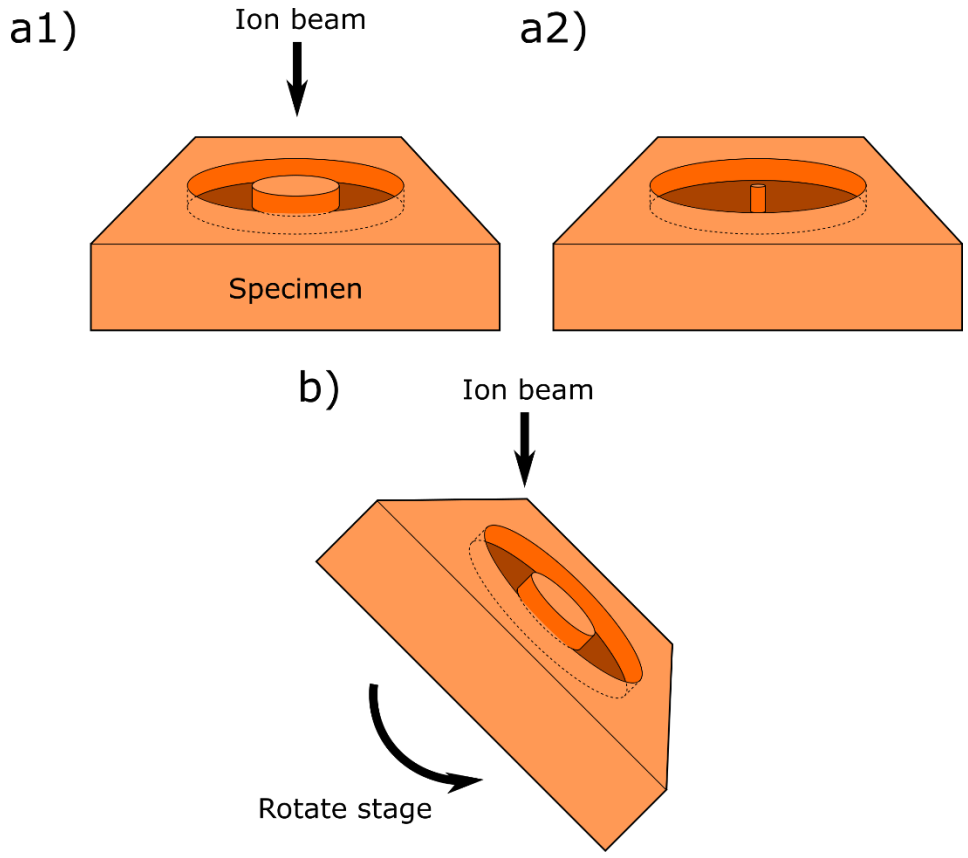

Figure 4-22 – Depictions of a) annular and b) lathe milling of micropillars. In annular milling, an annular trench is made in the specimen in (a1). Annuli of decreasing inner and outer radius are used until a pillar of desired dimension is milled in (a2). b) depicts lathe milling, where the sample stage is rotated and the sides of the pillar are milled at a large incident angle.

However, once the script is written, milling can be automated. This is not true for annular milling. Annular and lathe milling also each possess a distinct disadvantage. In annular milling, it can be difficult to control the final depth of milling at the end of pillar fabrication, leading to poorly defined geometry especially at the pillar base. The latter outcome is detrimental because it can make it difficult to determine if significant substrate compliance effects are present in the measured force displacement curve[40]. The disadvantage of lathe milling is that it may introduce greater ion beam damage than annular milling due to the increased angle of incidence between the beam and the pillar side. This effect becomes significant if dislocation nucleation is a limiting factor in deformation and is of importance in single crystals with dimensions less than a few microns[30,174]. Fabrication-induced artifacts are important to keep in mind, but other factors extrinsic to the material being tested may also alter test results.

4.4.2. Complications in micropillar compression

One of the most commonly discussed phenomena in micropillar compression is pillar size effects. It has been well-established that in general as pillar size decreases, measured yield stresses in pure metals increase to near-theoretical strengths[175]. This phenomenon is contingent on the sample microstructure of contained within a micropillar. A typical grain size for engineering metals is on the order of several tens of microns, so micropillars made on many commonly used alloys would contain one grain. In pure metals, this means that the pillar is single crystalline. As pillar size decreases to the nanoscale, dislocation sources become sparse in the pillar volume; this is called “dislocation starvation”. In this case, dislocations must nucleate from the pillar surface, which takes much more stress than operation of a more typical source like a grain boundary or Frank-Read source[176,177]. The probability that an energetically favorable dislocation source is found inside a micropillar is proportional to the micropillar volume, which in turn produces an

inverse relationship between pillar size and yield strength. For Cu/Nb, this effect is not observable at the few micron scale. This is due to the plethora of nucleation sites in the material. The in-plane grain size is 50-150 nm for Cu/Nb, and the interface spacing is on the order of a few tens of nanometers. Unless a nanoscale sample is tested, specimen size effects are unlikely to be observed in Cu/Nb.

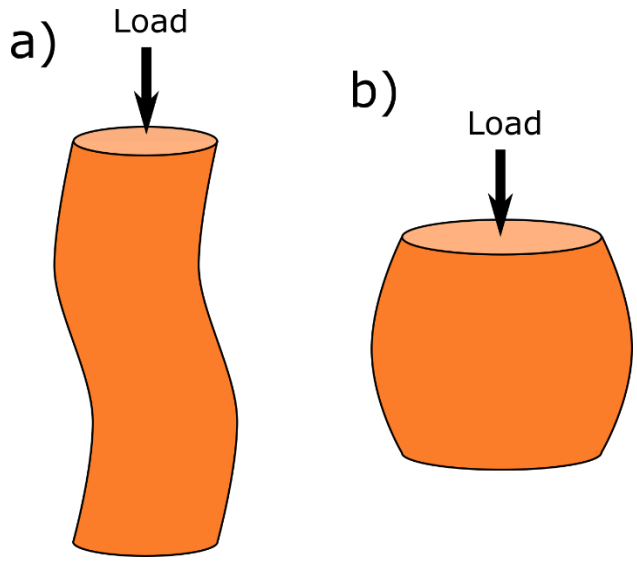

Figure 4-23 – Undesired geometric distortions in micropillar compression. a) Pillars with aspect ratio above 3:1 will elastically buckle, complicating the stress state of the pillar and introducing significant non-uniaxiality. b) Pillars with aspect ratio below 2:1 will barrel significantly. Constraints at the top and bottom of the pillar keep the cross-sectional area constant, while the middle of the pillar is free to widen. This also introduces non-uniaxiality to the stress state of the pillar.

Another complication to be aware of in micropillar compression concerns the geometric criteria that produce elastic instability modes characterized by barreling and buckling[178], shown in Figure 4-23. Pillar barreling occurs due to constraints at the top and bottom of the pillar and is indicated by widening of the pillar at its midpoint during compression. Pillar constraints arise at the pillar top by friction with the flat punch used for compression and at the pillar bottom because the pillar is attached to underlying material. Pillar buckling happens if the pillar has a high aspect

ratio and causes bending moments to develop in the pillar. These elastic instability modes cause deviations from uniaxial stress conditions in the pillar and complicate the measurement of elastic and plastic properties. Elastic barreling and buckling are only especially pronounced when elastic deformation dominates the strain response of a material, which is not the case for most metals. Nonetheless, care should be taken not to use high or low aspect ratios for micropillar testing, lest plastic buckling or barrelling complicate data analysis[40]. Typically, aspect ratios between 2 to 3 are used to obtain uniaxial stress states in micropillar compression.

Yet another geometrically related complication that can occur in micropillar compression is related to specimen fabrication. If annular FIB milling is used to produce micropillars, tapering of the pillar occurs due to the finite depth of field of a focused ion column[40,179,180]. This taper introduces a gradient in cross-sectional area from the top of the pillar to the bottom of the pillar. This means that in some cases it is inadvisable to use a constant value for cross-sectional area when evaluating stress-strain curves from load-displacement data in tapered micropillars. One way to address this concern is to assume a deformation model for the tapered pillar and adjust cross-sectional area as a function of pillar strain. This is done in the literature for Cu/Nb[16,146], where the top of the pillar is assumed to yield before any other material due to its smaller cross-sectional area. This model is outlined in Figure 4-24. A geometrical model is constructed and pillar taper is accounted for in the stress-strain curves in these papers. One of these papers is part of this work and the taper correction procedure will be covered in the Appendix.

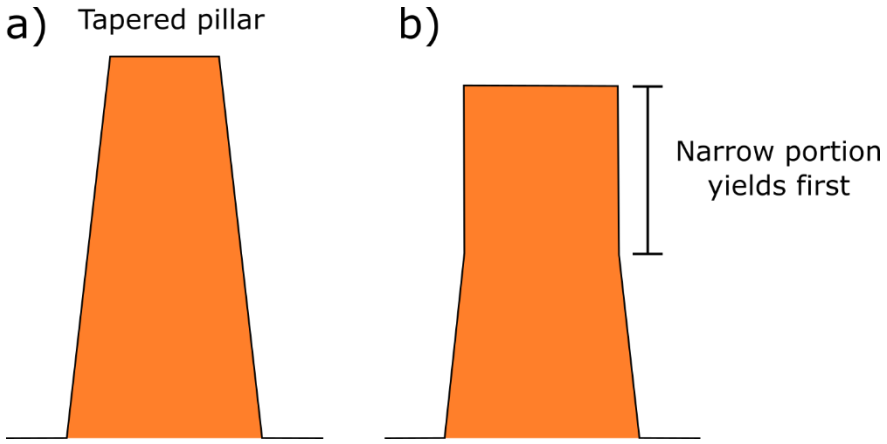

Figure 4-24 – A depiction of the pillar taper model used in this work. a) The pillar starts out with a taper, meaning that there is a gradient in cross-sectional area along the gage length of the pillar. b) During loading portions of the pillar with lower cross-sectional area deform first since they experience the highest stresses. As higher-stress regions flatten, they will match the cross-sectional area of wider portions of the pillar, creating a growing region of the pillar that is a right-cylinder.

Lastly, shear localization may occur during pillar compression and concentrate strain in a localized portion of the pillar[181]. This usually happens in nanocrystalline alloys, whose small grain size makes dislocation storage and the associated strain hardening energetically unfavorable. Nanolamellar composites are not immune from shear localization limiting their deformability[140]. Shear instabilities cause deviations from uniaxial stress states and are difficult to account for in constructing flow curves for nanostructured metals and alloys. This work will attempt to demonstrate methods for probing strength and deformability for Cu/Nb in the presence of shear instability.

4.5. Nanoindentation

Indentation is a technique for mechanical testing that can be used alone or as a complementary technique to other testing methods for characterizing elastic and plastic deformation. When indentation is performed at small depths below a few microns, then it is referred to as nanoindentation[36]. The essence of the technique is simple: a hard probe with known geometry and elastic properties is pressed into a sample with a controlled load or displacement

profile. This is shown in Figure 4-25. Once the indenter is withdrawn, a residual imprint is left in the sample. The peak load applied to the sample is divided by the projected contact area A_c left by the indenter, giving the Meyer hardness, or nanohardness H of the specimen. If load and displacement are continuously measured during indentation, the test is said to be "instrumented". For nanoindentation, instrumentation is crucial for determining contact area, so nanoindentation is usually implied to be instrumented. Instrumented indentation tests can also provide a reduced modulus E_r which is related to the Young's modulus of the specimen.

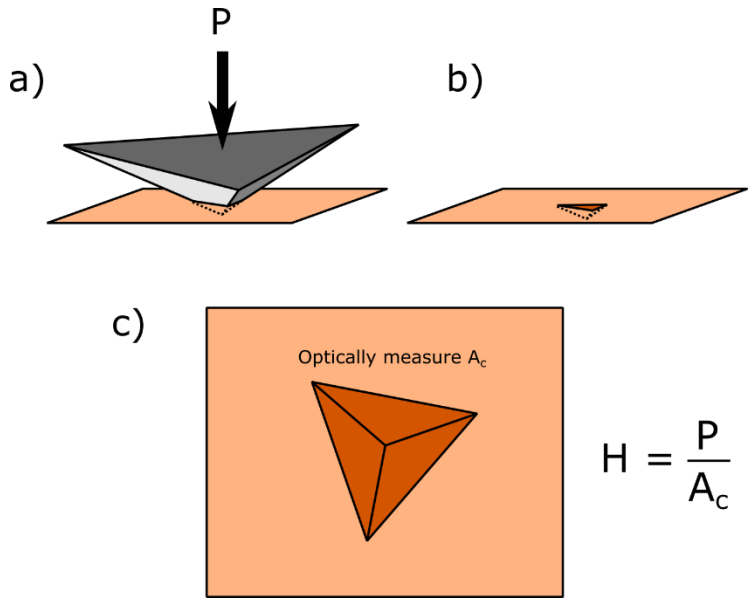

Figure 4-25 – An illustration of Meyer hardness measurement. a) a hard, stiff indenter is pressed into a specimen with load P. b) A residual indent is left in the specimen after unloading. c) The projected surface area of the residual indent is taken as the contact area A_c, which can then be used for hardness calculation.

Nanoindentation shares many of the same strengths of micropillar compression. It can be used to sample local mechanical properties, which is useful for the characterization of coatings, films, welds, surface-treated material, and even more exotic sample geometries such as wires and particles. Nanoindentation is also a high-throughput technique; because it is instrumented, data collection can be automated and mechanical properties can be obtained from hundreds of

indentation tests with only a few hours of operator time. However, as will be seen, data analysis and processing may be intensive. Micropillar testing is the opposite; it is very time-consuming to mill pillar specimens, but data analysis is often straightforward. Nanoindentation is widely used to test the mechanical behavior of nanocrystalline metals and alloys, which is especially useful considering that many nanostructured alloys can only be made in microscopic quantities[67]. While many works use indentation hardness to correlate to flow stress[15,65,99], the relationship between indentation and the stress-strain curve is still being explored and remains an active topic of research[182–185]. This is because the stress state under an indent is triaxial and varies depending on position below the indent, as well as the elastic modulus, flow stress, and work hardenability of the sample[39]. Nevertheless, nanoindentation remains a powerful tool for surveying the mechanical properties of nanostructured alloys, including Cu/Nb nanolaminates. This is provided that the experimental conditions during indentation are precisely controlled; nanoindentation is sensitive to changes in instrument calibration, specimen conditions, and plastic deformation phenomena such as indentation pileup considering that the force and displacement resolutions are on the order of a few micronewtons and a few Ångstroms, respectively. The most-often used method of nanoindentation data analysis is the Oliver-Pharr method. Any indentation information outside of the Oliver-Pharr method is based upon the textbook about nanoindentation by Fischer-Cripps, which is a useful handbook for overcoming practical difficulties in nanoindentation[36].

4.5.1. The Oliver-Pharr method

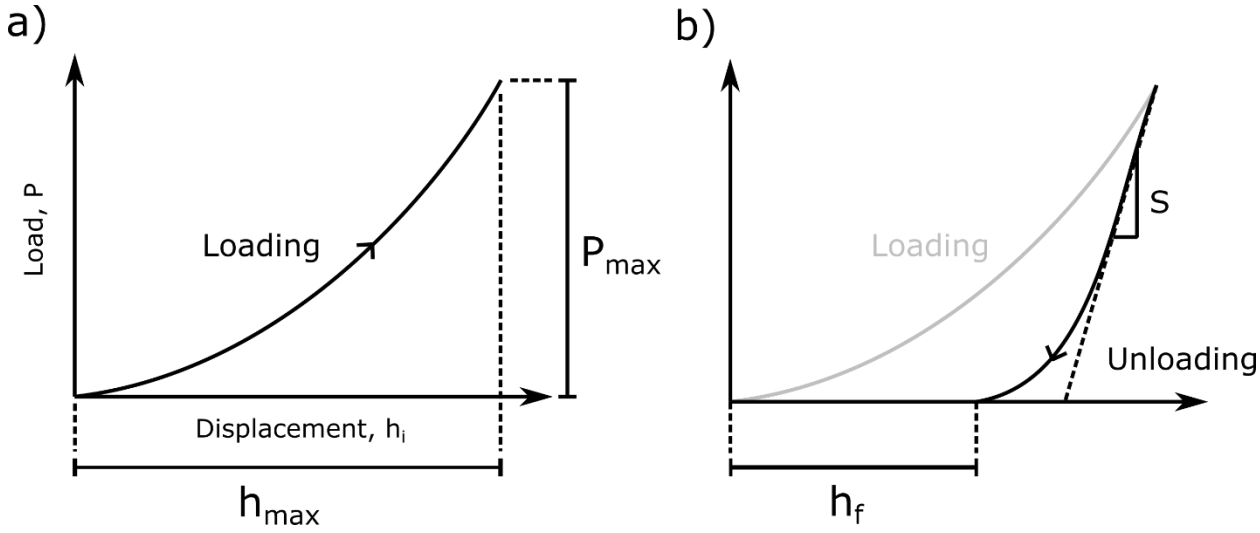

Figure 4-26 – Instrumented indentation produces load-displacement curves for a) loading and b) unloading. a) provides P_{max} and h_{max}, while b) produces unloading stiffness S. These quantities are sufficient to calculate hardness and reduced modulus.

The Oliver-Pharr method (depicted in Figure 4-26) is used to extract the contact area during a nanoindentation experiment by analysis of load-displacement data only. No direct observation of contact area is required, as is commonly used for microindentation[186]. While direct contact area measurement is robust against many indentation artifacts, it is not practical in nanoindentation without the use of secondary methods such as SEM or atomic force microscopy (AFM). In addition, direct measurement is not easily automated. The Oliver-Pharr method is described below. This method relies on measurement of unloading stiffness S, tip contact area A_c, and max load P_{max} to calculate hardness H and reduced modulus E_r[187]:

$$H = \frac{P_{max}}{A_c}$$

$$E_r = \frac{\sqrt{\pi}}{2}\frac{S}{\sqrt{A_c}} \quad (4\text{-}10)$$

The reduced modulus is used instead of the specimen Young's modulus because no matter how stiff the indenter tip is, it will still experience some elastic deformation. This is accounted for in the definition of reduced modulus given by Stilwell and Tabor[188]:

$$\frac{1}{E_r} = \frac{(1-\nu)^2}{E} + \frac{(1-\nu_i)^2}{E_i} \tag{4-11}$$

Here, E and ν are the specimen Young's modulus and Poisson's ratio, respectively, while E_i and ν_i are the indenter Young's modulus and Poisson's ratio, respectively. There is a non-trivial amount of data analysis to extract the required values from a load-displacement curve, so this method requires a sequence of steps. These are outlined as follows:

1. Measure the load-displacement response during indentation of a specimen using a predefined load function
2. Use the unloading segment of the test to measure unloading stiffness S
3. Find the contact depth h_c from the measured S assuming certain contact conditions
4. Find A_c with knowledge of h_c using a calibrated tip area function
5. Calculate H and E_r of the specimen

The practicalities of these steps are quite detailed and important to consider for understanding nanoindentation, so the next few sections will discuss how an indentation experiment is carried out and how the assumed model of contact mechanics relates to measured properties.

4.5.1.1. Load-displacement measurement and load functions

When a nanoindentation test is performed, the user chooses to control either applied load or displacement. All of the current work is based on load-controlled tests. In load-control,

displacement is measured as a function of load. When displacement controlled tests are performed, then load is measured as a function of indentation displacement. A user-specified load function instructs the indenter to follow a given load profile as a function of time. This load function determines the depths at which H and E_r are sampled, since an unloading segment is required to compute unloading stiffness. Load functions can be separated into two different types: quasi-static (QS) and continuous stiffness measurement (CSM). They are depicted in Figure 4-27. may also be referred to as dynamic indentation. In CSM, an oscillatory load is superimposed on a non-oscillatory load function to obtain practically continuous information about unloading stiffness as a function of indentation depth. It is important not to confuse CSM with dynamic strain rate indentation which refers to tests where strain rates exceed $10^3/s$[189], so CSM is used to refer to indentation using oscillatory loading.

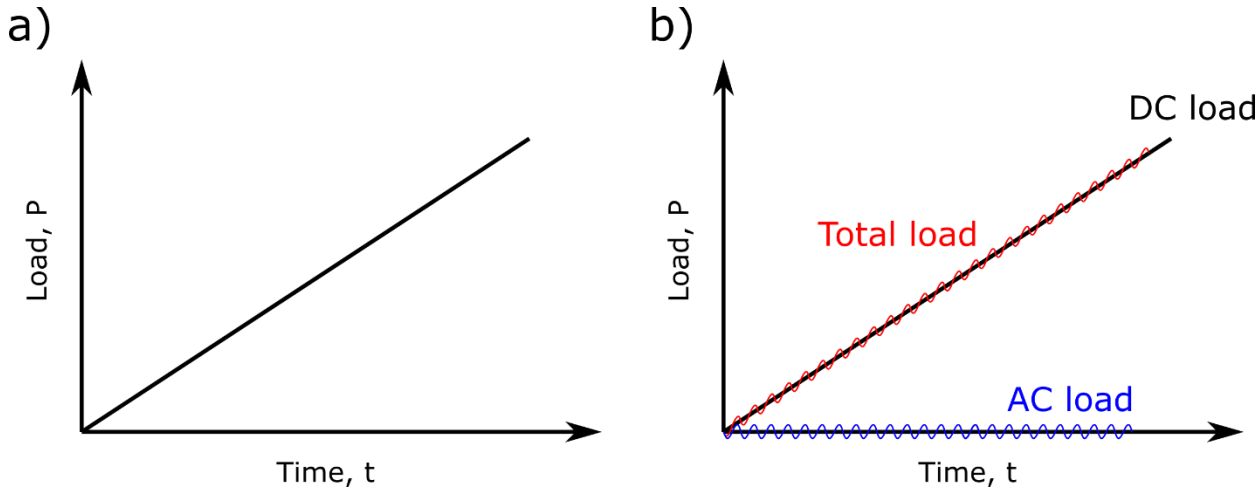

Figure 4-27 – a) Quasistatic loading, where load is monotonically increased. b) CSM loading, where a sinusoidal AC load is superimposed on a quasistatic DC load. This gives many unloading segments during the test, allowing for continuous measurement of hardness and modulus as a function of depth.

4.5.1.1.1. QS Trapezoidal

The QS trapezoidal load function is shown in Figure 4-28(a). It consists of three loading segments: a loading, a hold, and an unloading segment. The most important parameters in this load function are maximum load, hold time, and unloading rate. The maximum load attained by this load function can be tailored to achieve a desired penetration depth into the specimen. The hold segment time is important because it is instrumental in mitigating indentation creep. Indentation creep refers to the time-dependent increase in indentation depth at constant applied load, usually only encountered for sharp tip geometries[190]. Although one might expect indentation creep to only happen at high temperature as is the case for uniaxial tests, it happens at room temperature even for high flow stress materials such as ceramics. For hard materials, room temperature indentation creep is caused by dislocation glide driven by stress concentration at edges and points on indenters[190]. Regardless, a long hold time allows the indentation creep rate to reach steady state and decrease in magnitude to aid in unloading stiffness measurement. Lastly, the unloading rate is usually made reasonably fast to counter errors in unloading stiffness caused by indentation creep. The QS trapezoidal load function is used to sample hardness and modulus at one indentation depth per indentation site, which can be useful for comparative studies or quick indentation sessions for confirming material flow stress.

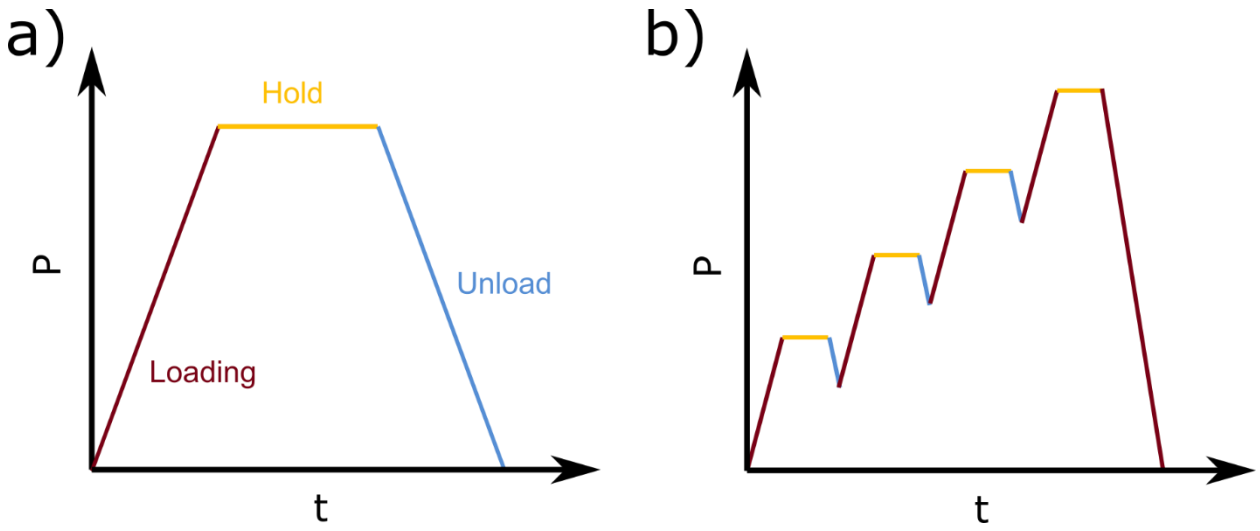

Figure 4-28 – A a) trapezoidal and b) partial load-unload load function. In a), a hold segment is included to minimize the effects of indentation creep on measurement of S. In b), multiple unloading segments are used to measure S as a function of depth. This can then be used to obtain H and E_r as a function of depth.

4.5.1.1.2. QS Partial load-unload

The QS Partial load-unload (PLUL) load function is very similar in principle to the QS trapezoidal load function, with the difference that in a PLUL function, multiple load, hold, and unload segments are completed at increasing loads to measure unloading stiffness for multiple penetration depths at one location. This is shown in Figure 4-28(b). Thus, H and E_r can be measured as a function of depth, which provides obvious benefits for samples with gradients in microstructure at the surface. Such samples include those that are shot peened, laser polished, or coated. Another use case for PLUL load functions is for samples where lateral surface area is limited, such as particulate and wire specimens, as well as epoxy-mounted samples whose cross-sectional area is limited (such as in fine electrical connectors). In this work, PLUL sees utility in characterization of thin film samples. Because the material of interest has a limited volume, it is quite possible for a deep indent to have an elastic strain field that extends into the substrate. The substrate then contributes to the measured E_r significantly, introducing error and giving rise to the

"substrate effect". PLUL is used to determine the depth at which substrate effect begins; data under this depth for which the tip area function is valid is used for H and E_r statistics.

4.5.1.1.3. Constant strain rate tests

When nanoindentation is used to study fundamental deformation physics, it is often desirable to control the strain rate at which the test is carried out. Because of the triaxial stress state under an indenter, it is often difficult to simply correlate indentation behavior to uniaxial tests. However, Lucas, et al. demonstrated that it is possible to create an indentation load function that produces strain rate-sensitive mechanical response as uniaxial tests[191]. This is done by defining the indentation strain rate:

$$\dot{\epsilon}_{ind} = \frac{1}{2}\frac{\dot{h}_i}{h_i} = \frac{1}{2}\left(\frac{\dot{P}}{P} - \frac{\dot{H}}{H}\right) \tag{4-12}$$

Where $\dot{\epsilon}_{ind}$ is the indentation strain rate, $\dot{h}_i$ is the indenter displacement rate, h_i is the instantaneous indenter displacement, $\dot{P}$ is the loading rate, P is the indentation load, $\dot{H}$ is the time derivative of hardness, and H is the sample hardness. If the material has a homogeneous microstructure and does not suffer from indentation size effect or pop-in, then the second term vanishes. Integration using dummy variables produces the load function corresponding to a constant strain rate:

$$\int_{t_o}^{t} \dot{\epsilon}_{ind}\, dt' = \int_{t_o}^{t} \frac{1}{2}\frac{\dot{P}'}{P'} dt' = \int_{t_o}^{t} \frac{1}{2P}\frac{dP'}{dt'} dt' = \int_{P_{min}}^{P} \frac{1}{2}\frac{dP'}{P'}$$

$$\dot{\epsilon}_{ind}\,(t - t_o) = \frac{1}{2}(\ln P - \ln P_{min})$$

$$\ln\left(\frac{\mathrm{P}}{\mathrm{P}_{min}}\right) = 2\dot{\epsilon}_{ind}\,(t - t_o)$$

$$P = P_{min} e^{2\dot{\epsilon}_{ind}\,(t - t_o)}$$

(4-13)

Here, A is an arbitrary constant, P_{min} is the indentation pre-load, and t_o is the time at which the pre-loading segment ends. Equation (4-13) is an expression for a constant strain rate (CSR) test, which can be used to measure strain rate-dependent hardness for correlation with flow stresses from uniaxial tests. A CSR load function takes the form depicted in Figure 4-29. Quantities that measure strain rate-dependence such as the creep exponent n or its reciprocal, the strain rate sensitivity m, match well with uniaxial tests[191–193]. Flow stress must be correlated to hardness using models like the expanding cavity model[39]. It must be noted that if hardness cannot be measured by instantaneous indentation depth, then this methodology must be coupled with CSM. Only deep indents in materials with little elastic rebound ($H << E_r$) can use instantaneous indentation depth h_i (not h_c) to find A_c, so most CSR tests are done with CSM to enable calculation of h_c.

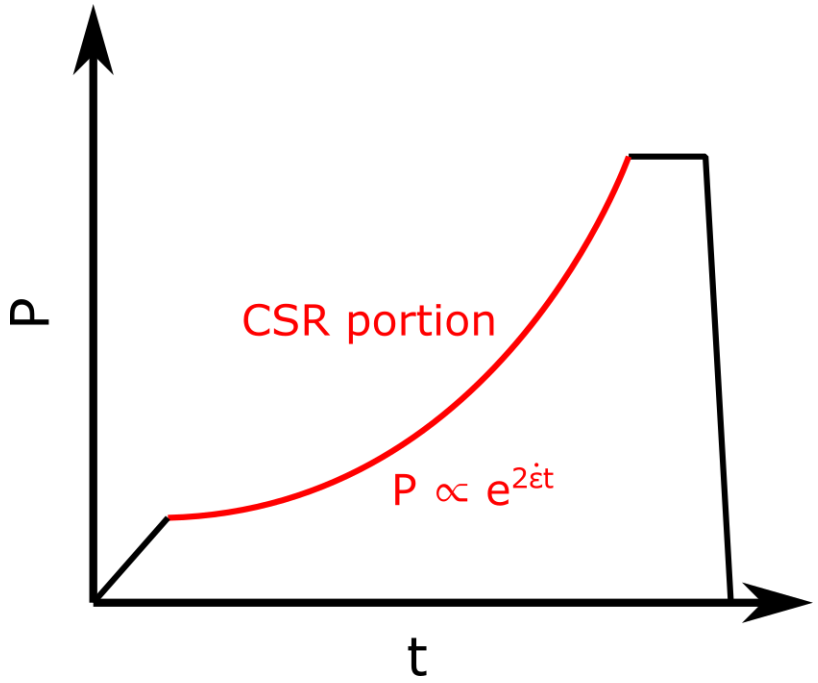

Figure 4-29 – A depiction of a CSR load function. The CSR portion is indicated in red, while other portions like pre-loading, holding, and unloading are in black.

4.5.1.2. Extraction of unloading stiffness

The unloading stiffness from a QS load function is found by calculating:

$$S = \frac{dP}{dh}\Big|_{h_i = h_{max}} \tag{4-14}$$

for the unloading segment. In theory, S can be extracted by direct calculation of this derivative. However, in practice indentation creep and experimental noise at the end of the holding segment make this method unreliable. Instead, the unloading segment is fit to a power law function:

$$P = A(h_i - h_o)^m \tag{4-15}$$

Here, A, h_o, and m are fitting parameters. Data is fit for a limited bound of the unloading segment (20-95% of load range by default for Hysitron Triboscan) to avoid fitting to transient behavior at

the end of the hold segment. The derivative with respect to h of this function is used to find the unloading stiffness:

$$S = \left.\frac{dP}{dh}\right|_{h_i=h_{max}} = mA(h_{max} - h_o)^{m-1}$$

(4-16)

This procedure is carried out for every unloading segment in the QS load function to obtain a contact stiffness for each unloading segment.

It should be noted that during an indentation test, the indenter and specimen are not the only elements in the nanoindenter that are deforming. The indenter transducer and frame must also deform due to Newton's Third Law. Thus, the indenter contributes extra compliance to the load-displacement curve that must be accounted for. This compliance is called the machine compliance C_m. Compliance and stiffness are reciprocals of each other, so C_m is easily decoupled from S. For a measured total compliance C_{total}:

$$C_{total} = C_m + C_{specimen}$$

(4-17)

Where $C_{specimen}$ is the compliance of the specimen, which is the reciprocal of S used to find H and E_r. The specimen properties can be substituted for $C_{specimen}$:

$$C_{total} = C_m + \frac{\sqrt{\pi}}{2}\frac{\sqrt{H}}{E_r}\frac{1}{\sqrt{P_{\max}}}$$

If C_m is known, then it can be subtracted out from C_{total}. Then $1/(C_{total}-C_m) = S$, the specimen stiffness that is required for calculation of H and E_r. In practice, indentation is carried out on a standard specimen with known H and E_r to find C_m, then the machine compliance is subtracted out on subsequent tests on specimens of interest. This can be done continuously as a function of load:

$$h_{corrected} = h_{measured} - C_m * P$$

(4-18)

Here, $h_{corrected}$ is the displacement with machine compliance subtracted and $h_{measured}$ is the transducer-measured displacement. If Equation (4-18) is used for load-displacement curves, then Equation (4-14) can directly be used in Equation (4-10) to find specimen stiffness free of machine compliance effects. Note that this carries the implicit assumption that C_m is the same between specimens, which means that specimen mounting to the indenter must be particularly secure. If specimens are free to flex or wobble during testing, then results will be inaccurate.

Care must be taken when combining the quasistatic Oliver-Pharr approach with CSR tests. Accurate measurements of S require a significant hold segment to avoid indentation creep effects, meaning that when using this method with CSR load functions the strain history of the material under the indent includes a constant strain rate deformation stage followed by an indentation creep stage. If the material being studied is sensitive to changes in strain history, then it is preferable to use a CSR load function with CSM enabled.

4.5.1.3. Contact conditions and h_c

Two conditions need to be met to obtain A_c using the Oliver-Pharr method. The first is that the specimen of interest produces Hertzian contact conditions and the second is that the the tip area function is known. During nanoindentation, instantaneous load and displacement are measured. The total tip displacement during the indentation test is accommodated by both elastic and plastic deformation in the specimen. Upon unloading, the elastic deformation recovers and the plastic, or residual, deformation leaves an indent in the specimen whose projected area is different than the projected area that was in contact with the specimen before unloading. This is illustrated in Figure

4-30. The contact area A_c that describes the area of the indenter in contact with the specimen during loading is required for property calculation, shown in Figure 4-30(a). This is characterized by the "contact depth" h_c that measures the distance along the indentation axis between the bottom of the indent and the surface of the specimen. The distance between the initial specimen surface and the bottom of the indenter tip h_{max} is used to find h_c. This is done by accounting for the elastic rebound of the specimen through assumption of certain contact conditions between the specimen and the indenter tip.

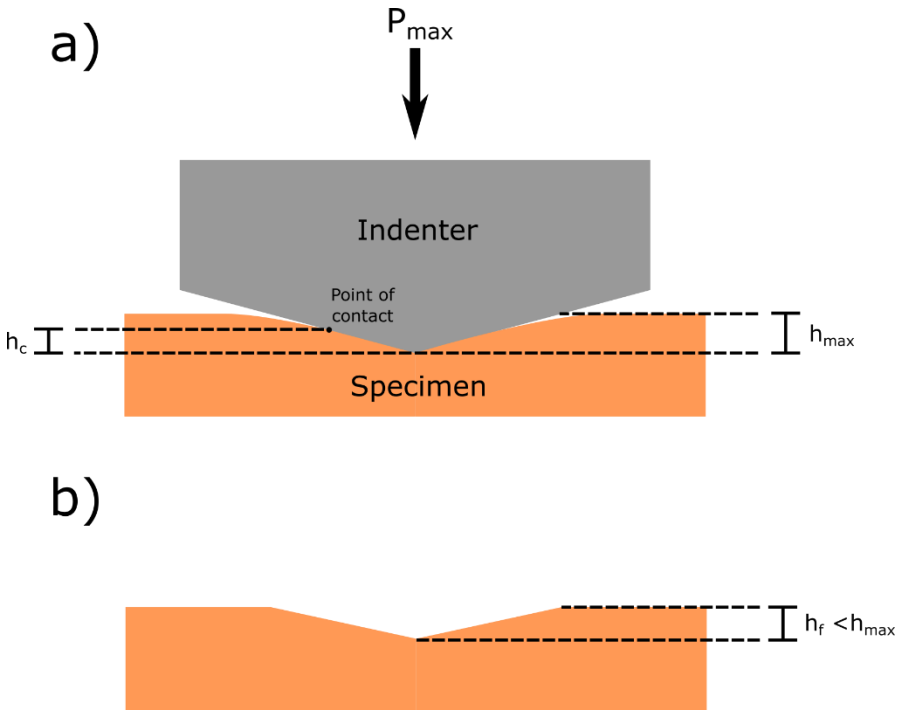

Figure 4-30 – Depiction of the specimen surface a) during loading and b) after unloading. H and E_r are calculated using h_c, which can be found using S and h_{max} in a). The residual indent depth h_f shown in b) is of little use for finding H and E_r

Oliver and Pharr use Sneddon's solutions for the indentation of radially symmetric indenters into an elastic half space to describe the load, displacement, and contact area relations used for indentation[194]. This work was based off the original solutions for contact pressure between two spherical surfaces derived by Hertz[195]. The Hertz solution reduces to elastic spherical

indentation onto a flat surface when one of the spherical surfaces is assigned an infinite radius of curvature. Practically, this means that indentation specimens must have flat surfaces with low surface roughness compared to the size of the indent and that the specimen surface area is large compared to the indenter size. The Hertz solution describes the elastic component of indenter displacement, the remainder of which is accommodated by plastic deformation in the specimen. While the mathematics of this situation are somewhat complex, knowledge of the elastic solution for indenter displacement and force required for elastic indentation produce the following relationship between load and displacement at an unloading segment:

$$h_{max} = h_c + \epsilon \frac{P_{max}}{S} \tag{4-19}$$

Here, h_{max} and P_{max} are the maximum displacement and load achieved by the indenter, respectively, S is the unloading stiffness, and ε is a geometric factor specific to a given indenter geometry. While one might expect a Berkovich tip to obey a geometry factor close to the one for a conical tip (0.72), it actually adopts a value of 0.75 experimentally, which is valid for paraboloid solids of revolution. Eq. (4-19) can be solved for h_c, given that the load-displacement curve was analyzed to extract S using Eq. (4-16). h_c is useful because it can be easily related to the geometry of the tip using the tip area function, which will be discussed next.

4.5.1.4. Calibration of the tip area function

Once unloading stiffnesses are obtained, certain assumptions about the contact conditions under the indent and the tip geometry are made to obtain A_c. Tip geometry is defined as a function of contact depth h_c. Different functional forms are used for different tip geometries. For a Berkovich tip, the most commonly used functional form is:

$$A_c(h_c) = c_0{h_c}^2 + c_1 h_c + c_2 h_c^{\frac{1}{2}} + c_3 h_c^{\frac{1}{4}} + c_4 h_c^{\frac{1}{8}} + c_5 h_c^{\frac{1}{16}} + \cdots$$

(4-20)

This is the tip area function, with c_n representing constants used for fitting the functional form to the measured tip area. Typically, anywhere from 3 to 6 terms are used in the tip area function, although more can be used if desired. For a perfect Berkovich tip, only the first term is needed, with $c_0 = 24.5$. Most tip area functions are fit with only constants past c_0 being adjustable. This ensures that the tip area function approaches that of a perfect tip area function as h_c tends towards infinity. This behavior reflects the reality that for a deep enough indent, or at a large enough length scale, a Berkovich tip reaches its ideal geometry. The number of constants used during tip area calibration reflect the imperfections in tip geometry. The more the tip deviates from ideal geometry, the more constants are used to fit the tip area function. If indentation is required to be restricted to shallow depths, c_0 can also be fit, meaning that only the tip apex will be used for indentation. Given that the tip apex changes shape after every indent due to wear, it does not reflect perfect Berkovich geometry at all. Thus, tip area functions with $c_0 \neq 24.5$ are useful for shallow indents, but unreliable for deep indents, and vice-versa with $c_0 = 24.5$. Other tip geometries may be used for indentation, but different tip area functional forms than that given in Eq. (4-20) must be used for tip area function fitting depending on tip geometry.

Calibration of the tip area function is carried out using a PLUL load function on a standard sample with known properties. Most commonly fused silica is used, but for the most accurate data a standard sample with properties similar to those of the specimen of interest should be used[196]. Calibration proceeds as follows:

1. The PLUL indent is performed on the standard sample.
2. Unloading stiffnesses are extracted as a function of h_c.

3. For each h_c, an A_c is calculated using Eq. (4-10) and E_r calculated from known moduli of the standard sample and indenter tip material.
4. A tip area function of the form in Eq. (4-20) with the desired number of coefficients is fit to the data in step 3.
5. H and E_r are obtained as a function of depth using Eqs. (4-10).

Example H and E_r depth profiles obtained on fused silica with a PLUL indent can be found in Figure 4-31. This procedure only provides a tip area function and H vs h_c data independently; the E_r vs h_c is dependent on an assumed E_r per step 3 and should always match the assumed E_r. Thus, the quality of the tip area function is judged using the H vs. h_c data; for fused silica, this curve should reach an asymptote at low h_c and stabilize near 9.25 GPa.

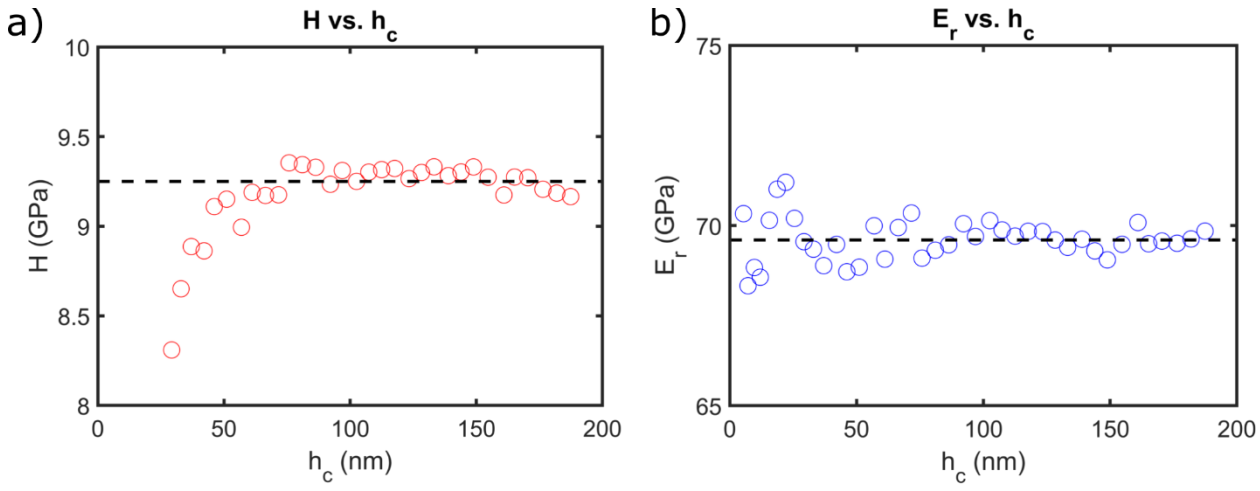

Figure 4-31 – a) H and b) E_r data obtained from fused silica, which is a commonly used nanoindentation standard. The tip area function used to calculate H and E_r was calculated using S measured on the same indent. The expected values of a) H = 9.25 GPa and b) E_r = 69.6 GPa are depicted with a black dotted line. b) naturally shows a good match and a flat slope because A_c is calculated at each h_c using E_r = 69.6 GPa and measured S. a) is of much more use when assessing the quality of a tip area function because it is obtained independent of the assumed E_r. It also has no slope past h_c = 75 nm and matches well with the expected value of H = 9.25 GPa up to h_c = 187 nm, indicating that data obtained with this tip area function on a specimen of interest should be reliable between h_c of 75 and 187 nm. The poor fit to expected values in a) below 75 nm is a consequence of tip imperfections and is unavoidable without letting c_o be adjustable during the tip area function fitting.

4.5.1.5. Obtaining data from a specimen of interest

A load function is chosen from Sections 4.5.1.1.1-4.5.1.1.3 and performed on the specimen. Stiffness is calculated from the load-displacement data as described in Section 4.5.1.2, h_c values are found using the procedure in Section 4.5.1.3, and finally the tip area function, h_c values, and S values are used with Eqs. (4-10) to obtain H and E_r. CSM is described next, as it provides additional functionality to a nanoindenter that can be useful in some circumstances.

4.5.2. Continuous stiffness measurement

Pethica and Oliver introduced a method to continuously measure unloading stiffness during and indentation depth without the need for significantly large unloading segments[197]. To do so, they superimposed a sinusoidal, or AC, load over the QS, or DC load in a typical indentation test. While in theory unloading stiffness can be simply calculated from the periods in the AC load with negative slope, in practice the mechanical resistance and damping from the indenter be taken into account. The indenter can be modelled as a mass-spring-dashpot system (Figure 4-32):

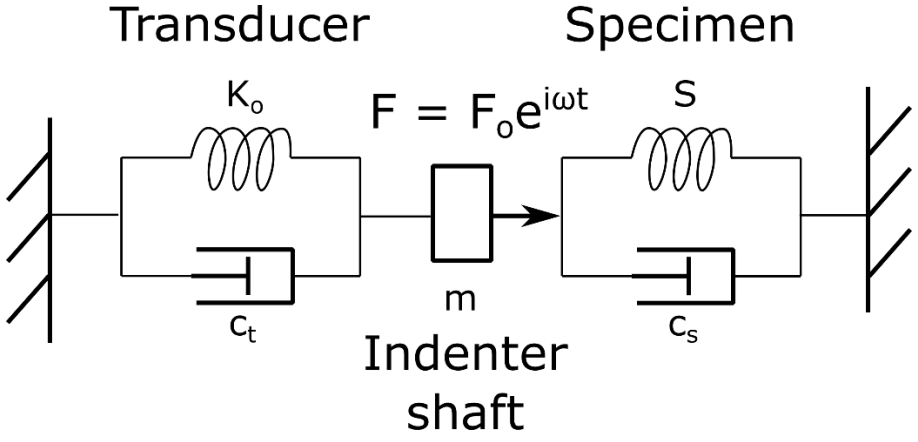

Figure 4-32 – A simplified mass-spring-dashpot model used to describe oscillatory motion of the transducer train.

The transducer and specimen-frame stiffnesses form two load trains in parallel. The transducer has a spring stiffness K_o and damping c_t. The specimen and frame are in series; the former has stiffness

S and damping c_s, while the latter contributes a compliance C_f. The mass being driven in this system is the transducer shaft with mass m. Given an AC force of the form $F = F_o e^{i\omega t}$, the indenter will exhibit a displacement response $h = h_o e^{i\omega t+\phi}$, with a phase lag ϕ introduced because of dissipative losses. Then, unloading stiffness can be solved for using the relation between force and displacement amplitude as well as the expression for dissipative loss:

$$\frac{F_o}{h_o} = \sqrt{\left(\left(\frac{1}{S} + C_f\right)^{-1} + K_o - m\omega^2\right)^2 + \omega^2 c^2}$$

$$\tan\phi = \frac{\omega c}{\left(\frac{1}{S} + C_f\right)^{-1} + K_o - m\omega^2}$$

(4-21)

These equations can be solved simultaneously for S, which has a real part S_s and a complex part S_l[198]. S_s is the storage stiffness, which accounts for the elastic deformation in the material. For viscoelastic materials, some mechanical energy is dissipated by viscous flow and is quantified by the loss stiffness S_l, which is negligible for hard materials such as metals. The expression for S_l is given by:

$$S_s = \left[\frac{1}{\frac{F_o}{h_o} cos\phi - (K_o - m\omega^2)} - C_f\right]^{-1}$$

(4-22)

Simplifying assumptions can be made at typically used oscillation frequencies:

$$S_s = \frac{F_o}{h_o}\cos\phi + m\omega^2 - K_o$$

(4-23)

This expression is used for Hysitron/Bruker equipment that are capable of CSM. Note that here, machine compliance is explicitly subtracted out of the measured stiffness. This is similar to Eq. (4-14), where it is assumed that machine compliance is subtracted out of the load-displacement data before calculation of S.

In CSM, S_s is substituted for S Eq. (4-14) and then used to find h_c using Eq. (4-19). These h_c values (which are obtained as a continuous function of load) can then be used to calculate A_c in (4-20) and finally H and E_r using Eqs. (4-10). Thus, H and E_r are found as a continuous function of h_c, made possible by the high AC load frequencies used during tests. AC load frequency can range from several tens to a few hundreds of Hz for the Hysitron TI 980, the indenter used in this work. CSM is useful for materials that are graded over the length scale of a few hundred nm along the indentation direction, or for mechanical testing that cannot tolerate the hold segment used in QS tests (such as CSR testing). Here, it is used to determine the useable portion of H vs h_c data; at shallow depths, the indenter tip has very imperfect geometry and most tip area functions do not produce accurate results. At larger depths, the substrate effect introduces errors in H and E_r. Thus, an intermediate range with reproduceable data is desired, and can be found easily using CSM. As a last note, the loss stiffness S_l can be useful to find a quantity called the loss modulus, which quantifies dissipative losses in viscoelastic materials.

4.5.3. Correlation of indentation data to flow curves

The quantity specifying plastic response in indentation tests, hardness, is not defined the same as flow stress. The latter is the most useful quantity to obtain when characterizing mechanical properties, so a simple method for correlating hardness and flow stress is desired. The Tabor factor C, also referred to as the constraint factor, is a constant for a given material and tip geometry that can be used to correlate H and σ_f (flow stress):

$$H = C\sigma_f$$

(4-24)

Tabor showed that for conventional engineering alloys with micron- or higher sized grains, C is about 3 for a Vickers tip geometry[35]. Later work demonstrated that C should not be expected to be consistent across all materials; early examples in the literature cite inorganic glass as a material that has a Tabor factor of 1.5[199]. There are many examples in literature that assume a C of 2.7-3 for nanostructured metals[15,99,130,134,145,200], but this may not be a good assumption. Tabor later established that C is a function of material properties and tip geometry[201]. C is dependent on E/σ_y ratio and included tip angle assuming a conical tip. Nanostructured metals therefore may not have a C of 3, as their microstructure increases strength by orders of magnitude over coarse-grained counterparts without significantly changing Young's modulus. Accurate correlation of indentation to flow data is paramount in using nanoindentation as a tool for studying fundamental deformation physics.

There are a few methods that provide more accuracy in correlating flow stress to hardness based off the principle of indentation strain. Usually, ε_i is assumed to be 8%[202,203], corresponding to a σ_f at 8% strain, or $\sigma_{8\%}$. ε_i can be thought of as an average strain under the indent for correlating H to σ_f. However, stress state is spatially varying under an indent, which should produce different strains as a function of material properties. Assuming a conical tip, indentation strain is calculated by[204]:

$$\varepsilon_i = \frac{E}{\sigma_y}\cot\alpha$$

(4-25)

The new quantities introduced are the indentation strain ε_i and included tip semiangle α. Later work establishes that ε_i should also depend on work hardening parameter n[39]. Pyramidal tips can be included in this analysis by assigning a representative conical tip angle to a given tip geometry[184]. It should be noted that much of the literature on correlating indentation results to uniaxial flow stresses use the idea of a representative cone angle to compare non-radially symmetric tips (i.e. Berkovich and Vickers) to each other and conical indentation tests[184,205]. As it happens, Berkovich and Vickers tips have the same representative cone angle, making conclusions for Vickers tests comparable to those from Berkovich tests.

While correlation of H to $\sigma_{8\%}$ is tempting to produce physically meaningful flow stresses from high throughput nanoindentation, it must be stressed that hardness is not a material property. Hardness is a test result partly dependent on many factors that may complicate use of the Tabor relation. Recent computational[206–209] and experimental[205,210,211] work has shown that ε_i is also dependent on material parameters[208]. The oft-quoted value of 2.7-3 for Tabor factor is from Vickers indentation completed by Tabor on annealed copper and mild steel that were subsequently work hardened to varying extent[202]; for other materials with dissimilar E, σ_y, and n, Tabor factor can deviate significantly from the assumed value even amongst different metals[39,203,204]. Complicating matters further, ε_i also depends on E, σ_y, and n[208]. Tabor factor and ε_i vary widely even within experimental work on nanocrystalline metals, which are expected to have similar combinations of mechanical characteristics. Work by Leitner, et al. claim that a Tabor factor of 2.8 works well for nanocrystalline Ni for pyramidal tips with different included angle with ε_i ranging between 8-24%[184], while comparison between micropillar and nanohardness data on nanotwinned Al-Fe 6% gives a Tabor factor of 3.4 at ε_i = 8%. Thus, experimental results do not seem to produce a conclusive criterion for hardness-flow stress correlation. Unfortunately, neither

does computation. Hernot, et al. use FEM simulation to determine representative plastic strain for materials with various H, E, $\sigma_{y,}$ and n[208]. Further work is needed to understand the Tabor correlation of 3D Cu/Nb hardness to uniaxial flow stress. For the current work, ε_i is assumed to be 8% with the caveat that future work may produce a more rigorously substantiated value.

5. Microstructure of 3D interface Cu/Nb

5.1. Crystallography and microstructure of 3D interfaces

5.1.1. Methodology

5.1.1.1. Synthesis

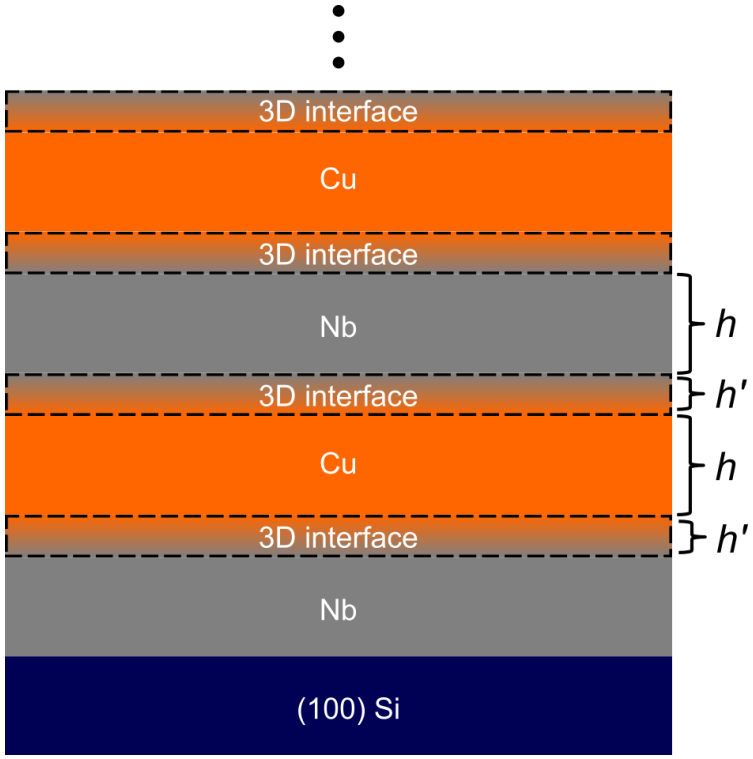

Figure 5-1 – A schematic depicting the PVD synthesis of 3D Cu/Nb and the microstructural metrics used to define the microstructure. The ellipses signify the repeat deposition of layers to form a thin film.

3D Cu/Nb is deposited using DC magnetron sputtering PVD to produce desired pure layer and 3D interface thicknesses. This process is depicted in Figure 5-1. Pure layer thickness will be represented by the variable *h*, while 3D interface thickness will use *h'*. The shorthand for samples used in this work reads "*h*-*h'* Cu/Nb*"* , so 20-10 Cu/Nb would have *h* = 20 nm for both the Cu and Nb pure phases and *h'* = 10 nm. For this work, 3D Cu/Nb was synthesized in an AJA1 system using DC sputter guns. Targets used were 1/4" thick and had a 2" diameter. Both Cu (99.999%

purity) and Nb (99.95% purity) targets were purchased from Kurt Lesker. Deposition occurred at a rate of 3 Å/s on a rotating, room temperature single-crystal [100] Si wafer with a native oxide. No substrate bias was used. Base pressure was $1 * 10^{-7}$ mTorr, while working pressure was 3 mTorr at 30 SCFM flow rate of argon. When depositing pure Cu and Nb, powers of 150W and 400W were used, respectively. To deposit 3D interfaces, deposition rates were varied linearly from 0 to maximum powers to achieve a nominal linear composition gradient. For example, when depositing from pure Cu to pure Nb, power was ramped from 150 to 0 W for Cu and 0 to 400 W for Nb. The thickness of 3D interfaces was controlled by the time it took to ramp from one phase to another. Thus, a 10 nm 3D interface had target powers ramped over 33.3 seconds. The deposition power profile for 10-10 Cu/Nb is depicted in Figure 5-2. Thin films of 2, 8, and 10 micron total thickness were used in this work.

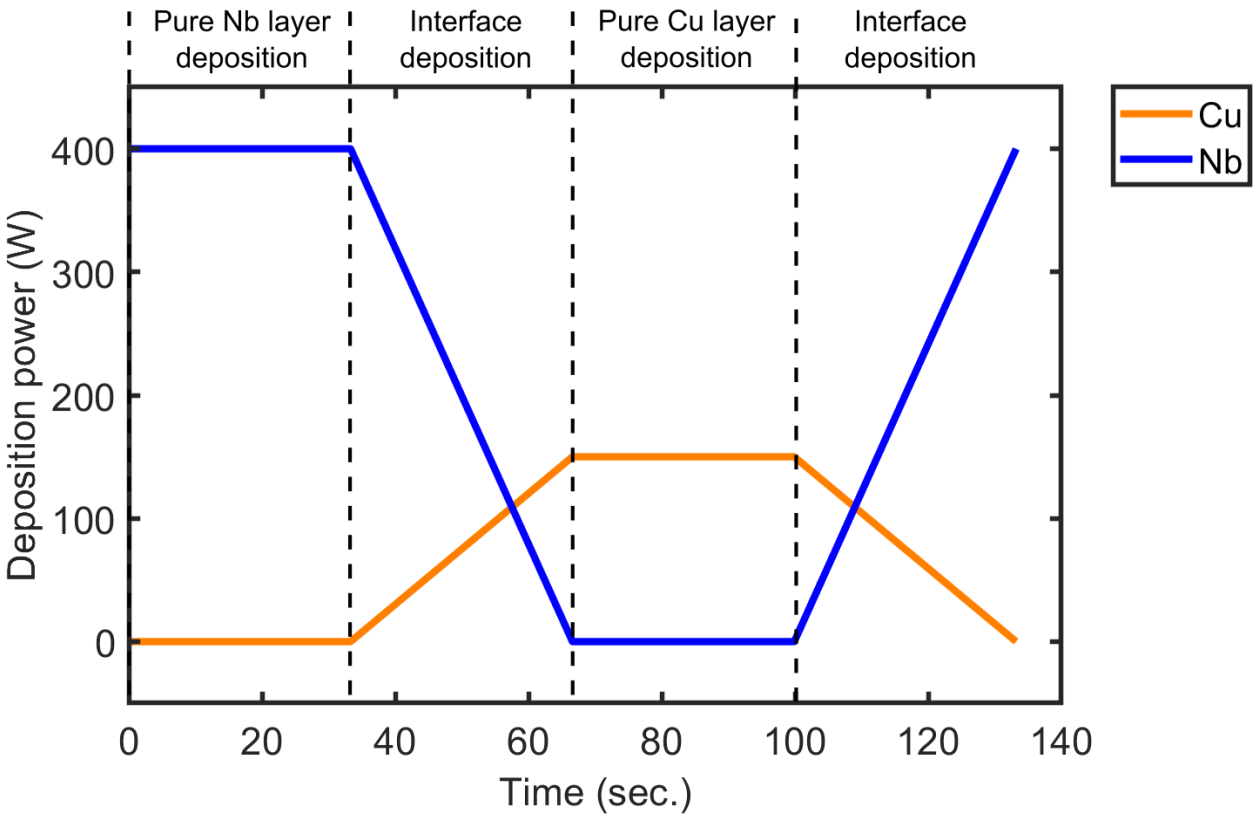

Figure 5-2 – The deposition profile used for 10-10 Cu/Nb for one bilayer consisting of a Nb layer, a 3D interface, a Cu layer, and another 3D interface. This profile is repeated until a thin film of desired thickness is deposited.

5.1.1.2. TEM specimen preparation

TEM specimen preparation for all TEM-based work was performed via cross-sectional FIB lamella procedures outlined in Chapter 4 using a FEI Helios NanoLab G4 FIB/SEM. Rough trenching and thinning was performed at 30 keV. Fine thinning was done at 5 keV, and final lamellae cleaning was done at 2 keV. If specimen thinning was uniform and beam conditions allowed, further ion polishing at 1 keV and 500 eV were done.

5.1.1.3. CTEM

CTEM was performed using an FEI Tecnai F30, Thermo Fisher Talos F200X, and an FEI Titan equipped with a probe corrector. The Tecnai and Titan were operated at 300 kV, while the

Talos was operated at 200 kV. The Tecnai and Titan were equipped with Gatan CCD cameras, while the Talos was equipped with a Thermo Fisher Ceta CMOS camera. CTEM micrographs at conventional magnification were obtained by inserting a 30 micron objective aperture on the center spot of the diffraction pattern. Diffraction patterns and high magnification CTEM produced crystallographic information at different length scales. High-magnification CTEM is also referred to as high-resolution TEM (HRTEM). HRTEM was conducted with no objective. Spot sizes 3-5 were used for CTEM imaging, while spot sizes 5-9 were used for diffraction patterns.

5.1.1.4. STEM

STEM was performed using a Thermo Fisher Talos F200X and an FEI Titan, operating at 200 keV and 300 keV, respectively. The Talos was used in nanoprobe mode for STEM-EDS at spot size 3-4 and using a 70-100 micron C2 aperture. Characteristic X-rays were collected with a Super-X G2 EDX detector with all four sensors enabled. EDS spectrum images were quantified by atomic percent using Cu K lines and Nb L lines. Specimens were prepared on Mo FIB grids to minimize grid background. The Titan was used for high-resolution STEM (HRSTEM) imaging. HRSTEM was done in nanoprobe mode at spot size 8, with a probe-limiting 50 micron C3 aperture. This resulted in a convergence angle of 25 mrad. Detectors and camera lengths for STEM images are indicated for each micrograph presented. Nanobeam diffraction (NBD) was performed on the Talos using microprobe mode at spot size 9 and using a 20 micron C2 aperture. Details and motivation for NBD will be covered below.

5.1.1.5. APT

APT was conducted on 40-10 Cu/Nb using needle-shaped specimens prepared on a Thermo Fisher Nova 200 FIB/SEM. A CAMECA local electrode atom probe (LEAP 4000X HR) was used for APT experiments. Specimens were run in laser mode with a 200 kHz pulse repetition rate,

0.5% detection rate, 30 K base temperature, and 30–60 pJ laser energy. APT data were reconstructed and analyzed using CAMECA's integrated visualization and analysis software (IVAS) 3.8.6.

5.1.1.6. X-ray Pole figure measurement

X-ray pole figure measurements were completed using a Bruker D8 Discover equipped with a graphite monochromated Co Kα source and a VÅNTEC-500 two-dimensional x-ray detector with 0.04˚ angle resolution at 20 cm sample-to-detector distance. ϕ scans were completed from 0-360° at various 2θ, ω, and ψ at 20 seconds per frame to achieve good coverage of Cu (111), (200), (220) and Nb (110), (200), (112) pole figures. Experimentally measured pole figures were imported into MTEX[212] for further processing. The first step in MTEX was to interpolate missing data points and remove Si (100) substrate peaks. Si substrate peaks were removed by deleting outlier data points in experimentally measured pole figures – these peaks were much more intense than the maximum signal from Cu or Nb in the sputtered film. Interpolation was done using the interp function in MTEX over a grid from 0-90° in α and 0-360° in β with a step size of 3˚ in both coordinates. The scaling factor associated with polarization, background, and detector factors was determined experimentally by measuring pole figures using APS 10-micron Cu powder sprinkled onto a thin layer of vacuum grease. These scaling factor pole figures were then divided pointwise out of interpolated Cu/Nb pole figures to produce quantitative pole figures[213]. Then, pole figures were normalized. Lastly, orientation distribution functions (ODF) were fit to pole figures at a resolution of 5° and using a de Vallee Poussin kernel width of 5° for modeling purposes. Pole figures presented in this work are projected from these ODFs.

5.1.2. Conventional TEM (CTEM)

5.1.2.1. Grain and interface morphology

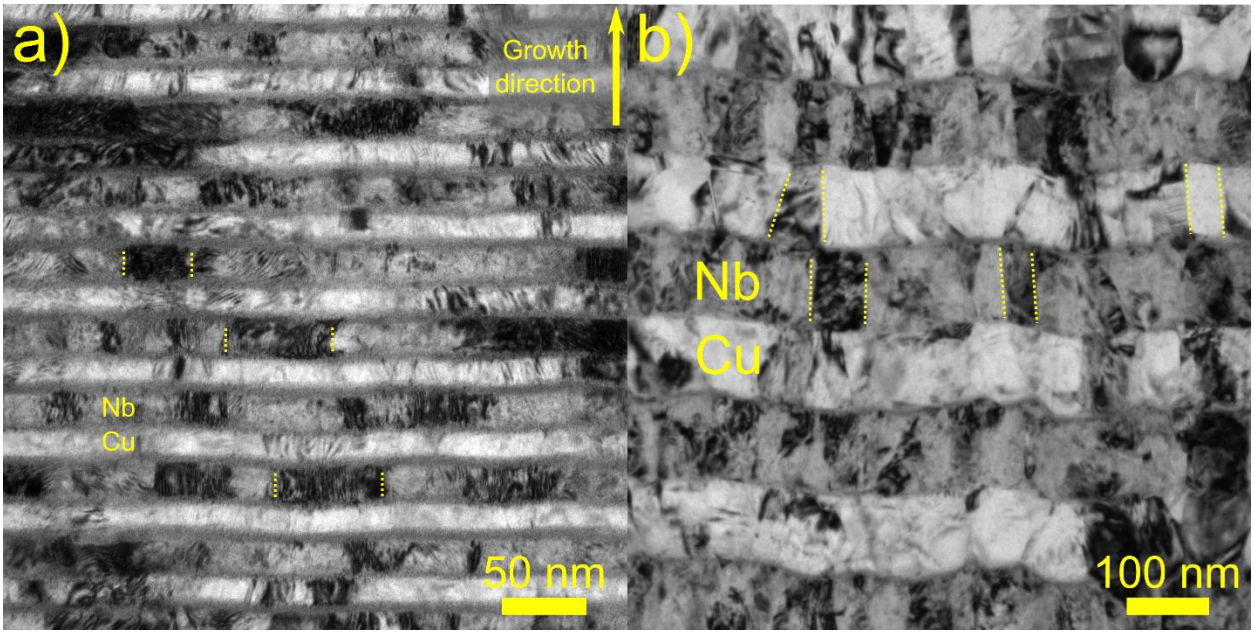

Figure 5-3 – CTEM micrographs of a) 10-10 Cu/Nb and b) 80-10 Cu/Nb. Dotted lines denote in-layer extent of grains in each specimen. 3D interfaces can be easily discerned at conventional magnification for 10-10 Cu/Nb. For 80-10 Cu/Nb, 3D interfaces are less visible due to interface roughness.

Grain and interface morphology can be determined using CTEM at conventional magnifications (<~ 300,000x). CTEM micrographs for 10-10 and 80-10 Cu/Nb are found in Figure 5-3. Mass-thickness contrast present in this imaging modality allows for identification of layers. Cu layers with lower Z number allow more transmission of the electron beam and appear bright in bright field images, while Nb layers with higher Z number scatter more of the beam away from the direct spot and appear darker in bright field images. Diffraction contrast occurs due to different orientations in different grains, making some grains in a layer appear dark while others appear bright. This allows for observation of grain structure and size in the in-plane direction. Both composites have lamellar microstructures as desired. In-plane grain size appears to be about 50 nm for both materials, indicating that *h* does not have a strong effect on in-plane grain size.

Because of this, for samples with h <~ 50 nm, grains have a high aspect ratio (greater width than thickness), while for samples with h>~50 nm, grains have a lower aspect ratio and are columnar. Deposited layers appear to be flat, while interfaces have some waviness. For 10-10 Cu/Nb, this waviness has an amplitude of a few nm, while for 80-10 Cu/Nb it appears to increase to about 10 nm.

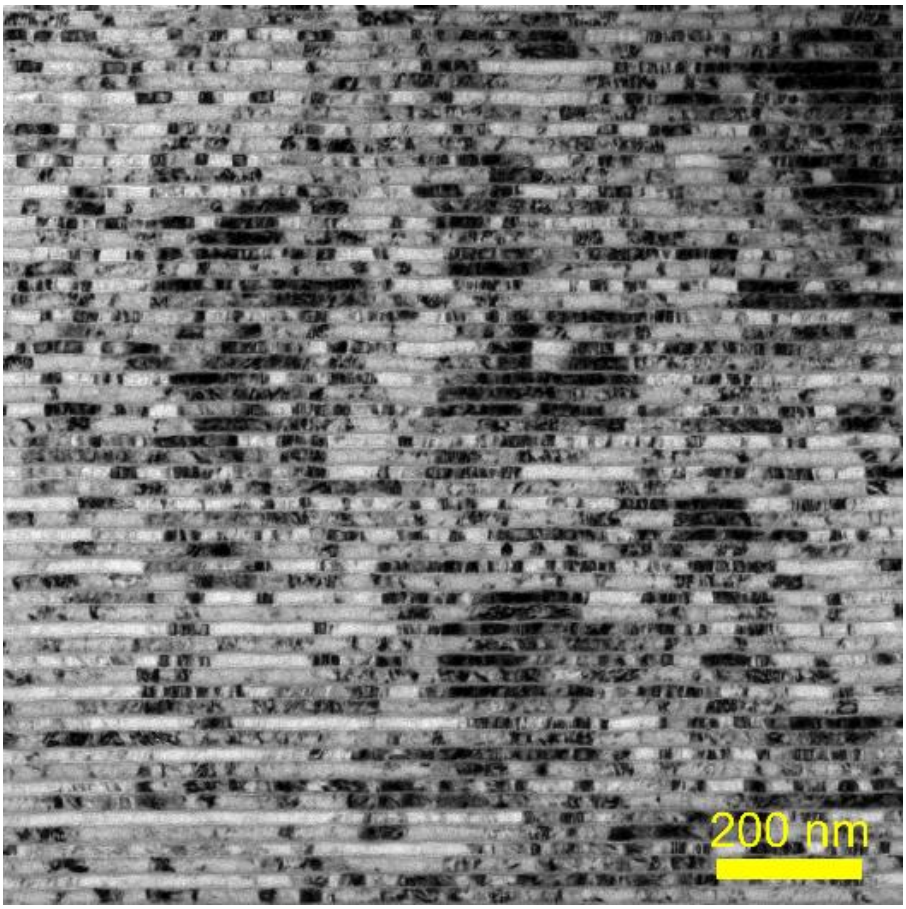

Figure 5-4 – A CTEM micrograph of 10-10 Cu/Nb. The TEM lamellae was tilted so that many grains are in strongly diffracting orientations, as evidenced by the large number of dark grains.

The in-plane grain size distribution is more accurately represented by a micrograph in which many grains are in strongly diffracting orientations. In this condition, many grains appear dark and can be more easily identified. This is shown in Figure 5-4 for 10-10 Cu/Nb. Here, some grains are

much larger in the in-plane direction than Figure 5-3 suggested. Some grains reach an in-plane size of 200 nm, meaning that in-plane grain sizes range from 50-200 nm.

3D interfaces can be distinguished from abutting phases in Figure 5-3. Diffraction contrast in between Cu and Nb layers is uniform, giving rise to a "fuzzy" appearance to heterophase 3D interfaces. No internal structure is visible at conventional magnification, suggesting that 3D interfaces are disordered. Whether they are finely polycrystalline with crystallite size of a few nm or amorphous cannot be determined at this magnification. The interfaces themselves have finite roughness, with peak-to-valley roughness amplitude of a few nm for 10-10 Cu/Nb and about 10 nm for 80-10 Cu/Nb. Other methods of 3D interface structure characterization are needed, which are presented in upcoming Sections.

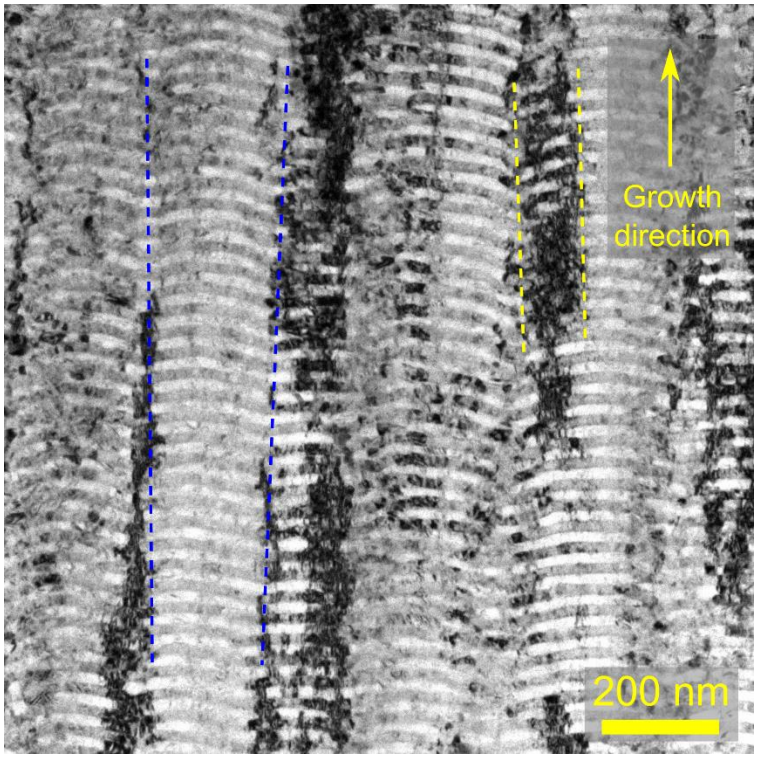

Figure 5-5 – A CTEM micrograph of h = 20 nm 2D Cu/Nb. While the microstructure is lamellar, layers are not as flat as in 3D Cu/Nb. Layers grow in colonies, forming columns of grains that are concave towards the substrate. One such colony is denoted by dotted blue lines. These colonies

are probably made of multiple grains in the in-layer direction, as shown by the grains identified between the dotted yellow lines.

The influence of 3D interfaces on nanolaminate growth can be determined by comparison with 2D Cu/Nb. Figure 5-5 shows a CTEM micrograph of h = 20 nm 2D Cu/Nb, taken near the top of a thin film with 8 micron total thickness. While this composite has a lamellar microstructure like 3D Cu/Nb, the constituent layers have significant curvature. The microstructure of 2D Cu/Nb is made up of columnar colonies of layers which are concave towards the substrate. The in-plane grain size of this material appears to be about 100 nm. Apparently, 3D interface encourage flat layer growth when synthesizing nanolaminates by PVD. This shall be discussed briefly in the Discussion section.

5.1.2.2. Crystallography and texture

The crystallography of 3D Cu/Nb films was studied mostly using TEM methods. Diffraction patterns in CTEM can provide information about crystal structure and texture over areas ranging from a few hundred nm to a few microns across. To interpret these patterns, it is useful to consult the FCC and BCC zone axis patterns associated with predominant biphase orientation relationships. Since most interfaces are of Nishiyama-Wasserman (N-W) and Kurdjumov-Sachs (K-S) type in 2D Cu/Nb[11], the relevant zone axes are [110] for Cu and [111]/[001] for Nb. The diffraction patterns for these zone axes are found in Figure 5-6.

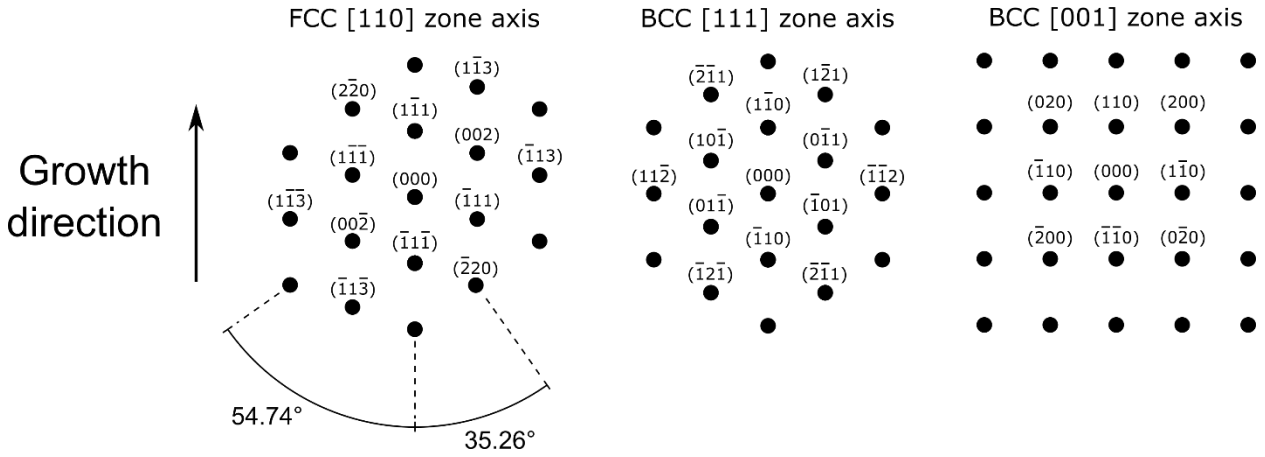

Figure 5-6 – FCC [110] and BCC [111] and [001] zone axis patterns are shown here[161], drawn to scale. Only the first allowed order of reflections is indexed for each family of planes. Compact FCC {111} and BCC {110} planes are aligned along a common growth direction to reflect the epitaxy expected for deposited materials.

This information allows interpretation of diffraction patterns taken from 3D Cu/Nb. A diffraction pattern from 10-10 Cu/Nb is shown in Figure 5-7. This diffraction pattern consists of short streaks, indicating a strong growth texture from PVD synthesis. Compact Cu (111) and Nb (110) planes are normal to the growth direction and parallel to in-layer directions. The low-order diffraction streaks present in the pattern belong to the FCC [110] and BCC [111] and [001] zone axes, showing that the N-W and K-S heterophase orientation relationships dominate in 3D Cu/Nb just as they do in 2D Cu/Nb. No other low-order diffraction streaks can be indexed from this pattern, suggesting that only FCC Cu and BCC Nb contribute significantly to the diffraction pattern. The Cu phase has two twin variants present in the diffraction pattern. No growth twins are observed in Figure 5-3 or Figure 5-4, implying that a given Cu grain should belong to the same twin variant through the thickness of the layer it belongs to. Since 3D interfaces appear to have significant disorder, Cu should not prefer one twin variant to another when grown on a 3D interface.

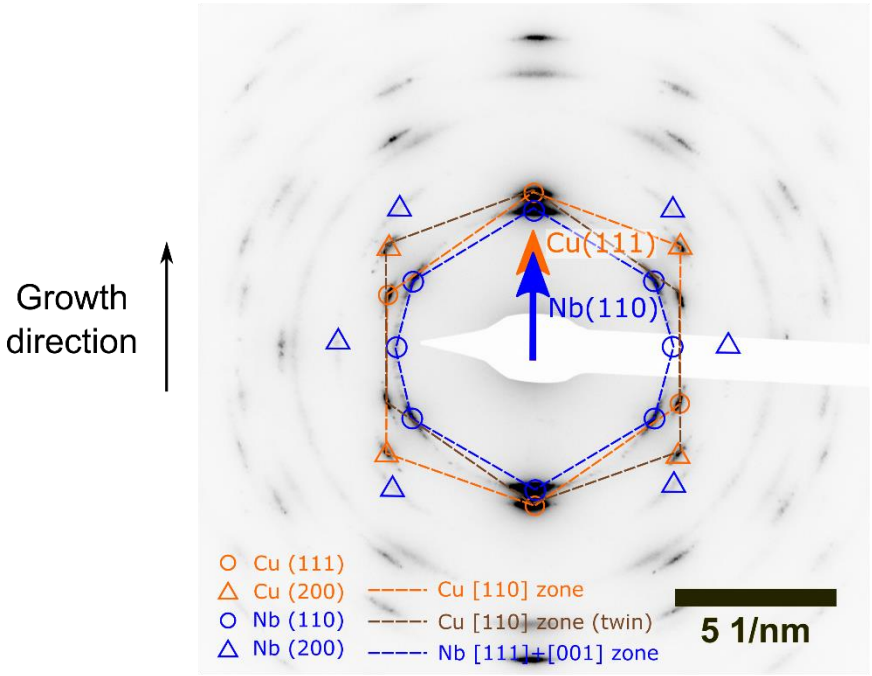

Figure 5-7 – A grayscale-inverted diffraction pattern from 10-10 Cu/Nb. Low-order diffraction streaks are indexed for Cu and Nb. The growth direction here matches that of Figure 5-3, demonstrating that Cu (111) and Nb (110) planes are parallel to in-layer directions and normal to the growth direction. Cu has streaks from the [110] zone axis present, while Nb has spots from the [111] and [001] zone axes. Low-order streaks from one phase are joined by dotted lines. The Cu phase has two twin variants present, giving rise to mirror symmetry about the growth direction.

The growth texture of 3D Cu/Nb was also quantified using X-ray pole figure measurement, as presented in Figure 5-8. These pole figures show that Cu and Nb deposit with a Cu (111)/Nb(110) fiber texture and quantifies the texture strength. Fiber textures are commonly found in PVD-deposited films[214].

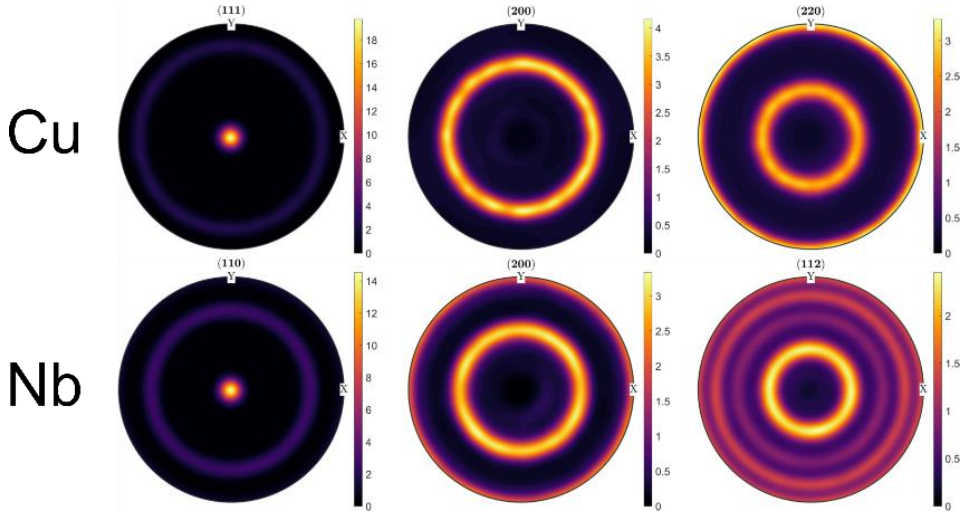

Figure 5-8 – Pole figures of Cu and Nb in 10-10 Cu/Nb, made by projecting ODFs fit to X-ray data. The growth direction is in the out-of-page direction. Since Cu (111) and Nb (110) plane normals are parallel to the growth direction and there is no preferred orientation in the x-y plane, both pole figures demonstrate a fiber texture.

5.1.2.3. Thick 3D interface morphology

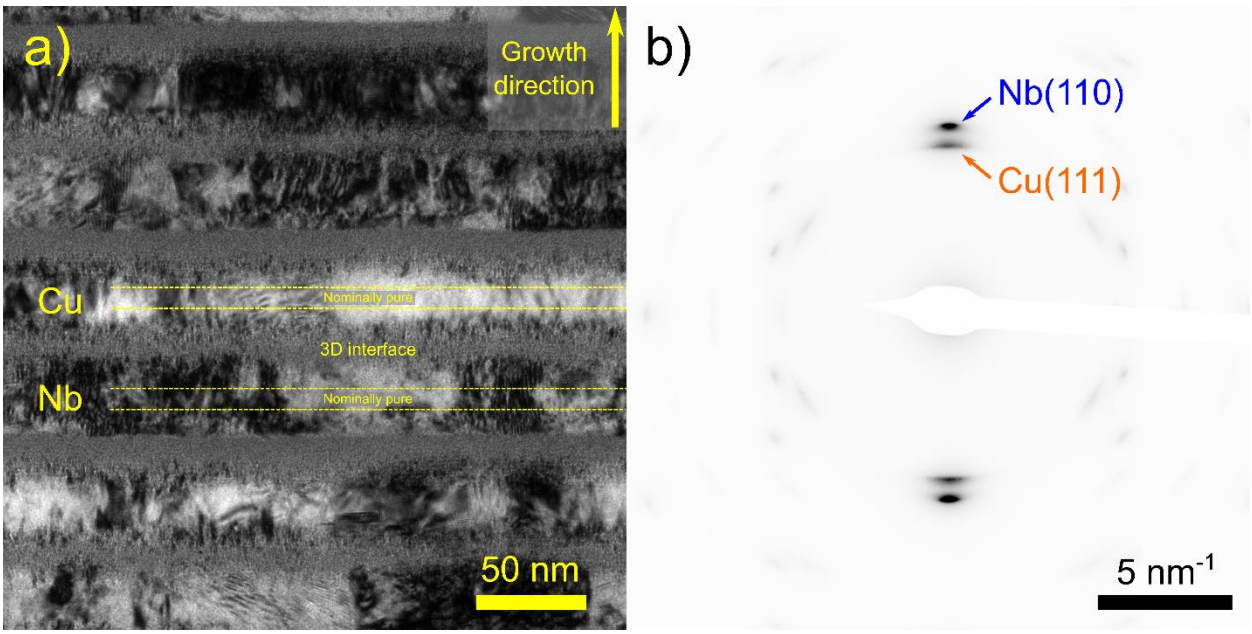

Figure 5-9 – a) A CTEM micrograph of 10-40 Cu/Nb and b) the associated electron diffraction pattern. a) overlays the nominal pure layer thickness over the observed microstructure, revealing diffraction contrast characteristic of long-range crystalline material present at the 3D interface periphery. This suggests that the dilute alloyed regions of the 3D interface are crystalline. b) shows that the fiber texture from PVD epitaxy is maintained, but with a reduction of intensity in the non-compact plane spots as compared to Figure 5-7.

The microstructure of 3D Cu/Nb with thick 3D interfaces is explored here. 10-40 Cu/Nb is used as a representative system for this investigation. The larger length scale of the interface facilitates observations and conclusions. CTEM of 10-40 Cu/Nb is presented in Figure 5-9(a). This demonstrates that thick interfaces do not interfere with the development of a lamellar microstructure in 3D Cu/Nb. In addition, diffraction contrast characteristic of crystalline material is present in the periphery of the 3D interface. 3D interface structure is much easier to discern here than in 10-10 Cu/Nb, where regions of uniform diffraction contrast clearly represent amorphous or very finely polycrystalline regions in the 3D interface interior. The boundaries of these disordered regions are diffuse in the 3D interfaces grown on Nb, but the 3D interfaces grown on Cu appear to have an abrupt boundary between disordered and crystalline material on the top side of the interface. The fiber texture in Cu and Nb are still present in Figure 5-9(b), but with much less intensity in planes not normal to the growth direction. This suggests that thick 3D interfaces reduce epitaxy strength between Cu and Nb.

5.1.3. High resolution TEM (HRTEM)

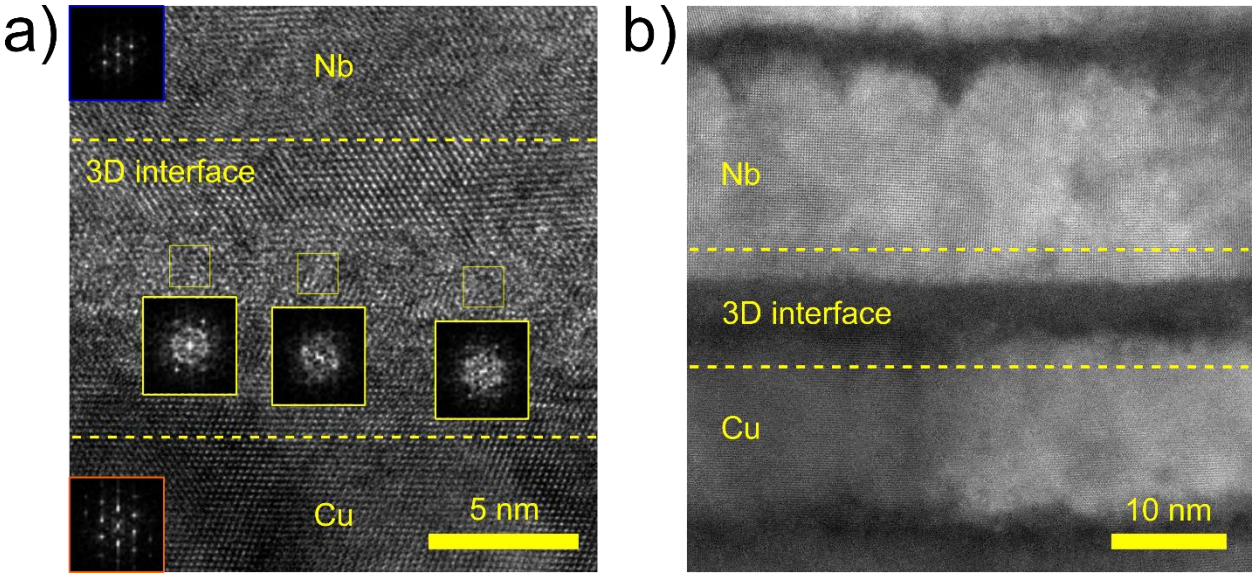

Figure 5-10 – a) HRTEM and b) HAADF HRSTEM of 10-10 Cu/Nb. a) demonstrates the atomic-scale structure in and near a 3D interface. Pure crystalline Cu and Nb are present at the top and bottom of the micrograph, as demonstrated by FFT insets in orange and blue, respectively. The Cu is viewed along the FCC [110] zone axis, while the Nb is viewed along the BCC [111] zone axis. The 3D interface is in between the Cu and Nb, with its nominal boundaries denoted by dotted yellow lines. b) is a Z-contrast HAADF HRSTEM micrograph of 10-10 Cu/Nb. The Nb layer here is viewed along the BCC [001] zone axis, while part of the Cu layer is viewed along the FCC [111] zone axis. The middle, disordered region of the 3D interface appears dark and lacks well-defined atomic columns. Some crystalline protrusions into the 3D interface grown on Nb can be observed at the top of the micrograph.

HRTEM and HRSTEM of 10-10 Cu/Nb are presented in Figure 5-10. Figure 5-10(a) contains a HRTEM micrograph of a 3D interface in 10-10 Cu/Nb. Crystalline material in HRTEM can be identified by atomic-resolution lattice fringes arising from phase contrast at high magnification in CTEM. A common strategy to characterize crystallography in HRTEM is to take the 2D fast Fourier transform (FFT) of a region and depict the power spectrum in logarithmic scaling. Regions that are on-zone will have FFT power spectra (FFT henceforth) that possess the symmetry of zone axis CTEM diffraction patterns. This is used in Figure 5-10(a), demonstrating that a significant portion of the 3D interface has long range order, having lattice fringes that are

uniform over the width of the micrograph. The term "long range order" describes uniform crystallography over several nm henceforth. The Cu-rich side of the interface is FCC and the Nb-rich side is BCC. These regions are completely coherent with the abutting pure layers. FFTs are also taken from the middle of the 3D interface at three different lateral positions, demonstrating lack of long range order and the presence of lateral crystallographic heterogeneity on the length scale of a few nm. Local crystallinity characterization was also performed using Z-contrast HRSTEM and is presented in Figure 5-10(b). Here, the HAADF detector was used at a camera length of 130 mm, which leads to an acceptance angle of 58.5-200 mrad. This ensures that incoherent scattering, which is proportional to mass-thickness, dominates the image signal. Note that some sources[27] consider Z-contrast signal to consist of electrons scattered to >50 mrad, while others use a threshold of >75 mrad[215]. Z-contrast HRSTEM has a few advantages over CTEM HRTEM[27]. First, intensity is often directly interpretable as mass-thickness down to atomic resolution. Second, the resultant micrograph is not as affected by specimen thickness or defocus as CTEM is. Lastly, STEM can extract highly localized information in a specimen, while information at a given location in a CTEM micrograph contains contributions from scattering in adjacent regions. Figure 5-10(b) shows much of the same information as Figure 5-10(a), including the semi-crystalline nature of the 3D interface. Figure 5-10(b) shows in addition that the interior of 3D interfaces appear dark, which is similar to loss of image intensity seen for Cu-Zr amorphous intergranular films[216]. This is due to loss of on-zone electron channeling effects that make zone axis-oriented crystalline regions appear brighter in Z-contrast HRSTEM[217,218]. The boundaries of disordered regions in 3D interfaces are not always flat, as seen in the 3D interface above the Nb layer at the top of the micrograph. Here, crystalline "fingers" protrude into the 3D interface interior, demonstrating a non-planar boundary between ordered and disordered material in the 3D interface.

While the information gleaned from CTEM and STEM presented so far is valuable, there remain ambiguities about crystallographic heterogeneity in the 3D interface. To that end, a specialized diffraction technique called diffraction STEM was performed and will be discussed next.

5.1.4. Nanobeam diffraction (NBD)

5.1.4.1. Description of NBD

Exploration of local crystallography on the nanoscale is a difficult task in specimens that do not have uniform structure through the thickness of a TEM lamella. 3D interfaces fit that description even for very thin lamella (<50 nm thick), prompting the use of nanobeam diffraction, or NBD. In this technique, diffraction patterns are recorded as a function of position in a specimen. This is akin to a methodology called 4D STEM, which nominally does the same but such terminology usually implies much faster diffraction pattern acquisition speeds[219]. For reference, each NBD experiment in this work collected ~200 diffraction patterns along a line profile and took a few minutes per profile. 4D STEM can collect multiple 1k x 1k STEM frames while recording diffraction patterns for every pixel in the same time. 4D STEM requires fast, sensitive electron cameras which were not readily available in the course of this work.

NBD combines the small convergence angle in CTEM, and with the ability to obtain structural information localized regions a few nm across in STEM. To motivate the use of NBD, the shortcomings of STEM for diffraction pattern analysis are discussed. This is shown in Figure 5-11. The goal of STEM is to achieve fine resolution in real space. This is achieved by using a high convergence angle on the order of a few tens of mrad, as shown in Figure 5-11(a,c). While this localizes the beam spatially, it makes it so that diffraction discs emanate from the specimen instead of diffraction spots. This is because the angular range of e-beam wavevectors entering the specimen must equal the angular range of wavevectors exiting the specimen[27]. Thus, if a

convergence angle of 25 mrad is used for STEM imaging, spots from diffracted beams are spread out into 25 mrad-wide discs in the resultant diffraction pattern (which is in reciprocal space). This makes interpretation and quantification of diffraction patterns difficult. NBD remedies this issue by excitation of the minicondenser lens. In FEI/Thermo Fisher instruments this mode of operation is called “microprobe” mode. Conventional STEM imaging uses “nanoprobe” mode. The minicondenser lens is used to make the beam near-parallel Figure 5-11(b,d). While this reduces the width of diffraction discs in reciprocal space, it increases the real space size of the probe. Use of a small C2 aperture is essential to localizing the beam as much as possible while maintaining a near-parallel beam. For this work, NBD conditions on a Thermo Fisher Talos F200X produced a beam with full width half maximum of 2.5 nm, while convergence semi-angle was 0.6 mrad, which was sufficiently small for interpretation of diffraction patterns. HAADF images were taken in NBD conditions at a camera length of 660 mm, producing images dominated by diffraction contrast.

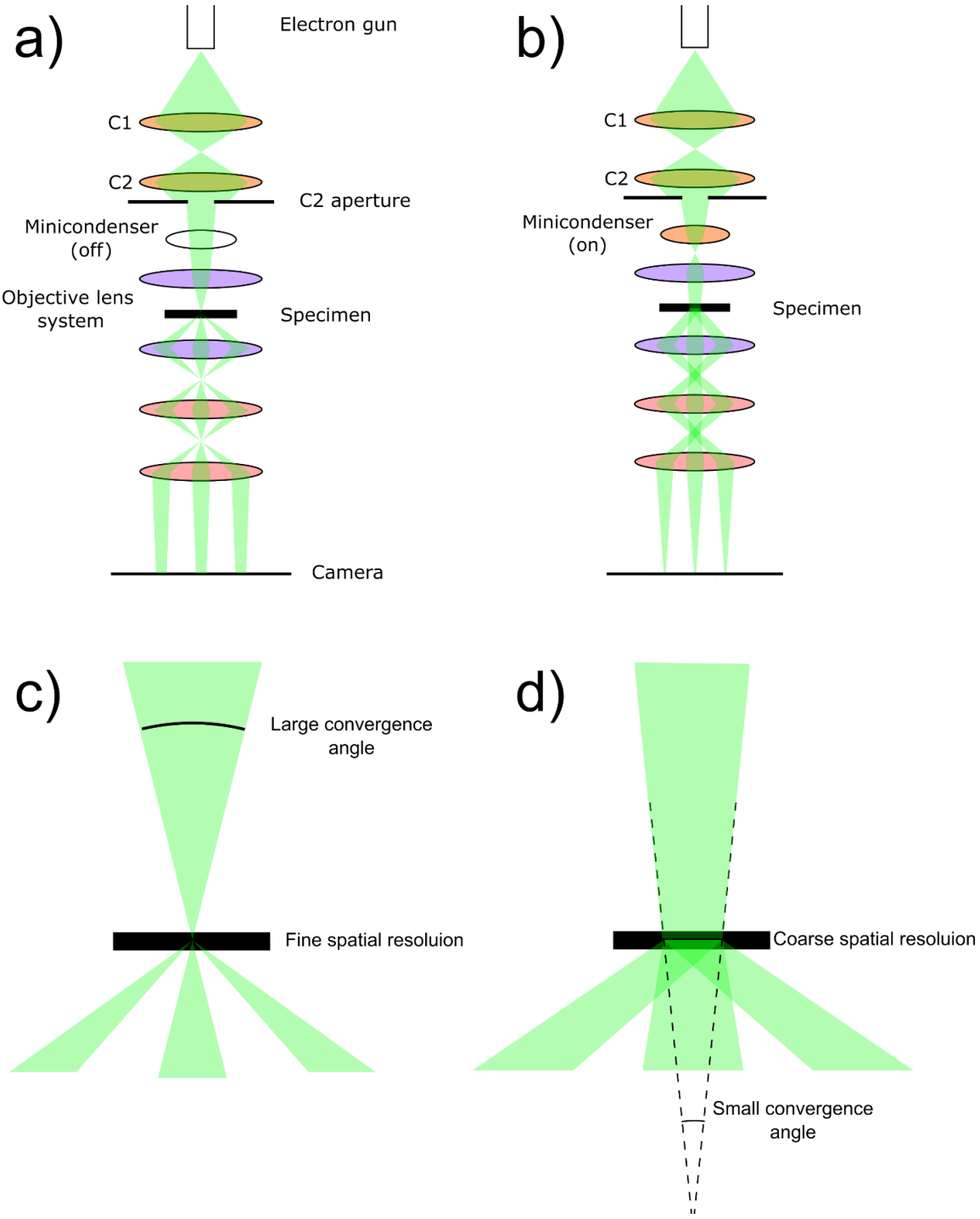

Figure 5-11 – a) A ray diagram of the TEM in conventional STEM imaging mode (nanoprobe mode for FEI/Thermo Fisher microscopes). The large convergence angle produces diffraction discs with large widths if diffraction patterns are recorded. b) A depiction of the TEM in NBD mode (microprobe mode). The near-parallel beam allows for collection of diffraction patterns containing spots with small width in reciprocal space. c) In-detail schematic beam geometry for

a). The large convergence angle affords fine spatial resolution of the probe. d) shows beam geometry for b), where a small convergence angle is traded off for a large real space probe width.

5.1.4.2. Interface-normal heterogeneity

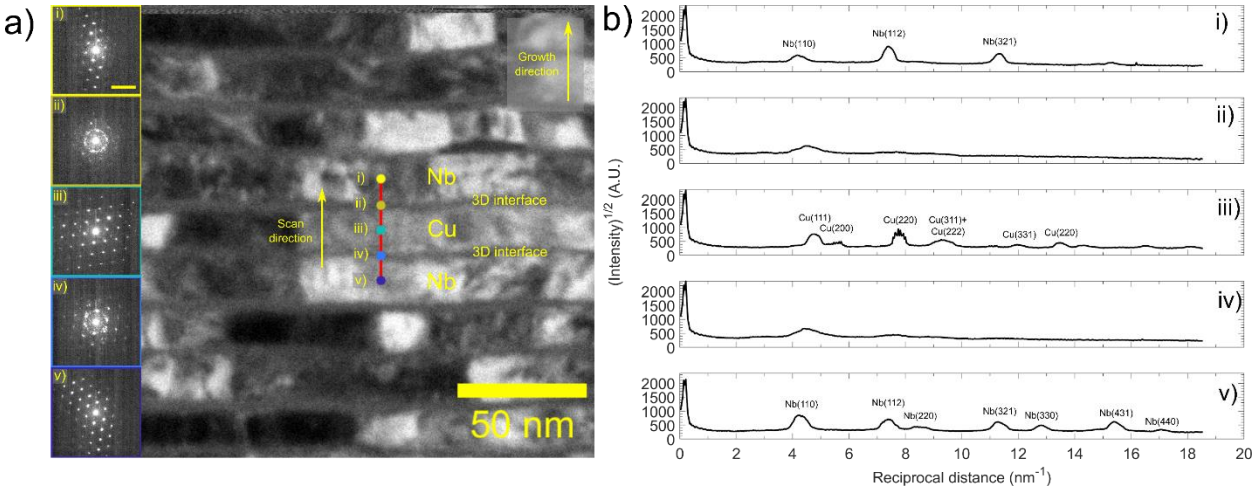

Figure 5-12 – a) A HAADF image of 10-10 Cu/Nb obtained at NBD imaging conditions. A NBD profile was taken along the red line at a step size of 0.2 nm. Selected diffraction patterns from regions (i-v) are presented as insets on the left. These patterns were then integrated azimuthally in polar coordinates to produce radial intensity profiles in b). Here, square root measured diffraction pattern intensity is plotted as a function of reciprocal distance from the direct spot. Profiles (i,v) represent pure Nb along the BCC [111] zone axis, while profile (iii) represents Cu along the FCC [110] axis. Significant peaks are indexed. The Cu (311) and (222) peaks are difficult to distinguish due to their similar reciprocal spacing and the finite size of the diffraction spots (convergence angle = 1.2 mrad = 0.7 nm^{-1}). The scale bar in (a.i) represents 10 nm^{-1} and is shared amongst (a.i-v).

NBD was used to probe the crystallographic heterogeneity of 3D interfaces in the interface-normal direction. 10-10 and 10-40 Cu/Nb were examined using this method. Figure 5-12 shows an interface-normal NBD profile in 10-10 Cu/Nb, along with radial profiles of intensity for each diffraction pattern. Diffraction patterns here and for all other NBD data are shown on a square root scale and have intensity normalized per pattern to reveal detail outside of the direct beam. The Nb phases are viewed along the [111] zone axis, while the Cu is viewed along the [110] zone axis. Figure 5-12(a) shows that the 3D interface grown on Nb has zone axis-like diffraction spots with a diffuse ring of intensity surrounding the direct beam. In contrast, the 3D interface grown on Cu

appears dominated by a diffuse ring of intensity with a few diffraction spots apparent in the diffraction pattern. There is a rotation between the STEM image and the diffraction patterns because scan rotation was applied to the STEM image, but not to diffraction patterns. As such, the diffraction patterns reflect the alignment of the specimen in the TEM holder.

This data shows that 3D interfaces have different structures when grown on Nb as compared to when they are grown on Cu. When considering the structural information from Figure 5-12, it is important to consider the interaction between the STEM probe and the specimen. Although the probe is 2.5 nm when it enters the specimen, it extracts information from a wider area because of beam spreading arising from beam-specimen interactions in the specimen. Thus, even though the 3D interface on Nb appears to produce a zone axis pattern characteristic of a large grain (compared to the probe size), this could simply be due to beam spreading. Even if the difference in diffraction patterns between the 3D interface on Nb (Figure 5-12(a.iv)) and the 3D interface on Cu (Figure 5-12(a.ii) arise solely from beam spreading, the data still shows that disordered regions in 3D interfaces grown on Nb are thinner in the interface-normal direction than those found in 3D interfaces grown on Cu.

One last point must be taken into consideration with respect to the diffraction spots seen in Figure 5-12(a.ii). Despite the difference of visual appearance in diffraction patterns in Figure 5-12(a.ii) and Figure 5-12(a.iv) representing 3D interfaces grown on Nb and Cu, respectively, the two interfaces are similarly disordered when quantified by diffraction intensity. This can be seen in the radial profiles of these diffraction patterns in Figure 5-12(b.ii) and Figure 5-12(b.iv). Even though intensity is scaled by its square root in these profiles (which accentuates signal scattered away from the direct beam), there does not appear to be any significant contribution to the

diffraction pattern from planes with reciprocal spacing more than 4.5 nm^{-1}. Most scattered intensity from both interfaces is found at the diffuse hump at 4.5 nm^{-1}, indicating lack of long range order.

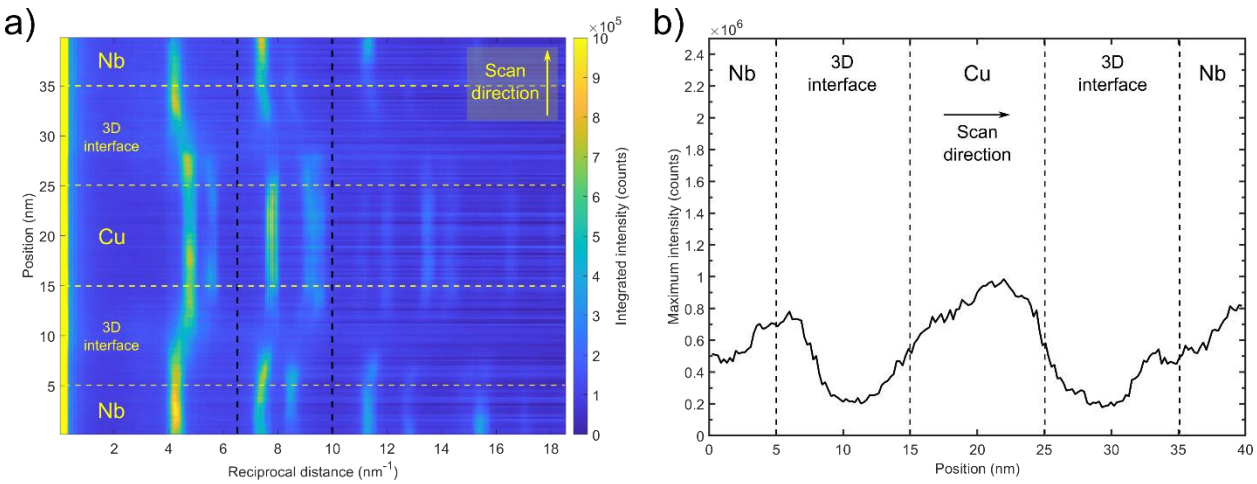

Figure 5-13 – a) Radial profiles for all spectra taken from 10-10 Cu/Nb along the profile in Figure 5-12. The x-axis represents reciprocal distance away from the direct beam in each spectrum, while the y-axis represents the distance along the profile that each pattern was taken from. The positive direction on the y-axis matches the scan direction indicated in Figure 5-12. The peaks between the dotted black lines are used to identify material that possesses long-range order. This is presented in b), where the maximum value for each radial profile is plotted against its position along the NBD profile. b) shows that interiors of 3D interfaces lack long-range order, while the edges of the 3D interfaces are crystalline.

Interface-normal heterogeneity can also be investigated by inspecting radial profiles of all diffraction patterns taken along the NBD profile. This is shown in Figure 5-13(a), where lack of long range order can be seen in 3D interface interiors. This manifests noticeably as loss of intensity in peaks between 6.5 and 10 nm^{-1}, which corresponds to the Nb (112) and (220) peaks and Cu (220), (113) and (222) peaks. These are planes with higher spatial frequency than the broad disordered hump seen in Figure 5-12(a.ii,a.iv), making them useful for differentiating long range ordered material from disordered material. To analyze these peaks, the maximum value between 6.5 and 10 nm^{-1} was found for each radial profile and plotted as a function of probe position in Figure 5-13(b). The maximum intensity value oscillates with a periodicity of 20 nm, which is

expected for a combination of a pure layer and a 3D interface in 10-10 Cu/Nb. The high values represent crystalline regions, while the low values represent disordered regions. It can be seen here that 3D interfaces contain significant amounts of disordered material in their interiors, while being crystalline at their edges. This matches observations from HRTEM and HRSTEM in Figure 5-10.

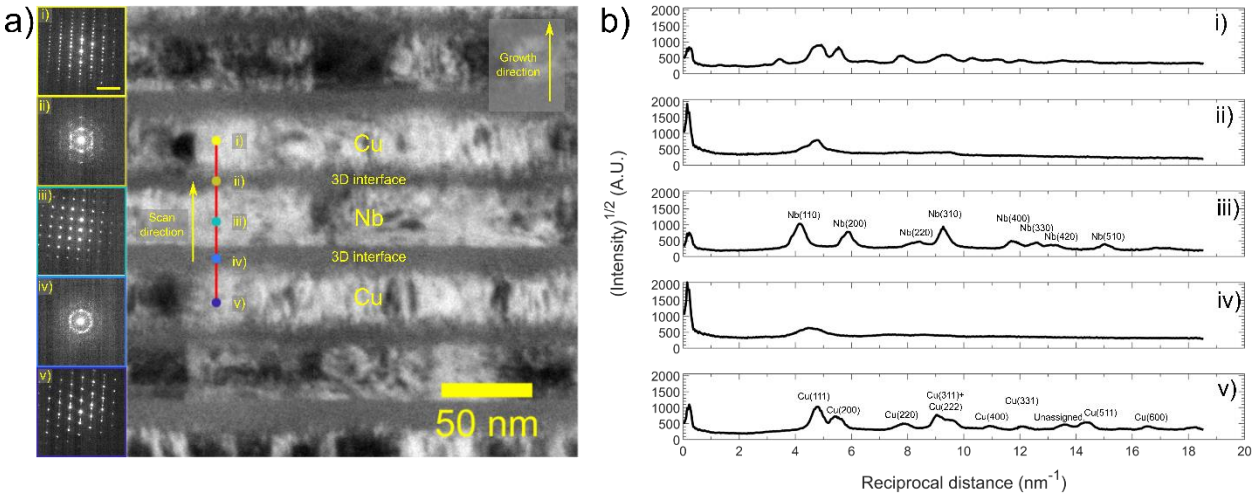

Figure 5-14 – a) A HAADF image of 10-40 Cu/Nb obtained at NBD imaging conditions. A NBD profile was taken along the red line at a step size of 0.5 nm. b) contains radial profiles of the diffraction patterns (a.i-v). Profiles (b.i,v) represent pure Nb along the BCC [111] zone axis, while profile (b.iii) represents Cu along the FCC [110] axis. The scale bar in (a.i) represents 10 nm^{-1} and is shared amongst (a.i-v).

NBD taken in the interface-normal direction in 10-40 Cu/Nb provides similar results as 10-10 Cu/Nb. A NBD profile with diffraction patterns and radial profiles can be found in Figure 5-14. Pure Nb and Cu can be distinguished by their zone axis diffraction patterns, and the 3D interfaces patterns are dominated by a diffuse ring of intensity. Note that extra twin spots are visible in Figure 5-14(a.i), producing a diffraction pattern characteristic of a region containing an incoherent Σ3 twin boundary[220]. There is streaking in the zone axis pattern in Figure 5-14(a.v) along the Cu [111] direction indicating the presence of stacking faults or a Cu-Cu grain boundary[221,222]. Radial profiles confirm that the interior of 3D interfaces (Figure 5-14(b.ii,b.iv)) in 10-40 Cu/Nb do not have significant intensity at high reciprocal spacings, meaning that they lack long range order. There is

an unassigned peak in Figure 5-14(b.v) attributed to the streaks observed in Figure 5-14(a.v). Note that the diffraction pattern for the 3D interface grown on Nb in Figure 5-14(a.ii) does not have as many high order spots as the pattern for the comparable interface in 10-10 Cu/Nb in Figure 5-12(a.ii). More quantitative information can be found in the radial profiles. Comparing Figure 5-12(b.ii) to Figure 5-14(b.ii), both profiles only have diffuse humps at 4.5 nm^{-1}, indicating that interfaces in both 10-10 and 10-40 Cu/Nb are disordered.

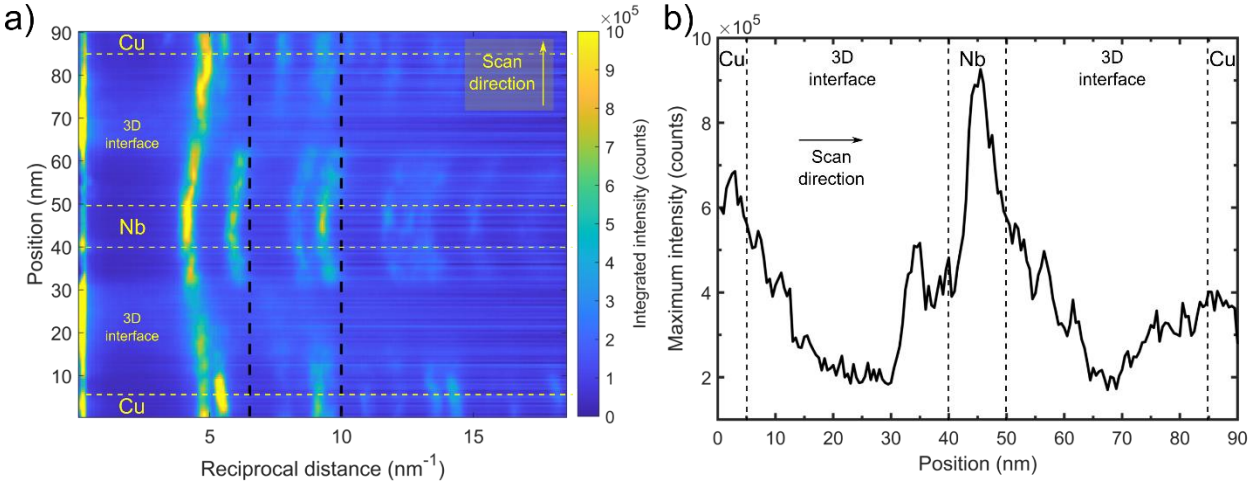

Figure 5-15 – a) Radial profiles for all spectra taken from 10-40 Cu/Nb along the profile in Figure 5-14. The peaks between the dotted black lines are used to identify material that possesses long-range order. b) shows that interiors of 3D interfaces lack long-range order, while the edges of the 3D interfaces are crystalline, which is the same as found for 10-10 Cu/Nb.

Figure 5-15 contains radial profiles for all diffraction patterns taken along the profile depicted in Figure 5-14. Figure 5-15(a) demonstrates that the interface-normal heterogeneity of 3D interface structure in 10-40 Cu/Nb is similar to that found in 10-10 Cu/Nb. The interior of 3D interfaces lack scattering at spatial frequencies above 4.5 nm^{-1}, indicating a disordered structure. The edges of 3D interfaces do have significant scattering at these higher frequencies, meaning that they are ordered at long-range. Figure 5-15(b) contains the max intensity found between 6.5 and 10 nm^{-1} for each spectrum plotted against diffraction pattern position. Similarly to 10-10 Cu/Nb,

low maximum intensity is found at the disordered interior of 3D interfaces, while higher maxima are found at the crystalline periphery of 3D interfaces. The periodicity in minimum intensity for Figure 5-15(b) is 40 nm, which is less than the expected 50 nm for one layer and one 3D interface, indicating that this specimen deposited less material than nominally expected.

5.1.4.3. Lateral heterogeneity

The lateral heterogeneity found in the disordered regions of 3D interfaces are of interest for assessing their effect on mechanical properties. Since 10-10 Cu/Nb showed possible signs of the NBD probe spreading outside the disordered region of the 3D interface, it is not suitable for this investigation. 10-40 Cu/Nb NBD results will be used to study 3D interface lateral crystallographic heterogeneity.

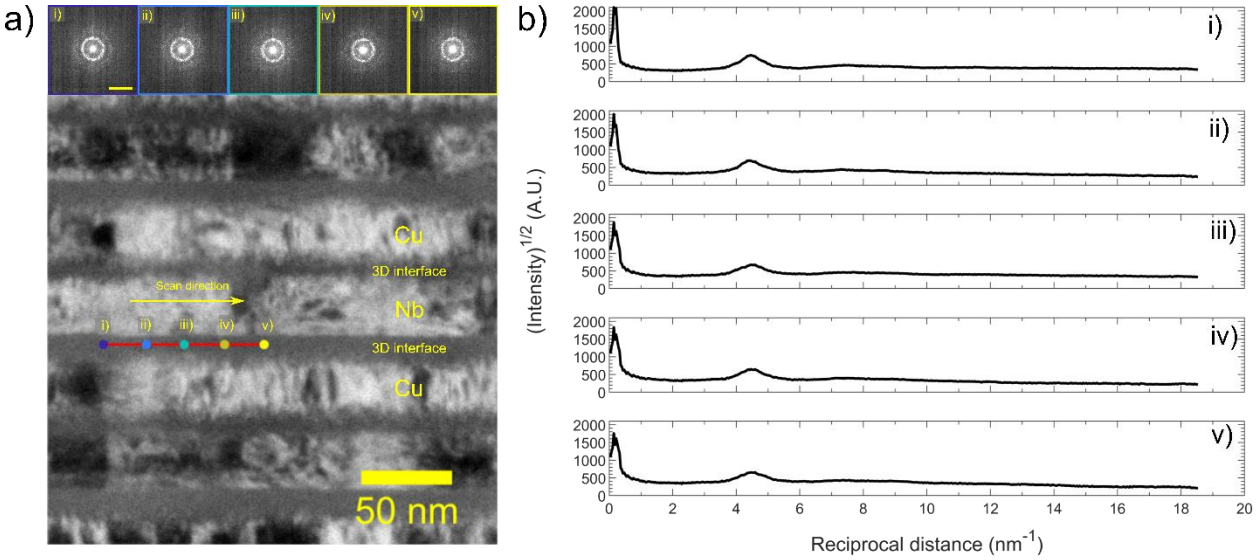

Figure 5-16 – a) A HAADF image of 10-40 Cu/Nb obtained at NBD imaging conditions. A NBD profile was taken at a 3D interface grown on Cu along the red line at a step size of 0.5 nm. b) contains radial profiles of the diffraction patterns (a.i-v). Profiles (b.i-v) are distinct from each other in terms of scattered intensity and peak shape at 4.5 nm^{-1}. The scale bar in (a.i) represents 10 nm^{-1} and is shared amongst (a.i-v).

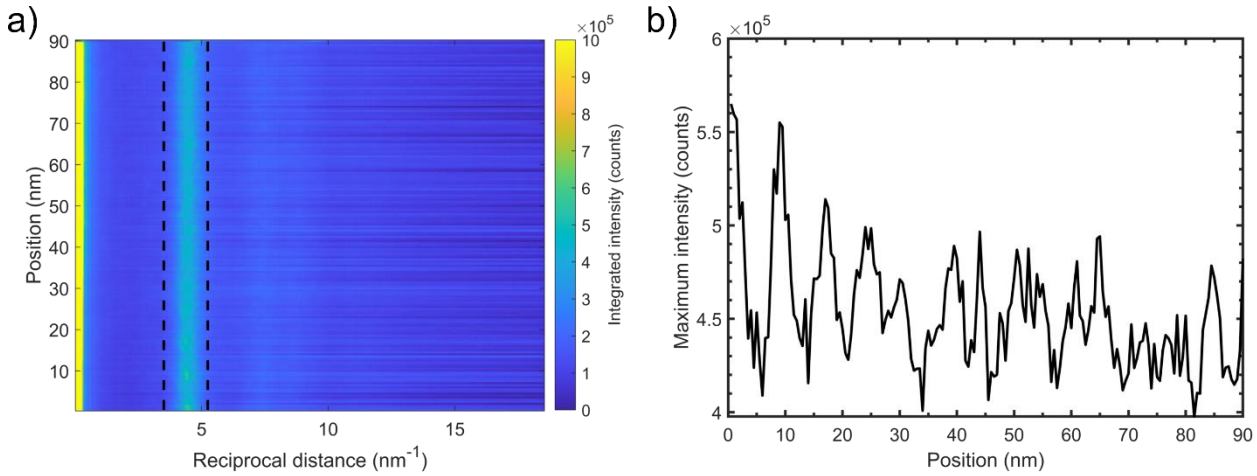

Figure 5-17 – a) Radial profiles for all spectra taken from 10-40 Cu/Nb along the lateral profile in Figure 5-16. The maximum value of peaks between the dotted black lines are used to characterize the short range order in the interface in b), showing that there are lateral heterogeneities in short range order on the length scale of 5-10 nm in this 3D interface.

A NBD profile was taken in the lateral direction for a 3D interface grown on Cu in Figure 5-16. Figure 5-16(a.i-v) shows that diffraction patterns in the lateral direction of the 3D interface appear similar, with a single prominent diffraction ring and no zone axis pattern spots. Figure 5-16(b.i-v) quantifies these diffraction patterns as radial profiles, where the diffuse hump at 4.5 nm^{-1} has different intensities and shapes for between all profiles. This indicates that there is lateral heterogeneity in the short range ordering of the 3D interface grown on Cu. This is further explored in Figure 5-17(a), where radial profiles for all diffraction patterns taken in Figure 5-16 are displayed. The maximum intensity scattered to the diffuse hump at 4.5 nm^{-1} varies as a function of position, further indicating lateral crystallographic heterogeneity. Figure 5-17(b) demonstrates the length scale associated with these heterogeneities, which is about 5-10 nm.

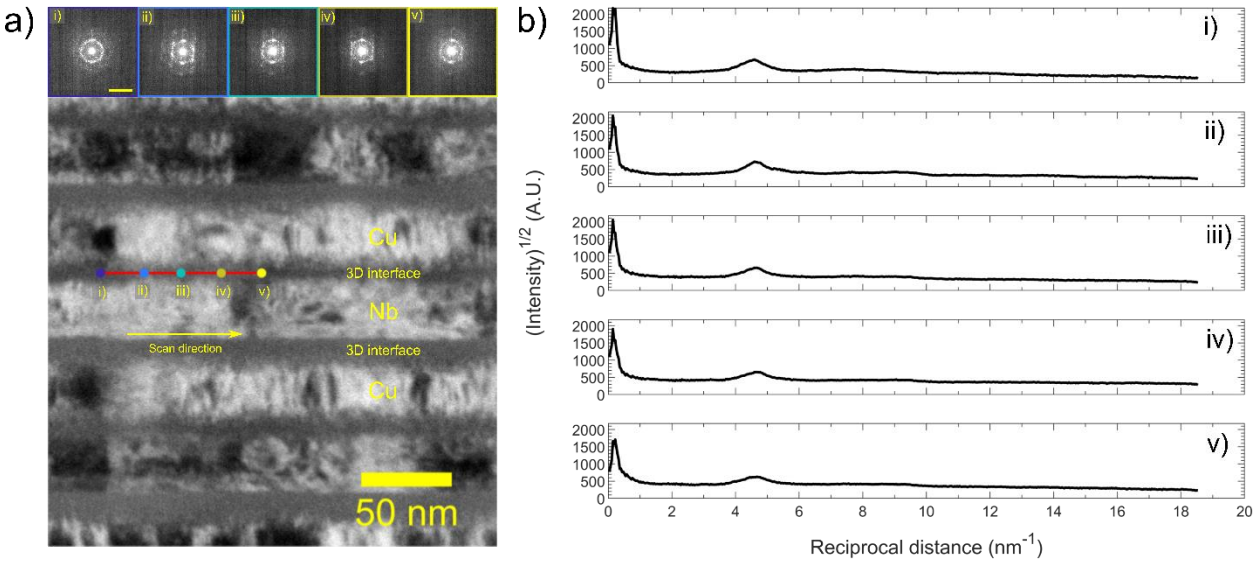

Figure 5-18 – a) A HAADF image of 10-40 Cu/Nb obtained at NBD imaging conditions. A NBD profile was taken at a 3D interface grown on Nb along the red line at a step size of 0.5 nm. b) contains radial profiles of the diffraction patterns (a.i-v). Profiles (b.i-v) are distinct from each other in terms of scattered intensity and peak shape at 4.7 nm^{-1}. The scale bar in (a.i) represents 10 nm^{-1} and is shared amongst (a.i-v).

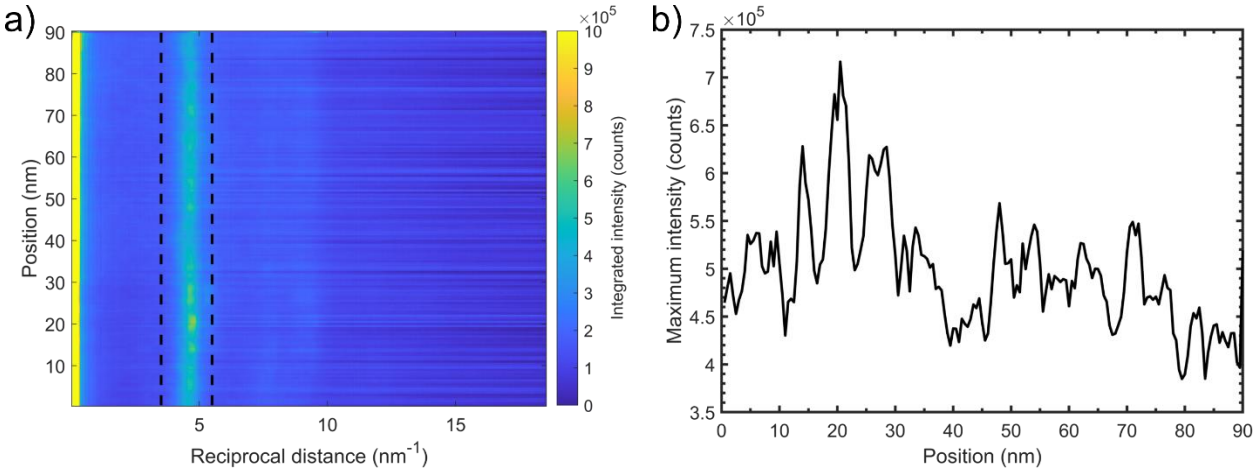

Figure 5-19 – a) Radial profiles for all spectra taken from 10-40 Cu/Nb along the lateral profile in Figure 5-18. The maximum value of peaks between the dotted black lines are used to characterize the short range order in the interface in b), showing that there are lateral heterogeneities in short range order on the length scale of 5-10 nm in this 3D interface.

The experiment in Figure 5-16 was repeated for a 3D interface grown on Nb and is presented in Figure 5-18. Figure 5-18(a.i-v) shows that diffraction patterns in the lateral direction of the 3D interface appear similar, with diffraction spots resembling those from zone axis patterns. Despite

these spots, Figure 5-18(b.i-v) shows that most diffracted intensity is scattered to the broad hump at 4.7 nm^{-1}. Figure 5-19(a) shows the radial profiles for all diffraction patterns taken in Figure 5-18. The intensity scattered to the diffuse hump at 4.7 nm^{-1} varies as a function of position, indicating lateral crystallographic heterogeneity. Figure 5-19(b) demonstrates the length scale associated with crystallographic heterogeneities, which is on the order of a few nm. Thus, 3D interfaces grown on both Cu and Nb in 10-40 Cu/Nb are crystallographically heterogeneous in the interface lateral direction on the length scale of a few nm.

5.2. Chemistry of 3D interfaces

5.2.1. STEM-EDS

5.2.1.1. 3D interface chemistry from TEM

The chemistry of 3D interfaces can be probed by STEM-EDS, the results of which are presented in Figure 5-20 for 10-10 Cu/Nb. Figure 5-20(b) shows a STEM-EDS map, demonstrating the lamellar distribution of Cu and Nb. There do not appear to be lateral chemical heterogeneities in 3D interfaces using this method. A composition profile taken perpendicular to layers to measure layer thickness is shown in Figure 5-20(c). 3D interfaces grown on Cu are distinguished from those grown on Nb since different epitaxy in these two cases could lead to microstructural differences. Layer and interface thicknesses are measured from the profile in Figure 5-20(c). First, layer thicknesses are determined by the width of the plateau regions in Figure 5-20(c). Then, the interface thicknesses are determined by the width of materials not included in pure layers. The measured thicknesses are summarized in Table 1. These results show that Cu, Nb, and 3D interface thicknesses are close to the nominal value of 10 nm.

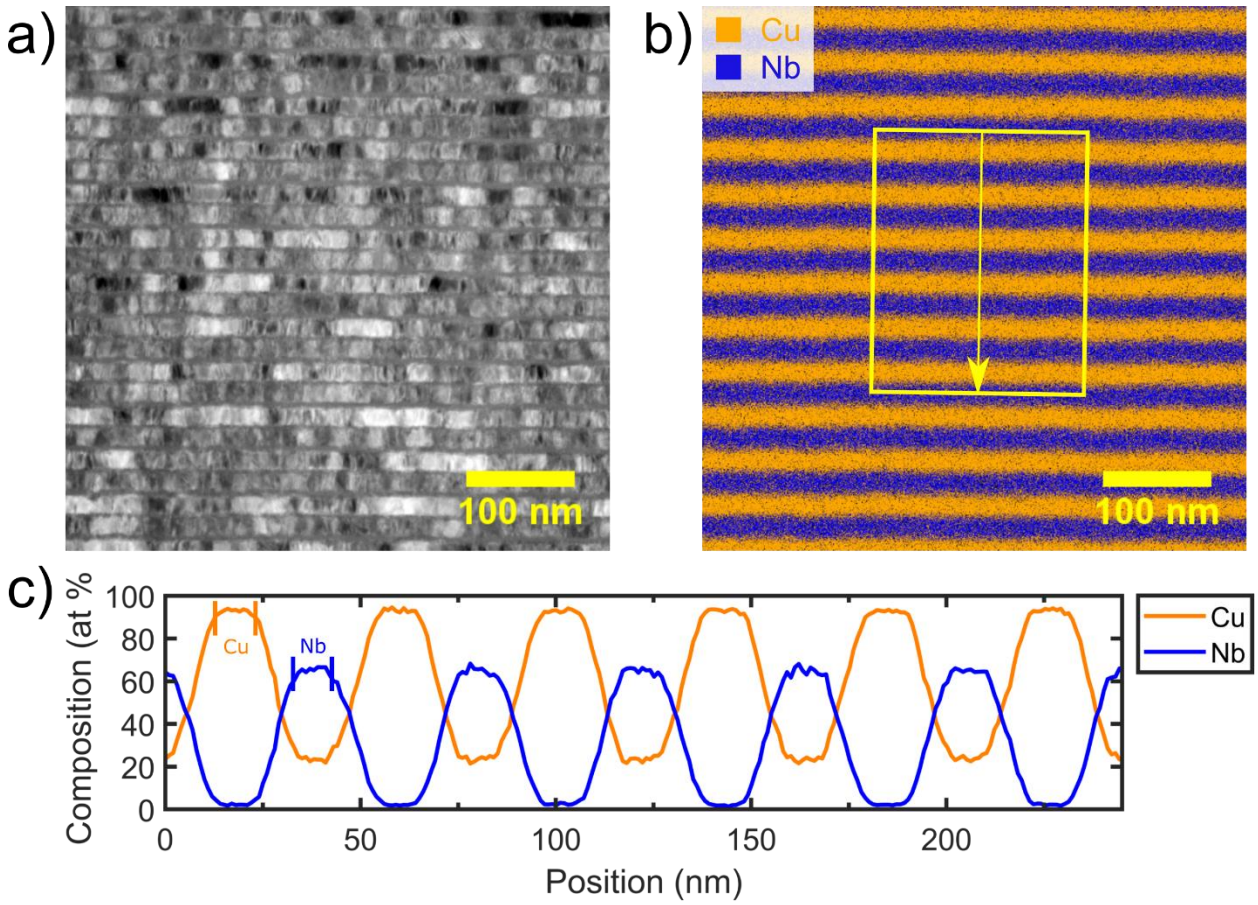

Figure 5-20 – a) HAADF-STEM image of undeformed 10-10 Cu/Nb taken at a camera length of 330 mm, giving an acceptance angle of 26-159 mrad. b) depicts a STEM-EDS map of region a) with Cu in orange and Nb in blue. c) depicts an elemental profile taken from b) along the direction of the yellow arrow and averaged along the width of the box encompassing that arrow. The layer and interface thicknesses taken from this profile are summarized in Table 1. Note that Nb layers appear impure due to the redeposition of more mobile Cu during FIB preparation of TEM specimens[223].

Table 1 – A summary of average Cu and Nb layer thickness, as well as 3D interface thickness for 10-10 Cu/Nb. *h'* was measured separately for 3D interfaces deposited on Cu and Nb layers to probe differences in growth for interfaces deposited on different layers. Sample size is 6 layers for h_{Cu} and 5 layers/interfaces for all other thicknesses.

	Average(nm)	**Std. Dev. (nm)**
$\boldsymbol{h_{Cu}}$	10.4	0.6
$\boldsymbol{h_{Nb}}$	9.6	0.4
***h*' (3D interface on Cu)**	11.0	0.5
***h*'(3D interface on Nb)**	10.8	0.3
Bilayer (h_{Cu} + h_{Nb} + 2*h*')	41.8	0.4

5.2.1.2. Thick 3D interfaces

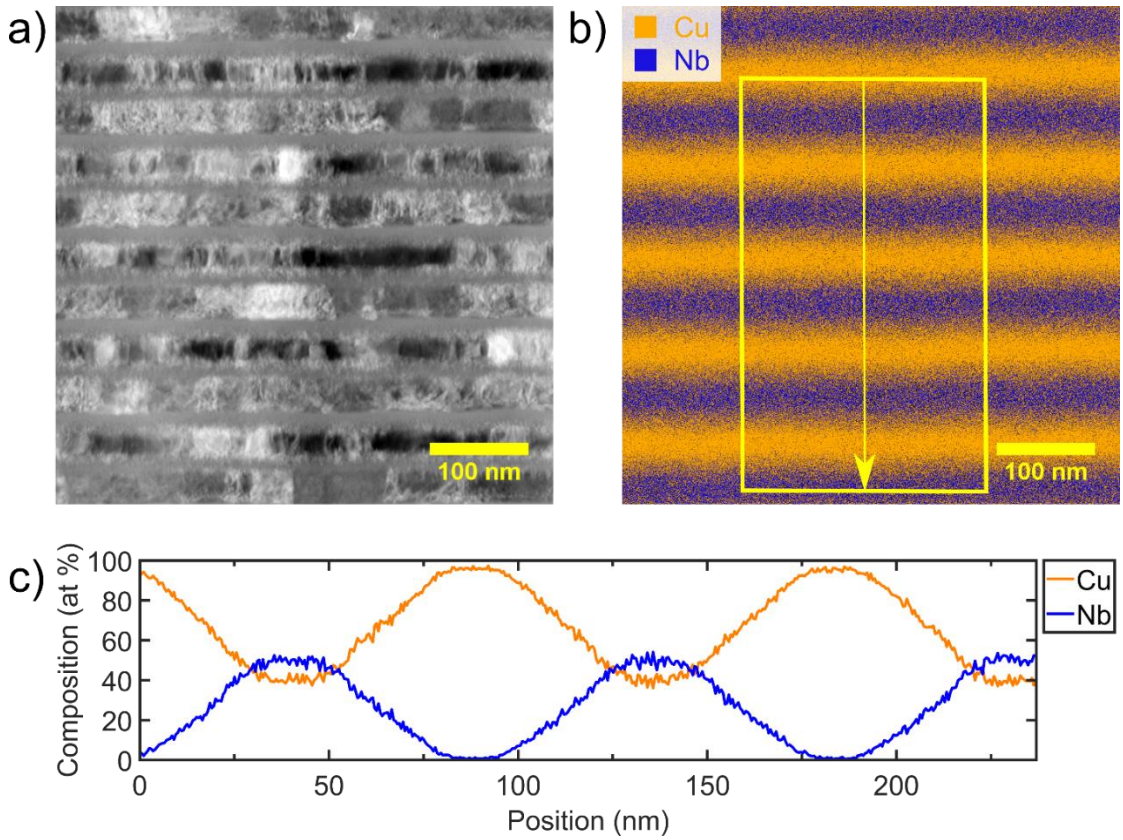

Figure 5-21 – a) HAADF-STEM image of undeformed 10-40 Cu/Nb taken at a camera length of 330 mm, giving an acceptance angle of 26-159 mrad. b) depicts a STEM-EDS map of region a) with Cu in orange and Nb in blue. c) depicts an excerpt of the elemental profile taken from b) along the direction of the yellow arrow and averaged along the width of the box encompassing that arrow. The layer and interface thicknesses taken from this profile are summarized in Table 1. FIB redeposition is more severe in this specimen as compared to 10-10 Cu/Nb characterized in Figure 5-20, as the Nb layers appear to contain 40 at. % Cu.

STEM-EDS was also completed on 10-40 Cu/Nb and is presented in Figure 5-21. Figure 5-21(a) is a HAADF image of 10-40 dominated by diffraction contrast, showing similar features as seen in CTEM in Figure 5-9. The EDS map of this region is shown in Figure 5-21(b). Again, Cu and Nb are distributed in layers as expected. The chemical profile extracted from the region indicated in Figure 5-21(b) is shown in Figure 5-21(c). This profile is used to measure layer

thickness and 3D interface thickness in the same manner as for 10-10 Cu/Nb. These results are shown in Table 2. These show that layer and interface thicknesses are less than nominal values, as the expected bilayer thickness for this material is 100 nm.

Table 2 – A summary of average Cu and Nb layer thickness, as well as 3D interface thickness for 10-40 Cu/Nb. Sample size is 4 for all thicknesses.

	Average(nm)	**Std. Dev. (nm)**
h_{Cu}	10.3	0.8
h_{Nb}	10.8	1.1
h' (3D interface on Cu)	38.7	0.9
h'(3D interface on Nb)	36.3	1.4
Bilayer ($h_{Cu} + h_{Nb} + 2h$')	96.1	2.1

5.2.2. Atom probe tomography

5.2.2.1. Interface-normal chemical heterogeneity

As mentioned in Chapter 4, APT is used to overcome the limitations of TEM, providing three dimensional chemical mapping of 3D Cu/Nb. Results were obtained for 10-10 Cu/Nb and were published elsewhere[224]. Interface-normal chemical heterogeneity is addressed in Figure 5-22. Here, chemical profiles normal to 3D interfaces are extracted from regions of interest (ROIs) from the top and bottom of the APT needle in Figure 5-22(a,d). At the top of the APT needle, Figure 5-22(b) shows a sigmoidal chemical gradient, expected for a smoothly graded interface, while Figure 5-22(c) shows a region of oscillating composition between the Cu and Nb layers centered around 50 at.% Cu and 40 at.% Nb. Similarly at the bottom of the needle, the interfacial chemical gradient in Figure 5-22(e) is sigmoidal, while the 3D interface contains a region with non-monotonic chemical gradient between the Cu and Nb layers in Figure 5-22(f). The regions with non-monotonic chemical gradients in Figure 5-22(c,f) span about 5 nm in the interface normal direction and provide signatures of chemical segregation in the interface-normal direction. This

data demonstrates that the interface-normal chemical heterogeneity for 3D interfaces is a function of lateral position in the interface.

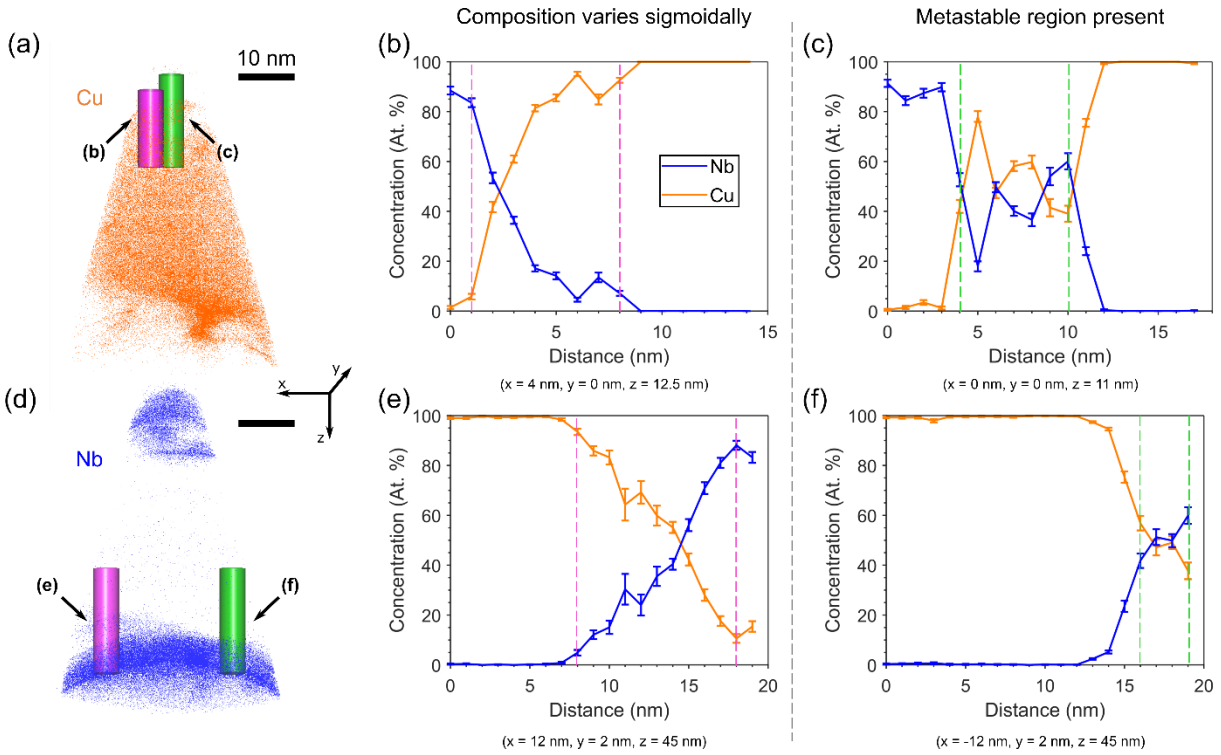

Figure 5-22 – (a) An APT Cu map on which ROIs 5 nm wide are extracted to produce chemical profiles with bin width of 1 nm shown in (b-c). ROIs are denoted by magenta and green bars embedded in the needle. These profiles are taken along the z direction starting at the top of the APT needle. Composition varies smoothly in the 3D interface at position (b). This smooth chemical gradation is indicated by magenta dotted lines. In contrast, regions with non-monotonically changing chemistry are present in the 3D interface at (c). This phenomenon is indicated by green dotted lines in (c). (d) An APT Nb map of the same sample as in (a), on which ROIs with the same parameters as (a) are extracted to produce chemical profiles shown in (e) and (f). Similarly, as seen in (b) and (c), (e) contains a smooth chemical gradient, while (f) displays a region with non-monotonic chemical gradient. Error bars for (b-c, e-f) represent one interval of standard error due to counting statistics of atoms included in the ROI[225]. Axes defining the frame of reference illustrated in (a) are the same as in (d). Scale bars in (a,d) represent 10 nm.

Statistically significant interface thickness measurements were made at the top of the needle in in Figure 5-23. 13 locations chosen in a grid pattern shown in Figure 5-23(b) were used for these measurements. For 3D interface thickness measurements, threshold values of 90 at.% Cu and 10 at.% Cu are used to define the boundaries of Cu and Nb pure layers, respectively (shown

in Figure 5-23(c)). These values correspond to a commonly used criterion in APT literature that sets diffuse interface boundaries at 90% and 10% of plateau concentrations of a given species[226,227]. The average thickness of the 3D interface at the top of the needle is 8.7 ± 0.9 nm based on 13 measurements. Thicknesses were not measured at the bottom of the needle because of missing data in a hemispherical region there due to specimen fracture during the APT experiment.

APT interface thickness measurements are slightly lower than interface thickness measurements made via STEM-EDS (10.6 ± 2.1 nm). This is to be expected, as interface waviness is averaged out using STEM-EDS and the criterion for interface boundary used in Ref. 228 was different; maximum and minimum values of Nb were used to define interface boundaries in that study. APT interface thickness measures are substantially greater than those made via HRTEM in Figure 5-10, indicating that chemical and structural methods of 3D interface characterization are distinct and represent independent and complementary information.

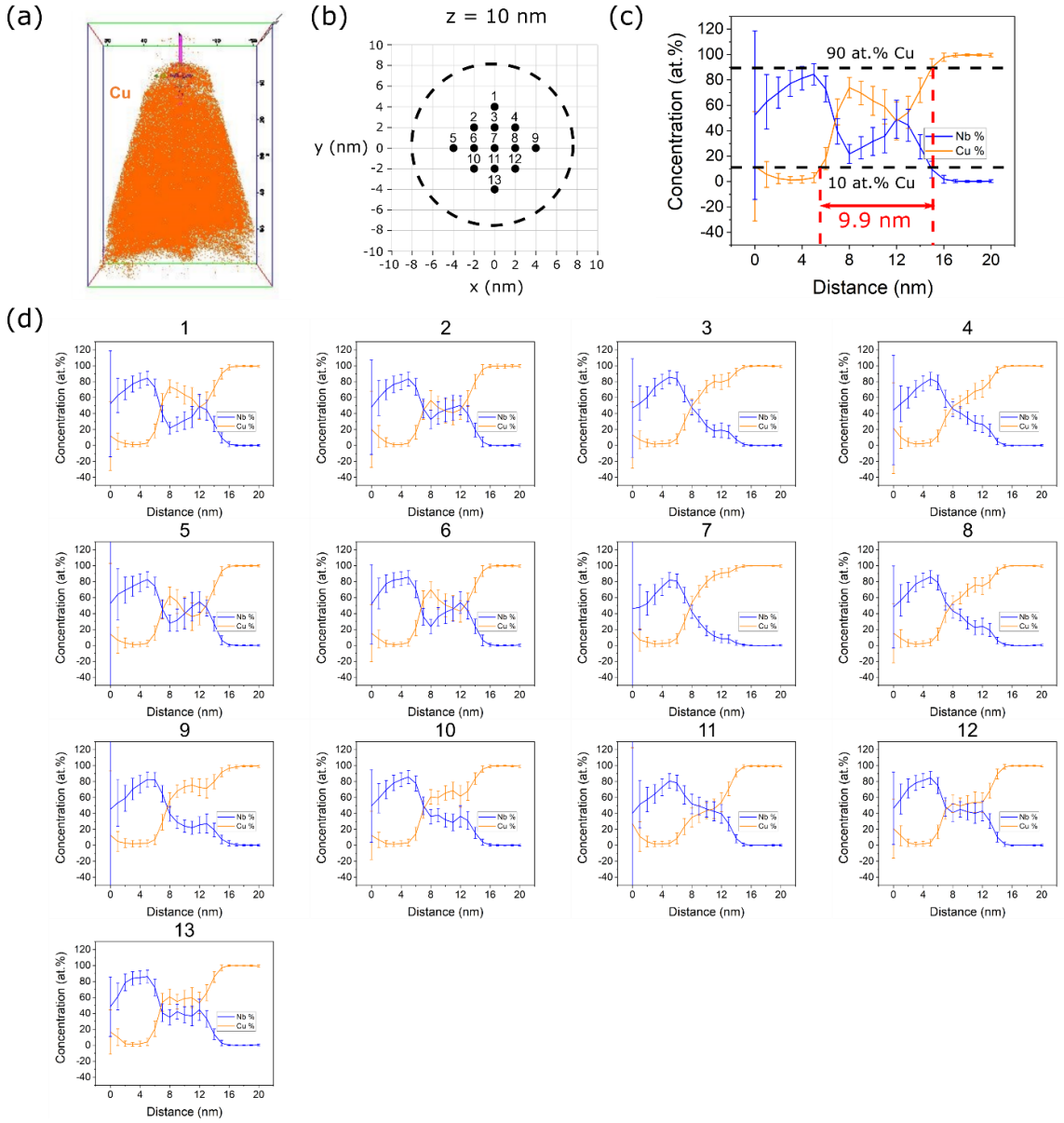

Figure 5-23 – (a) APT map demonstrating placement of an ROI to measure interface thickness, denoted by the magenta cylinder traversing the 3D interface. ROIs used for thickness measurement are oriented normal to nominal interface planes, i.e. parallel to pure layers. (b) Black dots denote the locations of cylindrical ROIs used for layer thickness measurement on the x-y section at the indicated z coordinate. The black dotted line denotes the boundaries of the needle section. (c) An example chemical profile extracted from the top 3D interface on the needle. The black dotted lines denote 90 and 10 at.% Cu, which are used to define the boundaries of the 3D interface. The red dotted lines are projected from where the Cu at.% profile intersects the black dotted lines down to the dependent axis of the profile plot. This profile gives an interface thickness of 9.9 nm, labeled in red. (d) Chemical profiles extracted from the numbered positions in (b). Lateral differences in

chemical gradient can be clearly seen from adjacent ROIs. Some regions contain Ga or O impurities, meaning that Cu and Nb concentrations do not add up to 100 at. %.

5.2.2.2. Interface-lateral chemical heterogeneity

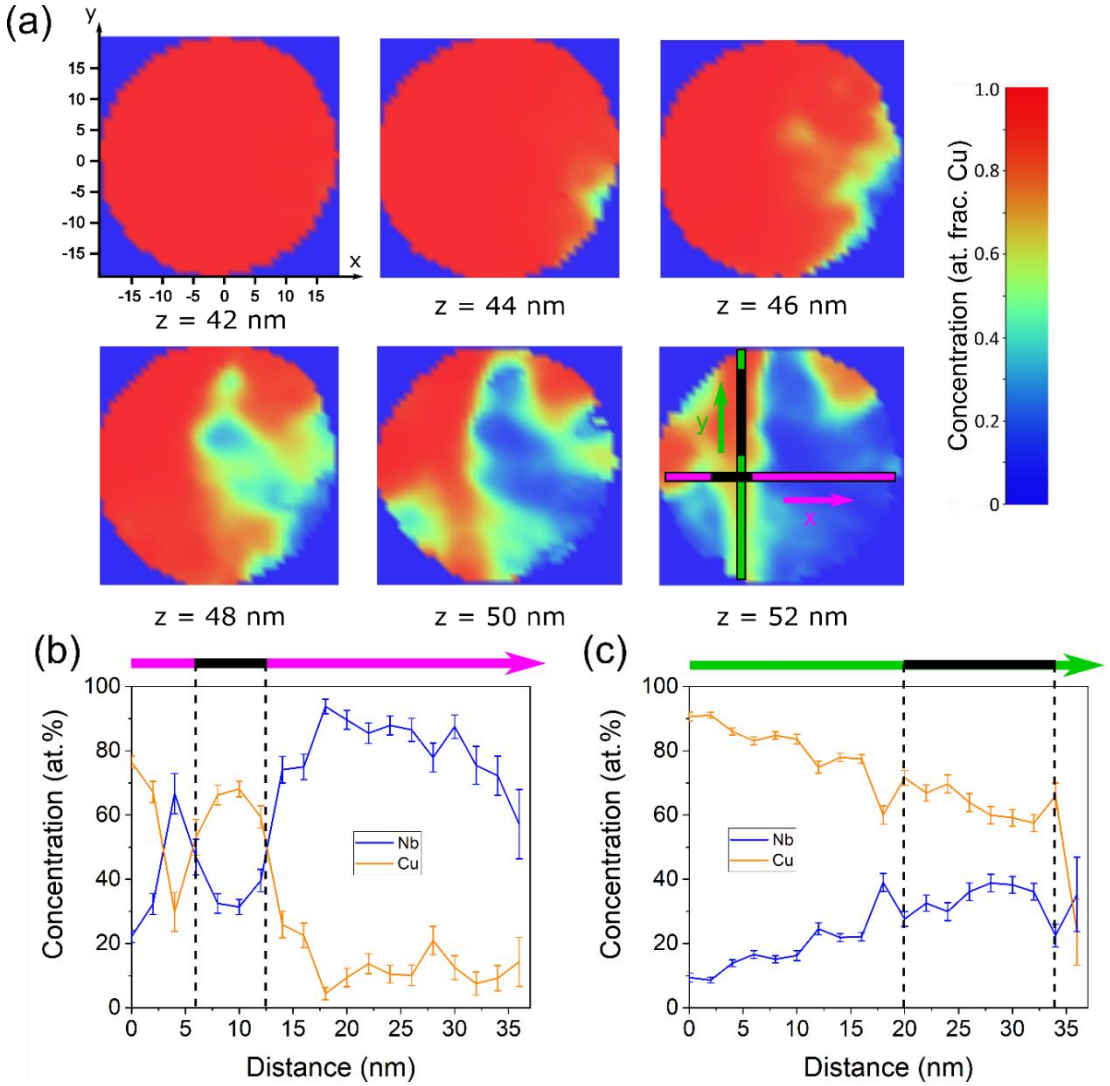

Figure 5-24 – (a) Cross-sectional chemical heat maps at z positions spanning from the middle of a pure Cu layer to the middle of a 3D interface, depicting the Cu concentration in x-y planes. Slices are 4 nm thick, except for z = 52 nm, which is 2 nm due its proximity to the limit of data at the bottom of the needle. Reference axes depicted at z = 42 nm are the same as in the rest of the slices and are in nm. Profiles are extracted from z = 52 nm with ROI width of 2 nm and bin width of 2 nm to demonstrate chemically segregated regions in the (b) x and (c) y directions. ROI width is increased and bin width is decreased relative to other ROIs in this work to ensure good sampling while keeping the ROI within the bounds of the z = 52 nm slice. The x and y profiles are aligned with the magenta and green lines in (a) at z = 52 nm, respectively. The solid black lines found in (a) at z = 52 nm, (b), and (c) indicate chemically segregated regions along respective chemical

profiles. (b) depicts a chemically segregated region that is ~7 nm wide in the x direction, while (c) depicts a chemically segregated region that is ~14 nm wide in the y direction. Error bars depict one interval of standard error.

Interface-lateral chemical heterogeneity is explored in Figure 5-24. Lateral heterogeneities are found in 3D interfaces of similar size to those observed in the interface-normal direction. In-plane chemical gradients are a function of lateral position similar to interface-normal gradients. This can be seen in x-y sections of Cu concentration maps taken at various values of z. All maps presented in this work are created using a voxel size of 1 nm x 1 nm x 1 nm and a delocalization of 3 nm x 3 nm x 3 nm. Sections depicted in Figure 5-24(a) span a region between the middle of a pure Cu layer and the middle of a 3D interface. A Cu-rich finger-like region measuring 40 nm and 10 nm in the x and y directions, respectively, is found at x = 52 nm. Chemically segregated regions are quantified in via chemical profiles in Figure 5-24(b-c) along the x and y directions. These profiles show that the length scales of lateral chemical features in the 3D interface characterized are 7 and 14 nm for the x and y directions, respectively. Local magnification may skew these values, but such artifacts skew size measurements of chemical features by a factor of 2-5 and so are accurate to well within an order of magnitude [19]. This analysis suggests that geometric features in the x-y directions in 3D interfaces are correlated to chemical heterogeneities. The same will be demonstrated for y-z and x-z directions.

5.2.2.3. Chemical landscape of 3D interfaces

The morphology of chemical heterogeneity is shown in Figure 5-25. 3D interface isoconcentration surfaces (isosurfaces) and chemical heat maps demonstrate the relationship between interface geometry and chemical heterogeneities in the y-z and x-z directions of 3D interfaces in Figure 5-25. 50 at.% Cu isosurfaces representative of interface geometry are presented from two different views in Figure 5-25(a,f). These figures show that interface curvature varies

laterally in 3D interfaces. To isolate and visualize interface geometry at specific regions of the APT needle, 2D Cu chemical concentration maps were extracted from the planes indicated in Figure 5-25(b,g) and show them in Figure 5-25(c-e,h-j). Some parts of the 3D interface are flatter than others; the top and bottom interfaces in Figure 5-25(e) are relatively flat, while in Figure 5-25(j), the top interface is diffuse in the z direction and the bottom interface contains a large excursion near x = 0 nm. Chemical profiles were extracted from these different interface types to determine if interface geometry is correlated with chemical heterogeneity. Profiles were extracted in the indicated regions in Figure 5-25(e,j) to produce Figure 5-25(e1-e6,j1-j6). The chemical profiles reveal regions with a sigmoidal-like chemical gradient typical of an interface in Figure 5-25(e1-e2,e4-e6,j3-j4) and regions that have metastable composition between the Cu and Nb layers in Figure 5-25(e3,j1-j2). Since regions with metastable compositions were found in both Figure 5-25(e) and Figure 5-25(j), 3D interfaces contain chemical heterogeneities regardless of local interface geometry. These heterogeneities may be nanoprecipitates of distinct chemical composition compared to adjacent material. The presence of these regions provides important clues regarding their mechanism of formation.

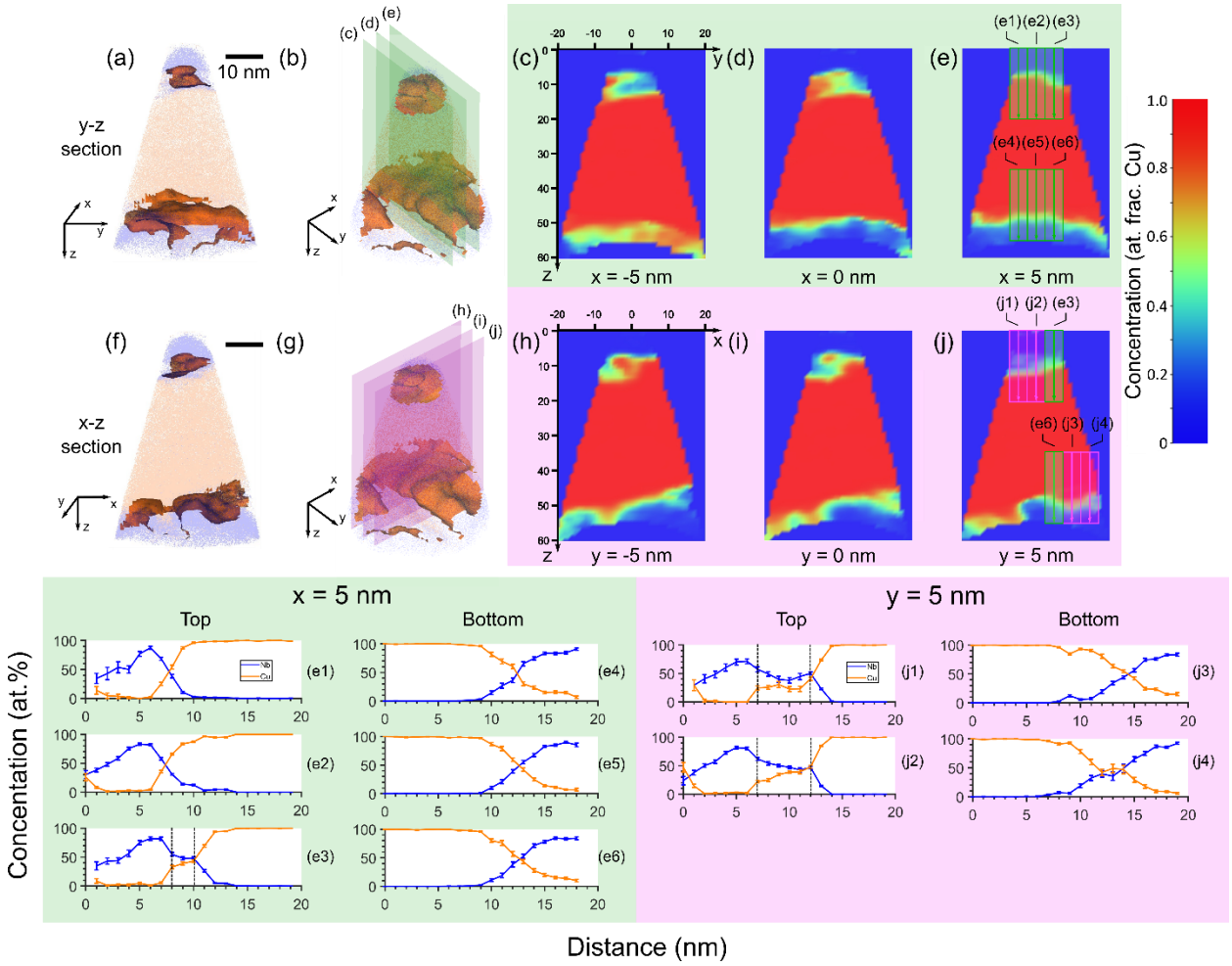

Figure 5-25 – Iso-concentration surfaces depicted in orange, taken at 50 at.% Cu when viewed parallel to the (a) x axis and (f) y axis. Surfaces are superimposed on atom maps using the same color key as in Figure 1(g) to depict their location in the needle. Cu concentration maps are presented for 5 nm-thick cross sections taken from the regions depicted in (b,g), which show the same isometric view of the 50 at.% Cu isosurfaces. These maps comprise (c-e) y-z sections and (h-j) x-z sections at the x and y axes indicated. Chemical profiles extracted from the regions indicated by boxed arrows in (e,j) are shown in (e1-e6,j1-j4). Dotted lines highlight regions with metastable compositions in (e3,j1-j2,j4). Scale bars are shared between (a-b,f-g), while reference axes are shared between (c-e,h-j). All scale bars are 10 nm, and reference axes are in nm. Legends in (e1) and (j1) are shared with the other chemical profiles. Error bars in profiles represent one interval of standard error. Note that (e) and (j) overlap partially, meaning that profiles placed at x = 5 nm in (j) would be duplicates of (e3,e6), which are also at x = 5 nm, y = 5 nm.

5.3. Discussion

5.3.1. Mechanism of heterogeneity formation

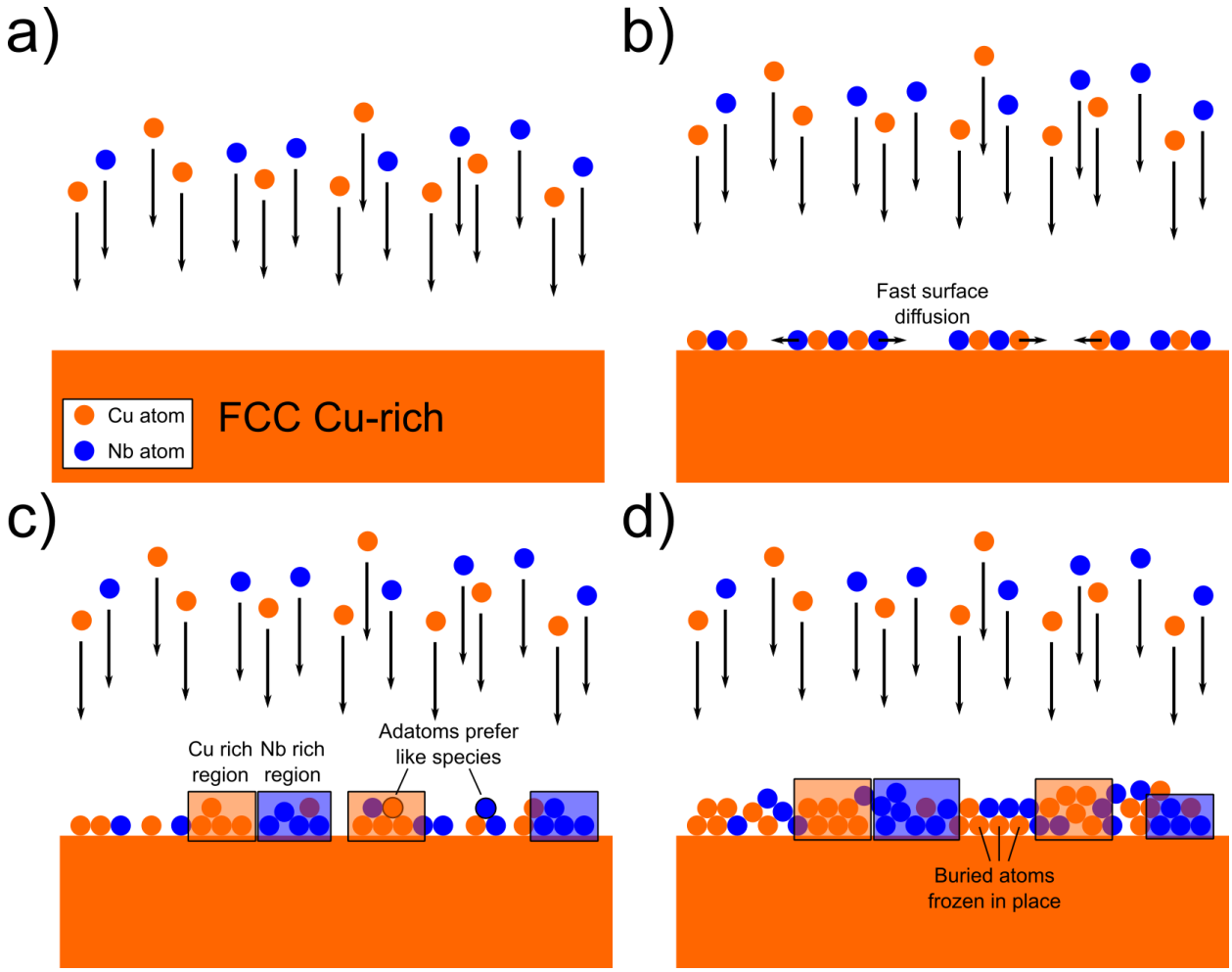

Figure 5-26 – a) depicts the PVD process on a Cu-rich FCC region in 3D Cu/Nb, representing the boundary of a 3D interface grown on Nb. The logic used here applies to 3D interfaces grown on Cu as well. b) shows the deposition of most of a monolayer on the underlying material. Surface diffusion happens rapidly at this stage of deposition. c) depicts deposition of most of a second monolayer. Thermodynamics pushes the system towards phase separation, and Cu- and Nb- rich regions form, denoted by the orange and blue-shaded regions, respectively. d) deposition of a third monolayer begins. The atoms in the first monolayer are nearly fully coordinated, and are frozen in place.

The origins of chemical and crystallographic heterogeneities in all three spatial dimensions found in 3D interfaces are discussed here. A proposed mechanism of chemical segregation is

proposed in Figure 5-26. In Figure 5-26(a), deposition onto the FCC Cu-rich region of a 3D interface grown on Cu is considered. During deposition of the first monolayer on this structure in Figure 5-26(b), surface diffusion occurs substantially. Since atoms have fewer bonds than when fully coordinated, they face low activation energy barriers to diffusion. During the deposition of a second monolayer in Figure 5-26(c), the Cu- and Nb- rich regions formed during Figure 5-26(b) provide energetic traps for adatoms of like species. This facilitates the growth of chemically segregated regions. The deposition of a third monolayer in Figure 5-26(d) constrains the atoms in the first monolayer. These atoms are now near full coordination, and are enthalpically bound to their positions. They do not diffuse further, freezing in a limited degree of chemical segregation in the 3D interface. This thought experiment provides the same conclusion for 3D interfaces grown on Nb, providing a mechanism for interface-normal and lateral heterogeneity formation.

Results from APT allow inferences about surface diffusivity during deposition. The mean surface diffusivity distance for Cu adatoms during deposition is given by[229]:

$$D_s = \frac{\lambda^2}{2t_d} \quad (1)$$

where D_s is the adatom surface diffusivity, λ is the characteristic adatom diffusion length, and t_d is the deposition time. Observed Cu-rich regions in the APT data are 10 nm wide, which is the characteristic length scale λ for diffusion. t_d is the time is allotted to an adatom to diffuse on the sample surface before being buried by an atomic monolayer. A Cu atom has 0.69 s to undergo surface diffusion before being buried by a monatomic layer of Cu at a deposition rate of 3 Å/sec. This length and time correspond to a surface diffusivity of 3.62×10^{-17} m^2/s, which is much faster than the bulk diffusivity of Cu at modestly elevated temperature (2.9×10^{-23} m^2/s at 574 K)[230]. Adatom diffusivity during PVD synthesis of 3D interfaces estimated from APT measurements can

be compared to Cu-on-Cu surface diffusivity values from literature. The surface diffusivity of Cu on (111) Cu was found via Monte Carlo simulation[231] to be 2×10^{-10} m^2/s and via field ion microscopy[232] to be 8×10^{-8} m^2/s, both at 300 K. Thus, the estimated surface diffusivity of Cu during deposition of 3D interfaces falls between the values for Cu bulk self-diffusivity and surface diffusivity of Cu on (111) Cu.

5.3.2. Possible 3D interface configurations

Understanding of the contribution of 3D interfaces to mechanical behavior requires knowledge of its atomic scale structure. It is clear from crystallographic and chemical characterization that 3D interfaces have chemical and crystallographic heterogeneities in all three spatial dimensions. The periphery of 3D interfaces adopt the crystallography of abutting pure phases. These 3D interface regions possess long range order on the length scale of the in-plane grain size of Cu and Nb layers. The interior of 3D interfaces has a more disordered structure that appears amorphous in HRTEM, semi-crystalline in NBD, and chemically segregated on the nanoscale in APT. Given these observations, there are a few possible models for the 3D interface structure. These are shown in Figure 5-27. Figure 5-27(a) shows Cu- and Nb- rich precipitates embedded in an amorphous matrix. This is supported mostly by HRTEM in Figure 5-10. Alternatively, the 3D interface could resemble a spinodally phase-separated region with very fine-scale features shown in Figure 5-27(b). This is most strongly supported by APT results in Figure 5-22Figure 5-25. Lastly, the 3D interface could be made up of interpenetrating “fingers” of Cu- and Nb- regions as shown in Figure 5-27(c). This is suggested by the crystalline protrusions seen in HRSTEM in Figure 5-10. In all cases, heterogeneities must be on the order of a few nm or below to produce the atomically disordered structure seen in TEM. The fine length scale of the characterization required to clarify the atom-scale structure of 3D interfaces eludes the limits of

modern characterization techniques, and may be prohibited by physical laws governing accuracy and resolution of materials characterization. Future work should include molecular dynamics and Monte Carlo simulation of 3D interface deposition to elucidate the probable structures comprising 3D interface with atomic fidelity.

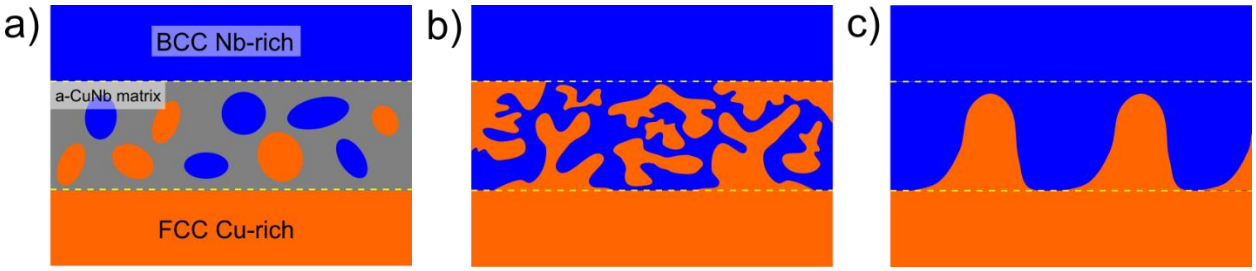

Figure 5-27 – Schematics of 3D interface structure consisting of a) precipitates embedded in an amorphous matrix, b) finely spinodally decomposed material, or c) interpenetrating protrusions of Cu- and Nb-rich material.

6. Influence of 3D interfaces on mechanical behavior

6.1. Introduction of 3D interfaces in multilayered Cu/Nb

6.1.1. Mechanical behavior of 40-10 Cu/Nb

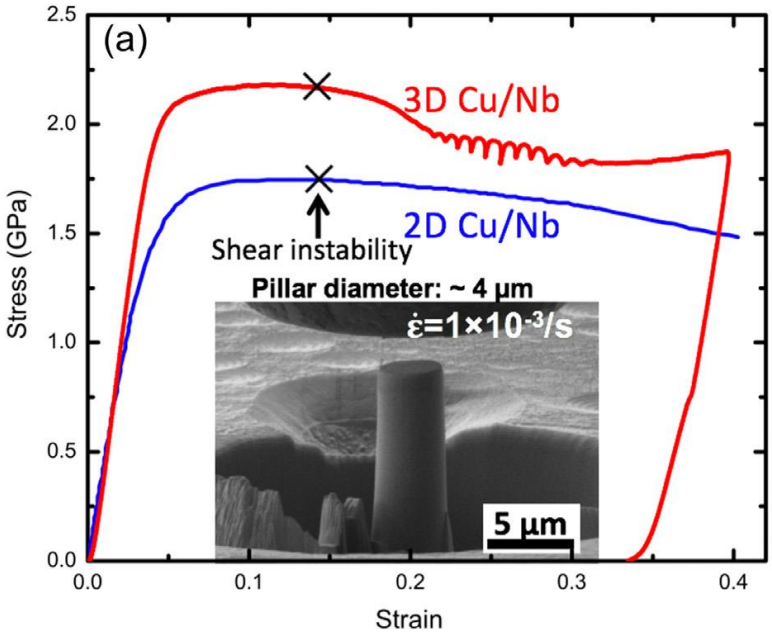

Figure 6-1 – A comparison of micropillar stress-strain behavior between 40-10 Cu/Nb and h = 40 nm 2D Cu/Nb.

Comparison of stress-strain behavior in Cu/Nb with 2D and 3D interfaces reveals the impact of 3D interfaces on plastic deformation. This was done for h = 40 nm in previous work and will be recapitulated here[233]. Figure 6-1 shows micropillar compression results for 40-10 Cu/Nb and h = 40 nm 2D Cu/Nb. Strains are engineering, while stress was corrected using a pillar taper model described in the Appendix. 40-10 Cu/Nb was compressed *in situ* in a SEM and h = 40 nm 2D Cu/Nb was compressed *ex situ* in a nanoindentation system[16]. The 3D Cu/Nb attains an ultimate compressive stress of 2.20 GPa, while the 2D Cu/Nb has a maximum compressive stress of 1.75 GPa. The strain at which shear instability is observed is marked for 40-10 Cu/Nb, while it is inferred by a maximum in stress for h = 40 nm. The strain at onset for shear instability is 0.14 for

both materials. The uniform plastic strain prior to shear localization will be referred to as deformability. This quantity is analogous to ductility in tensile tests for materials exhibiting symmetric tension/compression behavior, as is common in metallic materials. Note that the oscillations in load after shear localization for 40-10 data arise from instabilities in the control loop of the *in situ* test platform used. This data indicates that addition of a 3D interface with h' = 10 nm at h = 40 nm enhances strength without sacrificing deformability, revealing a new strategy to overcome the strength-ductility tradeoff.

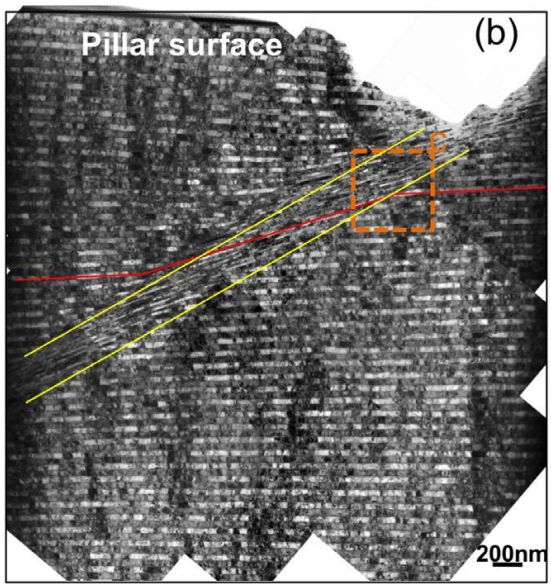

Figure 6-2 – Cross-sectional TEM of a deformed 40-10 Cu/Nb pillar. A shear band is found in between the yellow lines. A deformed layer is traced by the red line.

TEM characterization 40-10 Cu/Nb after micropillar compression reveals that deformability is limited by shear banding, just as it is in 2D Cu/Nb. Figure 6-2 presents cross-sectional TEM of 40-10 Cu/Nb, demonstrating that strain concentrates in a thin region comprising a shear band at advanced stages of plastic deformation. This indicates that at the length scale combination of h = 40 nm and h' = 10 nm, part of the material preferentially strain softens to form

a shear band. The microstructural causes of shear banding will be discussed in the context of 3D interfaces in Section 6.6.1.2.

6.2. Layer size effects in 3D Cu/Nb

As discussed in Chapter 2, the propensity for a material to shear localize is strongly tied to grain size in conventional alloys. Thus, layer thickness should have an outsize impact on shear banding and deformability in Cu/Nb. To this end, *h* was decreased from 40 to 10 nm with constant *h´* and the effect on shear banding during micropillar compression was reported in the journal *Nano Letters*[146] as part of this thesis.

6.2.1. Methodology

Micropillars and TEM-transparent lamella were fabricated in a FEI Helios NanoLab G4 FIB/SEM. Pillar dimensions were nominally 3 microns in diameter and 6 microns in height to achieve an aspect ratio of 2. Compression of pillars was conducted using a Bruker Hysitron PI 88 in-situ picoindenter in the aforementioned FIB/SEM. These tests were carried out in displacement control at an engineering strain rate of 10^{-4}/s. Conventional TEM, STEM, and HRTEM were conducted in a FEI Titan and a Thermo Fisher Talos FX200.

6.2.2. In-situ micropillar compression of 10-10 Cu/Nb

10-10 Cu/Nb was deformed using *in situ* micropillar compression. Stress-strain curves from three pillars are presented in Figure 6-3. Strains are engineering and stresses are calculated using a pillar taper model that accounts for changing instantaneous cross-sectional area during plastic deformation (See Appendix). Here, the pillar is modeled as a frustum which yields starting from the top of the pillar, which widens during plastic deformation. Regions of successively larger cross sectional area start yielding as material above widens to match their cross-sectional area. This model is used until the tapered pillar deforms into a right cylinder. Then, the cross-sectional

area at this point is used to calculate engineering stress for higher strains. Extent of deformation is approximated as engineering strain, with the gage length of each pillar determined by comparing video frames from *in situ* compression footage at the beginning and end of testing. The bottom of the gage length is defined by the bottom-most point on the pillar that exhibits a measurable change in width during testing. This can be determined by overlaying *in situ* snapshots as depicted in Figure 6-4.

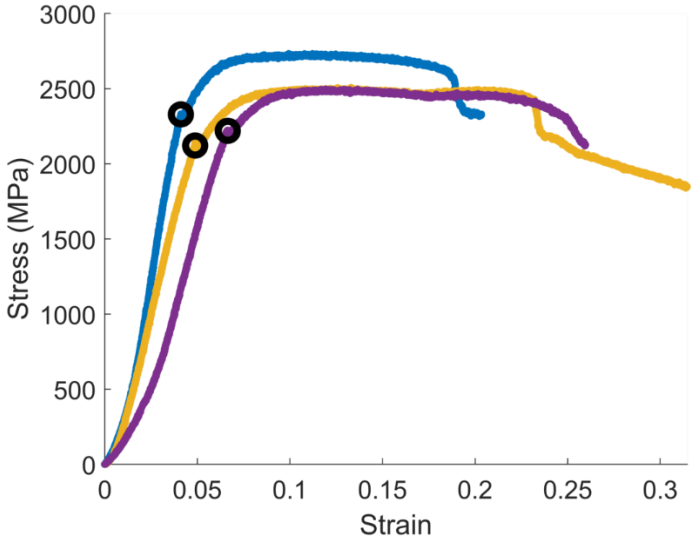

Figure 6-3 – Stress strain curves of three 10-10 Cu/Nb micropillars. The yield point on each curve is denoted with an open black circle.

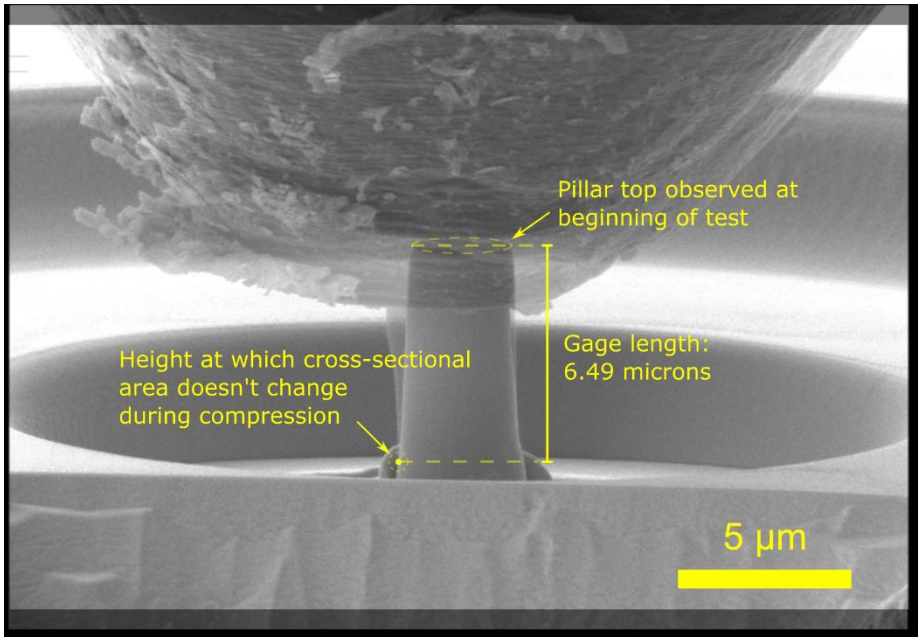

Figure 6-4 – Determination of gage length in micropillar compression experiments. Snapshots from in-situ footage are superimposed from the beginning of the test and right before catastrophic shear localization to determine the topmost position on the pillar at which cross-sectional area remains constant – this is the bottom of the gage length.

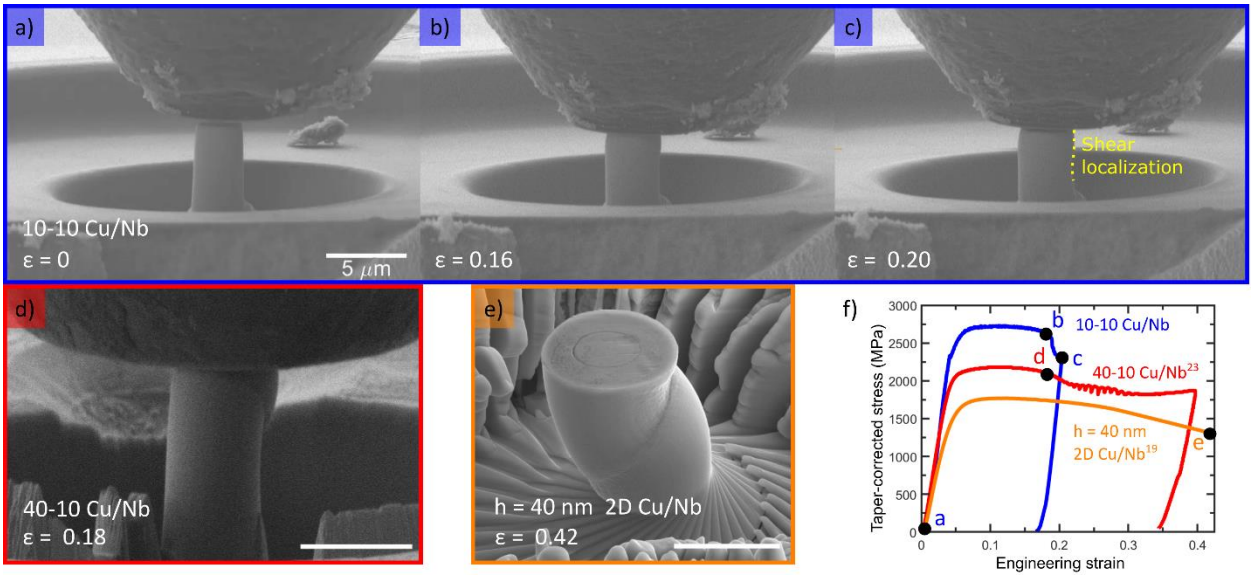

Figure 6-5 – Snapshots of the compressed 10-10 Cu/Nb micropillar: a) before compression, b) during homogeneous deformation, and c) after shear localization. d) A snapshot of 40-10 Cu/Nb at a comparable strain to b). e) A micrograph of h = 40 nm 2D Cu/Nb after *ex situ* compression. d) and f) show that 40-10 Cu/Nb shear localizes prior to the strains indicated in b) and d). Stresses are corrected for taper in all cases. Strains presented are engineering. All scale bars represent equal lengths.

Yield point is defined as where the stress-strain curve deviates in value by 5% from a line fit to the linear portion of the initial elastic loading portion of the curve. All curves are similar, demonstrating the repeatability of the results. Yield stress for the 10-10 Cu/Nb pillars is 2100±100 MPa via deviation from linearity, and ultimate compressive stress is 2500±70 MPa. Limits of linearity were determined visually from stress-strain plots. Engineering plastic strain to shear instability is 16±2%, which correlates with a gross shape change in the pillar and a significant stress drop. Application of higher stress in load control would lead to runaway deformation of the pillar. Use of displacement control in this work allows for controllable termination of the compression test after shear instability, within the constraints of the speed of the control loop. 10-10 Cu/Nb work hardens enough to resist plastic instability until 16% plastic strain, suggesting that it resists deformability-limiting shear localization for more strain than 40-10 Cu/Nb. Thus, 3D interfaces cause a departure from Hall-Petch behavior as described in Chapters 3-4. The deformability of 10-10 Cu/Nb is further explored and compared to other nanolaminates in Figure 6-5.

In situ video demonstrates that 10-10 Cu/Nb deforms homogeneously to higher stress and strain than 40-10. The in-situ video of pillar compression of the 10-10 and 40-10 3D Cu/Nb nanolaminates reveals that uniform deformation ends with the formation of a shear band. Figure 6-5(a-b) shows that 10-10 Cu/Nb can be strained to 0.16 total strain without gross shape change. Further straining to 0.20 total strain causes a gross shape change in 10-10 Cu/Nb, as seen in Figure 6-5(c). In contrast, straining to 0.18 total strain in 40-10 Cu/Nb causes not only shear localization, but rupture of the pillar in Figure 6-5(d). *In situ* video is not available for h = 40 nm 2D Cu/Nb, but *post mortem* SEM of a deformed pillar demonstrates severe shear localization in Figure

6-5(e)[16]. Stress-strain curves for all nanolaminates discussed are found in Figure 6-5(f), showing that 10-10 Cu/Nb has the highest flow stress of all nanolaminates discussed.

6.2.3. Pillar deflection in 40-10 and 10-10 Cu/Nb

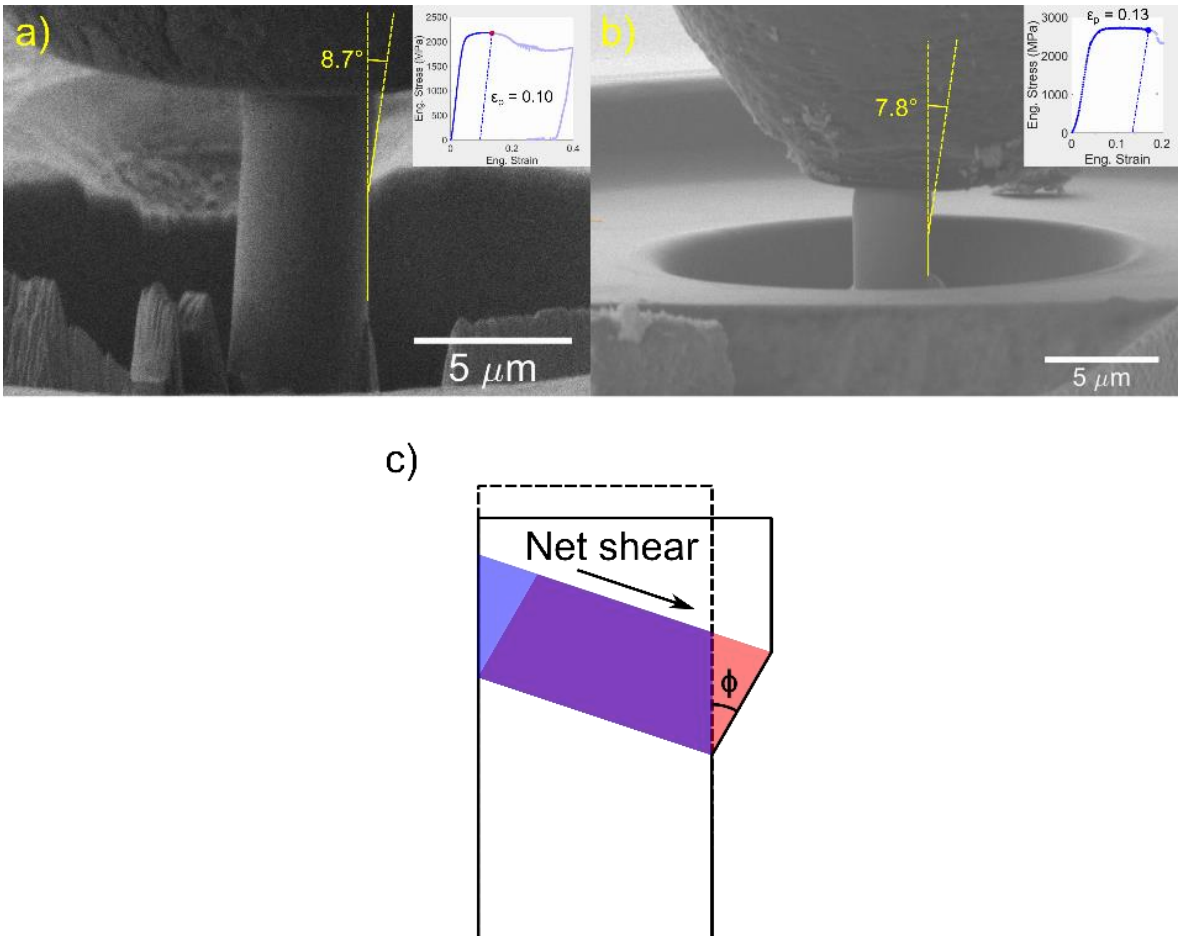

Figure 6-6 – Micropillar compression snapshots for a) 40-10 Cu/Nb at ε_p = 0.10 and b) 10-10 Cu/Nb at ε_p = 0.13, with deflection of the pillar indicated in degrees for each specimen. The pillar deflection is proportional to net shear in the shear band as shown in c), where blue shading denotes a gage section of undeformed material that deforms to the area shaded in red after pillar compression. The initial pillar geometry is denoted by black dotted lines, while the final geometry is denoted by solid black lines. The top left corner of the pillar does not shear due to friction from contact with the flat punch.

Differences in deformability between 10-10 and 40-10 can also be explored by measuring pillar deflection at comparable plastic strain. Figure 6-6(a-b) shows that 40-10 Cu/Nb deflects by 8.7° at a plastic strain of 0.10, while 10-10 Cu/Nb deflects by 7.8° at a plastic strain of 0.13. The deflection of the pillar is proportional to shear strain in the shear band of the material as shown by

Figure 6-6(c). Figure 6-6(c) shows that a standard rectangular gage section commonly used for simple shear cannot be applied, but if it could be used, then:

$$\gamma = \tan\frac{\phi}{2} \tag{6-1}$$

where γ is the shear strain and ϕ is the deflection angle. Assuming that the direction of maximum shear is the same for the 40-10 and 10-10 pillars, then Figure 6-6 shows that 10-10 Cu/Nb develops less shear strain in its shear band than 40-10 Cu/Nb at a greater global normal strain. In other words, shear banding is more severe in 40-10 Cu/Nb than it is for 10-10 Cu/Nb. Although the data here do not show that the direction of maximum shear is the same between the two pillars, the conclusions here are confirmed and supported by analysis of *post mortem* TEM.

6.2.4. Qualitative comparison of shear localization of 40-10 and 10-10 Cu/Nb

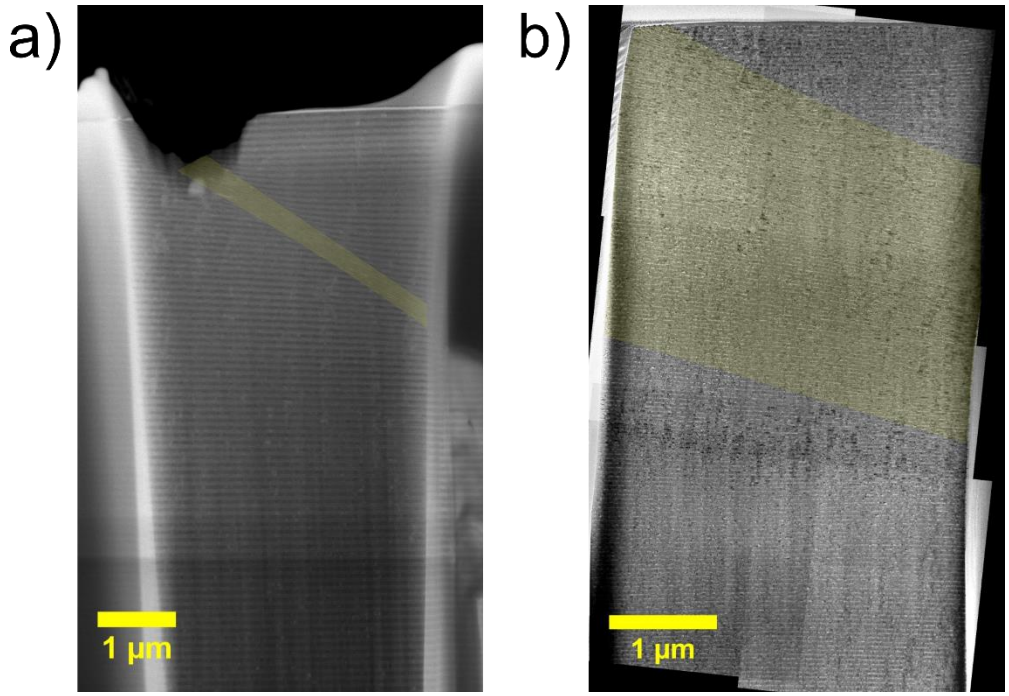

Figure 6-7 – TEM micrographs of highly deformed pillars in a) 40-10 Cu/Nb at 0.14 strain (HAADF-STEM) and b) 10-10 Cu/Nb at 0.16 strain (composite CTEM). Regions that have shear banded are shaded in yellow.

Figure 6-7 presents a qualitative comparison of shear banding in 40-10 and 10-10 Cu/Nb. Figure 6-7(a) shows that the shear band that develops in 40-10 Cu/Nb has a small width compared to the height of the pillar. After formation of the shear band, strain concentrates in a highly localized region, giving rise to a high strain gradient. In contrast, Figure 6-7(b) shows that the shear band in 10-10 Cu/Nb takes up a large portion of the pillar height. Layer rotation and thinning change gradually over the gage length of the pillar, constituting a low strain gradient. Strain in the shear band here is highly delocalized. This signifies that 10-10 Cu/Nb deforms more uniformly than 40-10 Cu/Nb. For reference, completely uniform deformation is synonymous with strain being distributed evenly over the entire pillar gage length; strain gradient is zero in this case. In the next

section, shear localization severity will be quantified through more detailed analysis of *post mortem* TEM.

6.3. Quantifying severity of plastic instability in Cu/Nb

Quantification of deformed 10-10 Cu/Nb microstructure and analysis of loading orientation on deformation of 10-10 Cu/Nb were reported in *Acta Materialia*[234] as part of this thesis. Sections 6.3-6.4 comprise content adapted from the *Acta Materialia* article. In this Section, quantification of shear localization severity is completed using CTEM and STEM. Layer-normal strain and strain gradient are found to correlate best to shear localization severity.

6.3.1. Methodology

Micropillars were made using a FEI Helios FIB/SEM by milling annular regions of decreasing inner and outer radius at an accelerating voltage of 30 keV and currents ranging from 65 nA down to 90 pA. Pillar dimensions were nominally 3 microns in diameter and 6 microns in height to achieve an aspect ratio of 2. Micropillar compression was performed *in situ* using a Bruker Hysitron PI 88 in a FEI Quanta 200 3D FIB/SEM. Pillars were compressed at an initial strain rate of 10^{-3}/s. Deformed pillars were then cut into electron transparent lamellae in the FEI Helios FIB/SEM, and characterized via conventional TEM (CTEM), high-resolution TEM (HRTEM), high angle annular dark field scanning TEM (HAADF-STEM) and scanning TEM energy dispersive spectroscopy (STEM-EDS) in a Thermo Fisher Talos F200X at 200 keV.

6.3.2. Layer and lattice rotation in 10-10 Cu/Nb

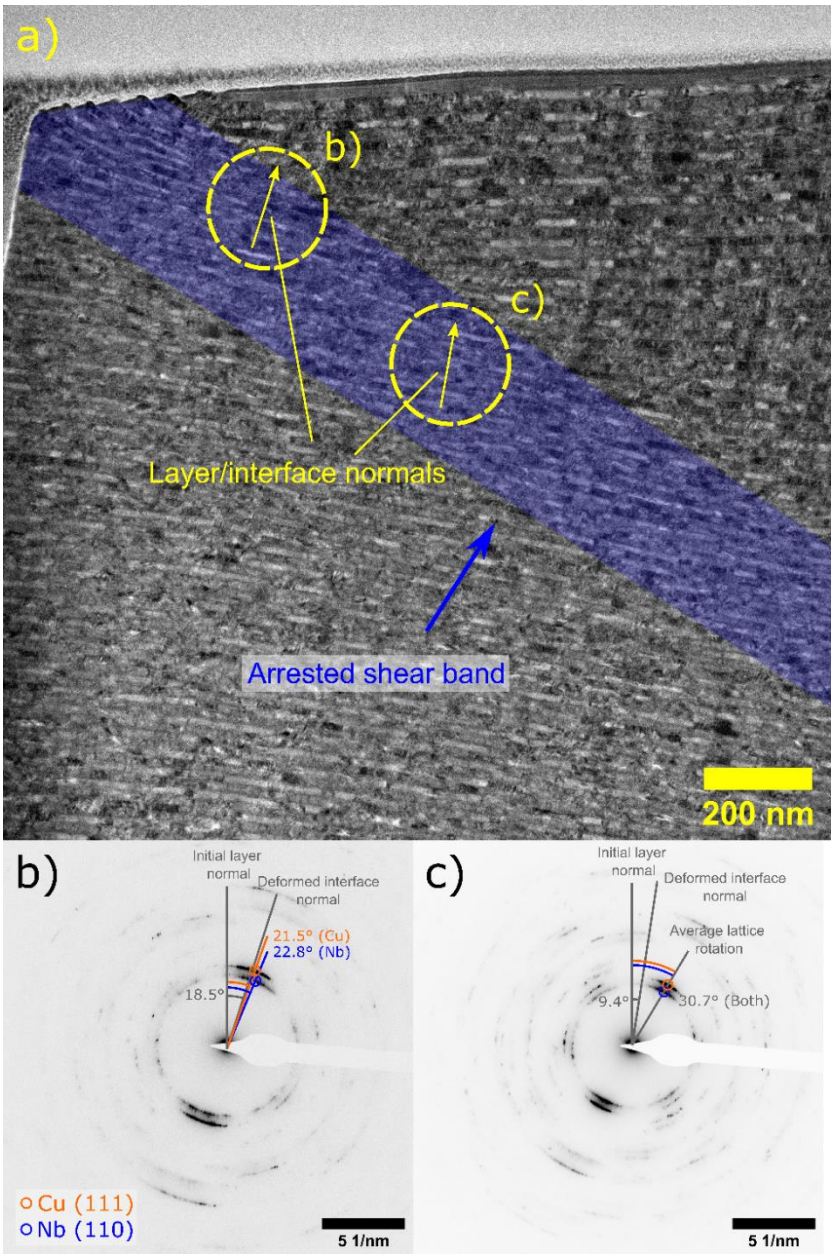

Figure 6-8 – a) A CTEM micrograph that depicts an arrested shear band that forms in the top of a pillar in 10-10 Cu/Nb compressed to 0.16 engineering strain. Layer rotation is observed for many layers under the shear band. (b-c) Selected area diffraction (SAD) patterns taken from circles indicated in a). Layer-normal directions are indicated with a yellow arrow in a), which are the same as in (b-c) since CTEM micrographs are aligned with SAD patterns. The maximum extent of lattice rotation is indicated by blue and orange angle markings in (b-c). The centers of diffraction streaks representing compact Cu(111) and Nb(110) planes which were initially oriented parallel to layers are indicated by orange and blue circles in (b-c).

The deformed microstructure of 10-10 Cu/Nb is analyzed using CTEM and selected area diffraction (SAD) patterns in Figure 6-8. Figure 6-8(a) depicts the top of the pillar, with an arrested shear band emanating from the top left corner of the pillar. Figure 6-8(a) presents regions from which the SAD diffraction patterns in Figure 6-8(b-c) were taken. Lattice and interface rotation are measured along with layer thinning, as these quantities are associated with the shear band formation process in nanolaminates[16,233]. Diffraction patterns near the origin of the shear band show that grains rotate by an average of about 22°, while inside the shear band the grains rotate by 31°. This lattice rotation is indicative of uneven slip system activation leading to a net shear in the direction of the shear band propagation direction. However, it cannot be trivially correlated to the severity of the shear instability, necessitating the use of other microstructural metrics for shear band analysis.

6.3.3. Measuring strain gradient in 10-10 Cu/Nb

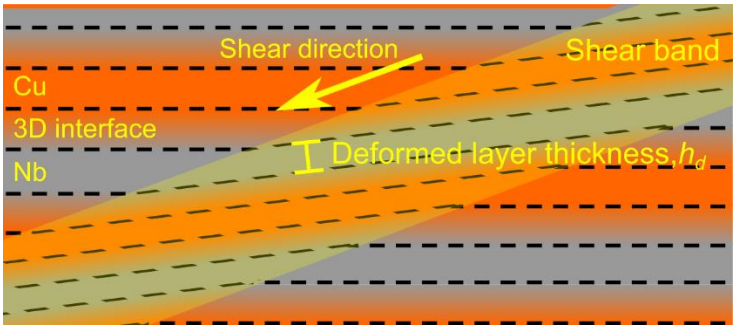

Figure 6-9 – A depiction of layer thinning during shear banding. The shear band is depicted by yellow shading.

Layer normal strain can be used to quantify shear localization severity. The utility of this quantity is illustrated by Figure 6-9. Here, a shear band is shown to traverse a nanolaminate. It is trivial to show that with increasing shear strain along the shear band, the deformed layer thickness h_d decreases. The decrease in layer thickness must be normalized as a layer-normal strain ε_{layer} defined by:

$$\varepsilon_{layer} = \frac{h_o - h_d}{h_o} \tag{6-2}$$

where h_d is the deformed layer thickness measured normal to the rotated interface and h_o is the undeformed layer thickness[16,233].

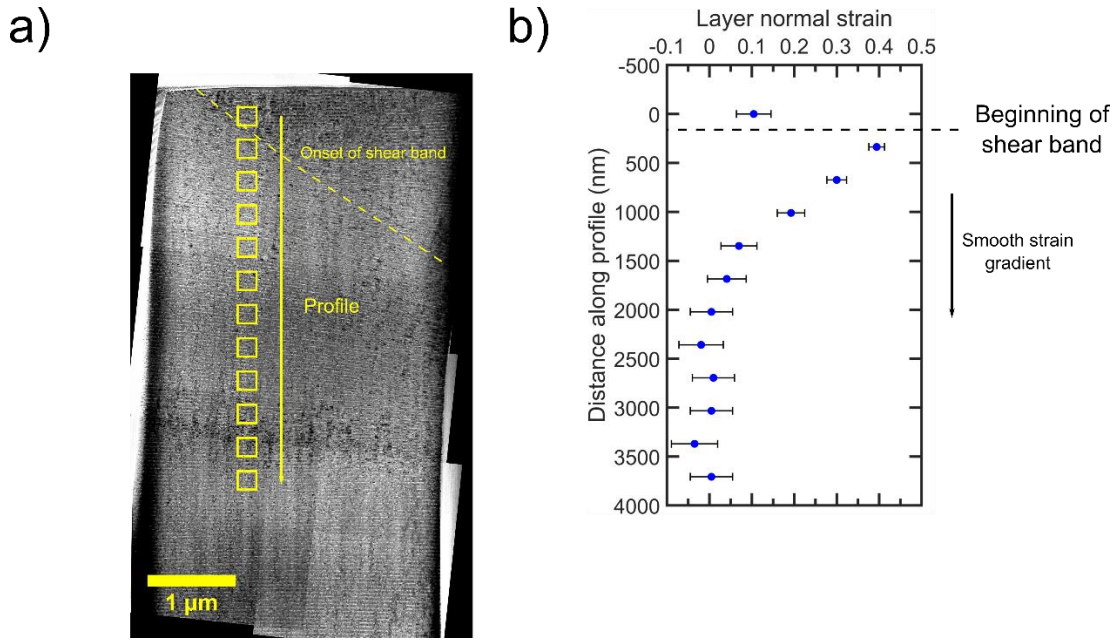

Figure 6-10 – a) Composite CTEM image of 10-10 Cu/Nb strained to 0.16 depicting a profile along which bilayer thickness measurements were taken. These thicknesses were used to calculate layer normal strain, which are presented in b) as a function of position along the profile. b) is drawn to the scale in a) and aligned such that y-axis values match up with boxes indicated in a). Layer thickness was averaged over each box in a) by dividing the number of layers by the distance across the box, both measured in the layer-normal direction. Layer normal strain was then calculated with Equation (6-2). Error bars are calculated assuming a layer counting error of one layer per box.

ε_{layer} is presented as a function of position along the compression axis in *post mortem* TEM of a deformed 10-10 Cu/Nb micropillar in Figure 6-10. ε_{layer} is measured at the regions indicated in the deformed microstructure depicted in Figure 6-10 (a). h_o is known from Figure 5-21and is measured per bilayer to include interface deformation. h_d is found in Figure 6-10(a) by measuring the distance across each box in the interface normal direction and dividing by the number of bilayers

in the same direction. This gives a bilayer thickness that is measured across several bilayers per box, ensuring a statistically representative ε_{layer} in each box. These strains are plotted as a function of position along the compression axis in Figure 6-10(b). ε_{layer} increases rapidly over ~300 nm moving from the material outside of the shear band to the interior of the shear band. The non-shear banded material at the pillar top arises from surface tractions imposed by the flat punch probe and is commonly referred to as "dead metal" in bulk compression tests[47]. Starting from the shear band interior to the regions outside of and below the shear band, the ε_{layer} decreases gradually from a peak value of 0.40 to near zero over ~1700 nm. This means that either the bottom of the pillar does not deform or the uncertainty of the ε_{layer} measurements cannot capture deformation in this region. This ambiguity is resolved by investigating the behavior of the pillar gage length. Figure 6-11 demonstrates that the pillar examined in Figure 6-10 deforms along the entire gage length. Thus, deformation still occurs far below the shear band in Figure 6-10 (a).

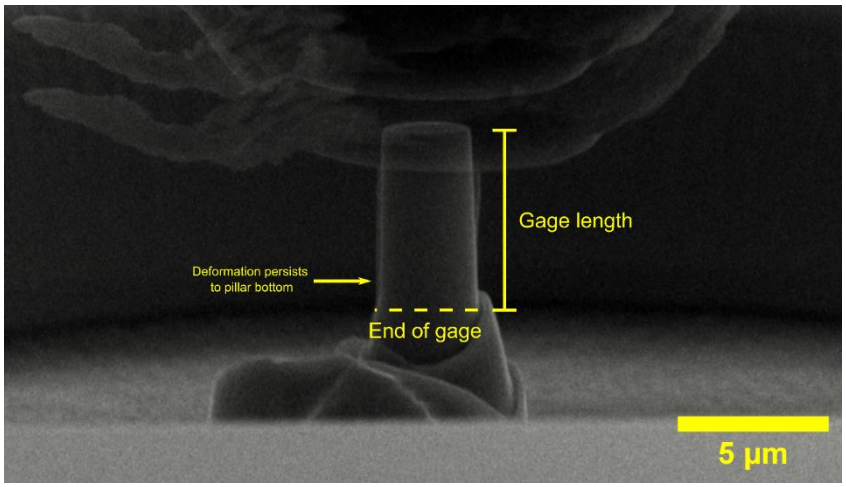

Figure 6-11 – Composite SEM micrograph consisting of frames from the beginning and end of the compression of the pillar sectioned for Figure 6-8 to Figure 6-10. The beginning frame is completely opaque, while the end frame is overlaid on the beginning frame at 50% opacity. Gage length is determined by the length of material that visibly deforms from the initial geometry.

Higher magnification characterization of the shear band in normal compressed 10-10 Cu/Nb can be found in Figure 6-12. Figure 6-12(a) provides a higher magnification image of the shear band, demonstrating gradual changes in layer normal strain below the onset of the shear band, consistent with the results in Figure 6-10. Figure 6-12(b) provides chemical mapping of the shear band. This map demonstrates that layer roughening occurs at the most severely strained regions of the shear band. This may indicate that small shear instabilities occurred at very small length scale (~50 nm)[235], but were prevented from coalescing into a fully developed shear band spanning the pillar width.

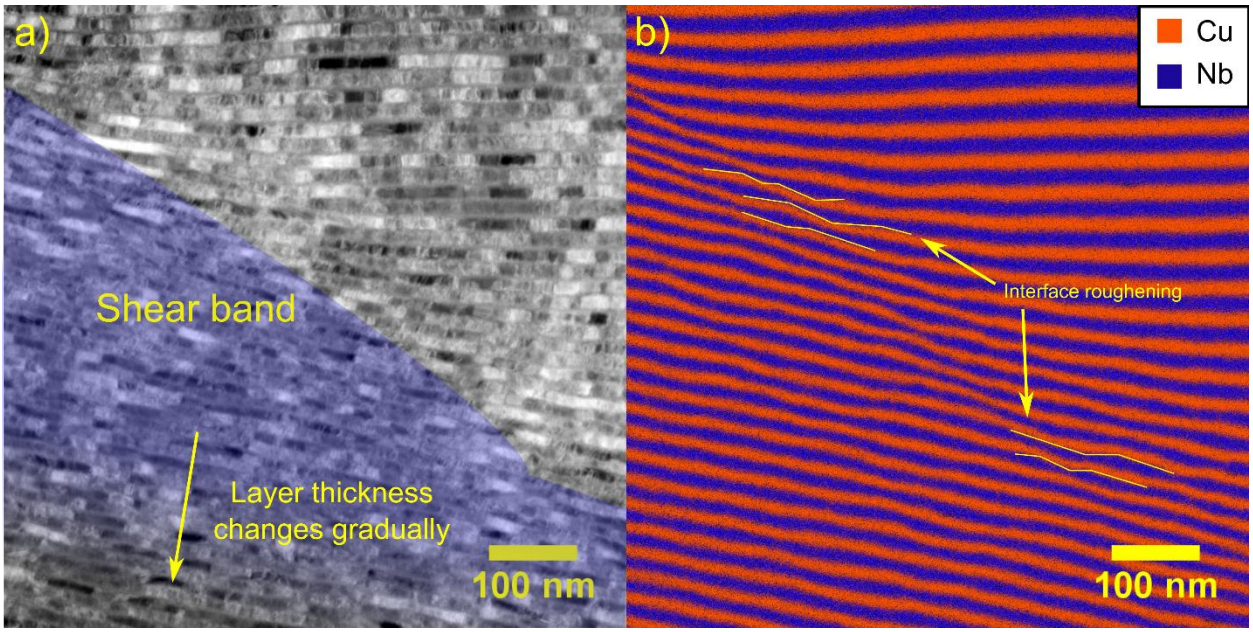

Figure 6-12 – a) HAADF-STEM micrograph close-up of the shear band in 10-10 Cu/Nb after compression. Below the onset of shear banding, layer thickness changes gradually with no discontinuities as a function of position. b) STEM-EDS of the region in a), demonstrating interface roughening at the top of the shear band.

6.3.4. Comparing 10-10 Cu/Nb to other nanolaminates

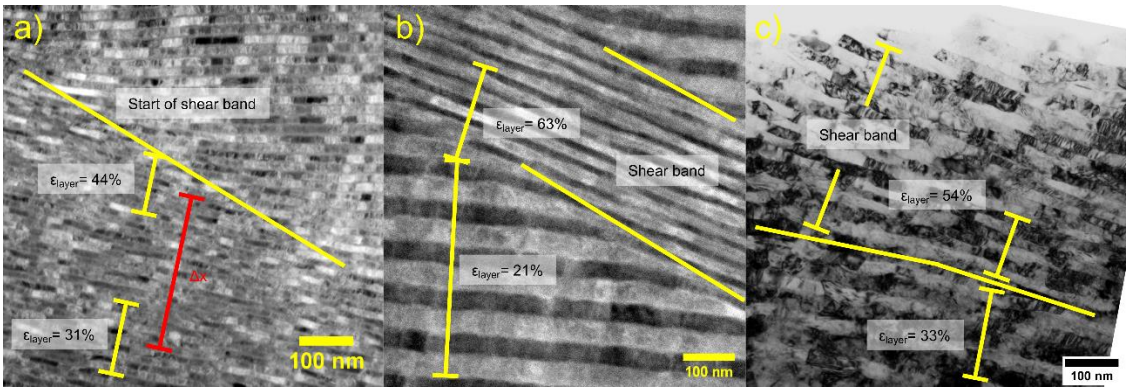

Figure 6-13 – TEM micrographs of shear bands in a) 10-10 3D interface Cu/Nb, b) 40-10 3D interface Cu/Nb, and c) h = 40 nm 2D interface Cu/Nb. (a-b) are HAADF-STEM micrographs, while c) is a bright field CTEM micrograph.

The current work is compared with prior Cu/Nb nanolaminate micropillar compression studies to gain insight into 3D interface mechanical behavior. The previous works focused on 40-10 Cu/Nb with 3D interfaces[233] and 2D interface Cu/Nb with h = 40 nm[16]. Figure 6-13 compares shear banding between 10-10 3D, 40-10 3D, and h = 40 nm 2D Cu/Nb. Here shear band intensity is quantified by comparing the maximum layer normal strain ε_{layer} normalized by bulk engineering strain ε_{bulk}, as well as maximum strain gradient among different samples. The ε_{bulk} is the absolute value of engineering strain $(l_f\text{-}l_o)/l_o$, where l_f and l_o are the post- and pre-deformation micropillar gage lengths. Note that Ref. 16 defines ε_{layer} differently than in Equation 1, opting for a true strain-like definition. Strain gradients are measured for these materials as follows: ε_{layer} is measured at two locations under the start of the shear band and the difference in ε_{layer} is taken. This difference is divided by the distance Δx between the centers of the regions at which ε_{layer} were measured. Locations are chosen to quantify strain gradient where ε_{layer} changes most rapidly with position. Other microstructural metrics associated with shear banding in the literature, e.g., lattice and

interface rotation, are considered for indicators of shear localization intensity. These quantities are summarized in Table 6-1.

Table 6-1 – A summary of shear band microstructural metrics among various Cu/Nb samples. Layer normal strain gradients are presented in percent per nm for readability.

Sample	**Bulk strain, ε_{bulk}**	**Max layer-normal strain, ε_{layer}**	**$\varepsilon_{layer}/\varepsilon_{bulk}$**	**ε_{layer} gradient**	**Lattice rotation**	**Interface rotation**
10-10 3D Cu/Nb	0.16	0.49	3.1	0.045%/nm	31°	9.4°
40-10 3D Cu/Nb[233]	0.14	0.63	4.5	0.13%/nm	30°	12°
h=40 nm 2D Cu/Nb[16]	0.14	0.54	5.5	0.12%/nm	Not measured	17.5°

These data show that 10-10 Cu/Nb has the lowest $\varepsilon_{layer}/\varepsilon_{bulk}$, as well as the lowest maximum strain gradient. This is correlated with superior deformability and strength as quantified by previous work[146]. These metrics are also consistent with the delocalized nature of deformation of 10-10 Cu/Nb as demonstrated in Figure 6-10. Material with measurable ε_{layer} and interface rotation extends a few microns under the top of the pillar. Additionally, the layer normal strain transitions gradually below the top of the shear band. This contrasts with 40-10 and h = 40 nm 2D Cu/Nb, which concentrate strain in a shear band a few hundred nm thick. Thus, 10-10 Cu/Nb is quantitatively shown to deform in a more delocalized manner compared to the other nanolaminates

discussed. Maximum layer normal strain and maximum strain gradient are demonstrated as useful metrics for assessing severity of shear localization. In contrast, the other quantities mentioned here such as lattice and interface rotation do not correlate well with shear localization severity.

6.4. Effect of loading orientation on mechanical behavior

The micropillar results shown so far are from specimens where the compression axis was normal to interfaces and layers. This loading configuration will be referred to as "normal compression". Literature on other nanolaminates such as 2D Cu/Nb[20], Al/SiC[236], and Mg/Nb[237] suggest that loading in other orientations can provide additional information about the contribution of interface structure to deformation. Of particular importance is the loading orientation where the loading axis inclined 45 degrees relative to layer normal directions, termed "45 degree compression" This loading orientation provides key insights into the shear response of heterophase interfaces and will be discussed in this Section. The two loading orientations discussed are depicted in Figure 6-14.

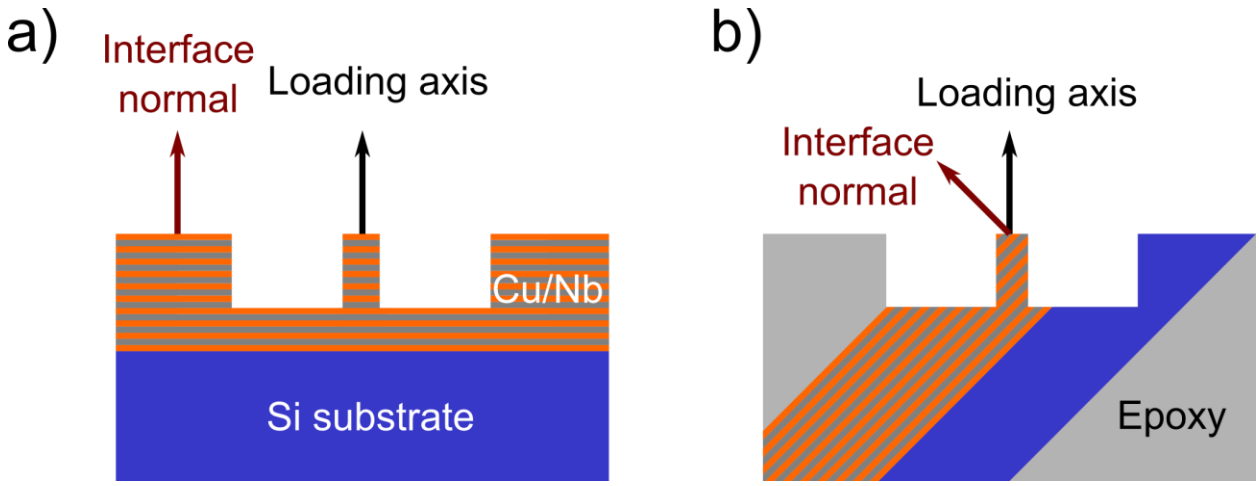

Figure 6-14 – Schematic of sample and loading orientation in a) normal and b) 45 degree compression.

6.4.1. Methodology

FIB, TEM, and micropillar compression procedures for this Section are the same as in 6.3. The 45 degree pillars required special preparation of the thin film specimen before FIB milling. This specimen was made by gluing a thin film specimen between two pieces of an SEM stub cut at 45 degrees. After casting the sandwich in a thin layer of cold mounting epoxy, the sample was ground on the top surface using SiC sandpaper from 400 to 1200 grit, polished using diamond lapping films from 9- to 1-micron particle size and alumina suspension with 0.3-micron particles, and finally vibratory polished using colloidal silica. FIB was used to prepare pillars on the specimen as described for normal compression.

6.4.2. Stress-strain response of 10-10 Cu/Nb in normal and 45 degree compression

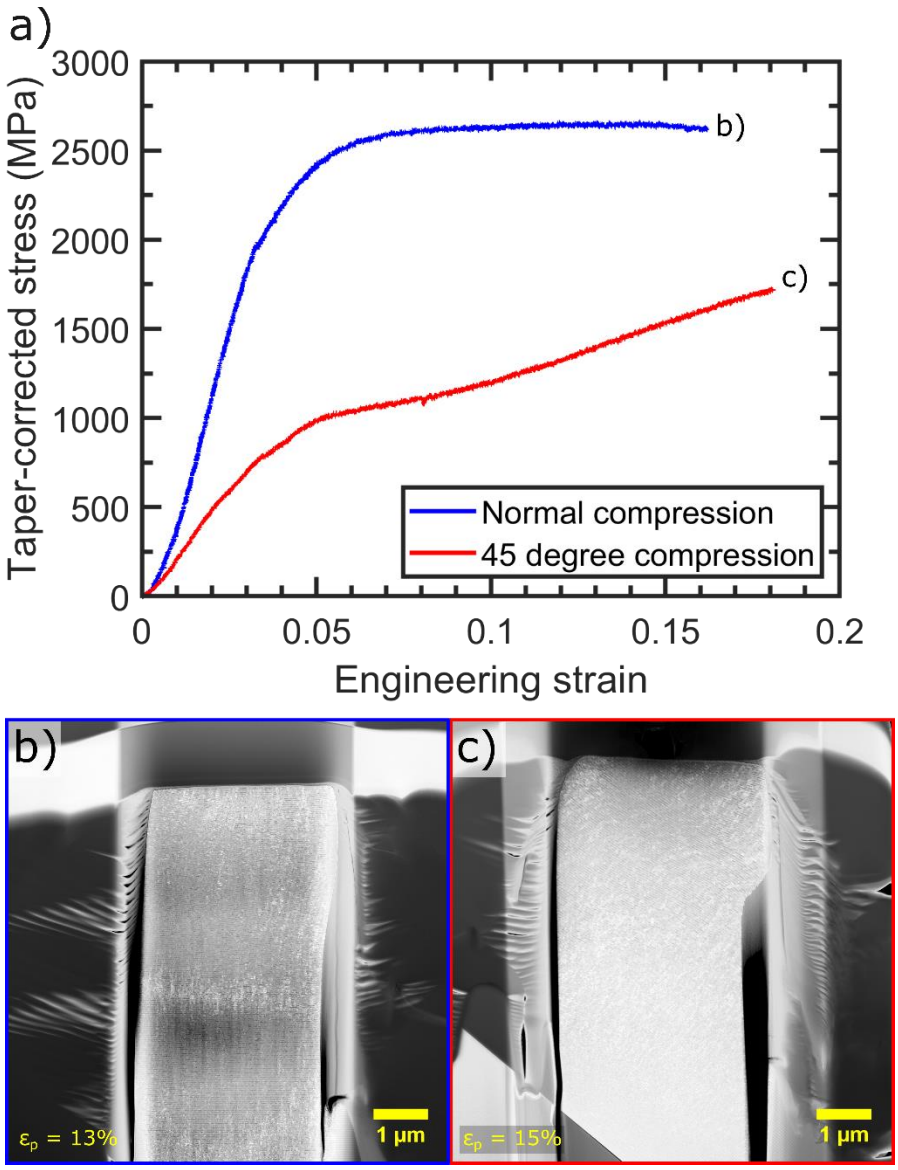

Figure 6-15 – a) Stress-strain curves for normal and 45 degree compression pillars. Post-deformation HAADF STEM images of b) layer-normal compression and c) 45 degree pillars.

Figure 6-15 shows representative stress-strain curves taken from normal and 45 degree compression pillars along with post-deformation microstructures using TEM. Three pillars were compressed for each loading state. The yield stress is taken from where the stress strain curve deviates in value from the initial linear portion by 5% as described previously. For layer-normal

compression pillars, the yield stress is 2080±170 MPa and for 45 degree pillars it is a substantially lower 820±53 MPa. This constitutes a yield stress ratio of 2.53:1 between normal and 45 degree compression. For reference, a yield stress ratio of 3.00:1 between normal and 45 degree compression was found for 2D interface Mg/Nb nanolaminates of comparable *h* in other work[237]. It should be noted that there is significant elastic anisotropy between normal and 45 degree compression, which will be further discussed in Section 6.6.

Post-mortem TEM in Figure 6-15(b-c) allows comparison of deformation between the two loading orientations. In both loading geometries, deformation occupies a significant fraction of the pillar gage length. For layer-normal compression pillars, shear localizes at the top of the pillar as seen in Figure 6-15(b). However, it does not traverse the width of the pillar, indicating that its propagation is frustrated. Deformation along the gage length of the pillar is indicated by layer rotation down to the base of the pillar. Figure 6-15(c) presents a similar situation for 45 degree pillars. Material extrusion towards the right side of the pillar occurs in the top third of the deformed pillar, while material below has deformed modestly (also indicated by layer rotation). The high deformability seen in both loading orientations is atypical for layered nanocrystalline composites, especially at such a fine layer thickness of 10 nm. The delocalized nature of deformation in both loading orientations is likely correlated with the significant work hardening observed. The 45 degree response is particularly remarkable since this work hardening occurs over a much greater extended range of plastic strain than the normal response.

6.4.3. Microstructural characterization of 45 degree compression

6.4.3.1. CTEM

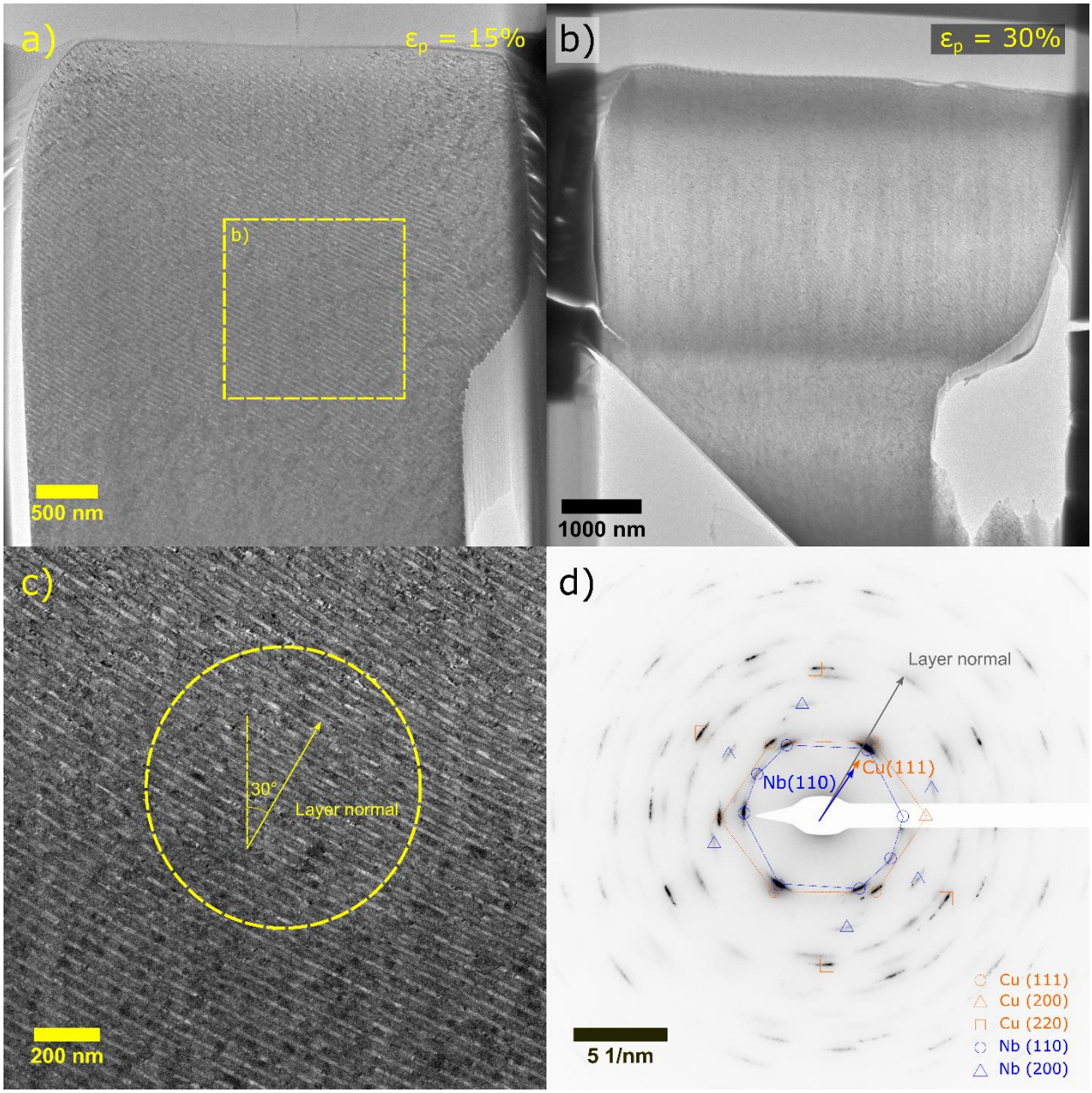

Figure 6-16 – a) CTEM micrograph of 45 degree compression sample after 0.15 plastic strain and b) 0.30 plastic strain. c) Higher magnification CTEM micrograph of area of interest in a) denoted by the dotted yellow box. The final orientation of planes parallel to Cu and Nb layers is depicted with respect to the compression axis. d) SAD pattern taken from the area in c) indicated by the dotted yellow circle. Orange and blue arrows depict the orientation of Cu and Nb compact planes

that began at 45 degrees incidence to the compression axis, respectively. The grey arrow depicts the orientation of layer/interface planes after compression.

Figure 6-16(a) contains cross-sectional CTEM of a 45 degree compressed Cu/Nb micropillar after 0.15 uniaxial engineering plastic strain. Material is seen bulging out of the side of the pillar in the top 2.5 microns of material, suggesting that some shear localization may have occurred. However, TEM of a pillar deformed to 0.36 strain presented in Figure 6-16(b) demonstrates that this is not the case. The bulged region of the pillar has expanded to encompass the entire gage length, constituting a substantial shape change without abrupt plastic instability. A plastic instability would tend to concentrate strain in the pillar and is generally associated with softening behavior. The stress strain curve for this pillar can be found in Figure 6-18 in Section 6.4.4, which demonstrates extensive work hardening. Cu/Nb did not fail at the interfaces in this loading configuration, despite the maximum resolved shear stress aligning with interface planes at the beginning of deformation. This indicates that 3D interfaces can work harden in shear, which is crucial for preventing shear instability and promoting overall deformability in other loading orientations.

Microstructural characterization reveals more information on the nature of deformation in 45 degree compressed 10-10 Cu/Nb. Figure 6-16(c) depicts the degree of layer rotation in the region of interest in (a), indicating that layers in this region rotated 15° from their initial orientation. Figure 6-16(d) contains a SAD pattern taken from the area depicted in (c), showing that compact planes in Cu and Nb that were parallel to interfaces at the start of deformation rotate the same amount as the interfaces after deformation. This indicates that the Cu, Nb, and 3D interfaces co-deform. As will be discussed later, co-deformation may explain the mechanical behavior of 3D interfaces.

6.4.3.2. STEM-EDS

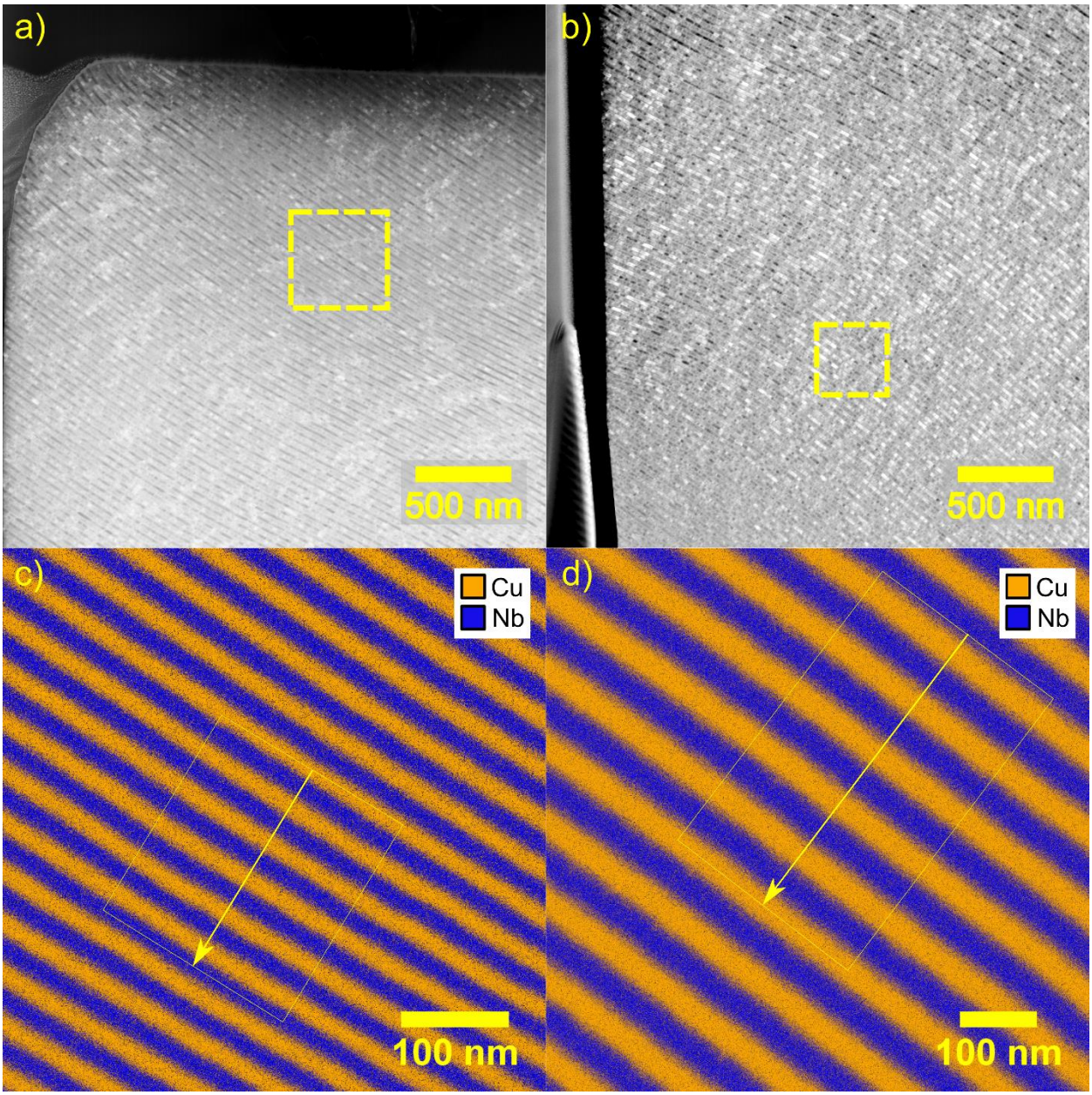

Figure 6-17 – a) HAADF image of a region near the top of a 45 degree pillar deformed to 0.18 plastic strain. b) HAADF image of a region near the bottom of a deformed 45 degree pillar. (c-d) STEM-EDS maps taken from the regions shown in (a-b); c) corresponds to the dotted yellow box in a) and d) corresponds to the dotted yellow box in b). Chemical profiles are taken along the yellow arrows in c) and d) to give layer and interface thicknesses presented in Table 6-2. Profiles are averaged along the width perpendicular to the arrows depicted by solid yellow boxes in (c-d).

STEM-EDS of 45 degree compressed Cu/Nb is used in Figure 6-16(a) to determine the extent of post-deformation layer thinning. Figure 6-17(a) and Figure 6-17(b) show, respectively, micrographs from the top and bottom of the pillar. Regions indicated in Figure 6-17(a-b) were chemically mapped to produce Figure 6-17(c-d). Line profiles are drawn in EDS maps to extract chemical profiles, which are then used to calculate the layer and 3D interface thicknesses given in Table 6-2. The bilayer thicknesses from these measurements suggest little to no layer thinning occurred during deformation. The thinnest bilayer, found from the chemical profile in Figure 6-17(c), is 39.4 nm thick, compared to 41.8 for undeformed material as determined from Figure 5-21. This reduction in thickness corresponds to a layer-normal strain of 0.06. This amount of strain does not correlate well with the global plastic strain of 0.15, indicating that in this loading orientation layer normal strain is not an indicator of local strain.

Table 6-2 – Summary of layer thicknesses measured at the top and bottom of 45 degree compressed Cu/Nb micropillar. *h'* for 3D interfaces grown on Cu are denoted h'_{3DonCu}, while it is denoted h'_{3DonNb}, for 3D interfaces grown on Nb.

	Pillar top		**Pillar bottom**	
	Average (nm)	**Std. Dev. (nm)**	**Average (nm)**	**Std. Dev. (nm)**
$\mathbf{h_{Cu}}$	8.9	0.3	10.5	0.6
$\mathbf{h_{Nb}}$	9.5	0.5	10.1	0.3
$\mathbf{h'_{3DonCu}}$	11.1	0.7	11.3	0.6
$\mathbf{h'_{3DonNb}}$	9.7	0.6	10.1	0.4
Bilayer	39.4	0.7	42.2	0.2

6.4.4. Shear strength of 3D interfaces

We can also compare 2D and 3D Cu/Nb in 45 degree compression using literature results on material with comparable *h*. Figure 6-18(a) shows that *h* = 5 nm 2D Cu/Nb under 45 degree compression yields at a resolved shear stress of about 0.5 GPa, and then work hardens to 0.8 GPa shear stress before failure. Failure occurs at 0.15 true plastic strain after subtracting elastic deformation for *h* = 5 nm 2D Cu/Nb. The pillar undergoes shear localization via sliding along a narrow plane starting near the top of the pillar (Figure 6-18 (b))[20]. In contrast, 10-10 Cu/Nb under similar loading yields at a resolved shear stress of 0.4 GPa and then work hardens to a shear stress of 0.9 GPa over an engineering plastic strain of 0.30, as seen in Figure 6-18(c). Here, 10-10 Cu/Nb deforms over a region a few hundreds of nm wide as seen in Figure 6-18(d). This contrasts with its 2D counterpart, where deformation is isolated to a band only a few tens of nanometers wide in Figure 6-18(b). This suggests that although yield stress is comparable under 45 degree pillar compression between 10-10 Cu/Nb and *h* = 5 nm 2D Cu/Nb, work hardenability and homogeneous deformability are much higher in the 3D interface case. This result demonstrates that composites containing 3D interfaces can work harden appreciably in shear in contrast to 2D interfaces, which undergo significant interfacial sliding and play an important role under several loading configurations[16,20].

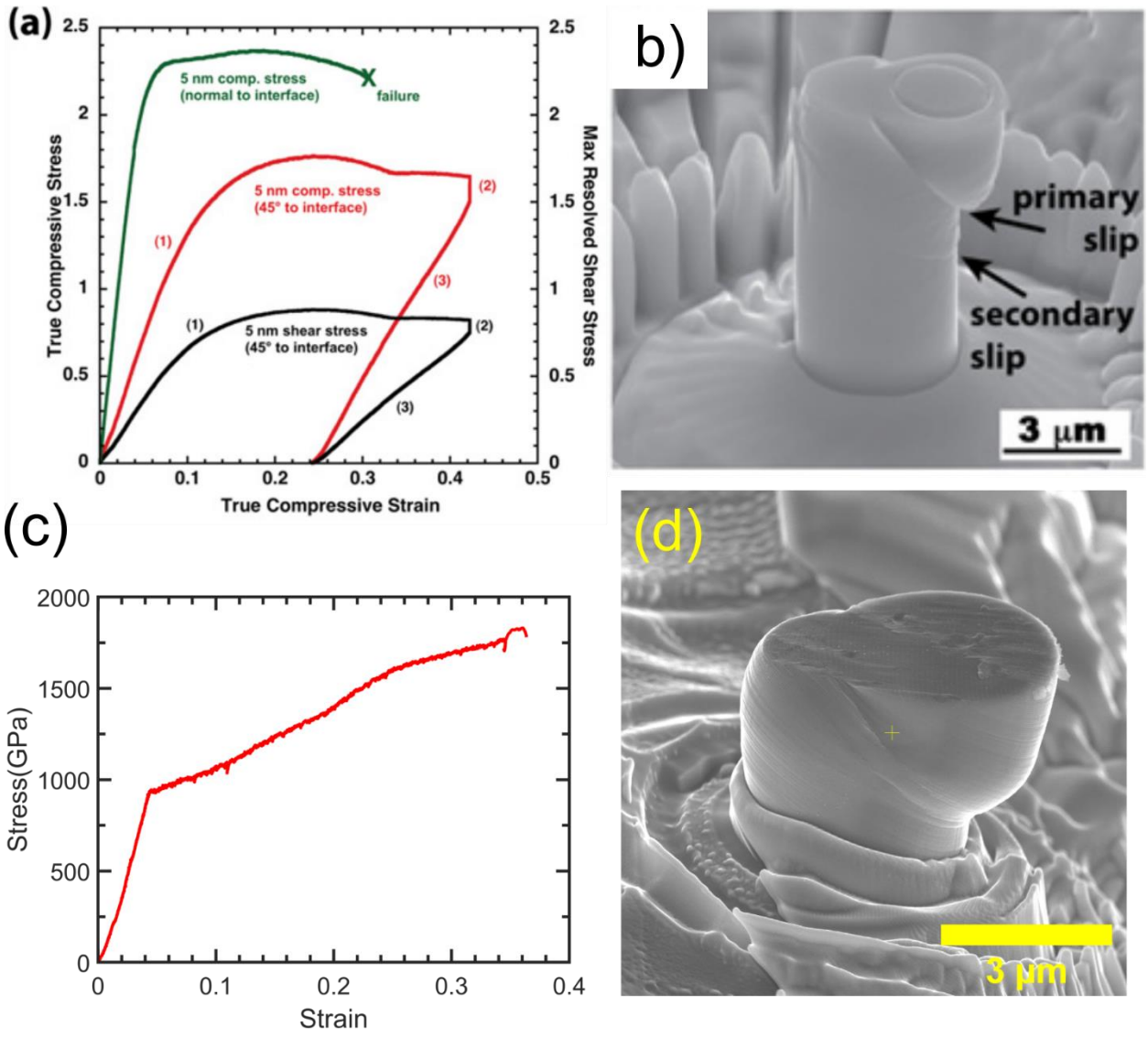

Figure 6-18 – Comparison of (a-b) h = 5 nm 2D Cu/Nb[20] *ex situ* and (c-d) 10-10 Cu/Nb *in situ* 45 degree micropillar compression results. From the stress strain curve in a), interfaces in h = 5 nm 2D Cu/Nb yield at about 0.5 GPa true resolved shear stress, and the material work hardens to ultimate compressive stress at 0.25 total true strain (0.15 plastic true strain), then begins strain softening. From the *post mortem* SEM micrograph in b), this material is observed to strain localize heavily at the top of the pillar. In comparison, c) shows that 10-10 Cu/Nb yields at about 0.8 GPa true compressive stress, or 0.4 GPa resolved shear stress. This stress-strain curve shows that 10-10 Cu/Nb does not strain soften like h = 5 nm 2D Cu/Nb. Instead, it work hardens continuously. d) depicts the *post mortem* SEM image of this pillar, which demonstrates the highly delocalized nature of deformation in 10-10 Cu/Nb.

The shear behavior of 2D Cu-Nb heterophase interfaces can be understood through prior molecular dynamics simulations showing that Kurdjomov-Sachs type 2-D Cu-Nb interfaces are relatively weak in shear[3,238]. Experimentally, 2D Cu-Nb interfaces have been shown to have shear strengths of 0.3-0.55 GPa in h = 5 nm 2D Cu/Nb using *ex situ* 45 degree micropillar compression (shown in Figure 6-18(a-b)) and *in situ* TEM straining experiments[20]. *In situ* results from this work show that after yield, 2D Cu-Nb interfaces slide without work hardening. This explains the highly localized strain observed in the vicinity of the bimetal interface. The shear strength of 2D interfaces is compared to that of the abutting phases. The critical resolved shear stresses of pure Cu and Nb below a grain size of 100 nm are at least 0.43 and 1.0 GPa, respectively (assuming a Schmid factor of 0.5)[65]. Thus, the limiting strength in this material is in either Cu or the interfaces. After yield in either of these regions, little work hardening occurs.

While there is no direct evidence for the shear strength of 3D interfaces, its lower bound is 0.4 GPa from the micropillar data in Figure 6-18(c). This is close to the critical resolved shear stress for pure nanocrystalline Cu. Therefore, it is likely that during the early stages of plastic deformation in 3D Cu/Nb, Cu layers and 3D interfaces work harden together to produce the delocalized deformation seen in Figure 6-18(d). Once they harden to match the high Nb flow stress, the entire composite can continue work hardening at the same rate. 3D interfaces are also found to enhance work hardenability in the nominally soft Cu phase. Pure nanocrystalline copper (nc Cu) with a grain size of 100 nm can work harden from a yield stress of 0.5 GPa to 0.8 GPa under uniaxial compression[239]. This grain size is used because it is the in-plane grain size of Cu grains in 10-10 Cu/Nb (see Figure 5-5). In contrast, the Cu phase in 3D Cu/Nb can work harden to possess a maximum resolved shear stress more than 1.0 GPa (ultimate compressive stress divided by 2). In other words, without the constraints imposed by 3D interfaces, Cu and Nb layers would have

divergent flow stresses. Evidence of this divergent plastic behavior is found in TEM of 45 degree compressed 10-10 Cu/Nb in Figure 6-19, where material extruded out to the pillar surface assumes a serrated morphology. Once Cu and Nb are extruded out to a free surface, they flow differently in the absence of the constraints imposed by 3D interfaces.

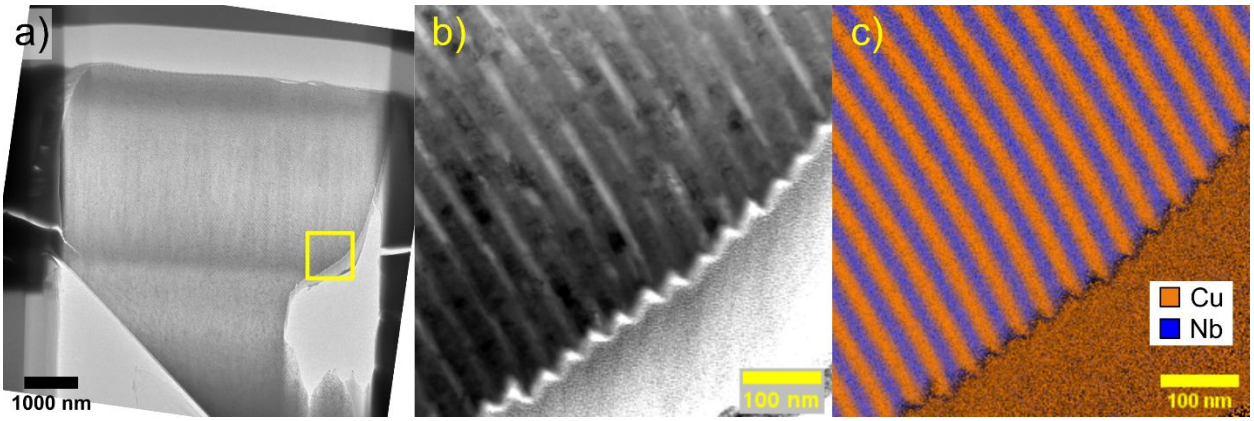

Figure 6-19 – STEM EDS maps were taken in a 45 degree compression pillar (same as Figure 6-16 (b)) from the region outlined by a yellow box in a). b) BF STEM and c) STEM EDS from this region are shown. Serration can be seen at the edge of the pillar in (b-c).

As an aside, Figure 6-18(a) shows that there is apparently significant elastic anisotropy between normal and 45 degree compression for h = 5 nm 2D Cu/Nb, just like there is for 10-10 Cu/Nb in Figure 6-15(a). Some of this may originate from differences in substrate compliance. The loading stiffness of micropillars can be affected by substrate morphology due to the pillar acting as a rigid flat punch[40]. However, a significant portion of the difference in elastic loading stiffness between normal and 45 degree compression in Cu/Nb can be attributed to real differences in elastic constants. The elastic constants of Cu and Nb are presented in Table 6-3, giving Zener ratios of 3.20 and 0.574 for Cu and Nb, respectively[240]. Elastically isotropic materials have Zener ratios of 1, so Cu and Nb are significantly elastically anisotropic. This leads to the elastic anisotropy between normal and 45 degree compression in h = 5 nm 2D Cu/Nb and 10-10 Cu/Nb.

Table 6-3 – Elastic constants of single crystal Cu and Nb.

Phase	C_{11}**(GPa)**	C_{12}**(GPa)**	C_{44}**(GPa)**
Cu	168.4	121.4	75.4
Nb	234	134	28.7

The results shown above for 45 degree compression have demonstrated two aspects of the influence of 3D interfaces to plastic deformation under shear loading. The first is that 3D interfaces have at least comparable interfacial shear strength, but much superior work hardenability compared to their 2D counterparts. The second is that 3D interfaces mediate codeformation and superior work hardenability in abutting pure layers. These behaviors will be explored in detail in Section 6.6.3.

6.5. Interface size effects on strength and deformability

The dislocation-interface interaction energy is dependent upon the length scale of dislocation ensembles relative to the grain size of the material. 3D Cu/Nb-influenced deformation mechanisms and resulting mechanical behavior are strongly dependent on layer thickness, just as they are in 2D Cu/Nb[15–17,144]. The introduction of 3D interfaces in nanolaminates introduces another length scale for consideration of interface-dominated deformation. The thickness of the interface *h'* potentially has an outsize effect on strength and deformability as well. The increase in flow stress and uniform deformability from that comes from decreasing *h* from 40 to 10 nm in the presence of 3D interfaces with *h'* = 10 nm raises a few key scientific questions:

1. Does the stress barrier that 3D interfaces pose to slip transfer across heterophase boundaries scale with absolute value of *h'?*

2. Does the absolute value of *h'* have any bearing on the uniform deformability of the composite – is there a strength-ductility tradeoff associated with 3D interface thickness?
3. Does absolute value of *h* and *h'* determine deformation mode, or is mechanical behavior solely dependent on *h/h'*?

Here, micropillar compression and nanoindentation results from nanolaminates with a variety of *h* and *h'* are presented to address these questions.

6.5.1. Methodology

3D Cu/Nb samples with various *h* and *h'* were deposited as 10 μm thin films on <100> single crystal Si substrates as described before. Additionally, a 10 μm thick amorphous equiatomic CuNb sample was deposited at total deposition rate of 3 Å/sec by using a continuous Cu target power of 75 W and Nb target power of 200 W. These samples can be separated into series designed to address the issues raised above:

Table 6-4 – Table of samples deposited for this work.

Series 1 **Constant *h'* = 10 nm**
80-10
20-10
10-10

Series 2 **Constant *h* = 10 nm**
10-40
10-20
10-10

Series 3 **Constant h/h' = 1**
40-40
20-20
10-10

These samples are used to construct different series based on their mechanical properties in Sections 6.5.3-6.5.6. TEM, FIB, and micropillar compression procedures are the same as in Sections 6.3.1 and 6.4.1. *Post mortem* SEM and bilayer thickness measurement was conducted in an FEI Helios G4 NanoLab. Bilayer thicknesses were measured for each sample in Table 6-4 by cross-sectioning using FIB and using SEM to measure bilayer thickness across 10 bilayers at 3 lateral positions, then dividing averages and standard deviations by 10 to produce bilayer thickness.

Nanoindentation tests were completed using a Hysitron TI 980 nanoindentation system. A high load 10 N transducer was used with a Berkovich tip. Tip area function was calibrated up to 600 nm on a fused silica standard, with calibration data showing good agreement of hardness with known standard values. CSM tests were performed at 100 Hz with a displacement amplitude ranging from 1-2 nm during the test. A constant strain rate profile was used for the DC portion of the load function with an indentation strain rate of $5*10^{-3}$/s between the loads of 10 and 300 mN. Total test time was 360s and data acquisition rate was 100 points/s for each indent. 10 indents were performed for each specimen with an indent spacing of 75 μm. Specimens were left in the indenter enclosure for 1 hour before the beginning of testing to minimize the influence of thermal drift. A thermal drift settling segment was performed before each indent for 100 sec. or the time it took for drift rate to fall below 0.500 nm/s, whichever was shorter. H, E_r, and P/S^2 profiles were smoothed with a Savitzky-Golay filter of polynomial order 2 with windows of 1001, 5001, and 5001 points, respectively. E_r and P/S^2 were smoothed twice.

All stress-strain curves here and the rest of this Section use engineering stress and strain. Stress is calculated using the diameter at the top of the pillar, producing the maximum engineering stress found in the pillar. Strain is calculated with gage length determined using the method in Sections 6.2 and 6.4. The reason for using separate methodologies is the different propensities of

samples to shear localize. Some samples shear localize before the pillar taper model used previously predicts flattening to a right cylinder, violating the assumptions about pillar geometry used in that model. For similar reasons, true stress and strain assuming volume conservation and cylindrical geometry cannot be used. Shear localization causes deviation from uniaxial stress conditions that nullify the assumptions used for true stress and strain calculations. In that light, engineering stress-strain curves allow for the most consistent comparison between all samples in this study. Where possible, comparisons are made to reflect the local stress state where the phenomenon of interest, e.g. shear onset, is occurring.

6.5.2. Bilayer thickness measurement

Table 6-5 – Bilayer thicknesses as measured by FIB cross-section for samples in Table 6-4.

Sample	**Average bilayer thickness (nm)**	**Std. dev. (nm)**	**Nominal Bilayer Thickness (nm)**	**Percent error**
10-10	42.8	0.57	40	6.98%
10-20	50.0	0.91	60	-16.69%
10-40	92.3	0.88	100	-7.75%
20-10	57.5	0.90	60	-4.13%
20-20	76.4	0.60	80	-4.44%
40-40	142.0	1.05	160	-11.27%
80-10	154.1	1.71	180	-14.41%

In order for conclusions about layer and 3D interface thickness influences on mechanical properties to be accurate, bilayer thickness must be close to nominal values as determined by h and h' during deposition. Bilayer thickness was measured by FIB cross-section and subsequent SEM and presented in Table 6-5. Most samples deposited within ~10% of nominal bilayer thickness, with exceptions for 10-20 and 80-10 Cu/Nb. These specimens have a measured bilayer thicknesses of about 5/6 their nominal bilayer thicknesses. These specimens did not produce outlier

behavior in mechanical characterization of these specimens, so their nominal thicknesses will be used for subsequent analysis.

6.5.3. Constant h'

Micropillar compression results are presented for 3D Cu/Nb with a constant *h'* of 10 nm in Figure 6-20. Stress-strain curves for representative pillars are shown in Figure 6-20(a). Figure 6-20(a) shows that for constant *h'*, flow stress is consistent for samples with $h <= 40$ nm. Increasing *h* further to 80 nm causes flow stress to decrease significantly. For samples with $h <= 40$ nm, strain softening caused by shear localization is severe enough to cause stress drops in their stress-strain curves at high plastic strain. For 80-10 Cu/Nb, this is not the case, indicating that the work hardening in grain interiors outside the shear band is enough to counteract strain softening in any shear bands and produce global strain hardening in the stress-strain curve. This is behavior that approaches the uniform work hardening and deformability found in coarser-grained alloys. Figure 6-20(b) shows the trends of yield stress and flow stress at 8% plastic strain ($\sigma_{8\%}$) as a function of *h*, reflecting the increase in flow stress as *h* decreases. Yield and flow stress saturate at $h = 40$ nm, indicating that there is a limit to how an increase in 3D interface volume fraction can strengthen Cu/Nb. Depictions of shear-banded pillars are found in Figure 6-20(c-d), showing that 20-10 and 80-10 Cu/Nb form shear bands during deformation. Combining these observations with results in previous Sections, it is found that all 3D Cu/Nb samples studied with $h' = 10$ nm shear band during deformation. Evidently, once *h* is high enough, shear banding is not severe enough to cause global strain softening as seen for 80-10 Cu/Nb.

It is important to note that the yield stress found for 10-10 here is different than reported in Sections 6.3 and 6.4. While the definition of yield stress as the point where the curve deviates from the linear elastic portion by 5% is the same, the limits of linearity were chosen differently for this

work. An interactive Matlab script was developed in which linear limits could be interactively changed while observing the change in linear fit to the elastic portion of a load-displacement curve. This script is a modified version of one used by Schmalbach for other work[241]. This script allowed for more accurate determination of the linear segment of the stress-strain curve. Yield stresses are 100 MPa lower using this method than in those found for Sections 6.3 and 6.4. The variation in yield stress between this method and previous methodology demonstrates the ambiguity of determining the transition from fully elastic to fully plastic behavior during a gradual elastoplastic transition.

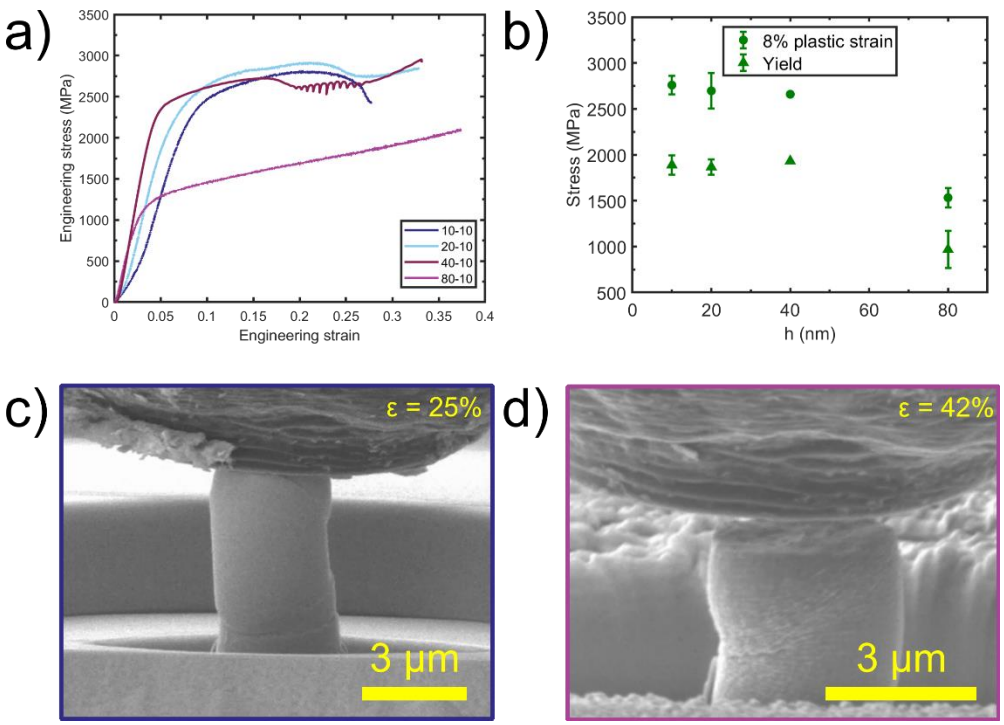

Figure 6-20 – a) Representative engineering stress-strain curves for samples with *h'* = 10 nm. b) $\sigma_{8\%}$ presented as a function of *h* for samples in a). (c-d) *In situ* micropillar compression snapshots at the end of the test for c) 10-10 and d) 80-10 Cu/Nb.

The micropillar results in Figure 6-20 allow for comparison of flow stresses between 2D and 3D Cu/Nb in Figure 6-21. It should be noted again that correlation between hardness and flow stress is ambiguous. For example, Hernot, et al. predict computationally that 10-10 Cu/Nb with

E/σ_y ratio of roughly 70 and unknown n, has ε_i =10-16% with a Tabor factor of 2.3-2.7. Given the ambiguity between computation and mismatch among nanocrystalline experiments discussed in Chapter 4, default values of ε_i of 8% and Tabor factor of 2.7 are assumed as a matter of convention with the caveat that other values may be more accurate in correlating indentation results to uniaxial compression.

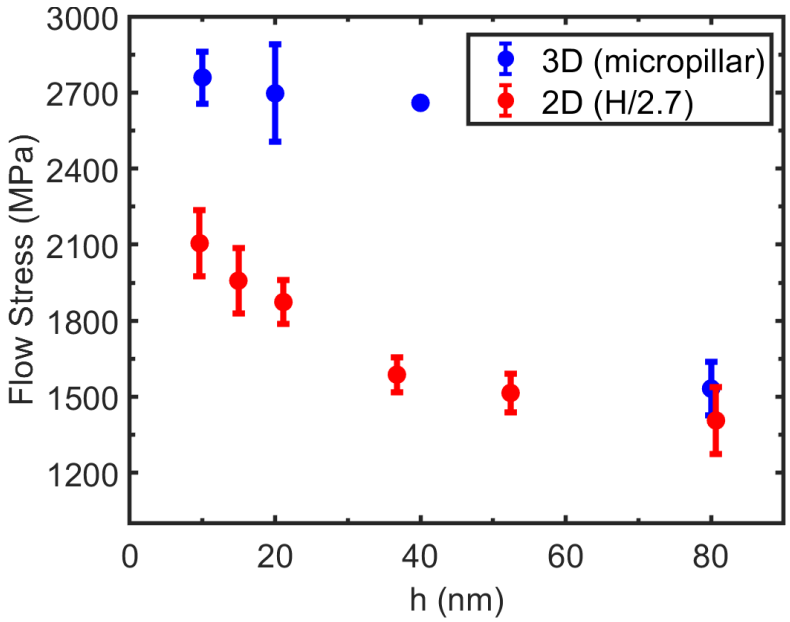

Figure 6-21 – A comparison of flow stress values from Figure 6-20(b) with flow stress values obtained from nanoindentation and Tabor factor correlation from Ref. 15.

Figure 6-21 compares *h'* = 10 nm 3D Cu/Nb micropillar $\sigma_{8\%}$ values with 2D Cu/Nb $\sigma_{8\%}$ obtained by H/2.7 under the preceding assumptions. At *h* = 80 nm, 3D and 2D Cu/Nb have similar flow stresses. As *h* decreases below 80 nm, 3D and 2D develop different trends in $\sigma_{8\%}$ with respect to layer thickness. Under the assumption that Tabor factor is 2.7 and ε_r = 8%, 3D Cu/Nb has higher $\sigma_{8\%}$ than 2D Cu/Nb when *h* < 80 nm. Additionally, $\sigma_{8\%}$ saturates differently at low *h* for 3D and 2D Cu/Nb. $\sigma_{8\%}$ saturates at a maximum of about 2700 MPa for 40-10 Cu/Nb. Ref. 15 shows that indentation-correlated $\sigma_{8\%}$ peaks at 2600 MPa at *h* = 1.2 nm. Thus, 3D interfaces do not increase

the peak stress attainable by Cu/Nb, but can produce peak stress at much larger layer thicknesses than in 2D Cu/Nb.

6.5.4. Constant h

6.5.4.1. h = 10 nm

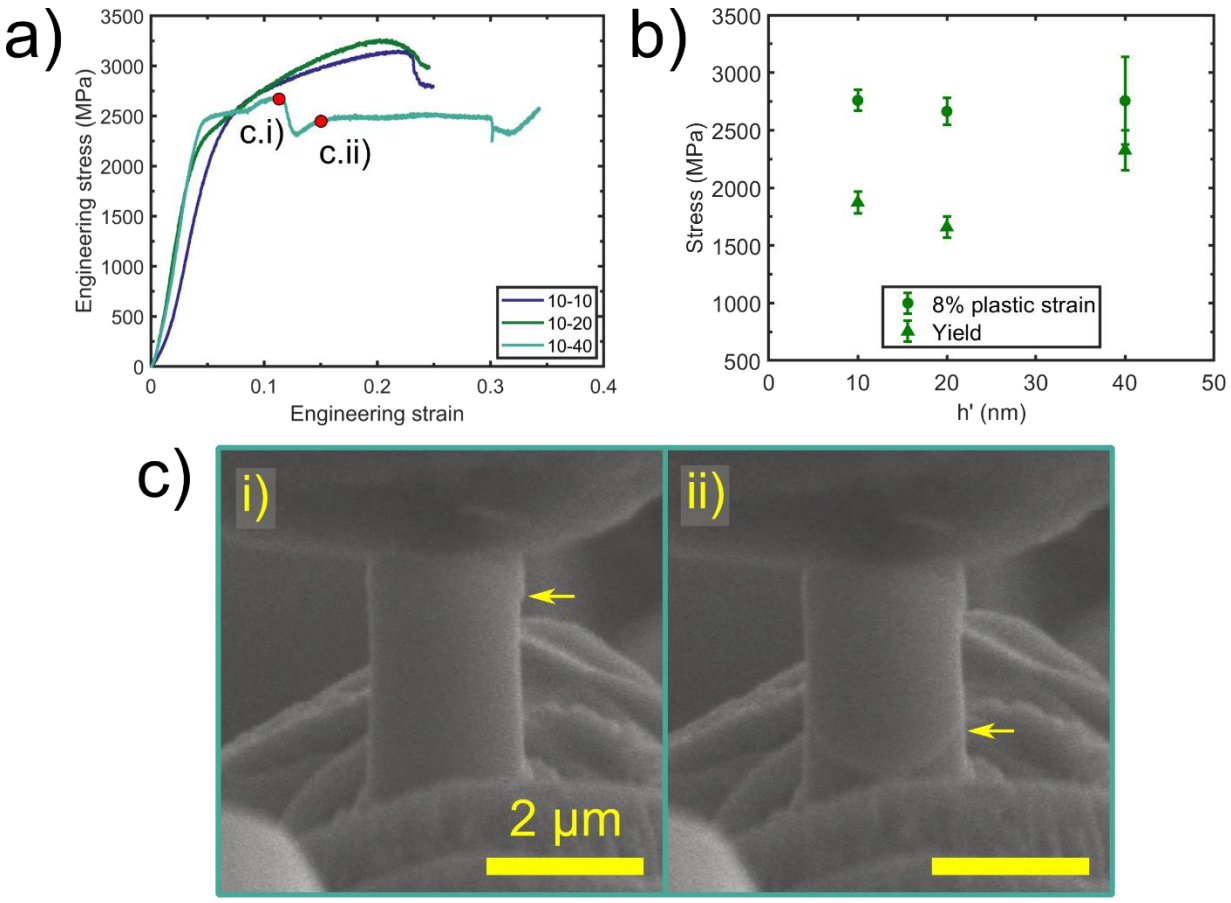

Figure 6-22 – a) Representative engineering stress strain curves from samples with h = 10 nm. b) $\sigma_{8\%}$ presented as a function of h' for samples in a). (c.i-ii) *In situ* micropillar compressions snapshots at the strains indicated by red dots in a). c.i) shows the formation of one shear band that emanates from the pillar side at the yellow arrow. c.ii) shows the formation of a second shear band at the bottom of the pillar.

In situ micropillar compression results for samples with constant h = 10 nm are presented in Figure 6-22. Figure 6-22(a) contains representative stress strain curves for all samples. Comparing 10-10 to 10-20 Cu/Nb shows that at this h, increasing 3D interface thickness from 10

to 20 nm has little effect on flow stress. Both curves have significant drops at extended plastic strain, demonstrating the formation of strain-softening shear bands that limit uniform deformability. Deformation mode changes drastically when comparing 10-20 to 10-40 Cu/Nb. Increasing the 3D interface thickness from 20 to 40 nm causes the material to reach peak stress at much lower strain than for samples with lower *h'*. After reaching peak stress at 0.10 total strain, the material experiences a significant stress drop, after which the material maintains consistent engineering stress before experiencing another load drop at 0.30 total strain. Figure 6-22(b) demonstrates trends in σ_y and $\sigma_{8\%}$ with respect to *h'*. σ_y remains consistent between 10-10 and 10-20 Cu/Nb, while it increases between 10-20 and 10-40 Cu/Nb. Meanwhile, $\sigma_{8\%}$ is comparable for all specimens. Thus, substantial work hardening occurs on average over the pillar volume between yield and 0.08 plastic strain for specimens with $h' < 20$ nm, while little work hardening occurs for $h' = 40$ nm. Figure 6-22(a) demonstrates 10-40 Cu/Nb work hardens rapidly before forming shear localizations that strain soften enough to counteract work hardening immediately after yield. This process is shown through *in situ* snapshots in Figure 6-22(c.i-ii). One shear band forms near the top of the pillar in Figure 6-22(c.i), corresponding to peak stress on the stress strain curve. By the time the material experiences a stress drop and stress begins rising to a steady value, another shear band forms in Figure 6-22(c.ii). Shear localization in 10-40 Cu/Nb will be examined in further detail in Section 6.5.7.1.

6.5.4.2. h = 20 nm

Figure 6-23 presents *in situ* micropillar compression results for samples with $h = 20$ nm. Figure 6-23(a) shows representative stress-strain curves for 20-10 and 20-20 Cu/Nb. Both pillars develop severe enough shear localization at extended plastic strain to exhibit load drops. Figure 6-23(b) shows that σ_y and $\sigma_{8\%}$ are comparable within statistical deviation for these samples. At *h*

= 20 nm, increasing *h'* from 10 to 20 nm has little effect on mechanical behavior, with both pillars developing stress drops at comparable strain. Figure 6-23(c-d) demonstrate the appearance of shear localization after pillar compression for 20-10 and 20-20 Cu/Nb. Both pillars develop shear localization after extended strain, which can be inferred to limit uniform deformability in both cases.

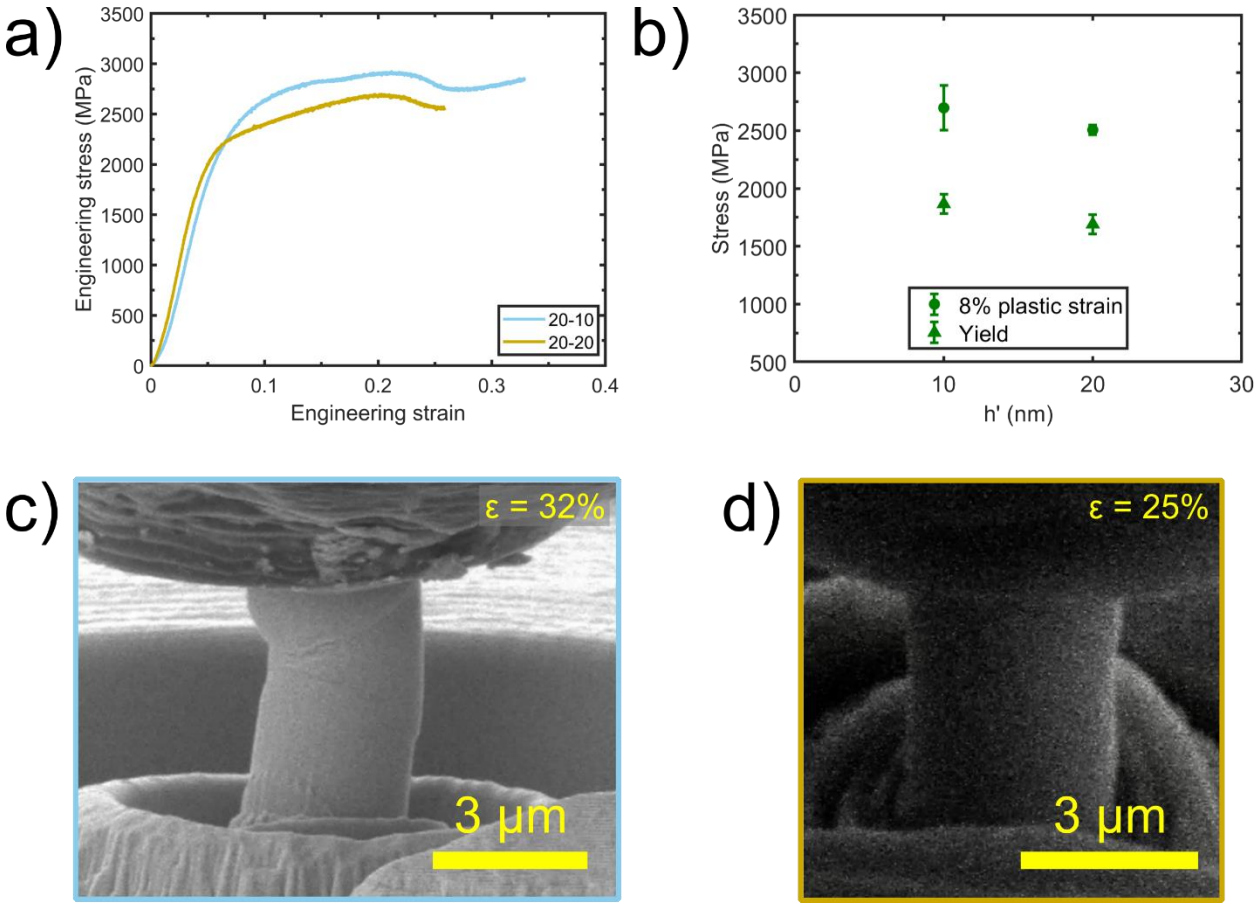

Figure 6-23 – a) Representative engineering stress-strain curves for samples with *h* = 20 nm. b) $\sigma_{8\%}$ presented as a function of *h'* for samples in a). (c-d) *In situ* snapshots at the end of pillar compression for c) 20-10 Cu/Nb and d) 20-20 Cu/Nb.

6.5.4.3. h = 40 nm

Figure 6-24 compares micropillar compression behavior between 40-10 and 40-40 Cu/Nb. Figure 6-24(a) compares stress-strain behavior, with both materials attaining similar flow stresses

before deformability-limiting plastic instability. 40-10 reaches maximum flow stress of about 2600 MPa before shear localization at 0.15 strain, while 40-40 reaches a maximum of about 2500 MPa before shear localization at 0.23 strain. Figure 6-24(b) shows that σ_y and $\sigma_{8\%}$ increase as *h'* increases from 10 to 40 nm (note that only one pillar was included in the prior work on 40-10 Cu/Nb, so error bars could not be calculated). Note that Figure 6-24(b) does not capture the extended work hardening behavior in 40-40 past 8% plastic strain. Figure 6-24(c) shows the rupture of a 40-10 Cu/Nb pillar due to severe shear localization after compression. Figure 6-24(b) shows that 40-40 Cu/Nb does shear localize, but not severely enough to cause rupture as found for 40-10 Cu/Nb. Evidently, increasing 3D interface thickness from 10 to 40 nm at this *h* does not enhance strength near yield, but does at higher plastic strain.

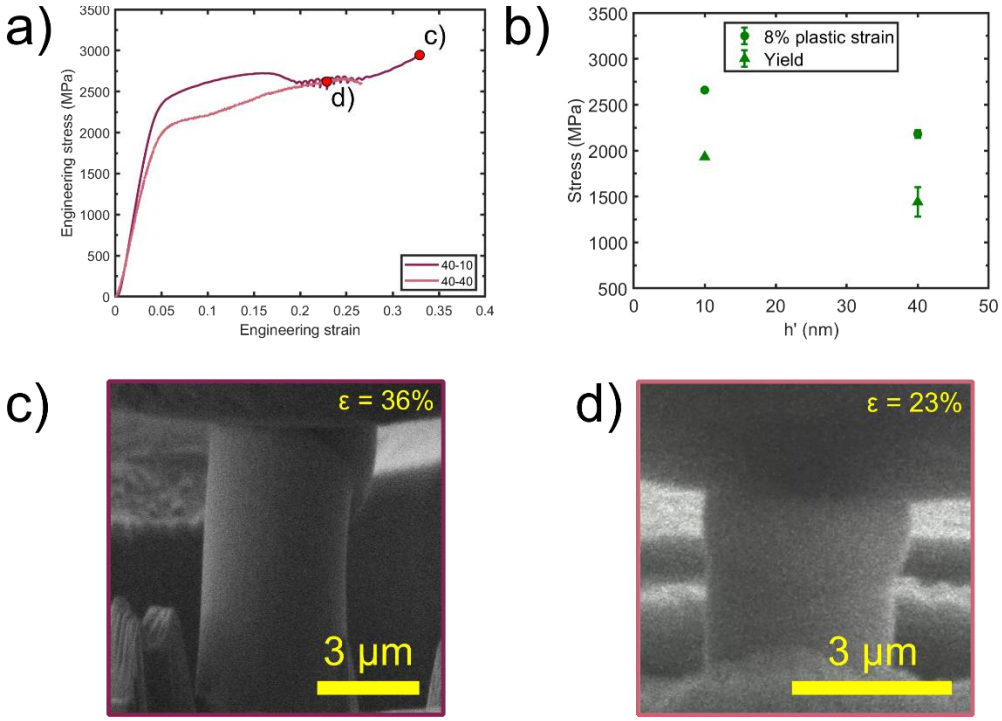

Figure 6-24 – a) Representative engineering stress-strain curves for samples with *h* = 40 nm. b) $\sigma_{8\%}$ presented as a function of *h'* for samples in a). (c-d) *In situ* micropillar compression snapshots for c) 40-10 and d) 40-40 Cu/Nb at the strains indicated by red dots in a).

6.5.5. Constant h/h'

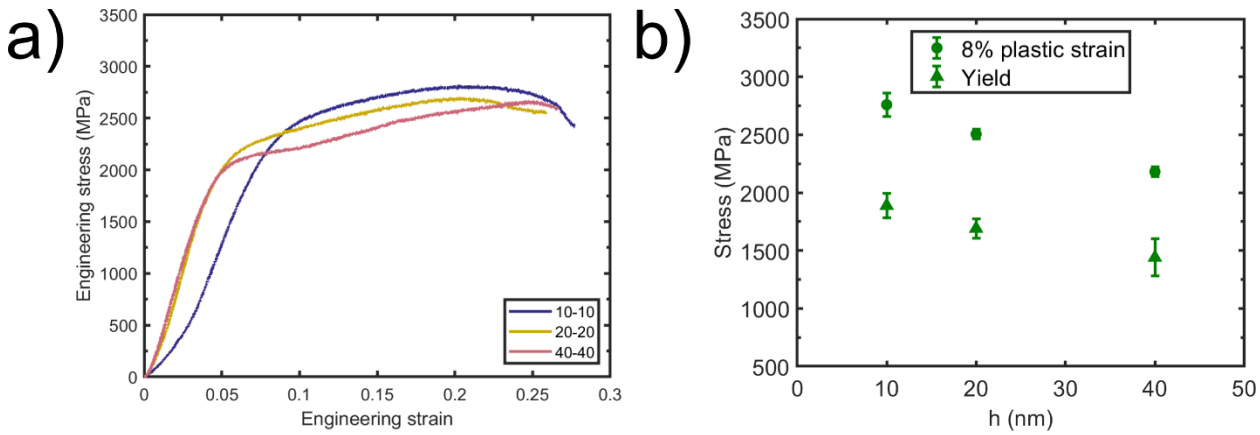

Figure 6-25 – a) Representative engineering stress-strain curves for samples with *h/h'* = 1. b) $\sigma_{8\%}$ presented as a function of *h* for samples in (a).

Figure 6-25 compares the micropillar behavior of samples with constant *h/h'* = 1, all of which have been examined via *in situ* snapshots in other figures. Figure 6-25(a) shows that as *h* is decreased with constant *h/h*' ratio, flow stress increases without sacrificing deformability. Significant stress drops all occur at comparable total strain of 0.22, which can be inferred to be comparable plastic strain due to similar elastic loading portions. Figure 6-25(b) confirms the flow stress trends seen in Figure 6-25(a) with respect to changing *h*. the difference between σ_y and $\sigma_{8\%}$ is similar between all specimens, indicating that work hardenability is maintained in the first 8% of plastic strain even as layer thickness, the effective grain size for the material, is decreased. This reinforces the findings of Section 6.2 that 3D interfaces provide a method for enhancing strength while maintaining deformability. The micropillar results here show that *h* and *h*' both dictate whether 3D interfaces can overcome strength-deformability tradeoff.

6.5.6. Flow stress when *h+h'* <= 50 nm

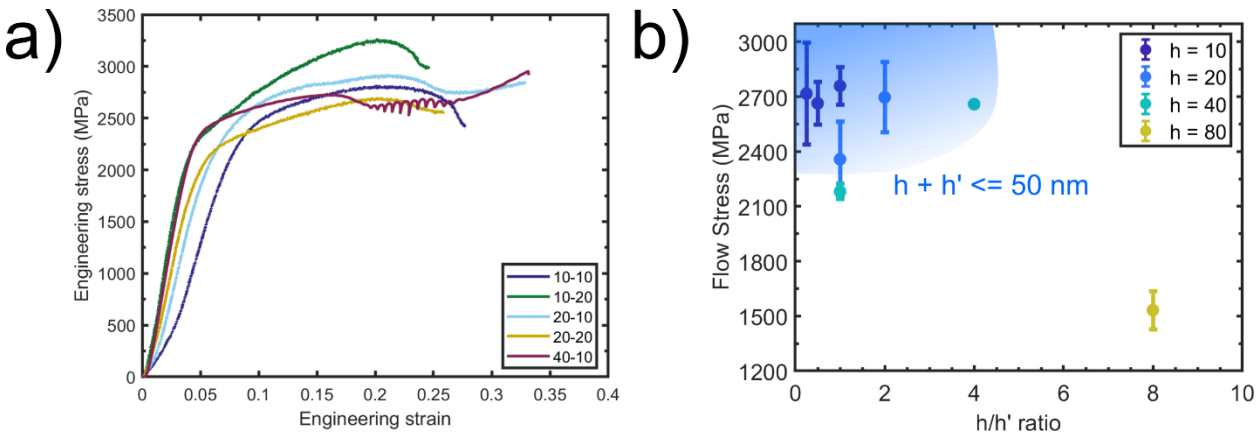

Figure 6-26 – a) Representative stress-strain curves for samples with *h+h'* <= 50 nm. b) $\sigma_{8\%}$ presented as a function of *h/h'* ratio for all samples studied. Samples with *h+h'* <= 50 nm all have similar flow stresses.

Figure 6-26 compares micropillar compression behavior for samples with *h+h'* <= 50 nm. Figure 6-26(a) shows the stress-strain behavior of this material, showing that they have similar $\sigma_{8\%}$. Flow stresses are similar between all specimens, and all have stress drops caused by shear localization at similar total strains of ~0.20 with the exception of 40-10 Cu/Nb. Comparison of flow stresses is quantified in Figure 6-26(b), which plots $\sigma_{8\%}$ for all samples tested in this works against *h/h'* ratio. Flow stresses are similar for specimens with *h+h'* <= 50 nm, demonstrating that mechanical behavior is not a strong function of layer or 3D interface thickness at this length scale. The reason for this behavior is discussed further in Section 6.6.5.

6.5.7. Limited deformability of 10-40 Cu/Nb

Many samples studied in this Section deform plastically in a similar manner, with a few exceptions at *h* > 20 nm. Notably, 10-40 Cu/Nb is the only *h* = 10 specimen to shear localize severely enough to produce a stress drop shortly after yield. The reasons for this are explored further with microstructural evaluation and comparison with amorphous CuNb.

6.5.7.1. Post mortem TEM

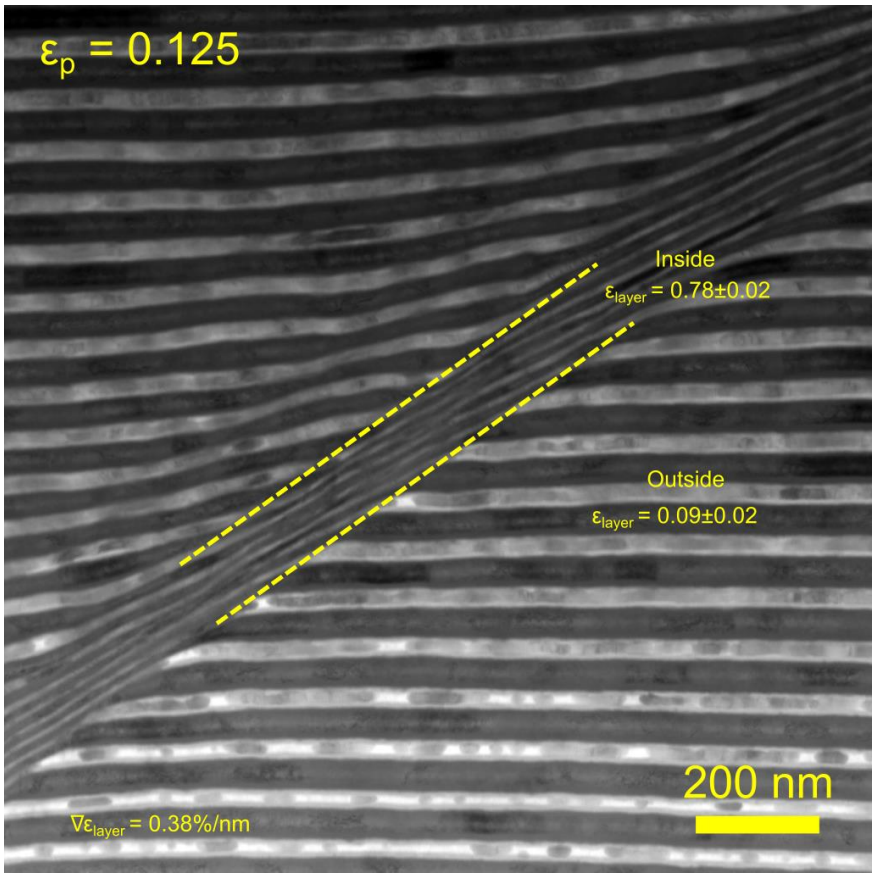

Figure 6-27 – Cross-sectional BF-STEM of 10-40 Cu/Nb deformed to 0.125 plastic strain. A shear band is found between the dotted yellow lines. ε_{layer} is calculated both inside and outside the shear band, giving a ε_{layer} gradient of 0.38%/nm. ε_{layer} gradient is denoted as $\nabla\varepsilon_{layer}$ in this figure.

Cross-sectional STEM of 10-40 Cu/Nb strained to a total strain of 0.125 is shown in Figure 6-27. A shear band passes through the center of the micrograph, in which layers and interfaces are heavily strained. ε_{layer} is found by averaging h_d across three bilayers inside and outside the shear band, then using h_o found from FIB cross-section. ε_{layer} gradient is also computed by calculating the change in ε_{layer} and dividing by the distance between bilayer measurement locations. The profiles used for measurement outside the shear band terminate at the shear band. Both maximum ε_{layer} and ε_{layer} gradient are higher than any nanolaminate previously studied in Table 6-1. The microstructural reasons for the high shear band severity and low deformability of 10-40 Cu/Nb

can be rationalized by considering the microstructure inside 10-40 3D interfaces. Material in the interiors of such 3D interfaces comprise co-sputtered CuNb in near-equiatomic proportions. Diffraction data from Chapter 5 suggest that this material is disordered enough to resemble amorphous material, and previous work confirms that equiatomically co-deposited CuNb prefers an amorphous structure[242]. In the next Section, the deformation of 10-40 Cu/Nb is compared to that of PVD amorphous CuNb to gain insights on shear localization in the former.

6.5.7.2. Comparison to amorphous equiatomic CuNb

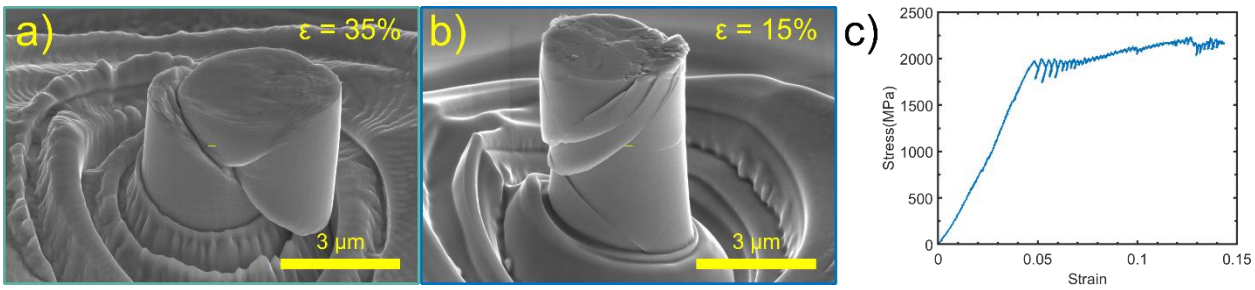

Figure 6-28 – Post-deformation SEM micrographs of a) 10-40 Cu/Nb at 0.35 total strain and b) cosputtered CuNb at 0.15 total strain. c) presents the engineering stress-strain curve associated with the pillar in b).

Post mortem SEM of deformed 10-40 Cu/Nb is compared to deformed amorphous CuNb in Figure 6-28(a-b). Figure 6-28(a) shows that 10-40 Cu/Nb compressed to 0.35 total strain shear localizes severely enough to rupture. The material forms multiple shear bands traversing the pillar width, with a smaller shear band impinging on a larger shear band that ultimately precipitated rupture. Figure 6-28(b) shows amorphous equiatomic CuNb that has been strained to 0.15 total strain. This material is more prone to shear localization than 10-40 Cu/Nb, with several shear bands traversing a significant fraction of the pillar width. Rupture has occurred in multiple locations, suggesting that uniform deformability is extremely limited in this material. The engineering stress-strain response of this pillar is shown in Figure 6-28(c). After the initial elastic loading portion of this curve, stress drops occur continuously along the stress-strain curve. These correspond to strain

softening and displacement bursts attendant with shear band formation in the pillar, as has been well-documented for many metallic glasses[243–245]. The apparent load-unload behavior in the stress-strain curve is attributed to momentary loss of displacement control by the control loop of the PI 88, which often happens during rapid load shedding events in nanomechanical testing. The correlation between severe shear localization and load drops are shared between 10-40 Cu/Nb and amorphous CuNb, indicating that disordered content plays a strong role in determining strength and deformability in 3D interfaces.

6.5.8. Nanoindentation of 3D Cu/Nb

The contribution of relative *h* and *h'* length scales to strength and deformability can also be characterized nanoindentation, which exerts a more complicated stress state on 3D interfaces than micropillar compression. Stress and strain gradients are found below an indent, which may influence measured hardness. Correlation of hardness to flow stress is conducted as well, with the caveat that such a correlation is not as trivial as assumed in the literature.

6.5.8.1. H and E_r depth profiles and validation of data

The CSM indentation used for this work produces depth profiles of E_r and H with respect to h_i for each indent performed. These profiles must be converted to representative moduli and hardnesses for calculation of statistics. This process will be described for 10-10 Cu/Nb as a representative example before examining hardness trends for 3D Cu/Nb. Figure 6-29(a-b) depicts E_r and H profiles for 10 indents. Here, h_i is used to denote indentation depth, to avoid confusion with *h* denoting Cu/Nb layer thickness. Both E_r and H are largely consistent with depth, which indicates reliability of the results, given the uniform microstructure of 3D Cu/Nb. Two indents produce outlier profiles of E_r and H, which will be disregarded for indentation statistics. There is

a slight decrease in H with increasing h_i, prompting an investigation of potential substrate influence on indentation results.

Substrate effects in nanoindentation of thin film specimens are well-documented in the literature[246–248], with recent work quantifying the maximum depths indentation can be conducted on thin films without significant influence of the substrate[249]. A seminal paper by Saha and Nix detail the detection of substrate effects, which will be detailed briefly here[250]. Saha and Nix raise common causes of substrate influence on thin film E_r and H measurements. These comprise indentation pile up, which influences A_c found by the Oliver-Pharr method, and substrate contributions to S, which influences measured E_r. The former is exacerbated by hardness mismatch between thin film and substrate, while the latter is triggered by elastic mismatch between the film and substrate. In either case, the assumptions underlying the Oliver-Pharr approach of E_r and H measurement are violated. Saha and Nix produce a method of detecting substrate influence on Oliver-Pharr property measurements independent of tip area function, a common confounder of nanoindentation data. They rearrange the expressions used to obtain E_r and H:

$$S = \beta \frac{2}{\sqrt{\pi}} E_r \sqrt{A_c}$$

$$P = H * A_c$$

(6-3)

If the quantity P/S^2 is computed:

$$\frac{P}{S^2} = \frac{1}{\beta^2} \frac{\pi}{4} \frac{H}{E_r^2}$$

(6-4)

The resultant expression is proportional to H/E_r^2, which is also known as the Joslin-Oliver parameter. All other terms in Equation (6-4) are constants. For a uniform material, the Joslin-

Oliver parameter should be constant with depth; any deviations on a thin film indicate that the substrate is likely contributing to measured quantities. It should be noted that other depth-dependent effects can cause deviations in P/S^2 such as imperfections in tip geometry[251] or indentation size effects[252]. The latter need not be considered for this work due to the fine size of the 3D Cu/Nb microstructure compared to the indentation depths used.

P/S^2 is presented in Figure 6-29(c), indicating that past 500 nm, no substrate influences are expected for the indents performed. Any depth-dependent trends can then be attributed to deviations of the tip area function from ideal behavior. For these tests, the indenter tip was calibrated to fused silica to a maximum depth of 600 nm using 4 tip area function coefficients with c_o fixed. Thus, results deeper than 600 nm are an extrapolation of the quartz calibration, which may produce slight E_r and H trends with respect to indentation depth despite the uniformity of the material. In light of the data from Figure 6-29(a-c), representative moduli and hardnesses for each indent were taken as averages from measured quantities between 800-1000 nm indentation depth.

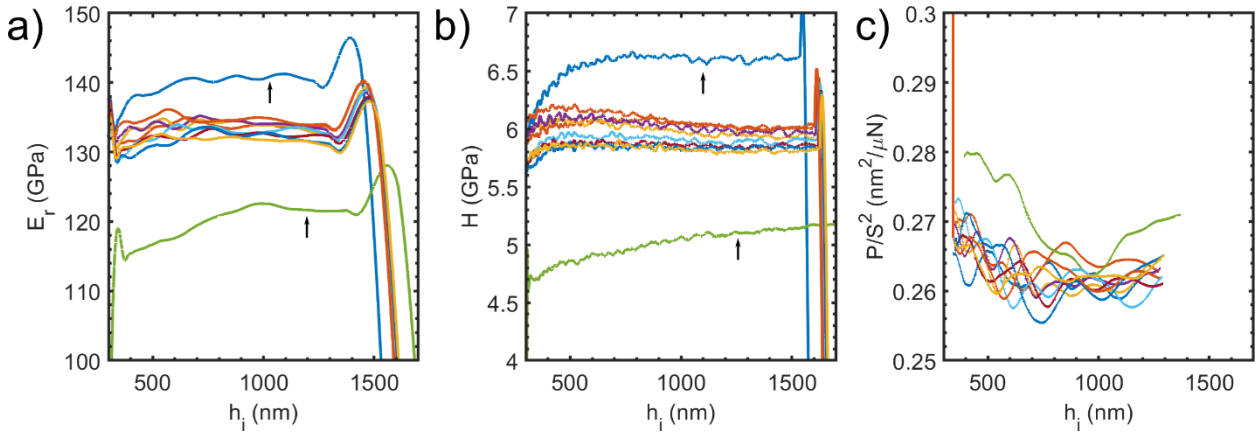

Figure 6-29 – a) E_r, b) H, and c) P/S^2 plotted as a function of h_i for 10-10 Cu/Nb for all indents performed. Outlier curves are indicated by black arrows in (a-b).

6.5.8.2. Nanohardness trends for 3D Cu/Nb

Figure 6-30 shows the representative hardnesses extracted from H profiles as discussed for Figure 6-29. E_r can be found in the Appendix for all samples and is consistently found to be between 125-135 GPa across all samples. Figure 6-30(a) depicts H as a function of *h* for specimens with constant *h'* = 10 nm. The 2D interface data from Figure 6-21 are included for comparison. Similar to micropillar flow stress, hardness increases as *h* decreases for 3D Cu/Nb. However, hardness does not saturate at *h* = 20 nm and increases from 20-10 to 10-10 Cu/Nb. Comparison of the 3D to 2D Cu/Nb indentation data shows that the presence of 10 nm thick 3D interfaces does not influence Berkovich hardness. Comparison to the differences between 2D and 3D interface-dominated deformation in Sections 6.2-6.4 indicates that the contribution of 3D interfaces to mechanical behavior is dependent on applied stress state. Figure 6-30(b) shows H trends with respect to *h´* in samples with constant *h* = 10 nm. As was found for flow stresses, hardness is not a strong function of 3D interface thickness for this *h*. Figure 6-30(c) depicts H trends as a function of *h* for samples with constant *h/h'* = 1. Again, results mirror flow stress trends found in micropillar tests, as hardness is found to increase with decreasing *h*. Comparing Figure 6-30(a) and Figure 6-30(c), the inclusion of 40 nm 3D interfaces increases measured hardness from ~4.2 GPa to 5 GPa at *h* = 40 nm. This suggests that 3D interface volume fraction must be higher for hardness testing than for micropillar compression to manifest changes in measured mechanical behavior. Figure 6-30(d) shows hardness trends with respect to *h'* for samples with constant *h* = 20 nm. No trend is found for the 3D interface thicknesses investigated. Comparison of Figure 6-30(b,d) shows that measured hardness is a strong function of *h* for various *h'*, which is different than flow stress trends demonstrated in Figure 6-26(b). This supports the earlier normal and 45 degree compression

results showing that 3D interface contribution to mechanical behavior is dependent on loading orientation.

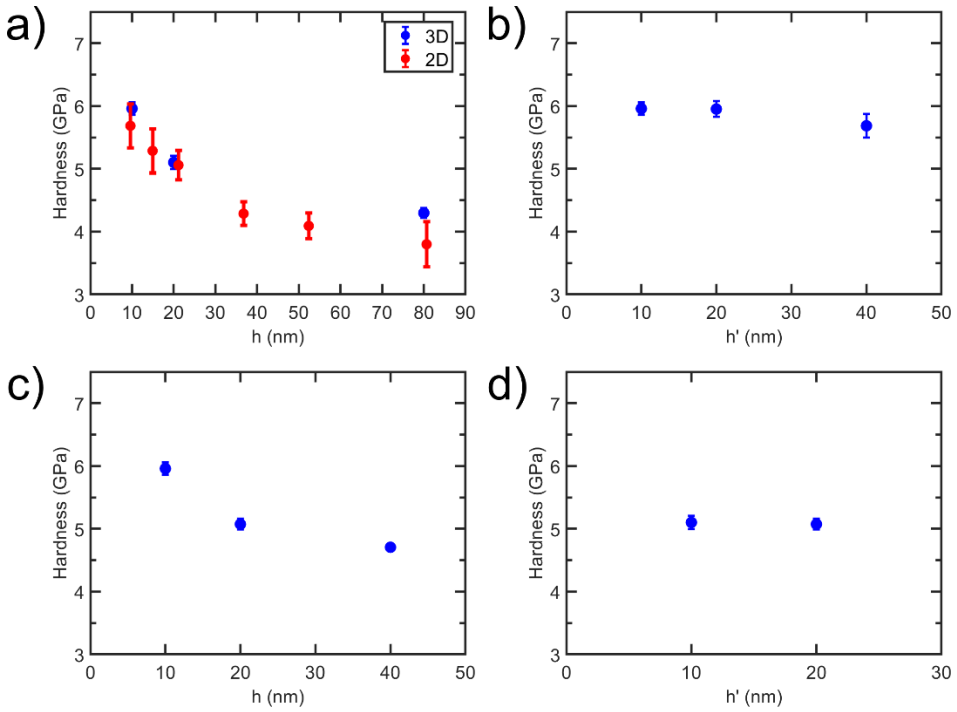

Figure 6-30 – Average indentation hardness for a) *h'* = 10 nm, b) *h* = 10 nm, c) *h/h'* = 1, and d) *h* = 20 nm samples. Indentation hardness for 2D Cu/Nb from Ref. 15 is included in a). Error bars represent one standard deviation.

6.5.8.3. Correlation of nanoindentation data to micropillar results

Availability of nanoindentation and micropillar data for the same materials provides an opportunity to interrogate stated assumptions about Tabor factor. Figure 6-31 presents Tabor factors all samples by dividing H values in Figure 6-30 by corresponding $\sigma_{8\%}$ values from Figure 6-22 to Figure 6-26. Tabor factors are similar across all samples except for 80-10. Tabor factors excluding that of 80-10 Cu/Nb range from 1.90-2.16. 80-10 Cu/Nb has a Tabor factor of 2.80, indicating that it behaves like a conventional engineering alloy when comparing hardness to uniaxial flow stress. For comparison, a Tabor factor of 2.7 corresponding to ε_r of 2-5% has been found for 2D Cu/Nb with *h* = 40 and 5 nm[16,17]. The divergent Tabor factors of the other samples

indicates that 3D interfaces change σ_y and n enough from 2D Cu/Nb that the common assumption of Tabor factor of 2.7-3 corresponding to $\varepsilon_i = 8\%$ does not apply. Recalculation of the 10-10 Cu/Nb Tabor factor using true stress-like taper corrected values from prior work gives a Tabor factor of 2.3, meaning that the difference between engineering and true stress is not enough to account for the discrepancy in Tabor factor. This discussion demonstrates that under the assumption of $\varepsilon_i = 8\%$, 3D interfaces modify mechanical behavior sufficiently to manifest a departure of Tabor factor from the 2.7-3 value found for conventional metals.

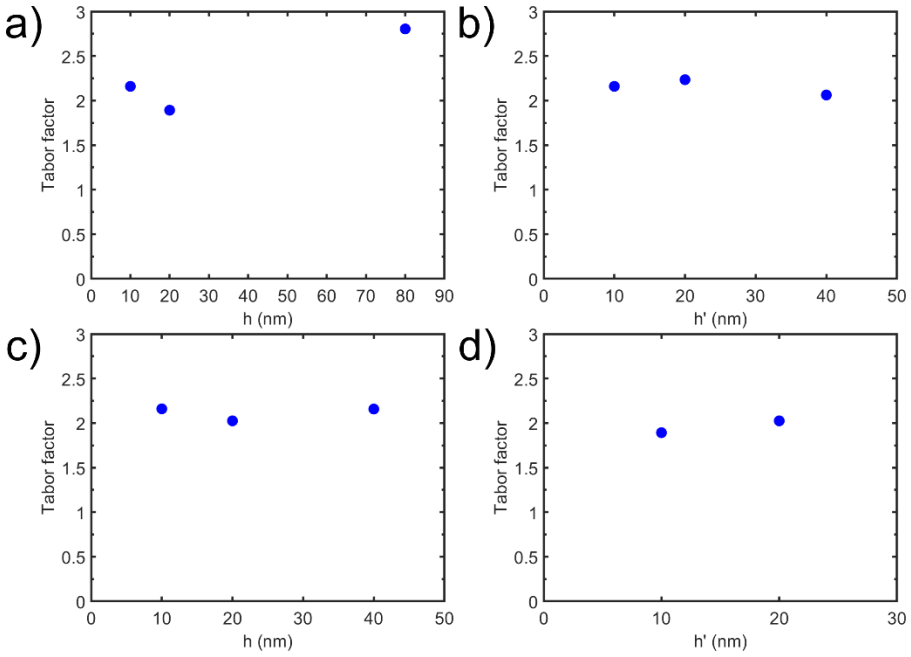

Figure 6-31 – Tabor factors for a) *h'* = 10 nm, b) *h* = 10 nm, c) *h/h'* = 1, and d) *h* = 20 nm samples.

6.6. Discussion

6.6.1. Shear band formation mechanism

6.6.1.1. Shear localization in 2D Cu/Nb

The shear localization process in 2D Cu/Nb should be briefly discussed to contextualize the effect of 3D interfaces on deformability. Mara, et al. present a model for this process, which is reproduced in Figure 6-32[16]. In Figure 6-32(a), the material begins with layer and interface normal

parallel to the loading axis. Slip systems can be categorized as initially non-parallel to interfaces (A and B) or parallel to interfaces C. At high plastic strain, the microstructure adopts the configuration in Figure 6-32(b). Stress concentrators such as pillar corners at the top of the micropillar produce uneven slip system activation, causing lattice rotation. Slip systems of type C rotate such that there is significant resolved shear stress on them, producing shear stress on heterophase interfaces when type C slip intersects the interfaces. This shear stress causes interface sliding, which precipitates deformability-limiting shear banding. Interface sliding is energetically favorable in Figure 6-32(b) due to the low interfacial shear stress of 2D Cu-Nb interfaces as found by MD and experiments[4,20].

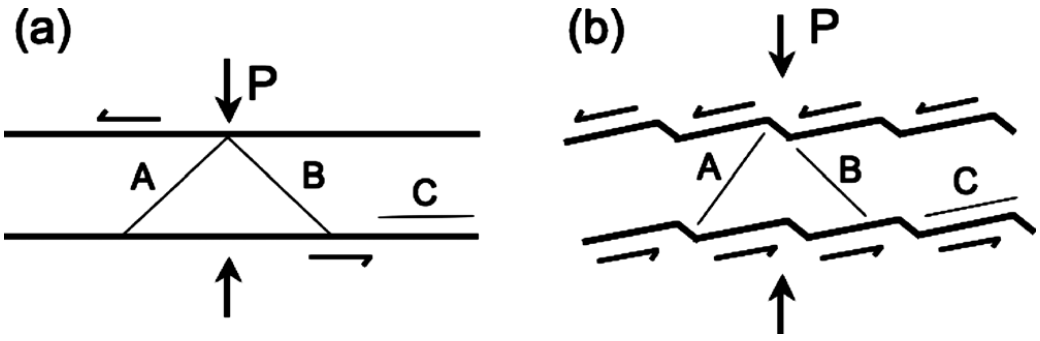

Figure 6-32 – Schematic diagram of shear band formation in 2D Cu/Nb. a) Slip systems A and B start inclined to layers, while slip system C is parallel to layers. b) Lattice rotation during deformation causes slip systems A-C to rotate, producing shear strain on interfaces, which then slide and precipitate failure. Reproduced from Ref. 16.

6.6.1.2. Shear localization in 3D Cu/Nb

3D Cu/Nb follows a similar shear localization process as 2D Cu/Nb. The model for shear localization was proposed by Chen, et al. in previous work[228], and the current work provides experimental substantiation of that mechanism. A schematic describing shear localization in 3D Cu/Nb is found in Figure 6-33. Similarly to 2D Cu/Nb, it is useful to categorize slip systems as initially interface non-parallel (Type I) and parallel (Type II) as shown in Figure 6-33(a). Again, lattice rotation is precipitated by stress concentrators in Figure 6-33(b). These occur at pillar

corners arising from moments at constrained pillar ends due to interaction of slip geometry and constraint-based displacement boundary conditions[253]. In Figure 6-33(c), Type II slip systems have rotated such that they experience substantial resolved shear stress. However, in this case, interface sliding does not follow. This is substantiated by the results of Section 6.4 demonstrating the substantial work hardenability of 3D Cu-Nb interfaces that allows them to sustain large shear strains without forming plastic instabilities. Instead, shear localization occurs when enough dislocation content builds up on aligned Type II slip systems across multiple adjacent layers in Figure 6-33. This forms a dislocation "super pile-up" across multiple layers that confers a mechanical advantage to slip transfer across heterophase boundaries despite the strengthening effect of 3D interfaces. This mechanism will be discussed in the context of layer thickness effects in the next Section.

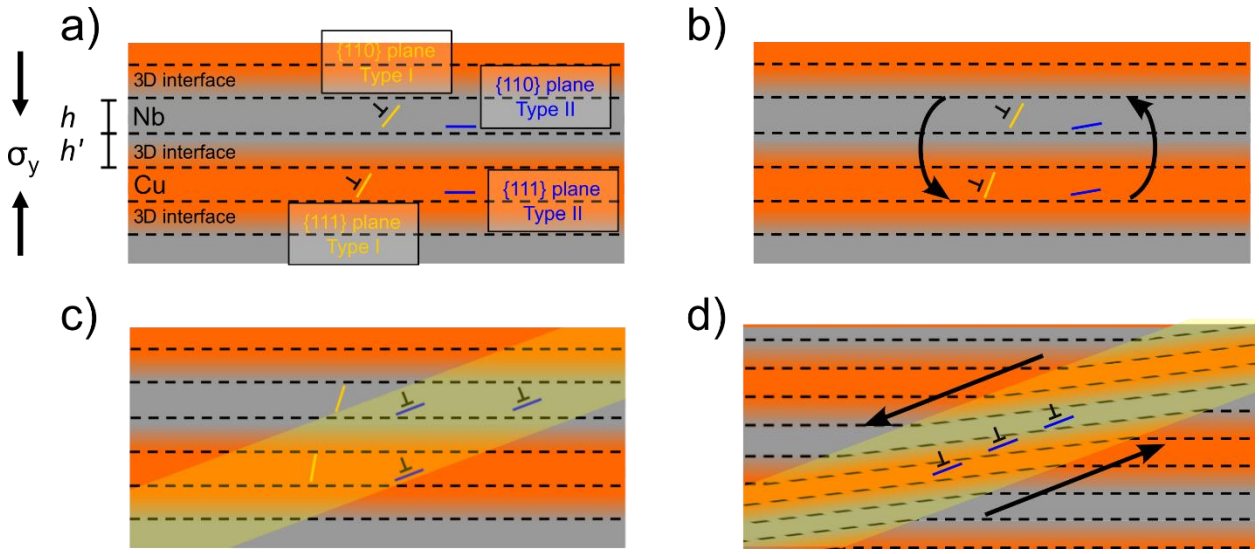

Figure 6-33 – A schematic diagram of shear band formation in 3D Cu/Nb. a) Slip planes can be divided into two categories, inclined to layers (type I) and parallel to layers (type II). b) Stress concentrators at pillar corners cause lattice and slip plane rotation. c) At high enough global strain, type II slip systems align across multiple layers. This allows for the formation of a shear band, in the region indicated by yellow shading. d) Accumulation of dislocations on common type II slip systems causes stress concentration sufficient to drive a shear band through the material. Adapted from Ref. 233.

6.6.1.3. Dislocation-based rationalization of shear localization

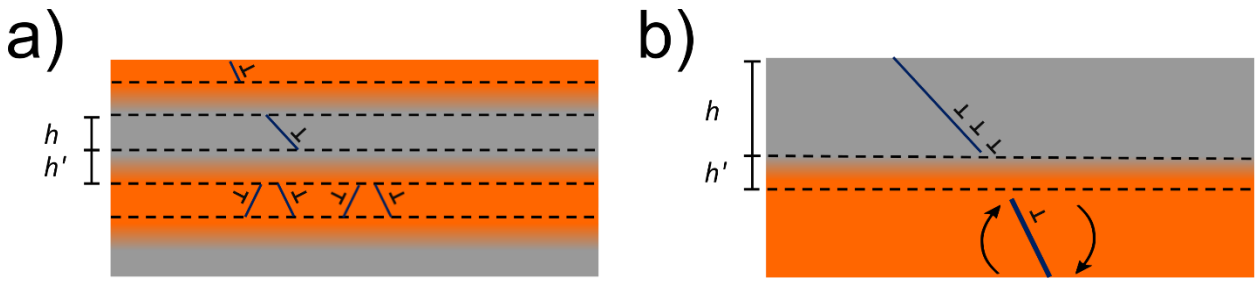

Figure 6-34 – Diagrams depicting hypothesized dislocation pileup-interface interactions in a) 10-10 and b) 40-10 Cu/Nb. a) depicts the effect of limited pileup size relative to 3D interface thickness – slip transfer is stifled enough to inhibit formation of a highly localized shear band. In b), pileup size is large enough to encourage slip transfer along common slip systems across pure metal layers, facilitating formation of a sharp shear band.

The results of Sections 6.2-6.3 show that strength and deformability is higher for 10-10 Cu/Nb when compared to 40-10 Cu/Nb. Also, shear localization is less severe in the former case than the latter. These motivations motivate the hypothesis that shear band propensity is dictated by the relative length scale between dislocation pileups and 3D interface thickness (Figure 6-34). Figure 6-34(a) proposes that in 10-10 Cu/Nb, there is not adequate room for dislocation storage in the form of pileups. This has the immediate consequence that no substantial mechanical advantage can develop to drive slip transfer across 3D interfaces on Type II slip systems across successive pure layers. This raises the global flow stress of the material, which then activates slip systems with non-maximal Schmid factor. Slip is more evenly distributed over all available slip systems and slows the lattice rotation that would drive shear band formation along Type II slip systems. In contrast, 40-10 Cu/Nb can store significantly sized dislocation pile-ups as depicted in Figure 6-34(b). Thus, less lattice rotation is required to drive interlayer slip across 3D interfaces along aligned, rotated Type II slip systems. Slip can transmit effectively across 3D interfaces in 40-10

Cu/Nb, and shear bands form earlier and limit deformability to a greater extent than in 10-10 Cu/Nb.

6.6.1.3.1. Description of PFDD

While the mechanism depicted in the previous Section appears compelling, it requires quantitative support to be plausible. Thus, this work was done in parallel with collaborators at University of California Santa Barbara to develop a hybrid experimental-computational approach to explore the impact of 3D interfaces on mechanical behavior. The computation arm of this work was done mainly using phase field dislocation dynamics (PFDD), a technique that will be described briefly here. The background required for this discussion is paraphrased from an article in *Computer Methods in Applied Mechanics and Engineering* completed in support of this thesis[254].

PFDD is a technique that can simulate the motion of multiple dislocations at quasi-static time scales while incorporating atomistically-derived details of slip. This is a capability not achievable through other methods such as MD or DDD[254]. PFDD takes material parameters such as elastic properties and generalized stacking fault energy curve (which encodes atomistic detail) as inputs and can output the stress needed to propagate collections of dislocations through a microstructure with nanoscale features such as 3D interfaces. Simulation is accomplished by use of a box comprised of continuum volume elements with step size on the order of interatomic distances. The key concept underlying PFDD is the use of a spatially varying order parameter φ. This parameter represents the amount that a volume element of material has slipped. Non-slipped material has $\varphi = 0$, while most slipped material takes on integer values of φ. For example, material that has slipped by one perfect Burgers vector has a φ of 1, while material that has slipped by two Burgers vectors has φ of 2, etc. Regions of material inside dislocation cores or in stacking faults can adopt non-integer values. Slip across multiple slip systems is tracked by a list of order

parameters $\boldsymbol{\varphi}$ whose elements are φ_α, where α denotes a specific slip system. The energetics of dislocation motion is encoded by a position-dependent energy density functional ψ that is dependent on $\boldsymbol{\varphi}$ and other parameters. At a given location, it takes the form:

$$\psi(\boldsymbol{\varepsilon}, \boldsymbol{\phi}) = \psi_{ela}(\boldsymbol{\varepsilon}, \boldsymbol{\phi}) + \psi_{lat}(\boldsymbol{\varepsilon}, \boldsymbol{\phi}) + \psi_{ext}(\boldsymbol{\varepsilon}, \boldsymbol{\phi})$$

(6-5)

Here, $\boldsymbol{\varepsilon}$ the applied strain in tensor form, $\boldsymbol{\varphi}$ is the list of order parameters, ψ_{ela} is an elastic strain energy density contribution, ψ_{lat} is the energy density contribution from plastic deformation of the lattice (i.e. the lattice energy parameterized by the generalized stacking fault energy curve along the slip direction), and ψ_{ext} is the strain energy density stored by the material due to an externally applied stress. The energy density contributions have the form:

$$\psi_{ela}(\boldsymbol{\varepsilon}, \boldsymbol{\phi}) = \frac{1}{2}\left(\boldsymbol{\varepsilon} - \boldsymbol{\varepsilon_p}(\boldsymbol{\phi})\right) \cdot \boldsymbol{C}\left(\boldsymbol{\varepsilon} - \boldsymbol{\varepsilon_p}(\boldsymbol{\phi})\right)$$

$$\psi_{ela}(\boldsymbol{\varepsilon}, \boldsymbol{\phi}) = \frac{\gamma_{gsf}(\boldsymbol{\phi})}{l_{gsf}}$$

$$\psi_{ext}(\boldsymbol{\varepsilon}, \boldsymbol{\phi}) = \boldsymbol{\sigma_{app}} \cdot \boldsymbol{\varepsilon_p}(\boldsymbol{\phi})$$

(6-6)

where $\boldsymbol{\varepsilon}$ is the total strain tensor resulting from an externally applied stress $\boldsymbol{\sigma_{app}}$, $\boldsymbol{\varepsilon_p}$ is the plastic strain contributed by dislocation slip, $\mathbf{C}$ is the stiffness tensor containing the crystal's elastic constants, γ_{gsf} is energy contribution from slipped regions as parameterized by GSFE curve, and l_{gsf} is the interplanar spacings on the active slip system. $\boldsymbol{\varepsilon_p}$ is determined by summing the amount of slip across all slip systems using each slip system's Nye tensor. For this work, $\mathbf{C}$ and γ_{gsf} were parameterized using MD simulations completed by the dissertation author[254]. Using Equation (6-5), the physics of dislocation-dislocation interactions, image forces on dislocations, elastic anisotropy

and dislocation core dissociation can be captured[255]. This gives PFDD the ability to simulate dislocation motion at the mesoscale while retaining the atomistic details of dislocation energetics.

To find the equilibrium position of dislocations at a given $\boldsymbol{\sigma_{app}}$, the time-dependent Ginzburg-Landau equation is used. For all φ_α the following expression is minimized:

$$\dot{\phi_\alpha} = -m_0 \partial_{\phi_\alpha}(\psi_{ela} + \psi_{lat} + \psi_{ext}) \tag{6-7}$$

The dot represents a time derivative and ∂_{ϕ_α} is the partial derivative with respect to φ_α. m_0 is a non-negative constant. It is important to note that time in Equation (6-7) is not a physical time. Equation (6-7) is recursively minimized to produce the equilibrium positions of dislocations in the box at a given $\boldsymbol{\sigma_{app}}$. To measure the stress required to move dislocations past obstacles, $\boldsymbol{\sigma_{app}}$ is increased in small increments. At each increment, Equation (6-7) is minimized until convergence or a set number of iterations, whichever comes first. The simulations presented here requires simulation of a heterogeneous system, which is done in a computationally efficient way by modifying Equation (6-5) to include virtual strains. This will not be discussed here and the reader is encouraged to refer to Ref. 254 for further detail.

6.6.1.3.2. Application of PFDD to shear localization

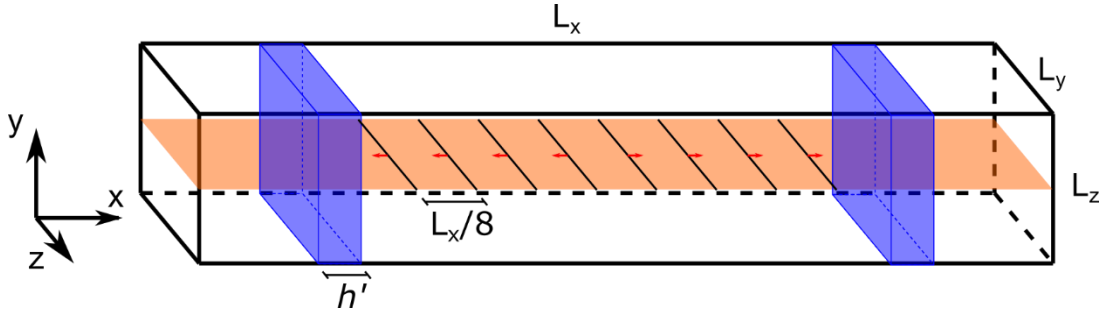

Figure 6-35 – Configuration of four-dislocation PFDD simulation box at no applied stress and before energy minimization. BCC Nb represents the pure layers and BCC $Nb_{0.9}Cu_{0.1}$ represents the 3D interfaces. L_x, L_y, and L_z are the x, y, and z box dimensions. 3D interfaces are found at the shaded blue regions, while the orange plane is the slip plane, chosen to be (110). Non-colored

regions are pure BCC Nb. Dislocation lines are depicted as black lines on the slip plane with red arrows depicting Burgers vectors. They are equally spaced with a spacing $L_x/8$. 3D interface thickness is denoted as *h'*. The box is symmetric about the y-z plane at the x-midpoint of the box. The box is not drawn to scale.

Figure 6-34 depicts the hypothesis explaining why strength and deformability increase simultaneously from 40-10 to 10-10 Cu/Nb. This argues that when *h*-limited dislocation pileup size is small compared to *h'*, shear banding is frustrated because interlayer slip is blocked by 3D interfaces. To that end, PFDD simulations were conducted to characterize the stress required to transmit the lead dislocation in a pileup across a 3D interface as a function of pileup size and *h'*. The nanolaminate was modeled as two pure BCC Nb regions abutting a BCC $Cu_{0.1}Nb_{0.9}$ region representing a 3D interface. Computation is conducted in a box large enough to accommodate dislocations at equilibrium spacing under no applied stress. This box is presented in Figure 6-35. Periodic boundary conditions are applied in all three dimensions. Dislocations are initialized as dipoles consisting of two edge dislocations with opposite Burgers vectors. Dipoles are used because this PFDD formulation requires that networks of simulations dislocations have a net Burgers vector of zero[256]. This also allows less material to be simulated on the side of the interface opposite the pileup, as the dislocation dipoles annihilate after transmission across the 3D interface. The simulation axes are oriented with crystallographic directions such that $x||[111]$, $y||[1\bar{1}0]$, and $z||[11\bar{2}]$. Only one slip system is active in this simulation, which will be denoted the $(1\bar{1}0)[111]$ slip system. Thus, only one order parameter is needed for this simulation. All dislocations lie on the mid-*y* plane of the box and are equidistant from each other. L_x, L_y, and L_z are the box dimensions in the *x*, *y*, and *z* directions, respectively. In all cases, L_y = 15 nm and L_z = 35 nm. Four dislocation dipoles were inserted in a box with L_x = 294 nm. Two 3D interfaces with interface normal direction along the x axis are found 9 nm from the box x boundaries. Values of a_0 and γ_{usf} in Nb are from

prior density functional theory (DFT) calculations; values of C_{11}, C_{12}, and C_{44} in Nb are from experiments; all values in $Cu_{0.1}Nb_{0.9}$, are from atomistic simulations using an embedded-atom method (EAM) potential. These quantities can be found in Table 6-6. The (110) plane is set as the common glide plane in both the Nb layer and 3D interface alloy. In $Cu_{0.1}Nb_{0.9}$, 20 GSFE curves are calculated using 20 random atomic structures, with the median GSFE curve taken as representative of the alloy. In each phase, the peak value of the GSFE curve parameterizing the Peierls barrier is also called the unstable stacking fault energy (USFE), γ_{usf}. A snapshot of a PFDD simulation is found in Figure 6-36.

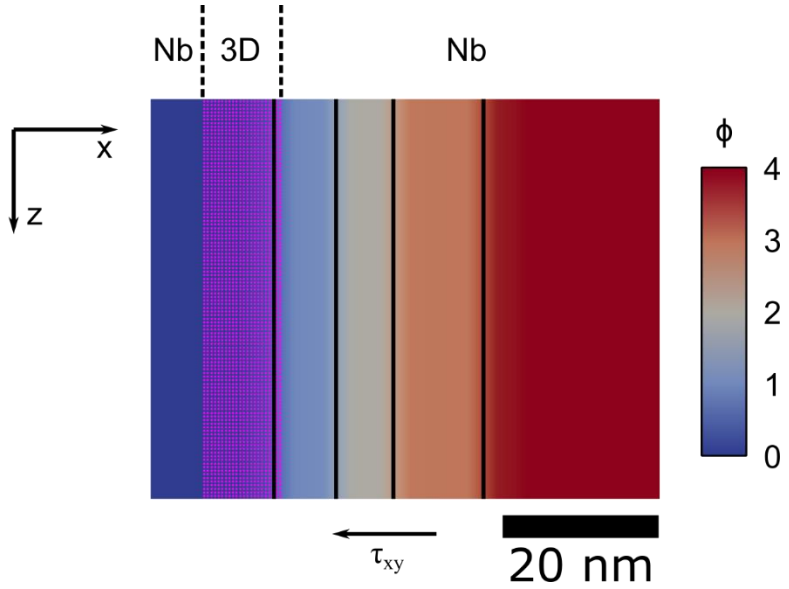

Figure 6-36 – A snapshot of a PFDD simulation normal to the slip plane in which a four dislocation pileup interacts with a 3D interface. Only part of the box is shown. Dislocations, denoted by solid black lines, are found in between regions of integer φ. The applied shear stress τ_{xy} acts to transmit the dislocations through the 3D interface. Here, the lead dislocation in the pileup has entered the 3D interface and begun transmission.

For each simulation, stress is increased until sufficient to pile up dislocations at the 3D interface. Applying additional stress transmits the leading dislocation into the 3D interface. Once the lead dislocation is injected into the 3D interface, it glides through to the other side of the 3D interface with no additional stress increment. This represents the critical stress for dislocation

transmission across the 3D interface. After the lead dislocation transmits, the pile up and associated mechanical advantage decrease, so an increased applied stress is required for the next dislocation to transmit. Figure 6-37(a-d) illustrates this phenomenon, depicting transmission of each dislocation in a four-dislocation wide pileup across a 3D interface of *h'* = 10 nm. As more dislocations cross the interface, the critical crossing stress increases from 1.53 GPa to 1.88 GPa.

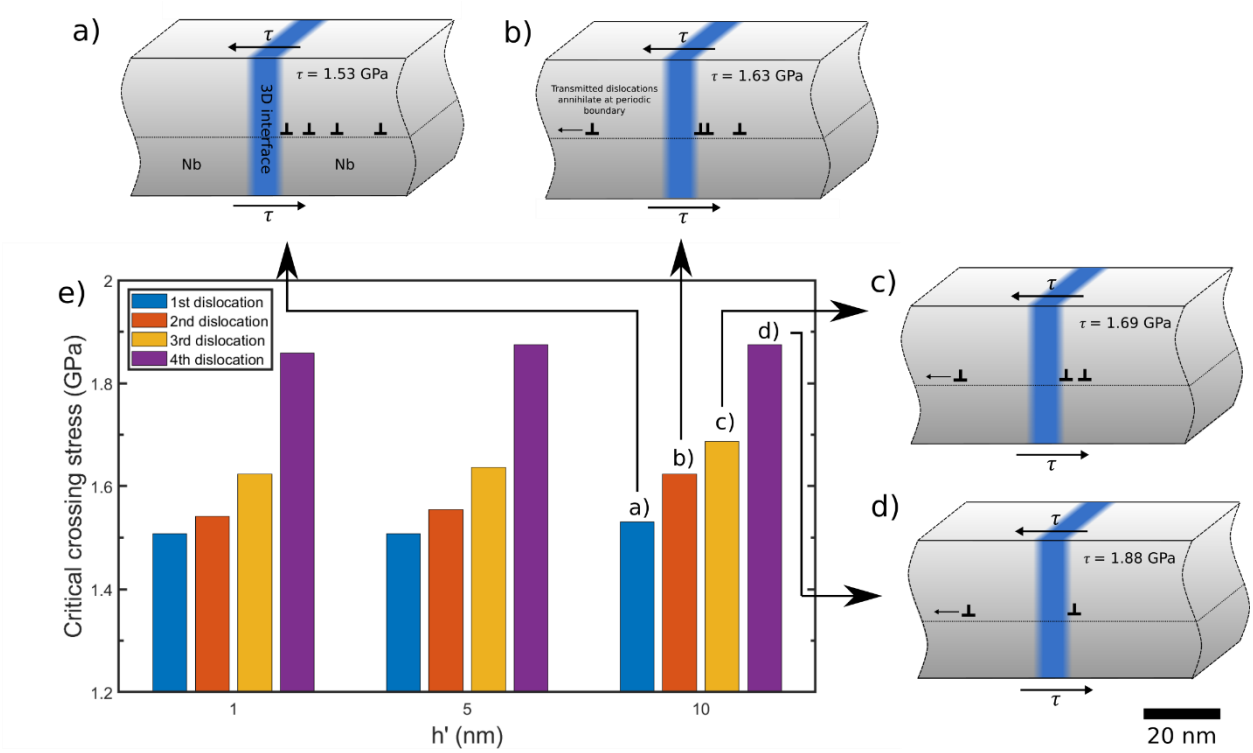

Figure 6-37 – (a-d) A depiction of the interaction of a 4 dislocation-wide pileup with a 10 nm 3D interface and e) charts of stress required to transmit each dislocation in a pileup across a 3D interface, presented as a function of *h'* on the horizontal axis and pileup size in chart titles. The y-axis in e) is truncated to aid in visualization of difference in dislocation transmission stresses. In (a-d), pileup dislocation positions are drawn to scale in relation to the 3D interface at the critical shear stress required to transmit the leading dislocation. The simulation box is truncated in this depiction to draw attention to details of the pileup.

PFDD is used to determine the stress required to transmit the lead dislocation across 3D interfaces with *h'* = 1, 5, and 10 nm for as each dislocation in a four-dislocation pileup transmits across the interface. Figure 6-37 shows that the critical crossing stresses for leading pileup

dislocations are inversely proportional to pileup size, while they are proportional to *h'*. This suggests that the thicker a 3D interface is, the higher stress barrier to slip transfer it poses. The largest effect that a 3D interface has on dislocation transmission manifests for *h'* = 10 nm in the critical crossing stress required for transmission of the second and third pileup dislocations. From Figure 6-37, when *h'* = 10 nm, the crossing stress for each dislocation increases by about 100 MPa for the second and third dislocations to cross as compared to lower *h'*. Although this represents a small stress difference, it is enough to encourage slip activation on other slip systems with nearly the same Schmid factor. This encourages homogeneous deformation and increases the applied stress required to plastically deform the material. The 3D interface also effectively blocks interlayer slip, frustrating shear band formation on slip systems shared among multiple layers. Clearly, sufficiently thick 3D interfaces attenuate the stress concentration produced by piled-up dislocations at heterophase interfaces. Combining PFDD results with the experimental observations that 40-10 Cu/Nb shear localizes more readily than 10-10 Cu/Nb shows that the relative scale between maximum pileup size allowed by *h* and 3D interface thickness *h'* determines whether interlayer slip is frustrated.

While the structure in the PFDD simulation is simplified compared to what is experimentally observed, it still captures the fundamental physics of dislocation-3D interface interactions. Here, the boundary between Nb and the 3D interface is assumed coherent, which is reasonable considering the similar lattice parameters for Nb and the Nb-rich side of the 3D interface. The boundary between pure Nb and Nb-rich regions of the 3D interface were also seen to be coherent in structural characterization presented in Chapter 5. These simulations capture the most important feature of 3D interfaces in that they present barriers to slip greater than the Peierls barrier found in a pure lattice. Here, this feature is encoded in a higher Peierls barrier in the CuNb

alloy and the image forces exerted by the stiffer alloy on the dislocation in the more-compliant pure material. These features are quantified by γ_{USF}, which is 703.46 mJ/m^2 for the alloy and 676.78 mJ/m^2 for pure Nb along the <110> direction and the shear modulus μ, which is 40.4 and 39.6 GPa in the alloy and pure Nb, respectively. These quantities are from Table 6-6. More complex PFDD models can be employed to simulate 3D interfaces with a more realistic model representation, which will be discussed in Section 6.6.5.1.

6.6.2. Strength-deformability synergy in 10-10 Cu/Nb

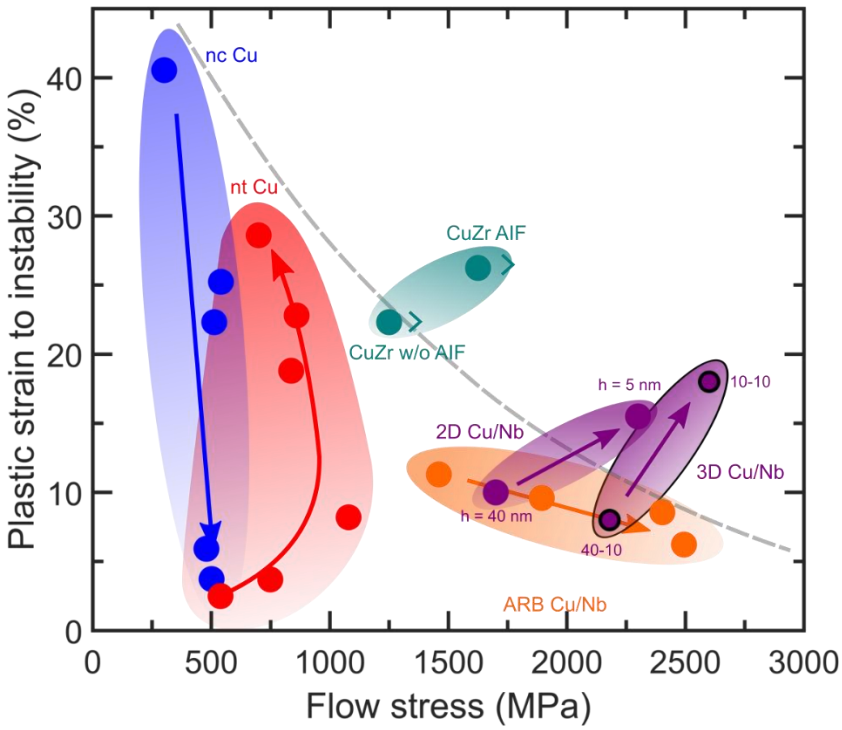

Figure 6-38 – Plastic strain at onset of plastic instability plotted against flow stress for nanocrystalline (nc) and nanotwinned (nt) Cu, PVD and ARB 2D Cu/Nb, CuZr alloy, and 3D Cu/Nb. Arrows indicate decreasing dislocation obstacle spacing (other dislocations, grain boundaries, twin boundaries, or heterophase interfaces). There is no arrow for CuZr, since properties are solely enhanced by introduction of AIFs (not by a change in obstacle spacing). Chevrons are also included for CuZr alloys to denote that deformability may be higher than indicated; *in situ* results were not available or tests were terminated prior to shear localization. Note that in both PVD 2D and 3D Cu/Nb, strength and plasticity do not exhibit a trade-off as layer thickness decreases. Below the dashed line, materials undergo the strength-ductility trade-off. These data comprise a mix of tensile and compressive tests and all stress and strain values are true (converted from engineering assuming uniform deformation where necessary).

Increasing deformability with finer nanoscale layer thickness is counterintuitive since most nanostructured materials become more prone to strain localization as grain size reduces and strength increases. These trends are examined in the context of other nanocrystalline alloys in Figure 6-38. Here the flow stress at onset of shear localization and the extent of homogeneous plastic strain are plotted in for 3D Cu/Nb and a variety of related materials, including 2D Cu/Nb made via PVD[16,17] and ARB[257], nanocrystalline (nc)[258] and nanotwinned (nt) Cu[259], and CuZr nanostructured alloys[260]. For Cu/Nb, onset of shear localization is defined by an abrupt change in pillar shape concurrent with a significant drop in flow stress. In nanostructured materials that do not display such instability, such as nc or nt Cu, the onset of shear localization is taken as the strain at which ultimate tensile/compressive stress occurs. In most nanocrystalline metals like nc Cu and nt Cu, flow stress is enhanced at the expense of plasticity by decreasing the mean distance between dislocation obstacles. This distance is dictated by grain size (nc Cu), twin boundary spacing (nt Cu), or layer thickness (ARB Cu/Nb). In the other nanostructured materials with controlled interfaces mentioned, there is no such tradeoff between flow stress and strain to shear instability. 3D Cu/Nb falls in the latter category, constituting an optimal combination of microstructural length scales to achieve strength and deformability. A lesser drop in layer thickness in 3D Cu/Nb is required to achieve comparable improvements in strength and deformability as compared to 2D Cu/Nb. This discussion demonstrates that 3D interfaces constitute a distinct method of engineering simultaneous strength and deformability in the context of previously studied nanostructured alloys and nanolaminates.

6.6.3. Slip system activity in 45 degree compression

6.6.3.1. Schmid factor analysis

The delocalized deformation and work hardening observed in 45 degree 10-10 Cu/Nb is somewhat surprising given the anisotropic nature of the material. One might expect that slip should favor either interfaces or only the Cu {111}<110> and Nb {110}<111> slip systems oriented parallel to the interface and layer planes, since these features are aligned along the direction of maximum resolved shear stress. The role of Schmid factors on slip system activation are used to predict the expected slip pathways in 10-10 Cu/Nb. Using the texture measurement in Figure 5-8, the Schmid factor is calculated for slip systems that are oriented for 45 degree compression for a range of rotation angles about the interface normal direction. Figure 6-39 shows that slip on planes parallel to layers is geometrically favored for most crystal orientations in the fiber texture, but some

orientations favor slip on non-layer parallel systems.

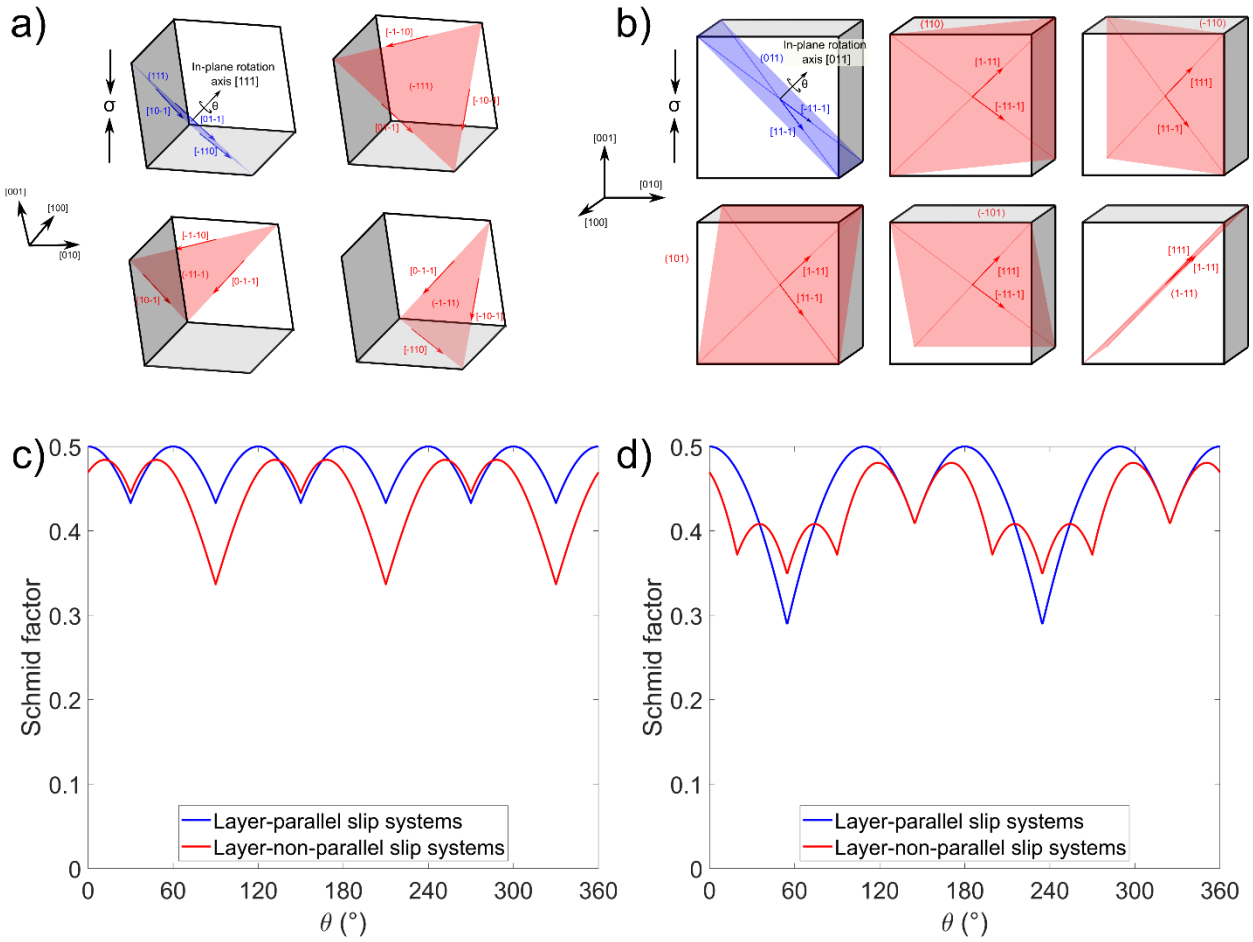

Figure 6-39 – Depictions of slip systems in (a) Cu and (b) Nb. In Cu, 1 slip plane containing 3 slip directions is parallel to the plane of maximum resolved shear stress parallel to interfaces and layers. 3 slip planes with 3 slip directions each are non-layer parallel. In Nb, 1 slip plane containing 2 slip directions is layer-parallel, while 5 slip planes containing 2 slip directions each are non-layer parallel. The maximum Schmid factor found in layer-parallel and non-layer parallel slip systems are plotted for (c) Cu and (d) Nb as a function of in-plane rotation.

In addition, many orientations in which a layer parallel slip system has the highest Schmid factor also contain non-layer parallel slip systems that are close in Schmid factor to the most favored system. Assuming different slip systems work harden independently, modest work hardening on layer-parallel slip systems can trigger slip on non-layer parallel slip systems. Only small amounts of lattice rotation are needed to re-orient the material to favor layer non-parallel slip systems. Since

Figure 6-16 shows that deformation induces lattice rotation in 10-10 Cu/Nb, the distribution of slip on different slip systems needs to be known as a function of strain. Crystal plasticity finite element simulations are used to quantify this.

6.6.3.2. Crystal plasticity finite element simulation of 10-10 Cu/Nb 45 degree compression

6.6.3.2.1. Description of technique

Finite element (FE) simulation is a computational technique that can be used to solve for pointwise stress and strains in bodies of arbitrary geometry within the limits of computational tractability[261,262]. In this method, a body is "meshed", or broken into a representation made of a finite number of nodes connected by a network of specified topology (usually triangular in 2D and tetrahedral in 3D). The mesh density can be varied, with denser meshes used near regions of highly varying stress, strain, or geometry. This allows regions of low deformation gradients to be simulated with less nodes, increasing computational efficiency. The deformation of the body is governed by constitutive relationships that relate displacements to forces, usually through linear stiffness relationships. At equilibrium, the sum of internal forces and surface tractions must equal zero and body displacements must match any boundary conditions enforced at the body surface. For a given body deformation, nodal displacements and forces are solved by inverting the matrix equation relating body displacements and forces required for equilibrium at each node. Knowledge of forces and displacements at every node allow for computation of location-dependent stresses and strains using continuum mechanics equations, allowing for the prediction of phenomena such as plastic flow and fracture on an arbitrarily shaped body.

Crystal plasticity finite element (CPFE) is a specific formulation of FE where displacements of nodes are constrained to be linear combinations of shear displacements along prescribed slip systems[263]. This is particularly useful for alloys, which are subject to elastic

anisotropy and plastic anisotropy dictated by the crystal symmetry of constituent grains. Since the combination of shear displacements and slip systems required to produce a given deformation is not unique, slip activity must be constrained by some constitutive law describing the energetics of defect-mediated deformation in metals. The simplest and most used constitutive relation is phenomenological, predicting shear rates proportional to the resolved shear stress on each slip system. It reads[264,265]:

$$\dot{\gamma^{\alpha}} = \dot{\gamma_0} \left| \frac{\tau^{\alpha}}{\tau_c^{\alpha}} \right|^{\frac{1}{m}} sgn(\tau^{\alpha}) \tag{6-8}$$

Where $\dot{\gamma^{\alpha}}$ and τ^{α} are the shear strain rate and resolved shear stress on slip system α, τ_c^{α} is the slip resistance of slip system α, and $\dot{\gamma_0}$ and m are material constants. Sgn is the sign function. Equation (6-8) is the slip rule governing deformation in the model used for this work.

More atomic-level detail can be input into CPFE models by relating shear rates to defect concentrations such as dislocation densities. In the example of dislocations, dislocation density accumulates as plastic strain increases as predicted by the Taylor-Orowan equation. Dislocation densities can be evolved through other equations predicting rates of dislocation annihilation, multiplication, and locking, etc. The model used here does not track defect populations, as the goal of the simulation is simply to relate slip system geometry and activity to macroscopic strain in 45 degree compressed 10-10 Cu/Nb.

6.6.3.2.2. Conclusions about slip system activity

CPFE is used to evaluate slip system activity in 45 degree compressed 10-10 Cu/Nb according to previously used methodology[237]. The same 3D finite element 45 degree laminate

model constructed in prior work is used[266], comprising linear tetrahedral C3D4 elements. The model microstructure consists of alternating stacks of Cu and Nb nanocrystalline layers. Each layer is spanned by one grain in the interface normal direction. The orientations of the grains are assigned according to the measured texture in Figure 5-8 and the orientation relationship of Cu/Nb grain pairs across the interface is chosen to be Kurdjumov-Sachs. The elastic anisotropy of Cu and Nb phases is accounted for in this model. The three independent elastic constants of the stiffness tensor **C** are taken from experimental measurements[267]. Plastic strain is accommodated by crystallographic slip on the {111}<110> slip systems for Cu and the {110}<111> slip systems for Nb. For simplicity, the slip strength used to activate each slip system in the flow rule in the CPFE constitutive law is assumed constant and equal among the slip systems within each phase. These are the only two unknowns in the hardening law and are estimated from fits to the yield strength measured experimentally. They are estimated to be 80 MPa in Cu and 485 MPa in Nb. These values are reasonable for two reasons. First, it is expected that the dislocations in Nb would be harder to move than in Cu and that both values would be higher than the slip strengths for the same dislocations in their coarse-grained form. Second, these values represent a nominal resistance from other defects in the nanostructure and not solely lattice friction. It should be noted that initially the Cu CRSS is low, around 80 MPa, and reflects the ease of forming dislocations from the GBs in the Cu layers between the interfaces[267]. These nucleation sites can be activated due to the loading orientation of 45 degree compression. In other orientations such as normal compression, dislocation nucleation must occur at Cu-Nb interface/GB intersections[268], which can require stresses that are an order of magnitude larger than stresses required for pure GB nucleation. Since the goal of these calculations was to gain basic insight on slip patterns in the 45 degree test, no attempt was made to explicitly account for multiple obstacles, such as interfaces, grain boundaries,

other dislocations, and defects. It is important to note that this approach models 3D interfaces better than 2D interfaces; as discussed in Section 6.4, 2D interfaces are either weaker or less work hardenable than 3D interfaces. To tailor the CPFE model to 2D interfaces well, weak traction at heterophase interfaces would have to be included. Since this model ensures compatible deformation, it approximates strong interfacial traction associated with 3D interfaces well. The model has periodic boundary conditions in all three spatial dimensions. In the deformation simulations, the deformation of each pair of boundary faces is equal and the stress tensors opposite in sign. Compression is only applied normal to the top face so that like in the experiment, the loading is 45 degrees to the Cu/Nb interface planes. The deformation is applied in fine strain increments and at each increment the total stress and slip activity in each grain in each layer are determined.

CPFE results are presented in Figure 6-40. The flow rules used for Cu and Nb were able to fit experimental behavior well as seen in Figure 6-40(b). The evolution of layer parallel and non-layer parallel slip is presented as a function of strain in Figure 6-40(c-d). For both Cu and Nb phases, most slip occurs on non-layer-parallel slip systems at yield. As deformation progresses, the distribution of slip does not change significantly. It is important to note that if slip were evenly distributed over all slip systems, then 25% of slip would occur on layer-parallel systems in Cu (3 layer-parallel and 9 non-layer-parallel slip systems) and 16.6% of slip would occur on layer-parallel systems in Nb (2 layer-parallel and 10 non-layer-parallel slip systems). Since layer-parallel slip only accounts for ~11% of activated slip in both phases, layer-parallel slip systems are under-represented during deformation. This runs counter to the Schmid factor calculations in Figure 6-39, signifying that other factors such as flow stress mismatch and traction at heterophase interfaces and grain boundaries, taken into account in the CPFE simulation, have an outsized effect on the

distribution of slip on different slip systems in Cu and Nb. In addition, the CPFE results show that most slip in 45 degree compressed 10-10 Cu/Nb occurs on slip systems that intersect the 3D interfaces over the entire range of strain investigated. This means that 3D interface-dislocation interactions must cause extended deformability without plastic instability as observed in 45 degree compression, which will be discussed in the next Section.

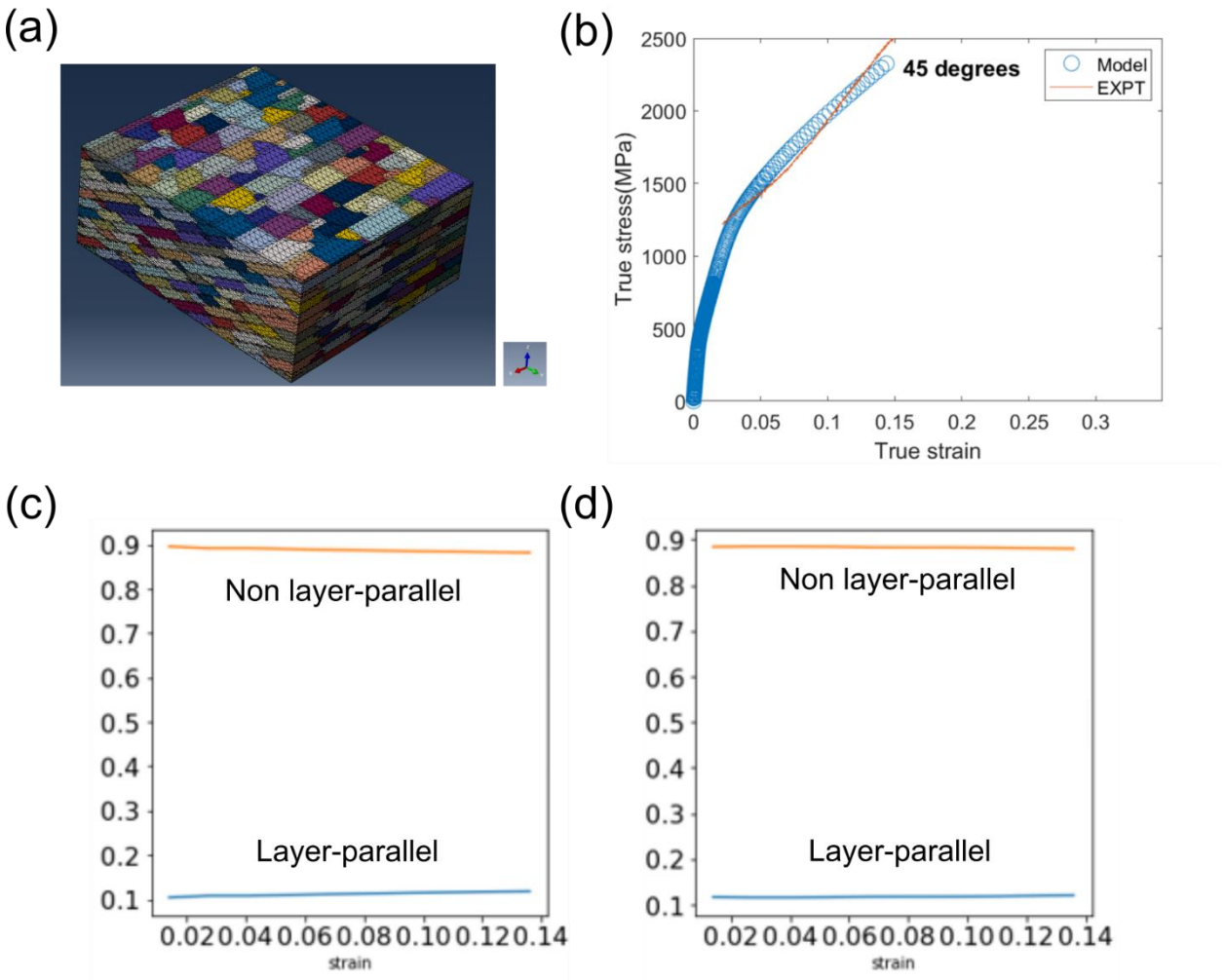

Figure 6-40 – a) Setup of simulation box used for CPFE. Grains are oriented so that one set of compact Cu (111) and Nb (110) planes are oriented 45 degrees to the compression axis. b) A comparison of the experimental plastic stress-strain curve from Figure 4 and the stress strain curve produced by the CPFE simulation. Slip evolution is presented for (c) Cu and (d) Nb, where slip systems are grouped according to parallel and non-parallel slip plane alignment to Cu-Nb heterophase interfaces.

6.6.4. Conclusions from normal and 45 degree compression

6.6.4.1. Enhanced plasticity in 45 degree and normal compression

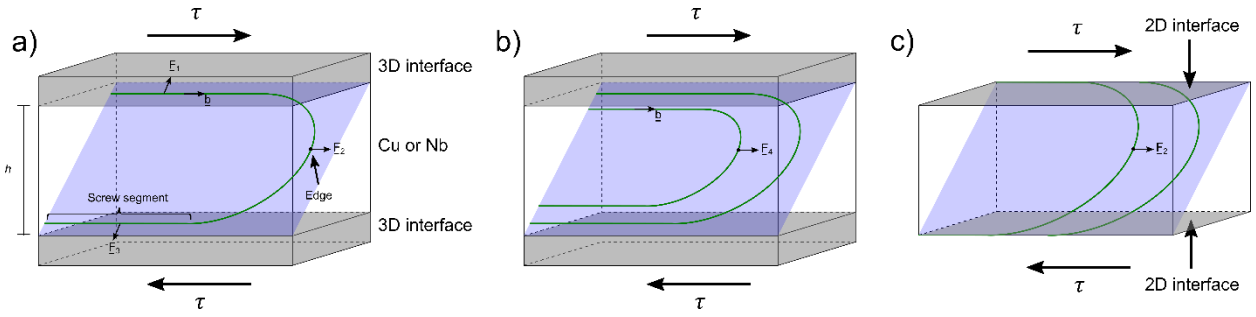

Figure 6-41 – a) A single hairpin loop in a pure layer in 3D Cu/Nb. The active slip plane is depicted in blue, the 3D interfaces are shaded in gray, and the loop is represented by a green line. The Burgers vector is also shown, allowing for identification of screw and mixed segments of the dislocation line. Forces on these segments are shown by $\underline{\mathbf{F}}_1$, $\underline{\mathbf{F}}_2$, and $\underline{\mathbf{F}}_3$. If another dislocation loop is nucleated on the same slip system as in a), the dislocation arrangement in b) arises. Here, the second dislocation line must have force $\underline{\mathbf{F}}_4$ exerted on it for it to propagate. Since it has lesser radius than the first loop, $\underline{\mathbf{F}}_4$ must be higher in magnitude than $\underline{\mathbf{F}}_2$, making it unfavorable to propagate. This contrasts with 2D Cu/Nb shown in c), where deposition of edge segments in the interface means that the second hairpin loop has the same radius as the first, and thus the same critical stress for propagation.

A possible mechanism of 3D interface-enabled plasticity is presented here. Previous work has shown that when *h* is on the order of a few 10s of nm, a deformation called confined layer slip (CLS) plausibly dominates nanolaminate material strength[15,269]. A schematic of this deformation mode is found in Figure 6-41(a). Here, a dislocation hairpin loop is propagating along a non-interface parallel slip system. The propagation direction is chosen to be parallel to the layer. This is because the in-plane grain size of 10-10 Cu/Nb is much larger than the layer thickness, as seen in Figure 5-4. It is assumed that the material cannot sustain a hairpin loop or multiple dislocations along slip directions at acute angles to the interface. The loop with slip direction parallel to the layer is under applied shear stress τ, with a Burgers vector oriented such that screw segments lie parallel to 3D interfaces and a mixed segment of semicircular geometry leads the hairpin. Under the applied stress, Peach-Koehler forces $\underline{\mathbf{F}}_1$, $\underline{\mathbf{F}}_2$, and $\underline{\mathbf{F}}_3$ are exerted on the hairpin loop at the

indicated locations in Figure 6-41(a). Figure 6-41(b) proposes dislocation-interface interactions that underpin deformation without plastic instability in 10-10 3D Cu/Nb under normal and 45 degree compression. If a second dislocation is nucleated on the same slip system as the loop in Figure 6-41(a), then it will form a second hairpin loop with smaller radius than the first. This is because of the interaction of the screw segments depicted in Figure 6-41 with Cu/Nb interfaces. For 3D Cu/Nb shown in Figure 6-41(a-b), the screw segments are blocked from absorption into or transmission across the 3D interfaces. This is supported by previous PFDD simulations demonstrating that 3D interfaces resist slip transfer caused by single dislocations or dislocation pileups[146]. This contrasts with 2D Cu/Nb, where previous work containing direct observation of CLS demonstrates that these segments likely deposit in the 2D interface, leaving a residual Burgers vector in the interface structure (Figure 6-41(c))[269]. These experiments are supported by molecular dynamics work that shows that it is energetically favorable for 2D PVD Cu/Nb interfaces to absorb incoming glide dislocations[4,270]. A subsequent dislocation on the same slip system in 2D Cu/Nb would have the same hairpin radius, and thus the same stress barrier to motion as the first loop. This follows from equations derived for Orowan bowing that give a $\frac{\ln(h)}{h}$ dependence of the critical stress required to move the dislocation. Thus, the force required to move the leading portion of the second loop would be the same as in the first, $\underline{\mathbf{F}}_2$. The second hairpin loop in 3D Cu/Nb as shown in Figure 6-41(b) behaves differently. Due to repulsive interactions between dislocations with the same Burgers vector, the second loop has a smaller leading radius than the first. Alternatively, the second loop has a lower effective *h* than the first loop. Thus, the second loop requires greater stress, or equivalently greater force $\underline{\mathbf{F}}_4$, to move than the first loop. This is quantified in detail for normal compression in the *Acta Materialia* article[234], showing that that the second loop requires 19.0 GPa

to move in Cu, while in Nb it requires 3.85 GPa. Both values are much higher than the observed flow stress of the material. In addition, the second loop would introduce unrealistically high strain energy. This is because the stress field of the second loop's trailing screw segments would repel each other strongly due to the small radius of the leading segment of the loop. Because of the multiple factors making propagation of the second loop energetically unfavorable, deformation must occur by some other mechanism. The may happen through slip activated in a different grain, or in the same grain on a slip system with non-maximal Schmid factor. In either case, dislocation storage is enhanced in the pure layers and uniform deformability is enabled.

6.6.4.2. Role of interfacial shear stress in plastic instability

Insights on 3D interface shear strength from 45 degree compression add to the understanding of mechanical behavior in layer-normal compression. It is known that in 2D Cu/Nb, interface sliding caused by low 2D interface shear strength induces shear localization under layer-normal compression[16]. 45 degree compression tests in this work show that not only are 3D interfaces strong in shear, they are also work hardenable. Therefore, 3D interfaces prevent interface sliding and allow 10-10 Cu/Nb to deform homogeneously to large strain and work harden significantly in normal compression. These observations at the micropillar length scale can be rationalized by literature results on the atomic-scale mechanical behavior of 2D interfaces. It is known that the low interfacial shear strength of PVD 2D Cu/Nb interfaces allows incoming glide dislocation cores to enter the interface, spread laterally as the interface shears, and become trapped [3]. This means that 2D interfaces can act as effective dislocation traps[271,272] and can strengthen materials under certain loading conditions[15]. However, they come with the price of early shear localization in other loading conditions like uniaxial compression[16]. Following this train of logic, the high strength and work hardenability of 3D interfaces is expected to inhibit glide dislocation

core absorption. It has already been shown that 3D interfaces hinder the transit of dislocations between abutting crystals using PFDD[146,273,274]. While PFDD incorporates atomic scale information of constituent phases such as crystal structure, lattice parameter, generalized stacking fault energy curve, etc., it does not explicitly model atomic scale structure of interfaces as has been done using molecular dynamics for 2D interfaces[270,275]. Further work should be done to study the interplay between 3D interface shear strength and their influence on the movement and activity of dislocations on the atomic scale. This work demonstrates that understanding of interface shear behavior using 45 degree compression tests can be used to explain mechanical behavior observed in other loading configurations in 2D and 3D Cu/Nb. Thus, interfacial shear strength should play a principal role in the search for ever stronger and deformable nanostructured alloys.

6.6.5. Interface and layer size effects

6.6.5.1. PFDD simulation of thick interface size effects

PFDD simulations of 3D interfaces with higher thickness than considered in Section 6.6.1.3.2 were conducted to bolster understanding of the experimentally observed mechanical behavior of Cu/Nb with varying *h* and *h'* in Section 6.5. Here, a more complex model of the 3D interface than previously considered is used. The 3D interface is modeled by a bilayer consisting of equal thicknesses of FCC $Cu_{0.1}Nb_{0.9}$ and BCC $Cu_{0.2}Nb_{0.8}$. Pure FCC Cu and BCC Nb layers abut the 3D interface on the Cu-rich and Nb-rich sides of the interface, respectively. This matches observations about 3D interface structure in Chapter 5. This simulation contained a four-phase heterogeneous system, which required modification of the code used in Ref. 146. Fully realized models of 3D interfaces are limited by current capabilities of the PFDD framework used in this work. Inclusion of the disordered 3D interface interior would require simulation of an amorphous-like region, which has a fundamentally different order parameter-based energy density functional

than used for long-range crystalline metals[276]. Future simulation work would incorporate deformation physics for phases deforming through mechanisms other than dislocation motion, such as disordered material and stress-induced phase transforming materials.

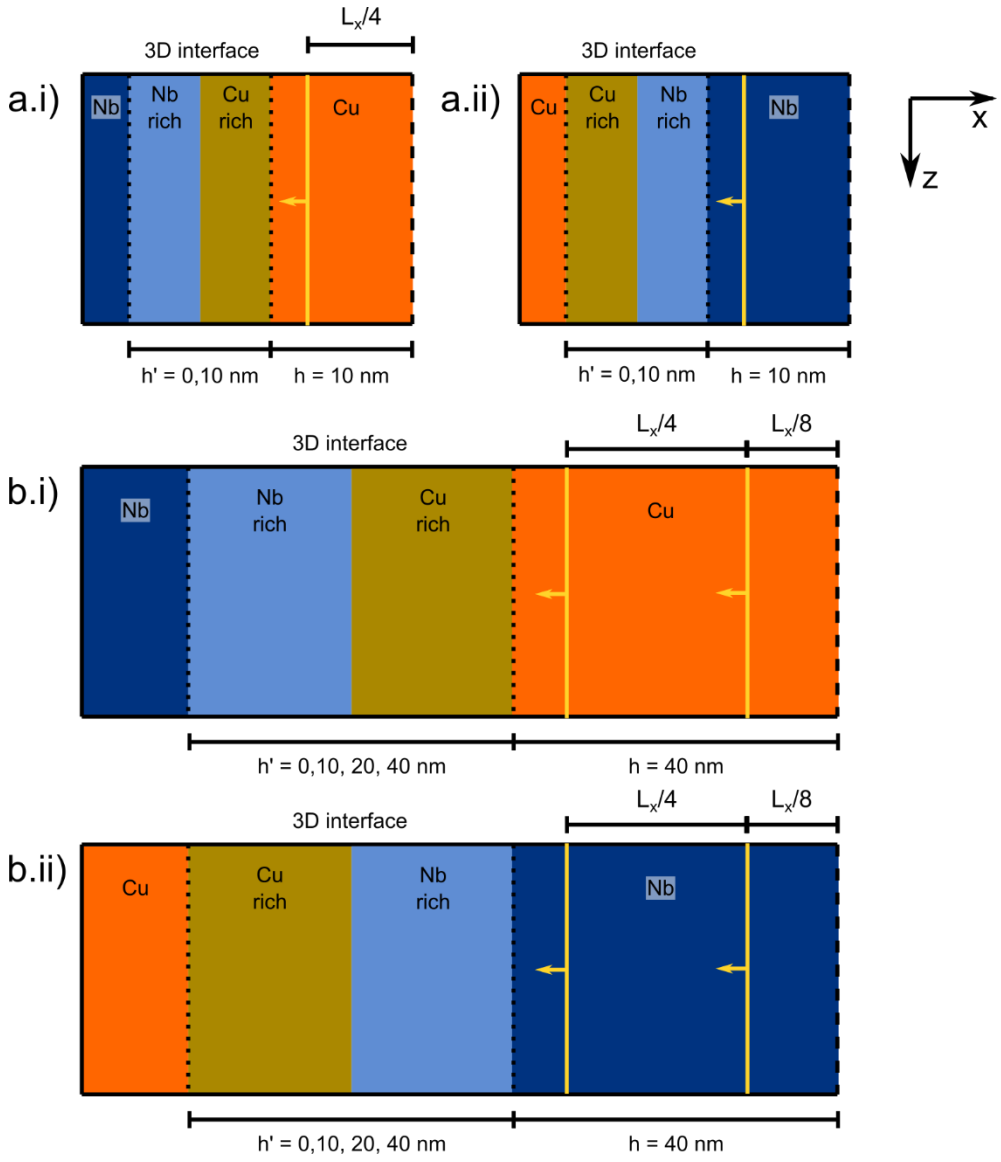

Figure 6-42 – Slip plane-normal views of simulations completed for a) h = 10 nm with single dislocations and b) h = 40 nm simulations with two-dislocation pileups. Dislocations are depicted with yellow lines with arrows showing their Burgers vectors. Only half of the simulation box is shown since it is symmetric about the z axis. The dotted lines denote the limits of the 3D interface, while the dashed line marks the center of the simulation box along the x direction. In a), simulations were done for h' = 0 and 10 nm. In b), simulations were completed for h' = 0, 10, 20, and 40 nm. FCC Cu and BCC Nb comprise the pure phases, while the 3D interface is represented

by a bilayer composite comprising FCC Cu-rich and BCC Nb-rich layers. In a), critical crossing stress was found for a dislocation moving from i) Cu to Nb and ii) Nb to Cu. In b), critical crossing stresses were found for both dislocations in the pileup for slip transmission from i) Cu to Nb and ii) Nb to Cu. Drawings are not to scale.

Figure 6-42 shows the simulation setup for the four-phase PFDD simulation. Again, dipoles were used to represent the transmission of single dislocations and two-dislocation pileups across the 3D interface. Simulations were conducted for a box with h = 10 nm and h' = 0 or 10 nm in Figure 6-42(a.i-ii). These simulations were done to simulate dislocation motion when layer thickness is comparable to 3D interface thickness (h' = 10 nm) and to provide a 2D interface control (h' = 0 nm). This builds on the *Nano Letters* simulations because while the effect of layer thickness on pileup size was captured there, the effect of pure layer thickness on image forces affecting dislocation motion was neglected[146]. Also, the current model incorporates FCC/BCC interfaces, whereas the previous model only considered BCC/BCC interfaces. Here, pure layer size is limited and is kept on the order of experimentally tested material, producing image forces on dislocations close to those found in experimental conditions. Because the 3D interface has mechanical anisotropy depending on which side is approached by the dislocation, different simulation boxes were used for when dislocations cross from Cu to Nb (Figure 6-42(a.i)) or Nb to Cu (Figure 6-42(a.ii)). Simulations were also conducted for h = 40 nm and h' = 0, 10, 20, and 40 nm in Figure 6-42(b.i-ii). Here, the larger pure layer thickness allows for inclusion of a second dislocation dipole in the box at equilibrium. While larger boxes could have been used to fit more dislocations, larger simulations requiring more computation time were out of the scope of this work. The boxes in Figure 6-42(b.i-ii) allowed simulation of the effect of 3D interfaces thicker than those studied in Ref. 146. Since the pure layer thickness in Figure 6-42(b.i-ii) (80 nm for the central pure region) is still more restricted than used in past work.

Crystallographic orientations are aligned with the simulation coordinates with $x||[111]$, $y||[1\bar{1}0]$, and $z||[11\bar{2}]$ in BCC material, while $x||[1\bar{1}0]$, $y||[111]$, and $z||[\bar{1}\bar{1}2]$ in FCC material. BCC material has one active $(1\bar{1}0)[111]$ slip system, while FCC material has one active $(111)[1\bar{1}0]$ slip system. The slip directions and planes are aligned, meaning that only one order parameter is needed per phase. In each cell, all dislocations are edge, lie on the mid-y plane, and are equally spaced at equilibrium under no applied stress. L_x, L_y, and L_z are the edge lengths of the simulation cell along the x, y, and z directions, respectively. In all cases, $L_y \approx 15$ nm and $L_z \approx 35$ nm, while L_x is set to be just over $2(h+h')$ to account for material on the interface side opposite of dislocation pleups. Material parameters required for the PFFD simulation are summarized in Table 6-6.

Table 6-6 – Lattice parameter a_0, elastic constants C_{11}, C_{12}, and C_{44}, and γ_{usf} the four phases used for PFDD. Isotropic shear modulus is in Voigt form $\mu = (3C_{44}+C_{11}-C_{12})/5$. Isotropic Poisson's ratio is in Voigt form $\nu = (C_{11}+4C_{12}-2C_{44})/(4C_{11}+6C_{12}+2C_{44})$. Values of a_0 and γ_{usf} in Nb and Cu are from prior DFT calculations[277], values of elastic constants in Nb and Cu are from experiments[278], and all values in $Cu_{0.1}Nb_{0.9}$ and $Cu_{0.8}Nb_{0.2}$ are from atomistic simulations[254].

Phase	a_0 (Å)	b (Å)	C_{11} (GPa)	C_{12} (GPa)	C_{44} (GPa)	μ (GPa)	ν	γ_{usf} (mJ/m^2)
Nb	3.324	2.879	245	132	28.4	39.64	0.392	676.78
$Cu_{0.1}Nb_{0.9}$	3.274	2.835	221.58	141.63	40.63	40.37	0.389	703.46
$Cu_{0.8}Nb_{0.2}$	3.759	2.658	195.16	128.44	79.32	60.94	0.322	463.52
Cu	3.634	2.57	169	122	75.3	54.58	0.325	519.05

In these simulations, the system is evolved according to previously established methodology[254,273,274]. A resolved shear stress (RSS) is applied to the system, until any dislocation transmits fully through the 3D interface. The minimum stress for the transmission is considered the critical crossing stress (CCS). In the case of a two-dislocation pileup, the CCS is recorded after transmission of the first dislocation. Only one dislocation remains at the interface, decreasing the mechanical advantage for interfacial slip transfer. RSS must be increased further until the next

transmission event occurs. A second, higher CCS value is recorded, resulting in two different values in CCS for the first and second transmitted dislocation.

Figure 6-43 presents CCS values for h = 10 nm simulations. Comparison of Figure 6-43(a-b) shows that CCS is similar whether the dislocation starts on the Cu or Nb side of a 2D/3D interface. For reference, the Peierls barrier in the absence of obstacles is 0.14 GPa for Cu and 1.33 GPa for Nb as computed by PFDD[254]. Note that details of dislocation core structure are omitted in Ref. 254 that would bring these stresses closer to predictions by atomistic simulations. Increasing h' from 0 to 10 nm increases CCS by 55% for transmission from Cu and 63% for transmission, showing that 3D interfaces hinder slip transmission more effectively than 2D interfaces in this computational framework. This is supported by previous experimental and computational results in Sections 6.2-6.4. The 2D interface results come with the caveat that the misfit dislocation array associated with 2D Cu/Nb heterophase interfaces is not simulated. This structure acts to block dislocation transmission strongly and should be included in future PFDD simulations of 2D interfaces[3].

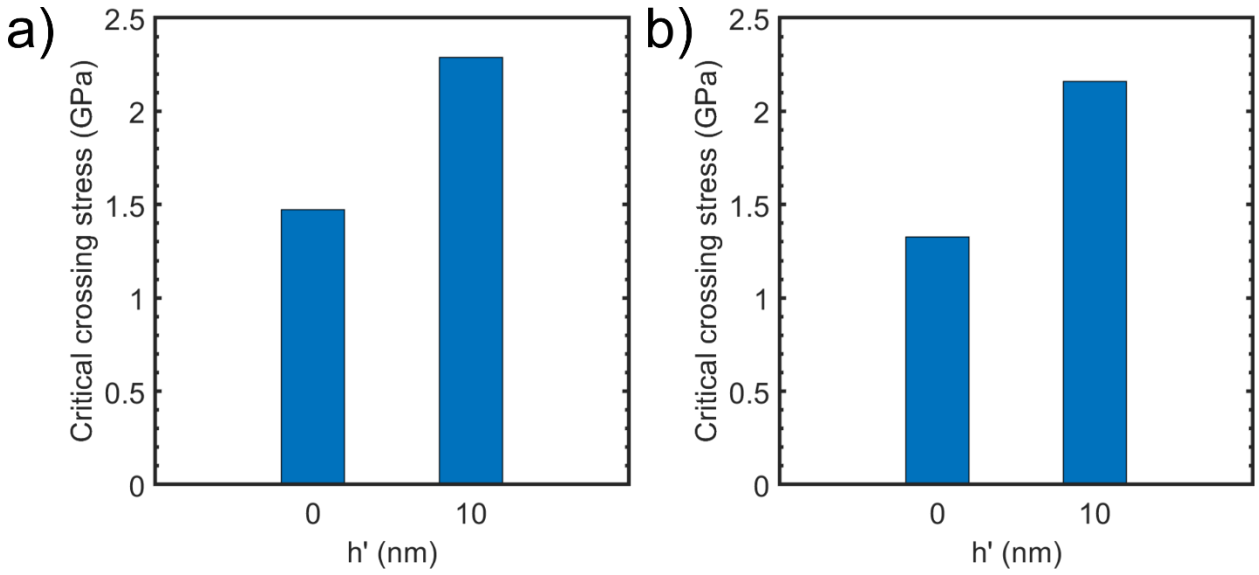

Figure 6-43 – Critical crossing stresses for a single dislocation crossing from a) Cu to Nb and b) Nb to Cu.

Figure 6-44 depicts CCS predictions for h = 40 nm, showing what happens as two piled up dislocations sequentially transmit across 3D interfaces of varying thickness. Transmission from the Cu and Nb sides of the interface are shown in Figure 6-44(a) and Figure 6-44(b), respectively. Figure 6-44(a-b) demonstrate that below h' = 20 nm, 3D interfaces offer increasing stress barrier to slip transmission as interface thickness increases. Beyond h' = 20 nm, increasing 3D interface thickness offers no greater barrier to slip transmission. This is reasonable, since CCS should approach the Peierls barrier of the harder phase in the 3D interface as h' approaches infinity. These simulations thus establish that 3D interface strengthening saturates at h' = 20 nm; beyond this thickness, 3D interfaces produce diminishing returns for material strength. Figure 6-44(a-b) also shows that the first dislocation in the pileup requires less stress to transmit than the second. This is expected, since the mechanical advantage that pileups confer to the lead dislocation to transmit across interfaces is proportional to the pileup size. Lastly, comparison of CCS for the second, singular dislocation for h' = 0, 10 nm from Figure 6-44(a-b) to CCS for h' = 0, 10 nm for a singular

dislocation in Figure 6-43(a-b) shows that that changing *h* from 10 to 40 nm has no effect on CCS. This indicates that the image forces exerted by pure phases on transmitting dislocations have no dependence on *h* at the length scales simulated.

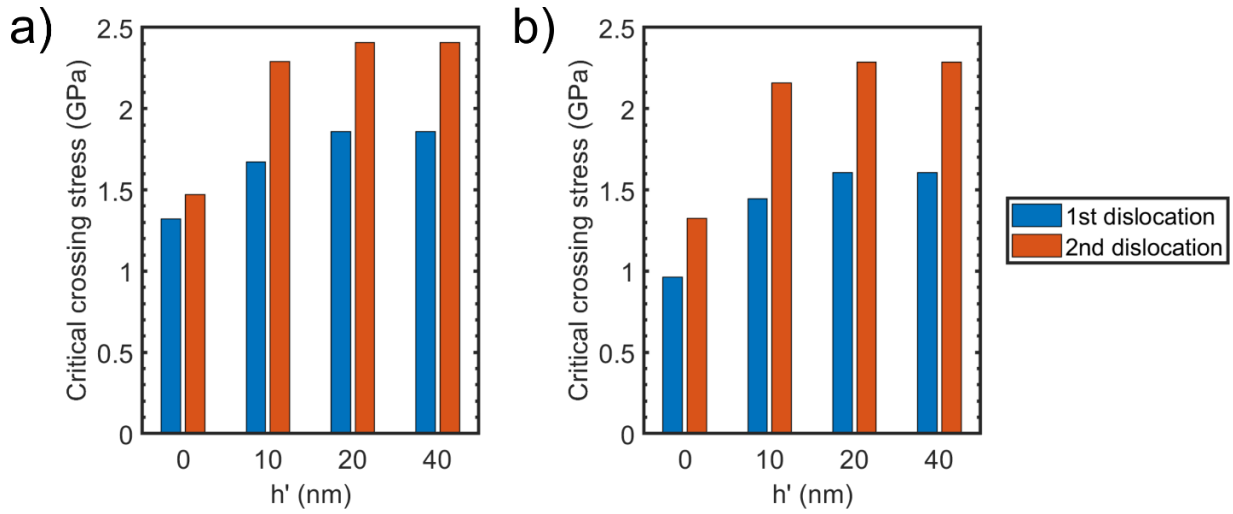

Figure 6-44 – Critical crossing stresses for the first (blue) and second (orange) dislocations in a two-dislocation pileup transmitting across a 3D interface from a) Cu to Nb and b) Nb to Cu.

Comparison of Figure 6-44(a) and Figure 6-44(b) reveals that 3D interfaces are stronger when approached from the Cu side than the Nb side. This can be explained by examination of the dislocation elastic line energy and γ_{USF} as a dislocation moves from phase to phase in the simulation. The change in elastic line energy as an edge dislocation moves from phase A to phase B can be estimated as[1]:

$$\frac{\mu_b b_b^2}{1-\nu_b} - \frac{\mu_a b_a^2}{1-\nu_a} \tag{6-9}$$

The other terms in dislocation self energy according to Weertman and Weertman multiply to order unity, so they will be disregarded. Here, μ_i, b_i, and ν_i are the shear modulus, Burgers vector magnitude, and Poisson ratio of phase i. The change in γ_{USF} as a dislocation moves from phase to

phase can be computed using values in Table 6-6. The change in line energies and γ_{USF} are summarized in Table 6-7.

Table 6-7 – Changes of dislocation line energies and USFE as an edge dislocation moves between different phases in the PFDD simulation.

	Line energy (10^{-11}J/m)	**USFE (mJ/m^2)**
Cu → $Cu_{0.8}Nb_{0.2}$	100.81	-55.53
$Cu_{0.8}Nb_{0.2}$ → $Cu_{0.1}Nb_{0.9}$	-103.84	239.94
$Cu_{0.1}Nb_{0.9}$ → Nb	9.11	-26.68
Cu → Nb	6.07	157.73

The anisotropy in 3D interface strength can be rationalized using these results. When a dislocation crosses the interface from the Cu side, it faces an energetic penalty due to a large increase in elastic line tension when moving from pure Cu to Cu-rich alloy. This can also be thought of as a repulsive image force. Then, to cross from Cu-rich to Nb-rich alloy, the dislocation must face a large increase Peierls barrier represented by an increase in γ_{USF}. The dislocation then faces no significant energetic penalties to transmit to the Nb side. When the dislocation approaches the 3D interface from the Nb side, it faces the opposite energetic changes as described for transmission from the Cu side. Thus, it should be easier to transmit a dislocation across the interface from the Nb side. Of course, the reality in the PFDD simulation is more complex, as changes in image forces and Peierls barrier compete as the dislocation moves from phase to phase, as seen by the changing signs of energy changes at each phase boundary. Analysis of dislocation motion before transmission can provide clues about the dominating factor in 3D interface slip transmission barrier.

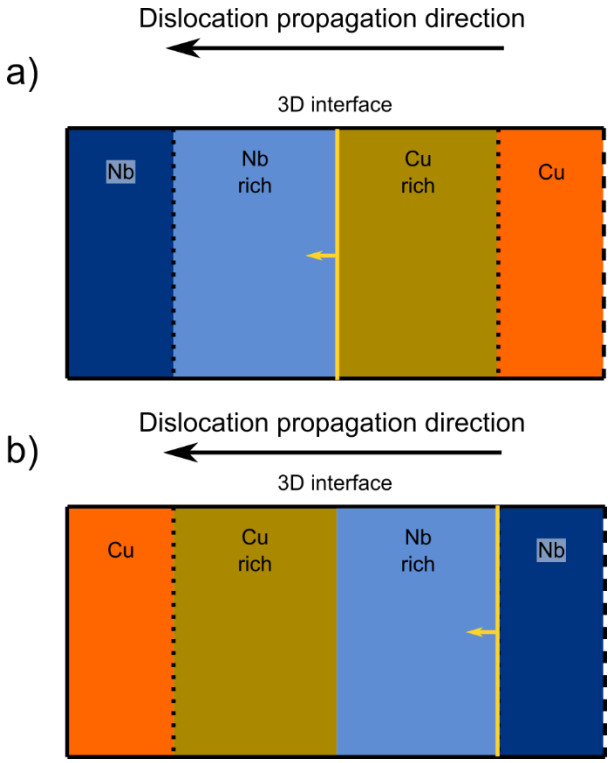

Figure 6-45 – Sub-critical dislocation configurations for dislocations crossing from a) Cu to Nb and b) Nb to Cu.

Figure 6-45 demonstrates "sub-critical" dislocation arrangements for transmission from the Cu and Nb sides of the 3D interface. A snapshot of the simulation box was taken at the stress increment before CCS was reached in the simulation, producing the sub-critical dislocation configuration. This provides information about the strongest region in the 3D interface before the dislocation transmits[146,273]. Figure 6-45(a) shows that the Nb-rich alloy arrests the transmission of a dislocation originating from the Cu before complete transmission. This is consistent with the large increase in Peierls barrier moving from the Cu-rich to Nb-rich alloy in Table 6-7. Figure 6-45(b) shows that a dislocation approaching from the Nb side is blocked by the Nb-rich alloy. According to Table 6-7, a modest barrier is provided by the Nb-rich alloy in the form of increasing Peierls barrier. While this exercise is informative, the relative contributions of image forces and Peierls barrier to CCS in PFDD is not entirely understood and must be pursued in future work.

6.6.5.2. Limits of strengthening from thick 3D interfaces

6.6.5.2.1. Saturation of flow stress above *h*' = 10 nm

Results from Section 6.5.4 show that for various *h*, strength does not increase at yield or 8% plastic strain with increasing *h'*. The stress-strain and strength data showing this can be found in Figure 6-23 to Figure 6-25. While this may seem to run counter to the results of Sections 6.3 and 6.4 showing that increasing the volume fraction of 3D interfaces enhances strength and deformability, the PFDD results in Section 6.6.5.1 provide a rationale for saturation of 3D interface strengthening. Considering only yield stress, it would not be reasonable to expect that 3D Cu/Nb would strengthen infinitely as *h'* increases. The 3D interface has its own structure with a finite yield strength that puts an upper bound on the achievable yield stress for 3D Cu/Nb. However, the simulations in Section 6.6.5.1 do not provide much information on work hardening; two dislocations were simulated there whereas work hardening of Cu and Nb grains in 3D Cu/Nb must consider mechanisms involving many dislocations, potentially up to a few tens of dislocations across a few bilayers. 3D interfaces do not appear to enhance work hardenability past *h'* = 10 nm for *h* = 10 and 20 nm, but they do at *h* = 40 nm. This is likely due to the large length scales associated with *h*+*h'* at *h*/*h'* ~ 1. For the 40-40 Cu/Nb investigated in this work, thick 3D interfaces seem to increase the effective layer thickness to 80 nm. This would make 40-40 Cu/Nb behave closer to 80-10 Cu/Nb, which displays uniform deformability to high plastic, than 40-10 Cu/Nb, which tends to shear localize readily. 3D interfaces contain substantial amounts of crystalline material as demonstrated in Chapter 5, so this is a plausible scenario. In essence, thick 3D interfaces at *h* > 20 nm provide more volume of crystalline material for dislocation storage, making the material behave more like nanolaminates with coarser layer thickness. In addition, the crystalline regions of 3D interfaces are solute strengthened by virtue of their alloyed nature. Thus,

3D interfaces strengthen the material through solute effects and oppose pileup-assisted slip transfer and shear banding, while enabling work hardening through storage of additional dislocation content over 2D interfaces.

As for Cu/Nb composites with $h+h' <= 50$ nm, the insensitivity of flow strength to 3D interface thickness is supported by PFDD simulations and theoretical calculations in Section 6.6.4.1. PFDD simulations in 6.6.5.1 establish a saturation h' of 20 nm for 3D interface strengthening through only consideration of Cu-rich and Nb-rich crystalline regions of the 3D interface. While it would be informative to include physics of amorphous/disordered material deformation in the PFDD model, the agreement between the PFDD results as-is with experimental results in Section 6.5 demonstrate that this is unnecessary. In addition, the dislocation hairpin loop calculations in 6.6.4.1 show that slip systems in layers with confined length scales cannot store more than one or two adjacent dislocations. The additional crystalline material contributed at 3D interface boundaries evidently does not add enough volume for dislocation storage to significantly enhance work hardening or influence shear band propensity. Combination of simulation and experimental results in this work thus establish 20 nm as the length scale below which strength and is insensitive to h' for h = 10-40 nm. Work hardening behavior changes among these specimens according to pure phase volume fraction and effective layer thickness dictated by $h+h'$. It would be interesting to probe smaller length scales of a few or even sub-nm h and h' to see if 3D interfaces modify the energetics of single-dislocation crossing mechanisms proposed for 2D Cu/Nb at those length scales.

6.6.5.2.2. Limited deformability of 10-40 Cu/Nb

While 80-10 Cu/Nb had notably high deformability in the micropillar experiments in Section 6.5, 10-40 Cu/Nb had notably low deformability. *Post mortem* SEM and TEM demonstrate

that shear banding is more severe than 2D Cu/Nb in some respects. Comparison to amorphous equiatomic CuNb revealed some similarities in deformation mode, suggesting that the interiors of 3D interfaces might be amorphous. If so, it would make sense that they would form large shear bands at large enough length scale. The dominant mechanism underlying room-temperature deformation for metallic classes is shear transformation zone (STZ) formation, where a few atomic clusters form regions of high shear strain according to local topology and atomic cluster orientation[279]. Metallic glasses display strong size effects at the nanoscale which are likely related to the volume required for formation of a STZ[280–282]. It might be that the disordered regions of *h'* = 10 nm 3D interfaces are too confined to allow STZ formation, while the larger volume of disordered material of *h'* = 40 nm do allow for STZ, which can then kick off runaway shear band across 3D interfaces and layers in 10-40 Cu/Nb. Even if the material in 3D interface interiors are found not to be amorphous in future work, micropillar experiments on 10-40 Cu/Nb show that a large volume fraction of solute-hardened alloyed material is detrimental for large uniform deformability.

6.6.5.3. Limited deformability in 40-10 Cu/Nb for h' = 10 nm samples

40-10 Cu/Nb was another notable sample in micropillar experiments on specimens with *h'* = 10 nm, apparently having neither optimal strength nor deformability; 80-10 Cu/Nb has a relatively higher uniform plastic deformability, while 20-10 and 10-10 Cu/Nb display a superior combination of strength and deformability. This suggests that 40-10 Cu/Nb represents a transition in mechanical behavior between conventional alloys and nanostructured 3D interface alloys. For 80-10 Cu/Nb, high deformability yet relatively low strength suggests that the layer thickness *h* is too high for the material to "see" 3D interfaces. This likely means that 3D interfaces do not influence the deformation of materials when 3D interface volume fraction is low. For 20-10 and

10-10 Cu/Nb, strength and deformability is enhanced by the dislocation-interface interactions demonstrated by PFDD and theoretical calculations for propagating hairpin loops. 40-10 Cu/Nb with an intermediate *h* seems to be in a "sweet spot" for shear band formation and thus has limited deformability. At this length scale there is enough volume in pure layers to store pileups on the Type II slip systems depicted in Figure 6-33 required for shear band formation, but not enough room to develop conventional work hardening behavior produced in conventional alloys arising from dislocation forest-based interactions.

6.6.6. Nanoindentation and micropillar compression

Discussion of nanoindentation results for this work must begin with a re-emphasis that knowledge of appropriate Tabor factor and ε_r for hardness-flow stress correlation appears to be severely lacking for conventional engineering alloys, let alone for the relatively exotic alloys studied in this work. Despite that acknowledgement, significant findings can be gleaned by comparing nanoindentation and micropillar results. Micropillar work in Sections 6.2-6.4 demonstrate that there are statistically significant differences found between 2D and 3D Cu/Nb flow stresses at comparable strain. However, no difference is found between 2D and 3D Cu/Nb hardness under Berkovich compression. This suggests that the contribution of 3D interfaces to mechanical behavior is highly dependent on applied stress state. This is made clear by the anisotropy in mechanical response shown by 10-10 Cu/Nb in Section 6.4. 10-10 Cu/Nb under normal compression appears to be strong and less deformable, while 10-10 Cu/Nb under 45 degree compression is weaker but highly deformable. The yield behavior between the two loading orientations demonstrates a real loading anisotropy. Crystal orientation fails to account for this entirely; 10-10 Cu/Nb yields at 1900-2100 MPa under normal compression (depending on measurement method), while it yields at 800 MPa under 45 degree compression. Meanwhile the

average Schmid factor is 0.34 in normal compression while it is close to 0.50 in 45 degree compression. This difference in Schmid factor is not enough to account for the difference in yield stress between loading states. Cu/Nb loading anisotropy may have additional contributions from classical composite considerations. Normal compression is an isostress condition for Cu, Nb, and 3D interfaces, requiring the maximum yield stress of all material to be achieved for global yielding to occur. However, Cu, Nb, and 3D interfaces are free to yield sequentially in order of increasing yield stress in 45 degree compression. In nanoindentation, isostress, isostrain, and mixed loading states can be found under the indent. Thus, conclusions about deformation in 2D and 3D Cu/Nb produced by nanohardness trends are expected to differ from those produced by micropillar flow stress trends. Lateral constraints in nanoindentation may also explain the difference in trends. While shear localization can limit deformability in micropillar compression since shearing material is free to extrude at free surfaces, shear banding material in nanoindentation would impinge upon material surrounding the plastic zone in nanoindentation. Nonetheless, Tabor factor is significantly different between 2D and 3D Cu/Nb, signaling different mechanical behavior as a function of interface structure. More work must be done to understand the relationship between nanoindentation and uniaxial straining of 2D and 3D Cu/Nb to fully explain differences in Tabor factor.

7. Conclusions

7.1. Key findings

7.1.1. 3D interface structure

7.1.1.1. Crystallographic structure

This work has established crystallographic heterogeneities in all three spatial dimensions in 3D interfaces. In the interface-normal direction, 3D interfaces accommodate the crystallographic mismatch between FCC and BCC structures by incorporating regions with different structures. FCC Cu-rich regions are found to share a coherent interface with pure Cu, BCC Nb-rich regions are coherently joined to pure Nb, and regions with intermediate composition in between the Cu- and Nb-rich regions appear to be disordered on the length scale of a few nm. The interface-lateral direction also contains crystallographic heterogeneities on the length scale of a few nm. HRTEM suggests that there may be regions of distinct crystallography a few nm wide in the interface, while NBD suggests that 3D interface interiors are amorphous over the size of the probe, which may spread to several nm.

7.1.1.2. Chemical structure

Similar to crystallographic heterogeneities, chemical heterogeneities can also be found in all spatial dimensions in 3D interfaces. Although 3D interfaces appear to have smooth chemical gradients in the normal direction and no heterogeneity in the interface-lateral direction when probed by STEM-EDS, this work shows that those results are tied to the projection of information from a volume of material onto the two-dimensional plane of an image. APT was able to demonstrate that 3D interface-normal chemical gradients vary as a function of interface-lateral position. Additionally, chemically segregated regions were found in the interface-lateral direction. The length scale of heterogeneities was found to be on the order of a few nm in all spatial

dimensions, another similarity found between chemical and crystallographic heterogeneities in 3D interfaces.

7.1.2. Effect of 3D interface on mechanical behavior

7.1.2.1. Layer and interface thickness size effects

3D interfaces were shown to enhance strength without sacrificing deformability at h = 40 nm in 40-10 Cu/Nb, while simultaneously boosting strength and deformability in 10-10 Cu/Nb. Thus, when h is decreased while holding h' constant at 10 nm, 3D interfaces are shown to break the tradeoff between strength and deformability in nanocrystalline alloys. This is tied to the severity of shear localization in the material, with the more severe shear localization in 40-10 Cu/Nb limiting uniform deformability. This implies a size effect, but since the two microstructural parameters h and h' can be independently varied, the size effect can depend on the relative scale between the two quantities. Different trends emerge depending on which quantity is held constant when h and h' are varied. For constant h' of 10 nm, flow stress becomes a weak function of h below h = 40 nm. For constant h of 10 nm, flow stress is a weak function of h', but deformability becomes limited when h' is much greater than h. Shear localization becomes very severe for 10-40 Cu/Nb, which exhibits the highest strain gradient out of 10-40, 10-10, 40-10, and h = 40 nm 2D Cu/Nb. For constant h of 20 nm, flow stress is also a weak function of h'. For constant h of 40 nm, flow stress is inversely proportional to h' while deformability is proportional. For h'/h = 1, higher flow stress is traded off with lower deformability as h decreases. Flow stress is shown to be similar for samples with $h + h' <= 50$ nm, indicating that a transition in deformation likely occurs below a layer and 3D interface thickness combination of 50 nm.

7.1.2.2. Orientation effects

Normal and 45 degree micropillar compression tests reveal significant plastic anisotropy for 10-10 Cu/Nb. Normally compressed 10-10 Cu/Nb has a high yield stress and relatively lower stable plastic deformability, while 45 degree compressed material has a low yield stress and higher stable plastic deformability. Both materials work harden to similar stresses but at different rates, with 45 degree compressed material work hardening at a slower rate. Comparison to 2D Cu/Nb shows that 3D interfaces enhance deformability without sacrificing flow stress in both loading orientations. Comparison of nanoindentation data to micropillar compression data shows that while 3D interfaces modify mechanical behavior under uniaxial stress, they behave similarly to 2D interfaces under a nanoindentation stress state. Since nanoindentation introduces gradients in principal stress orientation and maximum stress where there are none in uniaxial tests, this comparison indicates that 3D interface deformation is strongly orientation dependent and is possibly sensitive to strain gradients.

7.1.3. Effects of 3D interfaces on unit deformation and plastic instability

7.1.3.1. Effects on interfacial slip transfer

Experimental work on normally compressed 10-10 and 40-10 Cu/Nb show enhanced strength and deformability at lower h. This is tied directly to the relative length scale between dislocation pileups and 3D interface thickness with PFDD simulations. When dislocation pileups are small and 3D interfaces are thick, interfacial slip transfer is greatly hindered. The barrier that 3D interfaces pose to interfacial slip transfer does not scale infinitely with 3D interface thickness. The dislocation blocking potential of 3D interfaces saturates at length scales of $h' > 10$ nm.

7.1.3.2. Interfacial shear strength

45 degree tests of 10-10 Cu/Nb show that 3D interfaces not only enhance stable deformability, but they also enhance work hardenability of pure Cu grains. 3D interface are also found to be work hardenable themselves. This alters the behavior of Cu/Nb during shear localization, where 2D interfaces slide and precipitate failure while 3D interfaces delay shear localization by blocking interface slip transfer and maintain compatible deformation at heterophase boundaries between phases with disparate flow strengths. This provides insights on glide dislocation-interface interactions. 2D PVD interfaces, which are weak in shear, deform locally to absorb incoming glide dislocations. 3D PVD interfaces, which can work harden to high stresses, can plausibly store and block incoming glide dislocations without absorption. This leads to the development of a model of single dislocation-based work hardening.

7.1.3.3. Effects of 3D interfaces on dislocation propagation in pure layers

Previous work has shown that at small length scales, flow stress and deformability are dominated by mechanisms involving a few dislocations. At higher length scales in conventional engineering alloys, dislocation forest interactions act to produce extended work hardening and uniform deformability while dislocation pileups control flow stress as a function of grain size[70]. At nanoscale effective grain size in materials such as 10-10 Cu/Nb, dislocations likely propagate as constrained Orowan loops adopting hairpin morphologies. Here, insights from CPFE and experimental 45 degree compression tests aid development of a model predicting if slip systems can accommodate multiple dislocations in close proximity. This model shows that it is energetically unfavorable to store and propagate multiple closely spaced dislocations on layer non-parallel slip systems, which contribute significantly to deformation in both normal and 45 degree compression. Thus, dislocation activity must be dominated by spatially separated singular

dislocations evenly distributed on all available slip systems. This slows the onset of shear instability and simultaneously enhances strength and deformability.

7.2. Future work

The results of this work provided key insights into the structure and mechanical behavior of 3D interfaces. However, they raise new scientific issues that should prove fertile ground for future investigation. They can be divided into different topics as follows.

7.2.1. 3D interface structure

While nanoscale crystallographic and chemical heterogeneities were demonstrated in 3D interfaces, it is not known if chemical fluctuations are correlated with heterogeneities in crystal structure. While this work suggests that they are, the correlative work needed to definitively prove this connection needs to be done. On a related note, the crystallographic characterization of 3D interfaces provided ambiguous results depending on characterization method. Thus, the structure of 3D interfaces has not been resolved to atomic accuracy. Proposed techniques for doing so are discussed in the next Section.

The microstructural findings of this work also suggest scientific issues related to synthesis-structure relationships in 3D interfaces. Since nanoscale heterogeneities were found in the interface normal and lateral directions, it is natural to ask if these heterogeneities can be modified independent of each other using modification of synthesis parameters. It has yet to be shown if 3D interface structure can be controlled in the interface normal direction (for example, to include more or less disordered material) or the interface lateral direction (to produce desired morphologies such as precipitates, Cu- and Nb- rich protrusions, etc.). Also, the motivation of any fundamental science project such as this one is to uncover new physics to apply in engineering contexts. To that end, bulk preparation methods of 3D interfaces should be explored. This may be done using severe

plastic deformation techniques such as ARB or high-pressure torsion. Other deposition methods such as electrodeposition are much more amenable to bulk specimen preparation than PVD[283]. Lastly, more exotic methods such as controlled solid-state dealloying of initially uniform equimolar CuNb can be explored[284].

7.2.2. Proposed microstructural characterization of 3D interfaces

The correlative work suggested earlier may comprise correlative TEM/APT. Since APT needles are electron transparent if fabricated with small enough needle width, an APT specimen can be non-destructively characterized with TEM first before destructive vaporization in the LEAP. Chemical heterogeneities observed in APT can be directly and incontrovertibly correlated to crystallographic heterogeneities observed in TEM in this manner. Also, the TEM methodology used in this work comprised mostly of conventional 2D imaging techniques. Electron energy loss spectroscopy (EELS) in the TEM can be used to recover local changes in Cu and Nb bonding across the 3D interface through analysis of extended energy loss fine structure (EXELFS)[285]. This can be combined with bulk X-ray techniques such as near-edge X-ray absorption fine structure (EXAFS) to provide representative partial radial distribution functions of Cu and Nb[286]. Lesser-used techniques include TEM tomography, holography, ptychography, etc. that can recover three-dimensional information from a technique that usually outputs only two-dimensional images[27]. These rarity of these techniques are proportional to the difficulty in using them, so any inspiration taken from these suggestions should be tempered with an investigation into the effort/risk-reward ratio associated with each technique. Lastly, other methods such as field ion microscopy may be able to provide finer probes for 3D interface structure characterization than APT and TEM[287].

Computationally-based techniques can provide insight where experiments cannot, as was done for the mechanical behavior of 3D interfaces. MD can be used to simulate the PVD process,

and so can be used to elucidate the expected structure of 3D interfaces with atomic fidelity. Kinetic Monte Carlo (KMC) is another possibility for simulating PVD of 3D interfaces[288,289], but most KMC approaches require pre-defined assumptions about the crystal lattice expected in the simulation. The work required to remove the lattice assumption requirement for KMC is not trivial but would prove a viable technique for simulation of 3D interface deposition[290,291]. Any prospective computational work should consider the statistical representativeness of MD and KMC. These techniques usually only model a few μm^3 of material[69], so multiple simulations with different random seeds should be run to ensure consistent results.

7.2.3. Fundamentals of 3D interface-mediated deformation

While this work has shed much light on the dislocation-blocking ability of 3D interfaces, this ability must be quantified in terms of all relevant atomic-scale characteristics of the 3D interface. The barrier to slip that a 3D interface provides is a function of many different quantities. These quantities are listed here. 3D interface thickness plays a role as shown by this work, so *h'* contributes to the slip barrier. The number of dislocations n piled up at the interface also influences slip barrier significantly. Disordered content plays a role in work hardening rate and deformability, so the volume fraction of disordered material $\varphi_{disorder}$ should be considered. Any heterophase interface produces image forces on incoming dislocations as a function of the elastic properties of all phases comprising the interface and abutting layers, stored in a list of stiffness tensors $\mathbf{C}$. Since 3D interfaces have finite thickness, the spatial gradient in elastic properties between all considered phases should also be stored in a list $\nabla\mathbf{C}$. The difference in Peierls barrier between phases contributes to 3D interface slip resistance, so lists of USFE $\boldsymbol{\gamma_{USF}}$ and USFE gradient $\nabla\boldsymbol{\gamma_{USF}}$ are required. Dislocation dissociation, which depends on the intrinsic stacking fault energies $\boldsymbol{\gamma_{ISF}}$ contributes to slip transfer barrier. In BCC materials, variations in γ_{USF} laterally along the

dislocation line significantly modify kink population and morphology[292,293], which in turn moderates screw dislocation mobility and yield strength, so the lists of interface lateral variation in USFE $\boldsymbol{\nabla\gamma_{USF,lat}}$. Note that $\nabla\boldsymbol{\gamma_{USF}}$ mentioned above is calculated normal to the interface. Drawing inspiration from the energy functional in PFDD, a function quantifying the barrier to slip that 3D interfaces pose can be proposed with the general form:

$$\sigma_{barrier} = f(h', n, \phi_{disorder}, \boldsymbol{C}, \boldsymbol{\nabla C}, \boldsymbol{\gamma_{USF}}, \boldsymbol{\gamma_{ISF}}, \boldsymbol{\nabla\gamma_{USF}}, \boldsymbol{\nabla\gamma_{ISF}}, \boldsymbol{\nabla\gamma_{USF,lat}}) \tag{7-1}$$

Note that this function assumes one active slip system per phase and predetermined orientation relationships and interface planes between all phases. Future work relating to fundamental deformation physics of 3D interfaces should strive to quantify Equation (7-1), perhaps even in general for all bimetal couplings.

Other deformation mechanisms and defects must also be considered when calculating $\sigma_{barrier}$. Some materials can undergo stress-induced phase transformation, such as TRIP steels and multi-principal element alloys[294,295]. Some bimetal couplings may include third phases such as intermetallics and precipitates at 3D interfaces. This is inspired by grain boundary decoration of second phase particles[296]. Lastly, planar and volume defects must be accounted for. Some metals can be synthesized in ways that incorporate high stacking fault or twin content in the material[99,101,297]. These defects influence metallic deformation drastically and may contribute to deformation in different ways at 3D interfaces. Lastly, stacking faults and twins can form during deformation[298,299]. 3D interfaces may modify the energetics of deformation-induced faulting or twinning, which will have outsize effects on strength and ductility.

7.2.4. Dislocation-3D interface interactions

As shown for 2D interfaces, heterophase interfaces influence dislocation activity in other ways than simply blocking their motion. Some 2D interfaces can nucleate dislocations more efficiently than others and favor dislocation propagation on some slip systems over others according to misfit dislocation array geometry[5]. In materials where dislocations can dissociate into stacking faults, some 2D interfaces nucleate leading partial dislocations more efficiently than trailing partials[7,112]. This favors deformation twinning over perfect dislocation slip in some material systems and loading orientations. Future work should examine the energetics and crystallography of dislocation nucleation at 3D interfaces to establish their effect on dislocation nucleation. Such work may be able to explain differences in yield strength and slip system activity between 3D and 2D interface multiphase systems.

On a similar note, dislocation transmission criteria similar to Lee-Robertson-Birnbaum criteria have been developed for 2D interfaces to account for incoming and outgoing crystal alignment[94]. Atomic features at 2D interfaces such as atomic ledges can also modify slip transmissibility[300]. Slip transmissibility should be quantified as a function of interphase misorientation and atomic structure for 3D interfaces as well. It may be that 3D interfaces disrupt the influence of biphase crystallography on interfacial dislocation transmission due to their disorder. In systems other than Cu/Nb where 3D interfaces may be crystalline and coherent throughout their thickness, geometric dislocation transmission criteria may simply be accounted for by modifying Lee-Robertson-Birnbaum criteria. Future work can address crystallographic influences on 3D interface dislocation transmission criteria as well.

Other phenomena such as interfacial dislocation storage and annihilation are not as well understood as dislocation transmission or nucleation. Single dislocation storage aided by

interfacial core spreading has been demonstrated for 2D Cu/Nb interfaces[4], but the interaction of collections of interfacially stored dislocations is not well understood. Some sources address dislocation storage in interfaces in terms of their contribution to material strengthening[301], but the energetics and frequency of phenomena such as dislocation annihilation and reaction arising from multiple dislocation storage at interfaces have not been quantified in the literature. Dislocation cores have enhanced climb mobility when stored at 2D Cu/Nb interfaces, which could facilitate annihilation and reaction[302]. 3D interfaces could promote dislocation storage due to their finite volume while moderating dislocation annihilation and reaction. This would enhance hardening of grain interiors[70], allowing the material to dissipate more plastic energy per unit strain while maintaining homogeneous deformation for extended ranges of plastic strain.

Lastly, the effect 3D interfaces on dislocation activity in abutting phases must be further explored. This work establishes two-dislocation hairpin interactions that act to drive isotropic slip system activity and uniform deformability, but more complete understanding of dislocation activity in the presence of 3D interfaces demands consideration of at least several to tens, if not hundreds, of dislocations[303]. The effect of 3D interfaces on few-dislocation interactions such as the intersection of hairpin loops on different slip systems resulting in dislocation locks or multiplication must be explored to fully understand 3D Cu/Nb mechanical behavior[70,304].

7.2.5. Proposed mechanical characterization of 3D interfaces

While *in situ* SEM experiments provide many key observations of 3D interface-mediated behavior, other *in situ* methods should be considered. *In situ* TEM deformation of 3D Cu/Nb may lead to further understanding of unit deformation mechanisms mediated by 3D interfaces. Different microstructures should be studied; the nanocrystalline nature of the specimens studied in this work made setup of specific imaging conditions nontrivial. Bicrystal experiments incorporating 3D

interfaces analogous to those that providing atomic-scale understanding of grain boundary mediated deformation should be conducted[305,306]. Sample synthesis of 3D interface bicrystals will not be trivial even using top-down methods like PVD. Other imaging modalities should also be used for *in situ* straining of 3D interfaces. *In situ* deformation in transmission SEM is particularly promising, as the higher excitation error provided by the smaller Ewald sphere increases the probability of observing dislocation-3D interface interaction at arbitrary imaging orientations[307].

Simulations will continue to be essential to understanding unit deformation mechanisms at the atomic scale. MD simulations of 3D interface straining can provide insight on processes such as dislocation nucleation that are not experimentally accessible. PFDD simulations will be crucial to incorporating mesoscale details such as short range chemical ordering and pre-existing twins on dislocation transmission at 3D interfaces. Incorporation of multiple order parameters may even enable PFDD to provide information about work hardening or dislocation annihilation mechanisms. Given suitable constitutive relations for 3D interface mechanical behavior or dislocation behavior at 3D interfaces, coarser scaled simulation methods such as CPFE and discrete dislocation dynamics will enable the consideration of the behavior of hundreds or thousands of dislocations in the presence of 3D interfaces. In conclusion, the frontiers of experimental and simulation work on 3D interfaces are ripe for the picking.

8. Bibliography

1. Weertman, J. & Weertman, J. R. *Elementary dislocation theory*. (Macmillan, 1964).
2. Naebe, M. & Shirvanimoghaddam, K. Functionally graded materials: A review of fabrication and properties. *Appl. Mater. Today* **5**, 223–245 (2016).
3. Wang, J., Hoagland, R. G., Liu, X. Y. & Misra, A. The influence of interface shear strength on the glide dislocation- interface interactions. *Acta Mater.* **59**, 3164–3173 (2011).
4. Wang, J., Hoagland, R. G., Hirth, J. P. & Misra, A. Atomistic simulations of the shear strength and sliding mechanisms of copper-niobium interfaces. *Acta Mater.* **56**, 3109–3119 (2008).
5. Beyerlein, I. J., Wang, J. & Zhang, R. Mapping dislocation nucleation behavior from bimetal interfaces. *Acta Mater.* **61**, 7488–7499 (2013).
6. Eftink, B. P. Dislocation interactions with characteristic interfaces in Ag-Cu eutectic. (2016).
7. Beyerlein, I. J., Wang, J., Kang, K., Zheng, S. J. & Mara, N. A. Twinnability of bimetal interfaces in nanostructured composites. *Mater. Res. Lett.* **1**, 89–95 (2013).
8. Tschopp, M. A., Spearot, D. E., McDowell, D. L. & Hirth, J. Influence of grain boundary structure on dislocation nucleation in FCC metals. *Dislocations in solids* **14**, 43–139 (2008).
9. Sangid, M. D., Ezaz, T., Sehitoglu, H. & Robertson, I. M. Energy of slip transmission and nucleation at grain boundaries. *Acta Mater.* **59**, 283–296 (2011).
10. Liu, Y., Bufford, D., Wang, H., Sun, C. & Zhang, X. Mechanical properties of highly textured Cu/Ni multilayers. *Acta Mater.* **59**, 1924–1933 (2011).
11. Yu-Zhang, K., Embury, J. D., Han, K. & Misra, A. Transmission electron microscopy investigation of the atomic structure of interfaces in nanoscale Cu-Nb multilayers. *Philos. Mag.* **88**, 2559–2567 (2008).
12. Wenk, H. R., Huensche, I. & Kestens, L. In-situ observation of texture changes during phase transformations in ultra-low-carbon steel. *Metall. Mater. Trans. A Phys. Metall. Mater. Sci.* **38**, 261–267 (2007).
13. Ma, E. Alloys created between immiscible elements. *Prog. Mater. Sci.* **50**, 413–509 (2005).
14. Misra, A., Hoagland, R. G. & Kung, H. Thermal stability of self-supported nanolayered Cu/Nb films. *Philos. Mag.* **84**, 1021–1028 (2004).
15. Misra, A., Hirth, J. P. & Hoagland, R. G. Length-scale-dependent deformation mechanisms in incoherent metallic multilayered composites. *Acta Mater.* **53**, 4817–4824 (2005).
16. Mara, N. A., Bhattacharyya, D., Hirth, J. P., Dickerson, P. & Misra, A. Mechanism for shear banding in nanolayered composites. *Appl. Phys. Lett.* **97**, (2010).
17. Mara, N. A., Bhattacharyya, D., Dickerson, P., Hoagland, R. G. & Misra, A. Deformability of ultrahigh strength 5nm Cu/Nb nanolayered composites. *Appl. Phys. Lett.* **92**, 231901 (2008).
18. Mara, N. A. & Beyerlein, I. J. Review: Effect of bimetal interface structure on the mechanical behavior of Cu-Nb fcc-bcc nanolayered composites. *J. Mater. Sci.* **49**, 6497–6516 (2014).
19. Beyerlein, I. J. *et al.* Interface-driven microstructure development and ultra high strength of bulk nanostructured Cu-Nb multilayers fabricated by severe plastic deformation. *J. Mater. Res.* **28**, 1799–1812 (2013).
20. Li, N. *et al.* Ex situ and in situ measurements of the shear strength of interfaces in metallic multilayers. *Scr. Mater.* **67**, 479–482 (2012).

21. Hoagland, R. G., Kurtz, R. J. & Henager, C. H. Slip resistance of interfaces and the strength of metallic multilayer composites. *Scr. Mater.* **50**, 775–779 (2004).
22. Mattox, D. M. *Handbook of physical vapor deposition (PVD) processing*. (William Andrew, 2010).
23. Thornton, J. A. Influence of substrate temperature and deposition rate on structure of thick sputtered Cu coatings. *J. Vac. Sci. Technol.* **12**, 830–835 (1975).
24. Craig, S. & Harding, G. L. Effects of Argon Pressure and Substrate Temperature on the Structure and Properties of Sputtered Copper Films. *J. Vac. Sci. Technol.* **19**, 205–215 (1981).
25. Windischmann, H. Intrinsic Stress in Sputter-Deposited Thin Films. *Crit. Rev. Solid State Mater. Sci.* **17**, 547–596 (1992).
26. Giannuzzi, L. A. *Introduction to focused ion beams: instrumentation, theory, techniques and practice*. (Springer Science & Business Media, 2004).
27. Williams, D. B. & Carter, C. B. *Transmission Electron Microscopy*. (Springer US, 2009).
28. Larson, D. J., Prosa, T. J., Ulfig, R. M., Geiser, B. P. & Kelly, T. F. Local electrode atom probe tomography. *New York, US Springer Sci.* **2**, (2013).
29. Campbell, J. E. & Clyne, T. W. Nanoindentation and Micropillar Compression. in *Testing of the Plastic Deformation of Metals* 192–218 (Cambridge University Press, 2021).
30. Greer, J. R., Oliver, W. C. & Nix, W. D. Size dependence of mechanical properties of gold at the micron scale in the absence of strain gradients. *Acta Mater.* **53**, 1821–1830 (2005).
31. Burek, M. J. & Greer, J. R. Fabrication and microstructure control of nanoscale mechanical testing specimens via electron beam lithography and electroplating. *Nano Lett.* **10**, 69–76 (2010).
32. Daryadel, S., Behroozfar, A. & Minary-Jolandan, M. A microscale additive manufacturing approach for in situ nanomechanics. *Mater. Sci. Eng. A* **767**, 138441 (2019).
33. Uchic, M. D., Dimiduk, D. M., Florando, J. N. & Nix, W. D. Sample Dimensions Influence Strength and Crystal Plasticity. *Science* **305**, 986–989 (2004).
34. Shim, S., Bei, H., Miller, M. K., Pharr, G. M. & George, E. P. Effects of focused ion beam milling on the compressive behavior of directionally solidified micropillars and the nanoindentation response of an electropolished surface. *Acta Mater.* **57**, 503–510 (2009).
35. Tabor, D. *The Hardness of Metals*. (Oxford University Press, 1951).
36. Fischer-Cripps, A. C. *Nanoindentation*. *Springer* (Springer, 2011).
37. Fischer-Cripps, A. C. Critical review of analysis and interpretation of nanoindentation test data. *Surf. Coatings Technol.* **200**, 4153–4165 (2006).
38. Johnson, K. L. The correlation of indentation experiments. *J. Mech. Phys. Solids* **18**, 115–126 (1970).
39. Gao, X. L., Jing, X. N. & Subhash, G. Two new expanding cavity models for indentation deformations of elastic strain-hardening materials. *Int. J. Solids Struct.* **43**, 2193–2208 (2006).
40. Zhang, H., Schuster, B. E., Wei, Q. & Ramesh, K. T. The design of accurate micro-compression experiments. *Scr. Mater.* **54**, 181–186 (2006).
41. Dieter, G. E. *Mechanical Metallurgy*. (McGraw-Hill Book Company, 1961).
42. Taylor, G. I. & Elam, C. F. The distortion of iron crystals. *Proc. R. Soc. London. Ser. A* **112**, 337–361 (1926).
43. Tipper, C. F. E. *Distortion of metal crystals*. (Clarendon Press, 1935).

44. Haydn, H. W., Moffat, W. G. & Wulff, J. “The Structure and Properties of Materials”, Volume III. (1965).
45. Wert, J. A., Huang, X. & Inoko, F. Deformation bands in a [110] aluminium single crystal strained in tension. *Proc. R. Soc. A Math. Phys. Eng. Sci.* **459**, 85–108 (2003).
46. Abbaschian, R., Abbaschian, L. & Reed-Hill, R. E. *Physical Metallurgy Principles*. (Cengage Learning, 2009).
47. Hosford, W. F. *Mechanical behavior of materials*. (Cambridge university press, 2010).
48. Cai, W. & Nix, W. D. *Imperfections in crystalline solids*. (Cambridge University Press, 2016).
49. Swalin, R. A. *Thermodynamics of Solids*. (Wiley, 1962).
50. Duesbery, M. S. & Richardson, G. Y. The dislocation core in crystalline materials. *Crit. Rev. Solid State Mater. Sci.* **17**, 1–46 (1991).
51. Heidenreich, R. D. & Shockley, W. Study of slip in aluminum crystals by electron microscope and electron diffraction methods. *Rep. conf. Strength Solids* **57**, (1948).
52. Vítek, V., Perrin, R. C. & Bowen, D. K. The core structure of ½ 〈111〉 screw dislocations in B.C.C. crystals. *Philos. Mag.* **21**, 1049–1073 (1970).
53. Vitek, V. Structure of dislocation cores in metallic materials and its impact on their plastic behaviour. *Prog. Mater. Sci.* **36**, 1–27 (1992).
54. Joós, B. & Duesbery, M. S. The Peierls stress of dislocations: An analytic formula. *Phys. Rev. Lett.* **78**, 266–269 (1997).
55. Lu, G. & Kaxiras, E. An Overview of Multiscale Simulations of Materials. (2004).
56. Louchet, F., Kubin, L. P. & Vesely, D. In situ deformation of b.c.c. crystals at low temperatures in a high-voltage electron microscope Dislocation mechanisms and strain-rate equation. *Philos. Mag. A Phys. Condens. Matter, Struct. Defects Mech. Prop.* **39**, 433–454 (1979).
57. Weinberger, C. R., Boyce, B. L. & Battaile, C. C. Slip planes in bcc transition metals. *Int. Mater. Rev.* **58**, 296–314 (2013).
58. Wachtman, J. B., Cannon, W. R. & Matthewson, M. J. *Mechanical properties of ceramics*. (John Wiley & Sons, 2009).
59. Callister, W. D. & Rethwisch, D. G. *Fundamentals of materials science and engineering*. vol. 471660817 (Wiley London, 2000).
60. Hosford, W. F. *The Mechanics of Crystals and Textured Polycrystals*. (Oxford University Press, 1993).
61. Mughrabi, H. Dislocation wall and cell structures and long-range internal stresses in deformed metal crystals. *Acta Metall.* **31**, 1367–1379 (1983).
62. Hall, E. O. The Deformation and Ageing of Mild Steel: III Discussion of Results. *Proc. Phys. Soc. Sect. B* **64**, 747–753 (1951).
63. Cracknell, A. & Petch, N. J. Frictional forces on dislocation arrays at the lower yield point in iron. *Acta Metall.* **3**, 186–189 (1955).
64. Pande, C. S. & Cooper, K. P. Nanomechanics of Hall-Petch relationship in nanocrystalline materials. *Prog. Mater. Sci.* **54**, 689–706 (2009).
65. Cordero, Z. C., Knight, B. E. & Schuh, C. A. Six decades of the Hall–Petch effect – a survey of grain-size strengthening studies on pure metals. *Int. Mater. Rev.* **61**, 495–512 (2016).
66. Embury, J. D. & Hirth, J. P. On dislocation storage and the mechanical response of fine scale microstructures. *Acta Metall. Mater.* **42**, 2051–2056 (1994).

67. Kumar, K. S., Van Swygenhoven, H. & Suresh, S. Mechanical behavior of nanocrystalline metals and alloys. *Acta Mater.* **51**, 5743–5774 (2003).
68. Ma, E. & Zhu, T. Towards strength–ductility synergy through the design of heterogeneous nanostructures in metals. *Mater. Today* **20**, 323–331 (2017).
69. Meyers, M. A., Mishra, A. & Benson, D. J. Mechanical properties of nanocrystalline materials. *Prog. Mater. Sci.* **51**, 427–556 (2006).
70. Malygin, G. A. Plasticity and strength of micro- and nanocrystalline materials. *Phys. Solid State* **49**, 1013–1033 (2007).
71. Guo, X., Liu, Y., Weng, G. J. & Zhu, L. L. Tensile Failure Modes in Nanograined Metals with Nanotwinned Regions. *Metall. Mater. Trans. A Phys. Metall. Mater. Sci.* **49**, 5001–5014 (2018).
72. Cheng, S., Spencer, J. A. & Milligan, W. W. Strength and tension/compression asymmetry in nanostructured and ultrafine-grain metals. *Acta Mater.* **51**, 4505–4518 (2003).
73. Zhu, B., Asaro, R. J., Krysl, P. & Bailey, R. Transition of deformation mechanisms and its connection to grain size distribution in nanocrystalline metals. *Acta Mater.* **53**, 4825–4838 (2005).
74. Kurtz, R. J., Hoagland, R. G. & Hirth, J. P. Effect of extrinsic grain-boundary defects on grain-boundary sliding resistance. *Philos. Mag. A Phys. Condens. Matter, Struct. Defects Mech. Prop.* **79**, 665–681 (1999).
75. Misra, A., Hirth, J. P. & Kung, H. Single-dislocation-based strengthening mechanisms in nanoscale metallic multilayers. *Philos. Mag. A* **82**, 2935–2951 (2002).
76. Capolungo, L. *et al.* Dislocation nucleation from bicrystal interfaces and grain boundary ledges: Relationship to nanocrystalline deformation. *J. Mech. Phys. Solids* **55**, 2300–2327 (2007).
77. Van Swygenhoven, H. & Weertman, J. R. Deformation in nanocrystalline metals. *Mater. Today* **9**, 24–31 (2006).
78. Priester, L. *Grain Boundaries: From Theory to Engineering*. (Springer, 2013).
79. Hirth, J. P. Dislocations, steps and disconnections at interfaces. *J. Phys. Chem. Solids* **55**, 985–989 (1994).
80. Han, W. Z., Carpenter, J. S., Wang, J., Beyerlein, I. J. & Mara, N. A. Atomic-level study of twin nucleation from face-centered-cubic/body- centered-cubic interfaces in nanolamellar composites. *Appl. Phys. Lett.* **100**, (2012).
81. Sutton, A. . & Balluffi, R. . On geometric criteria for low interfacial energy. *Acta Metall.* **35**, 2177–2201 (1987).
82. Winning, M., Gottstein, G. & Shvindlerman, L. S. On the mechanisms of grain boundary migration. *Acta Mater.* **50**, 353–363 (2002).
83. Langdon, T. G. Grain boundary sliding revisited: Developments in sliding over four decades. *J. Mater. Sci.* **41**, 597–609 (2006).
84. Wang, L. *et al.* Grain rotation mediated by grain boundary dislocations in nanocrystalline platinum. *Nat. Commun.* **5**, 1–7 (2014).
85. Shen, Z., Wagoner, R. H. & Clark, W. A. T. Dislocation and grain boundary interactions in metals. *Acta Metall.* **36**, 3231–3242 (1988).
86. Khalfallah, O., Condat, M. & Priester, L. Image force on a lattice dislocation due to a grain boundary in B.C.C. metals. *Philos. Mag. A Phys. Condens. Matter, Struct. Defects Mech. Prop.* **67**, 231–250 (1993).

87. Barnett, D. M. & Lothe, J. An image force theorem for dislocations in anisotropic bicrystals. *J. Phys. F Met. Phys.* **4**, 1618–1635 (1974).
88. Murr, L. E. & Hecker, S. S. Quantitative evidence for dislocation emission from grain boundaries. *Scr. Metall.* **13**, 167–171 (1979).
89. Li, N., Wang, J., Huang, J. Y., Misra, A. & Zhang, X. In situ TEM observations of room temperature dislocation climb at interfaces in nanolayered Al/Nb composites. *Scr. Mater.* **63**, 363–366 (2010).
90. Kacher, J. & Robertson, I. M. Quasi-four-dimensional analysis of dislocation interactions with grain boundaries in 304 stainless steel. *Acta Mater.* **60**, 6657–6672 (2012).
91. Priester, L. On the accommodation of extrinsic dislocations in grain boundaries. *Interface Sci.* **4**, 205–219 (1997).
92. Livingston, J. D. & Chalmers, B. Multiple slip in bicrystal deformation. *Acta Metall.* **5**, 322–327 (1957).
93. Lee, T. C., Robertson, I. M. & Birnbaum, H. K. TEM in situ deformation study of the interaction of lattice dislocations with grain boundaries in metals. *Philos. Mag. A Phys. Condens. Matter, Struct. Defects Mech. Prop.* **62**, 131–153 (1990).
94. Werner, E. & Prantl, W. Slip transfer across grain and phase boundaries. *Acta Metall. Mater.* **38**, 533–537 (1990).
95. Spearot, D. E. & Sangid, M. D. Insights on slip transmission at grain boundaries from atomistic simulations. *Curr. Opin. Solid State Mater. Sci.* **18**, 188–195 (2014).
96. Pond, R. C. & Smith, D. A. On the absorption of dislocations by grain boundaries. *Philos. Mag.* **36**, 353–366 (1977).
97. Lu, L., Chen, X., Huang, X. & Lu, K. Revealing the maximum strength in nanotwinned copper. *Science* **323**, 607–610 (2009).
98. Bufford, D., Wang, H. & Zhang, X. High strength, epitaxial nanotwinned Ag films. *Acta Mater.* **59**, 93–101 (2011).
99. Li, Q. *et al.* High-Strength Nanotwinned Al Alloys with 9R Phase. *Adv. Mater.* **30**, 1704629 (2018).
100. Anderoglu, O. *et al.* Epitaxial nanotwinned Cu films with high strength and high conductivity. *Appl. Phys. Lett.* **93**, 083108 (2008).
101. Anderoglu, O. *et al.* Plastic flow stability of nanotwinned Cu foils. *Int. J. Plast.* **26**, 875–886 (2010).
102. Lu, N., Du, K., Lu, L. & Ye, H. Q. Transition of dislocation nucleation induced by local stress concentration in nanotwinned copper. *Nat. Commun.* **6**, 1–7 (2015).
103. Kaye, G. W. C. & Laby, T. H. *Tables of physical and chemical constants and some mathematical functions*. (Longmans, Green & Co., 1993).
104. James, A. M. & Lord, M. P. Macmillan's chemical and physical data. (1992).
105. Samsonov, G. V. *Handbook of the Physicochemical Properties of the Elements*. (Springer, 2012).
106. Beyerlein, I. J. *et al.* Structure–Property–Functionality of Bimetal Interfaces. *JOM* **64**, 1192–1207 (2012).
107. Shen, Y. & Anderson, P. M. Transmission of a screw dislocation across a coherent, non-slipping interface. *J. Mech. Phys. Solids* **55**, 956–979 (2007).
108. Jin, Z. H. *et al.* The interaction mechanism of screw dislocations with coherent twin boundaries in different face-centred cubic metals. *Scr. Mater.* **54**, 1163–1168 (2006).

109. Koehler, J. S. Attempt to Design a Strong Solid. *Phys. Rev. B* **2**, 547–551 (1970).
110. Rao, S. I. & Hazzledine, P. M. Atomistic simulations of dislocation-interface interactions in the Cu-Ni multilayer system. *Philos. Mag. A Phys. Condens. Matter, Struct. Defects Mech. Prop.* **80**, 2011–2040 (2000).
111. Eftink, B. P., Li, A., Szlufarska, I., Mara, N. A. & Robertson, I. M. Deformation response of AgCu interfaces investigated by in situ and ex situ TEM straining and MD simulations. *Acta Mater.* **138**, 212–223 (2017).
112. Eftink, B. P., Li, A., Szlufarska, I. & Robertson, I. M. Interface mediated mechanisms of plastic strain recovery in a AgCu alloy. *Acta Mater.* **117**, 111–121 (2016).
113. Porter, D. A., Easterling, K. E. & Sherif, M. Y. *Phase Transformations in Metals and Alloys*. (CRC Press, 2009).
114. Wang, J., Hoagland, R. G. & Misra, A. Phase transition and dislocation nucleation in Cu-Nb layered composites during physical vapor deposition. *J. Mater. Res.* **23**, 1009–1014 (2008).
115. Thompson, G. B., Banerjee, R., Dregia, S. A., Miller, M. K. & Fraser, H. L. A comparison of pseudomorphic bcc phase stability in Zr/Nb and Ti/Nb thin film multilayers. *J. Mater. Res.* **19**, 707–715 (2004).
116. Liu, Y., Yang, K. M., Hay, J., Fu, E. G. & Zhang, X. The effect of coherent interface on strain-rate sensitivity of highly textured Cu/Ni and Cu/V multilayers. *Scr. Mater.* **162**, 33–37 (2019).
117. Meier, G. H. Interphase Interfaces. in *Thermodynamics of Surfaces and Interfaces* 128–147 (Cambridge University Press, 2014).
118. Anderson, P. M., Foecke, T. & Hazzledine, P. M. Dislocation-based deformation mechanisms in metallic nanolaminates. *MRS Bull.* **24**, 27–33 (1999).
119. Mastorakos, I. N., Zbib, H. M. & Bahr, D. F. Deformation mechanisms and strength in nanoscale multilayer metallic composites with coherent and incoherent interfaces. *Appl. Phys. Lett.* **94**, (2009).
120. Popov, V. V. & Popova, E. N. Behavior of Nb and CuNb composites under severe plastic deformation and annealing. *Mater. Trans.* **60**, 1209–1220 (2019).
121. Li, Y. J. *et al.* Evolution of strength and microstructure during annealing of heavily cold-drawn 6.3 GPa hypereutectoid pearlitic steel wire. *Acta Mater.* **60**, 4005–4016 (2012).
122. Cammarata, R. C., Schlesinger, T. E., Kim, C., Qadri, S. B. & Edelstein, A. S. Nanoindentation study of the mechanical properties of copper-nickel multilayered thin films. *Appl. Phys. Lett.* **56**, 1862–1864 (1990).
123. Yasuna, K., Terauchi, M., Otsuki, A., Ishihara, K. N. & Shingu, P. H. Bulk metallic multilayers produced by repeated press-rolling and their perpendicular magnetoresistance. *J. Appl. Phys.* **82**, 2435–2438 (1997).
124. Ohsaki, S., Kato, S., Tsuji, N., Ohkubo, T. & Hono, K. Bulk mechanical alloying of Cu-Ag and Cu/Zr two-phase microstructures by accumulative roll-bonding process. *Acta Mater.* **55**, 2885–2895 (2007).
125. Lee, S.-B., LeDonne, J. E., Lim, S. C. V., Beyerlein, I. J. & Rollett, A. D. The heterophase interface character distribution of physical vapor-deposited and accumulative roll-bonded Cu–Nb multilayer composites. *Acta Mater.* **60**, 1747–1761 (2012).
126. Tambwe, M. F. *et al.* Haasen plot analysis of the Hall-Petch effect in Cu/Nb nanolayer composites. *J. Mater. Res.* **14**, 407–417 (1999).

127. Yang, L. W., Mayer, C. R., Chawla, N., LLorca, J. & Molina-Aldareguía, J. M. Nanomechanical characterization of the fracture toughness of Al/SiC nanolaminates. *Extrem. Mech. Lett.* **40**, 100945 (2020).
128. Lehoczky, S. L. Strength enhancement in thin-layered Al-Cu laminates. *J. Appl. Phys.* **49**, 5479–5485 (1978).
129. Banerjee, R., Ahuja, R. & Fraser, H. L. Dimensionally induced structural transformations in titanium-aluminum multilayers. *Phys. Rev. Lett.* **76**, 3778–3781 (1996).
130. Misra, A. *et al.* Structure and mechanical properties of Cu-X (X = Nb,Cr,Ni) nanolayered composites. *Scr. Mater.* **39**, 555–560 (1998).
131. Hazzledine, P. M., Grinfeld, M. A. & Rao, S. I. Coherency and loss of coherency in multilayers. *Mater. Res. Soc. Symp. - Proc.* **505**, 179–184 (1998).
132. Clemens, B. M., Kung, H. & Barnett, S. A. Structure and Strength of Multilayers. *MRS Bull.* **24**, 20–26 (1999).
133. Yamamoto, T. *et al.* Misfit Dislocations in Epitaxial Ni/Cu Bilayer and Cu/Ni/Cu Trilayer Thin Films. **673**, 1–6 (2001).
134. Mitchell, T. E., Lu, Y. C., Jr., A. J. G., Nastasi, M. & Kung, H. Structure and Mechanical Properties of Copper/Niobium Multilayers. *J. Am. Ceram. Soc.* **80**, 1673–1676 (1997).
135. Dahmen, U. Orientation relationships in precipitation systems. *Acta Metall.* **30**, 63–73 (1982).
136. Carpenter, J. S., Vogel, S. C., Ledonne, J. E., Hammon, D. L. & Beyerlein, I. J. Bulk texture evolution of Cu – Nb nanolamellar composites during accumulative roll bonding. *Acta Mater.* **60**, 1576–1586 (2012).
137. Wang, J. *et al.* Structure and property of interfaces in ARB Cu/Nb laminated composites. *Jom* **64**, 1208–1217 (2012).
138. Zheng, S., Carpenter, J. S., McCabe, R. J., Beyerlein, I. J. & Mara, N. A. Engineering Interface Structures and Thermal Stabilities via SPD Processing in Bulk Nanostructured Metals. *Sci. Rep.* **4**, 4226 (2014).
139. Zhou, Q. *et al.* The mechanical behavior of nanoscale metallic multilayers: A survey. *Acta Mech. Sin.* **31**, 319–337 (2015).
140. Nasim, M., Li, Y., Wen, M. & Wen, C. A review of high-strength nanolaminates and evaluation of their properties. *J. Mater. Sci. Technol.* **50**, 215–244 (2020).
141. Zheng, S. J. *et al.* Plastic instability mechanisms in bimetallic nanolayered composites. *Acta Mater.* **79**, 282–291 (2014).
142. Anwar Ali, H. P., Radchenko, I., Li, N. & Budiman, A. The roles of interfaces and other microstructural features in Cu/Nb nanolayers as revealed by in situ beam bending experiments inside an scanning electron microscope (SEM). *Mater. Sci. Eng. A* **738**, 253–263 (2018).
143. Wang, Y. Q. *et al.* Fracture behavior and deformation mechanisms in nanolaminated crystalline/amorphous micro-cantilevers. *Acta Mater.* **180**, 73–83 (2019).
144. Bhattacharyya, D., Mara, N. A., Dickerson, P., Hoagland, R. G. & Misra, A. Transmission electron microscopy study of the deformation behavior of Cu/Nb and Cu/Ni nanoscale multilayers during nanoindentation. *J. Mater. Res.* **24**, 1291–1302 (2009).
145. Misra, A. & Kung, H. Deformation Behavior of Nanostructured Metallic Multilayers. *Adv. Eng. Mater.* **3**, 217–222 (2001).
146. Cheng, J. Y. *et al.* Simultaneous High-Strength and Deformable Nanolaminates With Thick

Biphase Interfaces. *Nano Lett.* **22**, 1897–1904 (2022).
147. Demkowicz, M. J. & Thilly, L. Structure, shear resistance and interaction with point defects of interfaces in Cu-Nb nanocomposites synthesized by severe plastic deformation. *Acta Mater.* **59**, 7744–7756 (2011).
148. Mortensen, A. & Suresh, S. Functionally graded metals and metal-ceramic composites: Part 1 Processing. *Int. Mater. Rev.* **40**, 239–265 (1995).
149. Schulz, U., Peters, M., Bach, F.-W. & Tegeder, G. Graded coatings for thermal, wear and corrosion barriers. *Mater. Sci. Eng. A* **362**, 61–80 (2003).
150. Dillon, S. J., Tang, M., Carter, W. C. & Harmer, M. P. Complexion: A new concept for kinetic engineering in materials science. *Acta Mater.* **55**, 6208–6218 (2007).
151. Fan, Z. *et al.* "Ductile" Fracture of Metallic Glass Nanolaminates. *Adv. Mater. Interfaces* **4**, 1–9 (2017).
152. Kim, J., Jang, D. & Greer, J. R. Nanolaminates Utilizing Size-Dependent Homogeneous Plasticity of Metallic Glasses. *Adv. Funct. Mater.* **21**, 4550–4554 (2011).
153. Le, M. T., Sohn, Y. U., Lim, J. W. & Choi, G. S. Effect of sputtering power on the nucleation and growth of Cu films deposited by magnetron sputtering. *Mater. Trans.* **51**, 116–120 (2010).
154. Arnell, R. D. & Kelly, P. J. Recent advances in magnetron sputtering. *Surf. Coatings Technol.* **112**, 170–176 (1999).
155. Kim, M. J. & Carpenter, R. W. Composition and Structure of Native Oxide on Silicon by High Resolution Analytical Electron Microscopy. *J. Mater. Res.* **5**, 347–351 (1990).
156. Chen, Y. *et al.* Microstructure and strengthening mechanisms in Cu/Fe multilayers. *Acta Mater.* **60**, 6312–6321 (2012).
157. Anders, A. A structure zone diagram including plasma-based deposition and ion etching. *Thin Solid Films* **518**, 4087–4090 (2010).
158. Cullity, B. D. *Elements of X-ray Diffraction*. (Addison-Wesley Publishing, 1956).
159. Demkowicz, M. J., Hoagland, R. G. & Hirth, J. P. Interface Structure and Radiation Damage Resistance in Cu-Nb Multilayer Nanocomposites. *Phys. Rev. Lett.* **100**, 136102 (2008).
160. Fultz, B. & Howe, J. M. *Transmission electron microscopy and diffractometry of materials*. (Springer, 2012).
161. Edington, J. W. *Electron Diffraction in the Electron Microscope*. (Red Globe Press, 1975).
162. Bell, D. C., Russo, C. J. & Kolmykov, D. V. 40keV atomic resolution TEM. *Ultramicroscopy* **114**, 31–37 (2012).
163. Marquis, E. A., Geiser, B. P., Prosa, T. J. & Larson, D. J. Evolution of tip shape during field evaporation of complex multilayer structures. *J. Microsc.* **241**, 225–233 (2011).
164. Larson, D., Prosa, T., Ulfig, R., Geiser, B. P. & Kelly, T. F. Local electrode atom probe tomography. in *Local electrode atom probe tomography* 137 (Springer, 2013).
165. Miller, M. K. & Hetherington, M. G. Local magnification effects in the atom probe. *Surf. Sci.* **246**, 442–449 (1991).
166. Kelly, T., Voelkl, E. & Geiser, B. Practical Determination of Spatial Resolution in Atom Probe Tomography. *Microsc. Microanal.* **15**, 12–13 (2009).
167. Mara, N. A., Bhattacharyya, D., Hoagland, R. G. & Misra, A. Tensile behavior of 40 nm Cu/Nb nanoscale multilayers. *Scr. Mater.* **58**, 874–877 (2008).
168. Haque, M. A. & Saif, M. T. A. In-situ tensile testing of nano-scale specimens in SEM and TEM. *Exp. Mech.* **42**, 123–128 (2002).

169. Kumar, K. *et al.* Use of miniature tensile specimen for measurement of mechanical properties. *Procedia Eng.* **86**, 899–909 (2014).
170. Daryadel, S., Behroozfar, A. & Minary-Jolandan, M. A microscale additive manufacturing approach for in situ nanomechanics. *Mater. Sci. Eng. A* **767**, 138441 (2019).
171. Hütsch, J. & Lilleodden, E. T. The influence of focused-ion beam preparation technique on microcompression investigations: Lathe vs. annular milling. *Scr. Mater.* **77**, 49–51 (2014).
172. Uchic, M. D., Shade, P. A. & Dimiduk, D. M. Plasticity of Micrometer-Scale Single Crystals in Compression. *Annu. Rev. Mater. Res.* **39**, 361–386 (2009).
173. Uchic, M. D., Dimiduk, D. M., Florando, J. N. & Nix, W. D. Sample dimensions influence strength and crystal plasticity. *Science* **305**, 986–989 (2004).
174. Volkert, C. A. & Lilleodden, E. T. Size effects in the deformation of sub-micron Au columns. *Philos. Mag.* **86**, 5567–5579 (2006).
175. Shan, Z. W., Mishra, R. K., Syed Asif, S. A., Warren, O. L. & Minor, A. M. Mechanical annealing and source-limited deformation in submicrometre-diameter Ni crystals. *Nat. Mater.* **7**, 115–119 (2008).
176. Chen, L. Y., He, M. R., Shin, J., Richter, G. & Gianola, D. S. Measuring surface dislocation nucleation in defect-scarce nanostructures. *Nat. Mater.* **14**, 707–713 (2015).
177. Parthasarathy, T. A., Rao, S. I., Dimiduk, D. M., Uchic, M. D. & Trinkle, D. R. Contribution to size effect of yield strength from the stochastics of dislocation source lengths in finite samples. *Scr. Mater.* **56**, 313–316 (2007).
178. Beatty, M. F. & Hook, D. E. Some experiments on the stability of circular, rubber bars under end thrust. *Int. J. Solids Struct.* **4**, 623–635 (1968).
179. Singh, D. R. P., Chawla, N., Tang, G. & Shen, Y. L. Micropillar compression of Al/SiC nanolaminates. *Acta Mater.* **58**, 6628–6636 (2010).
180. Jiang, L. & Chawla, N. Mechanical properties of Cu6Sn5 intermetallic by micropillar compression testing. *Scr. Mater.* **63**, 480–483 (2010).
181. Ma, E. Controlling plastic instability. *Nat. Mater.* **2**, 7–8 (2003).
182. Hay, J. L., Olive, W. C., Bolshakov, A. & Pharr, G. M. Using the Ratio of Loading Slope and Elastic Stiffness to Predict Pile-Up and Constraint Factor During Indentation. *MRS Proc.* **522**, 101 (1998).
183. Pathak, S. & Kalidindi, S. R. Spherical nanoindentation stress-strain curves. *Mater. Sci. Eng. R Reports* **91**, 1–36 (2015).
184. Leitner, A., Maier-Kiener, V. & Kiener, D. Extraction of Flow Behavior and Hall–Petch Parameters Using a Nanoindentation Multiple Sharp Tip Approach. *Adv. Eng. Mater.* **19**, 1–9 (2017).
185. Leitner, A., Maier-Kiener, V. & Kiener, D. Essential refinements of spherical nanoindentation protocols for the reliable determination of mechanical flow curves. *Mater. Des.* **146**, 69–80 (2018).
186. Bückle, H. Progress in micro-indentation hardness testing. *Metall. Rev.* **4**, 49–100 (1959).
187. Oliver, W. C. & Pharr, G. M. An improved technique for determining hardness and elastic modulus using load and displacement sensing indentation experiments. *J. Mater. Res.* **7**, 1564–1583 (1992).
188. Stilwell, N. A. & Tabor, D. Elastic recovery of conical indentations. *Proc. Phys. Soc.* **78**, 169–179 (1961).
189. Subhash, G. Dynamic indentation testing. *ASM Handb. Mech. Test. Eval.* **8**, 519–529 (2000).

190. Li, W. B., Henshall, J. L., Hooper, R. M. & Easterling, K. E. The mechanisms of indentation creep. *Acta Metall. Mater.* **39**, 3099–3110 (1991).
191. Lucas, B. N. & Oliver, W. C. Indentation power-law creep of high-purity indium. *Metall. Mater. Trans. A* **30**, 601–610 (1999).
192. Maier-Kiener, V. & Durst, K. Advanced Nanoindentation Testing for Studying Strain-Rate Sensitivity and Activation Volume. *Jom* **69**, 2246–2255 (2017).
193. Schmalbach, K. M. & Mara, N. A. Algorithms for Nanoindentation Strain Rate Jump Testing and Analysis. *Exp. Mech.* **62**, 885–888 (2022).
194. Sneddon, I. N. The relation between load and penetration in the axisymmetric Boussinesq problem for a punch of arbitrary profile. *Int. J. Eng. Sci.* **3**, 47–57 (1965).
195. Hertz, H. Über die Berührung fester elastischer Körper. *J reine und Angew. Math.* **92**, 156 (1881).
196. Gabriele, B. P. A., Williams, C. J., Lauer, M. E., Derby, B. & Cruz-Cabeza, A. J. Nanoindentation of molecular crystals: Lessons learned from aspirin. *Cryst. Growth Des.* **20**, 5956–5966 (2020).
197. Pethica, J. B. & Oliver, W. C. Mechanical Properties of Nanometre Volumes of Material: use of the Elastic Response of Small Area Indentations. *MRS Proc.* **130**, 13–23 (1988).
198. Li, X. & Bhushan, B. A review of nanoindentation continuous stiffness measurement technique and its applications. *Mater. Charact.* **48**, 11–36 (2002).
199. Swain, M. V. & Hagan, J. T. Indentation plasticity and the ensuing fracture of glass. *J. Phys. D. Appl. Phys.* **9**, 2201–2214 (1976).
200. Suryanarayana, C., Mukhopadhyay, D., Patankar, S. N. & Froes, F. H. Grain size effects in nanocrystalline materials. *J. Mater. Res.* **7**, 2114–2118 (1992).
201. Tabor, D. The hardness of solids. *Rev. Phys. Technol.* **1**, 145–179 (1970).
202. Tabor, D. A simple theory of static and dynamic hardness. *Proc. R. Soc. London. Ser. A. Math. Phys. Sci.* **192**, 247–274 (1948).
203. Gram, M. D., Carpenter, J. S. & Anderson, P. M. An indentation-based method to determine constituent strengths within nanolayered composites. *Acta Mater.* **92**, 255–264 (2015).
204. Johnson, K. L. The correlation of indentation experiments. *J. Mech. Phys. Solids* **18**, 115–126 (1970).
205. Eswar Prasad, K., Chollacoop, N. & Ramamurty, U. Role of indenter angle on the plastic deformation underneath a sharp indenter and on representative strains: An experimental and numerical study. *Acta Mater.* **59**, 4343–4355 (2011).
206. Dao, M., Chollacoop, N., Van Vliet, K. J., Venkatesh, T. A. & Suresh, S. Computational modeling of the forward and reverse problems in instrumented sharp indentation. *Acta Mater.* **49**, 3899–3918 (2001).
207. Ogasawara, N., Chiba, N. & Chen, X. Representative strain of indentation analysis. *J. Mater. Res.* **20**, 2225–2234 (2005).
208. Hernot, X., Moussa, C. & Bartier, O. Study of the concept of representative strain and constraint factor introduced by Vickers indentation. *Mech. Mater.* **68**, 1–14 (2014).
209. Cao, Y. & Huber, N. Further investigation on the definition of the representative strain in conical indentation. *J. Mater. Res.* **21**, 1810–1821 (2006).
210. Tiryakioğlu, M. & Robinson, J. S. On the representative strain in Vickers hardness testing of 7010 aluminum alloy. *Mater. Sci. Eng. A* **641**, 231–236 (2015).
211. Chollacoop, N. & Ramamurty, U. Experimental assessment of the representative strains in

instrumented sharp indentation. *Scr. Mater.* **53**, 247–251 (2005).
212. Bachmann, F., Hielscher, R. & Schaeben, H. Texture analysis with MTEX- Free and open source software toolbox. *Solid State Phenom.* **160**, 63–68 (2010).
213. He, B. B. *Two-dimensional X-ray Diffraction*. (John Wiley & Sons, 2018).
214. Kocks, F., Tomé, C. & Wenk, H.-R. *Texture and Anisotropy: Preferred Orientations in Polycrystals and Their Effect on Material Properties*. (Cambridge University Press, 2000).
215. Pennycook, S. J. & Jesson, D. E. High-resolution Z-contrast imaging of crystals. *Ultramicroscopy* **37**, 14–38 (1991).
216. Schuler, J. D. *et al.* Amorphous intergranular films mitigate radiation damage in nanocrystalline Cu-Zr. *Acta Mater.* **186**, 341–354 (2020).
217. Mitchson, G. *et al.* Application of HAADF STEM image analysis to structure determination in rotationally disordered and amorphous multilayered films. *Semicond. Sci. Technol.* **31**, (2016).
218. Yu, Z., Muller, D. A. & Silcox, J. Effects of specimen tilt in ADF-STEM imaging of a-Si/c-Si interfaces. *Ultramicroscopy* **108**, 494–501 (2008).
219. Ophus, C. Four-Dimensional Scanning Transmission Electron Microscopy (4D-STEM): From Scanning Nanodiffraction to Ptychography and Beyond. *Microsc. Microanal.* **25**, 563–582 (2019).
220. Chen, Y. *et al.* Damage-tolerant nanotwinned metals with nanovoids under radiation environments. *Nat. Commun.* **6**, (2015).
221. Clarebrough, L. M. & Forwood, C. T. Diffraction from single and overlapping stacking faults in F.C.C. crystals. *Phys. Status Solidi* **33**, 355–366 (1976).
222. Hagége, S., Carter, C. B., Cosandey, F. & Sass, S. L. The variation of grain boundary structural width with misorientation angle and boundary plane. *Philos. Mag. A Phys. Condens. Matter, Struct. Defects Mech. Prop.* **45**, 723–740 (1982).
223. Cairney, J. M. & Munroe, P. R. Redeposition effects in transmission electron microscope specimens of FeAl-WC composites prepared using a focused ion beam. *Micron* **34**, 97–107 (2003).
224. Li, Z. *et al.* Critical length scales for chemical heterogeneity at Cu/Nb 3D interfaces by atom probe tomography. *Scr. Mater.* **223**, 115078 (2023).
225. Poplawsky, J. D. *et al.* Structural and compositional dependence of the CdTe x Se 1− x alloy layer photoactivity in CdTe-based solar cells. *Nat. Commun.* **7**, 1–10 (2016).
226. Larson, D. J., Foord, D. T., Petford-Long, A. K., Cerezo, A. & Smith, G. D. W. Focused ion-beam specimen preparation for atom probe field-ion microscopy characterization of multilayer film structures. *Nanotechnology* **10**, 45–50 (1999).
227. Hwang, J. Y. *et al.* Evolution of the γ/γ′ interface width in a commercial nickel base superalloy studied by three-dimensional atom probe tomography. *Scr. Mater.* **61**, 92–95 (2009).
228. Chen, Y. *et al.* Effects of three-dimensional Cu/Nb interfaces on strengthening and shear banding in nanoscale metallic multilayers. *Acta Mater.* **199**, 593–601 (2020).
229. Derby, B. K., Chatterjee, A. & Misra, A. Metal-ion-controlled growth and nanoindentation response of 3D, bicontinuous Cu–Fe thin films. *J. Appl. Phys.* **128**, 035303 (2020).
230. Maier, K. Self-diffusion in copper at "low" temperatures. *Phys. Status Solidi* **44**, 567–576 (1977).
231. Agrawal, P. M., Rice, B. M. & Thompson, D. L. Predicting trends in rate parameters for

self-diffusion on FCC metal surfaces. *Surf. Sci.* **515**, 21–35 (2002).
232. Kapoor, A., Yang, R. T. & Wong, C. Surface Diffusion. *Catal. Rev.* **31**, 129–214 (1989).
233. Chen, Y. *et al.* Effects of three-dimensional Cu/Nb interfaces on strengthening and shear banding in nanoscale metallic multilayers. *Acta Mater.* **199**, 593–601 (2020).
234. Cheng, J. Y. *et al.* 3D Interfaces Enhance Nanolaminate Strength and Deformability in Multiple Loading Orientations (In revision). *Acta Mater.*
235. Liang, Y. *et al.* Effect of interface structure and layer thickness on the mechanical properties and deformation behavior of Cu/Ag nanolaminates. *Phys. B Condens. Matter* **661**, 414933 (2023).
236. Mayer, C. R. *et al.* Anisotropy, size, and aspect ratio effects on micropillar compression of Al SiC nanolaminate composites. *Acta Mater.* **114**, 25–32 (2016).
237. Wang, J., Knezevic, M., Jain, M., Pathak, S. & Beyerlein, I. J. Role of interface-affected dislocation motion on the strength of Mg/Nb nanolayered composites inferred by dual-mode confined layer slip crystal plasticity. *J. Mech. Phys. Solids* **152**, 104421 (2021).
238. Wang, J., Hoagland, R. G. & Misra, A. Mechanics of nanoscale metallic multilayers: From atomic-scale to micro-scale. *Scr. Mater.* **60**, 1067–1072 (2009).
239. Okamoto, N. L., Kashioka, D., Hirato, T. & Inui, H. Specimen- and grain-size dependence of compression deformation behavior in nanocrystalline copper. *Int. J. Plast.* **56**, 173–183 (2014).
240. Zener, C. *Elasticity and anelasticity of metals*. (University of Chicago Press, 1965).
241. Wang, Z. *et al.* Effects of Phase Purity and Pore Reinforcement on Mechanical Behavior of NU-1000 and Silica-Infiltrated NU-1000 Metal-Organic Frameworks. *ACS Appl. Mater. Interfaces* **12**, 49971–49981 (2020).
242. Michaelsen, C., Gente, C. & Bormann, R. The thermodynamics of amorphous phases in immiscible systems: The example of sputter-deposited Nb–Cu alloys. *J. Appl. Phys.* **81**, 6024–6030 (1997).
243. Geng, C. *et al.* Evolution of local densities during shear banding in Zr-based metallic glass micropillars. *Acta Mater.* **235**, 118068 (2022).
244. Ye, J. C., Lu, J., Yang, Y. & Liaw, P. K. Study of the intrinsic ductile to brittle transition mechanism of metallic glasses. *Acta Mater.* **57**, 6037–6046 (2009).
245. Yang, Y., Ye, J., Lu, J., Gao, Y. & Liaw, P. K. Metallic glasses: Gaining plasticity for microsystems. *JOM* **62**, 93–98 (2010).
246. Burnett, P. J. & Rickerby, D. S. The mechanical properties of wear-resistant coatings. II: Experimental studies and interpretation of hardness. *Thin Solid Films* **148**, 51–65 (1987).
247. Korsunsky, A. M., McGurk, M. R., Bull, S. J. & Page, T. F. On the hardness of coated systems. *Surf. Coatings Technol.* **99**, 171–183 (1998).
248. Pharr, G. M. & Oliver, W. C. Measurement of Thin Film Mechanical Properties Using Nanoindentation. *MRS Bull.* **17**, 28–33 (1992).
249. Zak, S., Trost, C. O. W., Kreiml, P. & Cordill, M. J. Accurate measurement of thin film mechanical properties using nanoindentation. *J. Mater. Res.* **37**, 1373–1389 (2022).
250. Saha, R. & Nix, W. D. Effects of the substrate on the determination of thin film mechanical properties by nanoindentation. *Acta Mater.* **50**, 23–38 (2002).
251. Fischer-Cripps, A. C. The sharpness of a berkovich indenter. *J. Mater. Res.* **25**, 927–934 (2010).
252. Nix, W. D. & Gao, H. Indentation size effects in crystalline materials: A law for strain

gradient plasticity. *J. Mech. Phys. Solids* **46**, 411–425 (1998).
253. Di Gioacchino, F. & Clegg, W. J. Mapping deformation in small-scale testing. *Acta Mater.* **78**, 103–113 (2014).
254. Xu, S., Cheng, J. Y., Li, Z., Mara, N. A. & Beyerlein, I. J. Phase-field modeling of the interactions between an edge dislocation and an array of obstacles. *Comput. Methods Appl. Mech. Eng.* **389**, 114426 (2022).
255. Beyerlein, I. J. & Hunter, A. Understanding dislocation mechanics at the mesoscale using phase field dislocation dynamics. *Philos. Trans. R. Soc. A Math. Phys. Eng. Sci.* **374**, 20150166 (2016).
256. Koslowski, M., Cuitiño, A. M. & Ortiz, M. A phase-field theory of dislocation dynamics, strain hardening and hysteresis in ductile single crystals. *J. Mech. Phys. Solids* **50**, 2597–2635 (2002).
257. Snel, J. *et al.* Deformation Mechanism Map of Cu/Nb Nanoscale Metallic Multilayers as a Function of Temperature and Layer Thickness. *JOM* **69**, 2214–2226 (2017).
258. Wang, Y., Chen, M., Zhou, F. & Ma, E. High tensile ductility in a nanostructured metal. *Nature* **419**, 912–915 (2002).
259. Lu, K., Lu, L. & Suresh, S. Strengthening Materials by Engineering Coherent Internal Boundaries at the Nanoscale. *Science* **324**, 349–352 (2009).
260. Khalajhedayati, A., Pan, Z. & Rupert, T. J. Manipulating the interfacial structure of nanomaterials to achieve a unique combination of strength and ductility. *Nat. Commun.* **7**, 10802 (2016).
261. Akyuz, F. A. & Merwin, J. E. Solution of nonlinear problems of elastoplasticity by finite elementmethod. *AIAA J.* **6**, 1825–1831 (1968).
262. Zienkiewicz, O. C., Taylor, R. L. & Zhu, J. Z. *The finite element method: its basis and fundamentals*. (Elsevier, 2005).
263. Roters, F. *et al.* Overview of constitutive laws, kinematics, homogenization and multiscale methods in crystal plasticity finite-element modeling: Theory, experiments, applications. *Acta Mater.* **58**, 1152–1211 (2010).
264. Asaro, R. J. & Needleman, A. Overview no. 42 Texture development and strain hardening in rate dependent polycrystals. *Acta Metall.* **33**, 923–953 (1985).
265. Hutchinson, J. W. Bounds and self-consistent estimates for creep of polycrystalline materials. *Proc. R. Soc. London. A. Math. Phys. Sci.* **348**, 101–127 (1976).
266. Su, Y. *et al.* Elastic constants of pure body-centered cubic Mg in nanolaminates. *Comput. Mater. Sci.* **174**, 109501 (2020).
267. Chen, T., Yuan, R., Beyerlein, I. J. & Zhou, C. Predicting the size scaling in strength of nanolayered materials by a discrete slip crystal plasticity model. *Int. J. Plast.* **124**, 247–260 (2020).
268. Huang, S., Beyerlein, I. J. & Zhou, C. Nanograin size effects on the strength of biphase nanolayered composites. *Sci. Rep.* **7**, 1–10 (2017).
269. Li, N., Wang, J., Misra, A. & Huang, J. Y. Direct Observations of Confined Layer Slip in Cu/Nb Multilayers. *Microsc. Microanal.* **18**, 1155–1162 (2012).
270. Jian, W. R., Su, Y., Xu, S., Ji, W. & Beyerlein, I. J. Effect of interface structure on dislocation glide behavior in nanolaminates. *J. Mater. Res.* **36**, 2802–2815 (2021).
271. Shen, Y. & Anderson, P. M. Transmission of a screw dislocation across a coherent, slipping interface. *Acta Mater.* **54**, 3941–3951 (2006).

272. Wang, J., Hoagland, R. G., Hirth, J. P. & Misra, A. Atomistic modeling of the interaction of glide dislocations with 'weak' interfaces. *Acta Mater.* **56**, 5685–5693 (2008).
273. Xu, S., Cheng, J. Y., Mara, N. A. & Beyerlein, I. J. Thick interface size effect on dislocation transmission in nanolaminates. *IOP Conf. Ser. Mater. Sci. Eng.* **1249**, 012005 (2022).
274. Xu, S., Cheng, J. Y., Mara, N. A. & Beyerlein, I. J. Dislocation dynamics in heterogeneous nanostructured materials. *J. Mech. Phys. Solids* **168**, 105031 (2022).
275. Demkowicz, M. J. & Hoagland, R. G. Structure of Kurdjumov-Sachs interfaces in simulations of a copper-niobium bilayer. *J. Nucl. Mater.* **372**, 45–52 (2008).
276. Zheng, G. P. Application of phase-field modeling to deformation of metallic glasses. *Curr. Opin. Solid State Mater. Sci.* **15**, 116–124 (2011).
277. Xu, S., Su, Y., Smith, L. T. W. & Beyerlein, I. J. J. Frank-Read source operation in six body-centered cubic refractory metals. *J. Mech. Phys. Solids* **141**, 104017 (2020).
278. Martienssen, W. & Warlimont, H. *Springer handbook of condensed matter and materials data*. (Springer, 2006).
279. Liu, Y. H., Wang, K., Inoue, A., Sakurai, T. & Chen, M. W. Energetic criterion on the intrinsic ductility of bulk metallic glasses. *Scr. Mater.* **62**, 586–589 (2010).
280. Jang, D. & Greer, J. R. Transition from a strong-yet-brittle to astronger-and-ductile state by size reductionofmetallicglasses. *Nat. Mater.* **9**, 215–219 (2010).
281. Li, L., Homer, E. R. & Schuh, C. A. Shear transformation zone dynamics model for metallic glasses incorporating free volume as a state variable. *Acta Mater.* **61**, 3347–3359 (2013).
282. Jiang, F. *et al.* Shear transformation zone volume determining ductile-brittle transition of bulk metallic glasses. *Acta Mater.* **59**, 2057–2068 (2011).
283. Koch, C. C. Structural nanocrystalline materials: An overview. *J. Mater. Sci.* **42**, 1403–1414 (2007).
284. Wada, T., Yubuta, K. & Kato, H. Evolution of a bicontinuous nanostructure via a solid-state interfacial dealloying reaction. *Scr. Mater.* **118**, 33–36 (2016).
285. Alamgir, F. M., Jain, H., Williams, D. B. & Schwarz, R. B. The structure of a metallic glass system using EXELFS and EXAFS as complementary probes. *Micron* **34**, 433–439 (2003).
286. Alamgir, F. M. *et al.* EXAFS and EXELFS Study of the Structure of Pd-Ni-P Bulk Metallic Glasses. *MRS Proc.* **644**, L2.4 (2000).
287. Isheim, D., Siem, E. J. & Seidman, D. N. Nanometer-scale solute segregation at heterophase interfaces and microstructural evolution of molybdenum nitride precipitates. *Ultramicroscopy* **89**, 195–202 (2001).
288. Voter, A. F. & Mendeley. Introduction to the Kinetic Monte Carlo Method. *Radiat. Eff.* 1–23 (2005).
289. Wang, L. & Clancy, P. Kinetic Monte Carlo simulation of the growth of polycrystalline Cu films. *Surf. Sci.* **473**, 25–38 (2001).
290. Xu, H., Osetsky, Y. N. & Stoller, R. E. Self-evolving atomistic kinetic Monte Carlo: fundamentals and applications. *J. Phys. Condens. Matter* **24**, 375402 (2012).
291. Henkelman, G. & Jónsson, H. Long time scale kinetic Monte Carlo simulations without lattice approximation and predefined event table. *J. Chem. Phys.* **115**, 9657–9666 (2001).
292. Zhang, T. *et al.* Recent progresses on designing and manufacturing of bulk refractory alloys with high performances based on controlling interfaces. *J. Mater. Sci. Technol.* **52**, 29–62 (2020).
293. Zhou, X. *et al.* Models of dislocation glide and strengthening mechanisms in bcc complex

concentrated alloys. *MRS Bull.* **48**, 777–789 (2023).
294. Wang, M. M., Tasan, C. C., Ponge, D., Dippel, A. C. & Raabe, D. Nanolaminate transformation-induced plasticity-twinning-induced plasticity steel with dynamic strain partitioning and enhanced damage resistance. *Acta Mater.* **85**, 216–228 (2015).
295. Miracle, D. B. & Senkov, O. N. A critical review of high entropy alloys and related concepts. *Acta Mater.* **122**, 448–511 (2017).
296. Zhao, H. *et al.* Segregation assisted grain boundary precipitation in a model Al-Zn-Mg-Cu alloy. *Acta Mater.* **156**, 318–329 (2018).
297. Barry, A. H., Dirras, G., Schoenstein, F., Tétard, F. & Jouini, N. Microstructure and mechanical properties of bulk highly faulted fcc/hcp nanostructured cobalt microstructures. *Mater. Charact.* **91**, 26–33 (2014).
298. Wei, S. & Tasan, C. C. Deformation faulting in a metastable CoCrNiW complex concentrated alloy: A case of negative intrinsic stacking fault energy? *Acta Mater.* **200**, 992–1007 (2020).
299. Zhu, Y. T., Liao, X. Z. & Wu, X. L. Deformation twinning in nanocrystalline materials. *Prog. Mater. Sci.* **57**, 1–62 (2012).
300. Zhang, R. F. *et al.* Manipulating dislocation nucleation and shear resistance of bimetal interfaces by atomic steps. *Acta Mater.* **113**, 194–205 (2016).
301. Subedi, S., Beyerlein, I. J., LeSar, R. & Rollett, A. D. Strength of nanoscale metallic multilayers. *Scr. Mater.* **145**, 132–136 (2018).
302. Wang, J., Hoagland, R. G. & Misra, A. Room-temperature dislocation climb in metallic interfaces. *Appl. Phys. Lett.* **94**, 1–4 (2009).
303. Van der Giessen, E. & Needleman, A. Modelling and Simulation in Materials Science and Engineering Related content Discrete dislocation plasticity : a simple planar model Discrete dislocation plasticity : a simple planar model. *Model. Simul. Mater. Sci. Eng.* **3**, 689–735 (1995).
304. Wang, L. *et al.* Plastic Deformation through Dislocation Saturation in Ultrasmall Pt Nanocrystals and Its in Situ Atomistic Mechanisms. *Nano Lett.* **17**, 4733–4739 (2017).
305. Balluffi, R. W., Komem, Y. & Schober, T. Electron microscope studies of grain boundary dislocation behavior. *Surf. Sci.* **31**, 68–103 (1972).
306. Imrich, P. J., Kirchlechner, C., Kiener, D. & Dehm, G. In Situ TEM Microcompression of Single and Bicrystalline Samples: Insights and Limitations. *Jom* **67**, 1704–1712 (2015).
307. Callahan, P. G. *et al.* Transmission scanning electron microscopy: Defect observations and image simulations. *Ultramicroscopy* **186**, 49–61 (2018).

9. Appendix

Pillar taper model

Deformation of a tapered pillar (or frustum) is done by modeling it as a finite stack of *N* cylindrical slices of whose diameters/areas match the corresponding width of the frustum. Assuming that yield only occurs in the slices with the lowest cross-sectional area in the yielding frustum and that plastic flow is volume-conserving, the strain required to flatten a right cylinder consisting of previously yielded sections to match the cross-sectional area of the next unyielded slice is found. As the compresssion test proceeds, the right-cylindrical portion of the pillar includes more and more yielded slices with uniform area.

Given a stack of *N* right cylinders of decreasing radius approximating a frustum, the stress $\sigma_i^{\text{yielded}}$ in the yielded segment of the pillar as more slices yield is given by:

$$\sigma_{\text{i}}^{\text{yielded}} = \sigma_{\text{o}} \times \frac{A_o}{A_i} = \sigma_o \times \frac{d_o^2}{d_i^2} = \sigma_o \times S_i$$

where A_o is the initial area at the top of the frustum and σ_o is the stress applied to the pillar assuming that area, i represents the number of slices that have yielded, A_i represents the actual area of the right cylinder once i slices have yielded, d_o and d_i are the diameters corresponding to A_o and A_i, and S_i represents a correction factor that accounts for the changing diameter of the right cylinder. The range of displacements that correspond to a given S_i is found by iteratively calculating the increment of displacement Δl_i required to flatten a right cylinder containing i slices so that its area increases to the area of the next unyielded slice A_{i+1}. This requires calculation of the lengths $l_i^{\text{unyielded}}$ and l_i^{yielded} of the right cylinder before and after flattening:

$$l_i^{yielded} = \left(l_i^{unyielded} + dl\right) \times \frac{A_i}{A_{\text{i+1}}} = \left(l_i^{unyielded} + dl\right) \times \frac{d_{\text{i}}^2}{d_{\text{i+1}}^2}$$

$$\Delta l_i = l_i^{unyielded} - l_i^{yielded}$$

where dl represents the thickness of a slice l_o/N and l_o is the initial height of the frustum. Iteration requires that

$$l_{i+1}^{unyielded} = l_i^{yielded}$$

This produces a set of displacements h_i at which a given S_i applies as a sequence of a finite series. These displacements represent displacement achieved in the pillar after yield:

$$h_i = \sum_{1}^{k=i} \Delta l_k$$

Note that the last series corresponding to h_N gives the final displacement to which this taper correction applies. The stress afterwards is simply calculated as an engineering stress corresponding to the area of the widest slice, A_N. This correction is applied to 10-10 Cu/Nb because it deforms without shear localization to high strain. This is not the case for the 40-10 Cu/Nb, which shear localizes before it can flatten out to a right cylinder. Therefore in the 40-10 case, the average pillar area is used to calculate stress and strain is taken as engineering strain. Yield stresses are extracted from these curves by determining the point at which the stress-strain curve deviates in value by 5% from the linear portion of the curve.

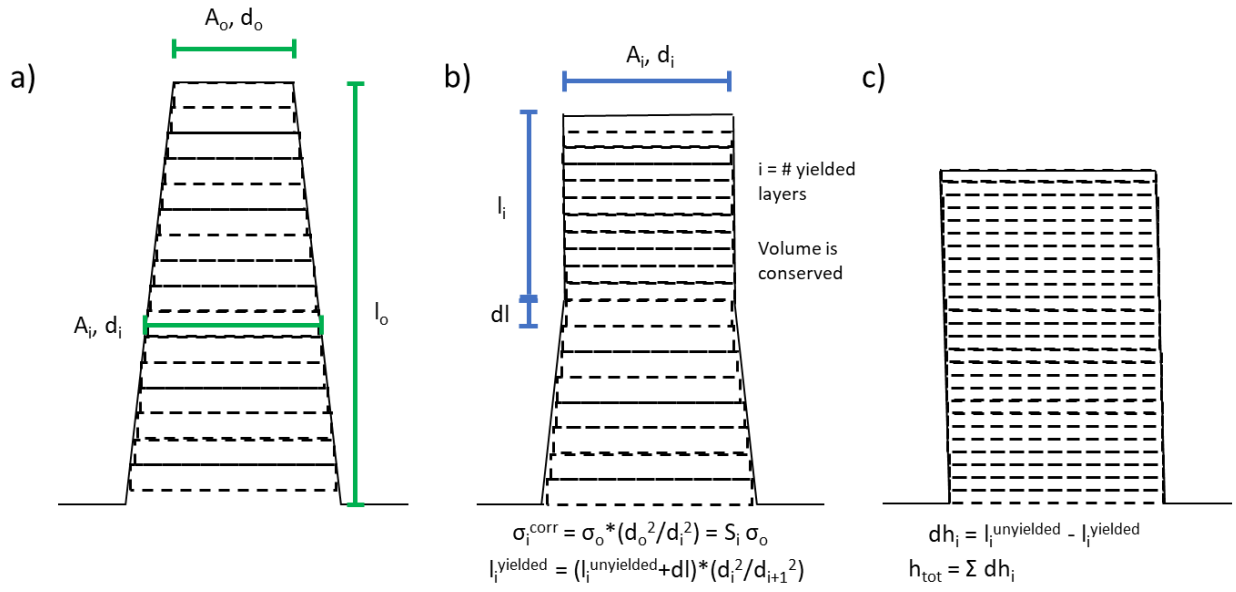

A depiction of the pillar taper correction applied to micropillar tests conducted in this work. a) shows an unyielded, tapered pillar. b) shows a tapered pillar in the process of flattening to a right cylinder. Note that layers higher in the pillar undergo more strain than those that are below. c) shows a fully flattened pillar.

STEM imaging conditions for Chapter 6

Figure	Imaging mode	Acceptance angle (mrad)
6-12	HAADF	26-159
6-13	HAADF	a) 26-159 b) 59-200
6-17	HAADF	(a,c) 26-159
6-15	HAADF	(b,c) 26-159
6-27	BF	0-33

E_r for indentation tests

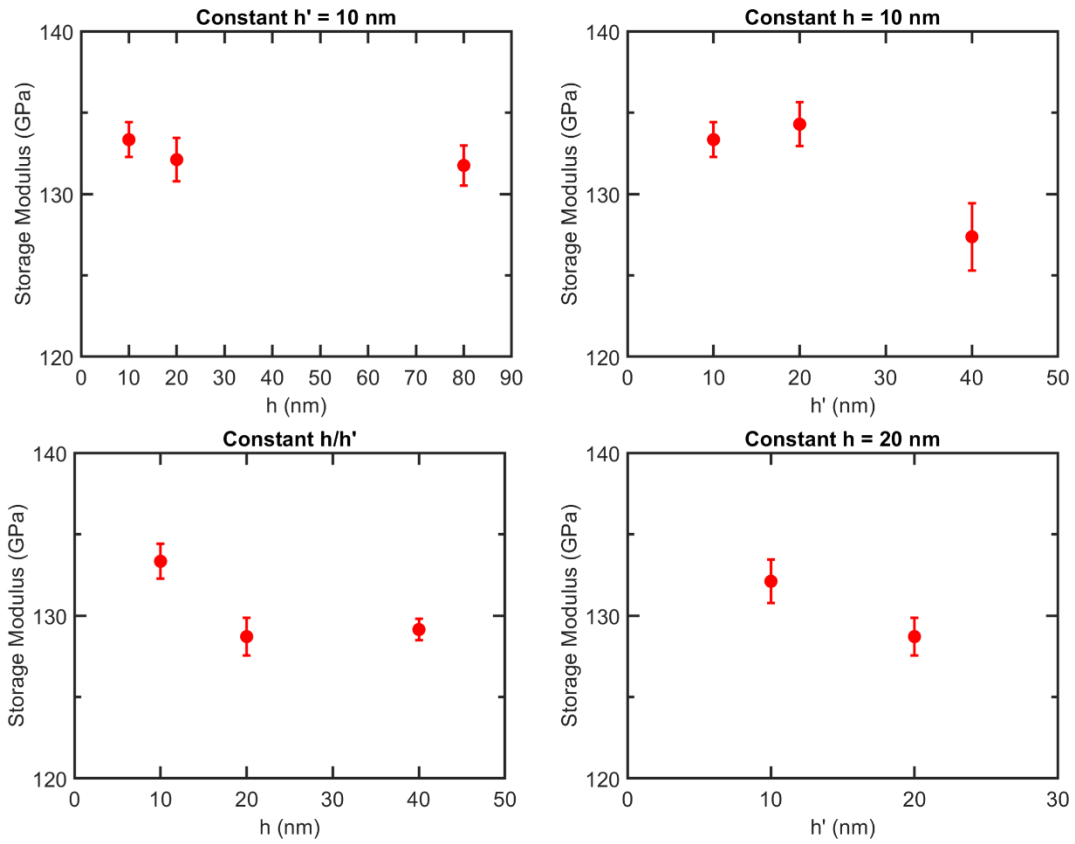

E_r averages obtained for the same series of 3D Cu/Nb specimens as in Figure 6-30.